TWO-PHASE MODELING OF GRANULAR SEDIMENT FOR SHEET FLOWS AND SCOUR.

A Dissertation

Presented to the Faculty of the Graduate School

of Cornell University

in Partial Fulfillment of the Requirements for the Degree of

Doctor of Philosophy

by

Laurent Olivier Amoudry

January 2008

TWO-PHASE MODELING OF GRANULAR SEDIMENT FOR SHEET FLOWS AND SCOUR.

Laurent Olivier Amoudry, Ph.D.

Cornell University 2008

Even though sediment transport has been studied extensively in the past decades, not all physical processes involved are yet well understood and represented. This results in a modeling deficiency in that few models include complete and detailed descriptions of the necessary physical processes and in that models that do usually focus on the specific case of sheet flows. We seek to address this modeling issue by developing a model that would describe appropriately the physics and would not only focus on sheet flows.

To that end, we employ a two-phase approach, for which concentration-weighted averaged equations of motion are solved for a sediment and a fluid phase. The two phases are assumed to only interact through drag forces. The correlations between fluctuating quantities are modeled using the turbulent viscosity and the gradient diffusion hypotheses. The fluid turbulent stresses are calculated using a modified $k-\varepsilon$ model that accounts for the two-way particle-turbulence interaction, and the sediment stresses are calculated using a collisional granular flow theory.

This approach is used to study three different problems: dilute flow modeling, sheet flows and scouring. In dilute models sediment stresses are neglected. Near bed processes are instead modeled through the bottom boundary conditions and we consider and compare two widely used approaches. We also introduce and validate a concentration dependent Schmidt number.

The sheet flow model is validated for different flow conditions. Several well-

known results and formulae are confirmed such as reduced turbulence in the diluted region, the bed load layer thickness and the dependence of the sediment transport rate on the Shields parameter. It also provides a counterexample to modeling the bed shear stress in phase with the free stream velocity. Finally, it provides information on the vertical sediment flux, which could be used to model the bottom boundary condition in dilute models.

The two-phase model is also shown to be able to represent two-dimensional sediment transport issues. A simple benchmark test case (scouring downstream of an apron) is performed and results are found to reproduce reasonably well existing experimental data.

Future work on sediment transport modeling is also discussed.

BIOGRAPHICAL SKETCH

I was born in Suresnes (just outside of Paris) in 1978. Upon high school graduation and still undecided about my future, I chose to follow the path to the "Grande Ecoles". There I hated math, loved physics and discovered fluid mechanics. In 1998, I went to the Ecole Centrale de Lyon. In 2000, I came to Cornell as an exchange student for one year. The path after graduation, with both masters from Cornell and Ecole Centrale de Lyon, should have been to find a job in the aerospace industry. Fortunately, I found out that environmental fluids were way cooler (and the aerospace industry wasn't doing so great in 2001). So I started the last part of my studies in 2002 in Environmental Fluid Mechanics at Cornell.

ACKNOWLEDGEMENTS

So many people, so little space. I would like to first thank my advisor Prof. Philip L.-F. Liu. I don't think it is possible to accurately portray how much he helped, but I would have ever finished without his support, guidance and advice. Both Prof. James T. Jenkins and Prof. Edwin A. Cowen have also contributed and helped tremendously in so many different ways.

The contribution of Prof. Tian-Jian Hsu (University of Florida) also has to be acknowledged. So do Prof. Michel Y. Louge's comments and Prof. Charles K. Williamson's help. The interaction with many other researchers and professors both at Cornell and elsewhere has allowed me to broaden and deepen my knowledge of sediment transport and fluid mechanics. I'm also thankful to all the people in the Environmental Fluid Mechanics and Hydrology group at Cornell through the years.

My family has always been amazingly understanding and supportive, and I'll never thank them enough. I also would have never made it that far without all my friends on both sides of the Atlantic, if you ever read this (which, somehow, I doubt), you'll know who you are.

TABLE OF CONTENTS

LIST OF TABLES

LIST OF FIGURES

LIST OF SYMBOLS

Greek letters

α: correlation between fluid velocity and sediment velocity fluctuations

α_{bed}: angle between the bed and the x-axis

α_{s0}: upstream scour slope

β: drag coefficient

$\bar{\beta}$: concentration-weighted drag coefficient

β': fluctuation of the drag coefficient

γ: dissipation of sediment fluctuation energy

δ: boundary layer thickness

δ_s: bed load layer thickness

δ_{ij}: Kronecker delta

$\delta\tilde{u}_i^f$: $\delta\tilde{u}_i^f \equiv \bar{u}_i^f - \tilde{u}_i^f$

$\delta\tilde{u}_i^s$: $\delta\tilde{u}_i^s \equiv \bar{u}_i^s - \tilde{u}_i^s$

Δt: time step

Δu_i^f: i^{th} component of the fluid phase velocity fluctuation

Δu_i^s: i^{th} component of the sediment phase velocity fluctuation

Δx: grid size in x-direction

Δz: grid size in z-direction

ε_B: bed load transport efficiency

ε_f: fluid turbulence dissipation rate

ε_S: suspended load transport efficiency

ζ: location of bottom boundary respect to undisturbed bed for dilute model

η: Kolmogorov turbulent length scale

θ: Shields parameter

θ_c: critical Shields parameter for initiation of sediment motion

θ_l: Shields parameter value used in reference concentration approximation

θ_s: critical Shields parameter for initiation of suspension

κ: von Karman constant

κ_c: collisional sediment fluctuation energy diffusivity

λ: linear concentration

λ_{fs}: parameter in added mass interphase momentum transfer

Λ: wave length

μ_c: collisional shear viscosity

μ_d: parameter in *Engelund and Fredsøe* (1976) model

μ_e: shear modulus

μ_f or μ^f: fluid dynamic viscosity

ν or ν_f: fluid kinematic viscosity

ν_T: turbulent eddy viscosity

ν_t: small-scale turbulence eddy viscosity

Π_h: dimensionless parameter representing the influence of the water depth

ρ_f or ρ^f: fluid density

ρ_s or ρ^s: sediment mass density

σ_c sediment Schmidt number

σ_{c0}: sediment Schmidt number for at the zero concentration limit

σ_k: Prandtl number for turbulent kinetic energy

σ_ε: Prandtl number for turbulence dissipation rate

τ_{ij}^f: total fluid stress tensor

τ_{ij}^s: total sediment stress tensor

τ_{ij}^{sc}: collisional sediment stress tensor

τ_{ij}^{se}: enduring contacts sediment stress tensor

τ_b: mixture bed shear stress

τ_L: time scale related to lift force momentum transfer

τ_M: time scale related to added mass momentum transfer

ϕ: phase for periodic flows

ϕ_c: phase lag between concentration and free stream velocity

$\phi_{A/B}$: phase lag between A and B for periodic flows

Φ_B: bed load sediment transport rate

Φ_S: suspended load sediment transport rate

Φ_T: total sediment transport rate

ψ: angle of friction of sediment

Ψ_p: pick-up function

ω: angular frequency of periodic flow

ω_c: collisional bulk viscosity

ω^f: vorticity of fluid flow

Ω_{ij}^f: fluid phase rate of rotation tensor

Lower case roman letters

c: sediment concentration

$\bar{c}$: averaged concentration

c': concentration fluctuation

$c_\star$: random loose packing concentration ($c_\star = 0.57$)

$c^\star$: random close packing concentration ($c^\star = 0.635$)

c_{exp}: experimental concentration

c_{max}: saturation concentration in reference concentration formula

c_{num} numerical concentration

c_{ref}: reference concentration

c_{z0}: concentration at bottom of the suspension layer

c_1, c_2: constants in $C_{\varepsilon 2}$ formula

d: particle diameter

e: collision restitution coefficient

f_w: wave friction factor

g: gravitational constant

g_i: i^{th} component of the gravitational force

g_0: radial distribution function

$g_0^\star$: modified radial distribution function

h: water depth

h_0: water depth above apron

k_f: turbulent kinetic energy

k_s sediment fluctuation energy

l_c: mean free path between collisions

l_e: turbulence integral length scale

m: empirical constant in *Meyer-Peter and Müller* (1948) and *Ribberink* (1998) formulas

n: power in concentration dependence of the drag

n_σ: power in concentration dependent Schmidt number

n_s: power in time dependence of maximum scour depth downstream of an apron

p_c: collisional pressure

$q = \bar{c}\tilde{u}^s$: horizontal sediment flux

q^+: positive part of q

q^-: negative part of q

q_{exp}: experimental q

q_n: present numerical q

q_o: numerical q obtained using *Hsu et al.* (2004)

s: specific gravity of sediment

t: time

$\bar{u}$: depth averaged velocity

u_i^f: i^{th} component of the fluid velocity

$\tilde{u}_i^f$: i^{th} component of the concentration-weighted averaged fluid velocity

$\tilde{u}^f$: flow direction (horizontal) component of the averaged fluid velocity

$\hat{u}_i^f$: i^{th} component of the tentative fluid velocity

$u_i^r \equiv u_i^f - u_i^s$

u_i^s: i^{th} component of the sediment velocity

$\tilde{u}_i^s$: i^{th} component of the concentration-weighted averaged sediment velocity

$\tilde{u}^s$: flow direction (horizontal) component of the averaged sediment velocity

$u_\star$: friction velocity

$u_{\star 0}$: friction velocity above apron

$u^+ \equiv \tilde{u}^f / u_\star$

$\tilde{w}^f$: normal to the flow direction (vertical) component of the averaged fluid velocity

$\tilde{w}^s$: normal to the flow direction (vertical) component of the averaged sediment velocity

x: flow direction or horizontal direction

x_i: i^{th} direction

x_{smax}: location in x direction of the maximum scour depth downstream of an apron

z: vertical direction or direction normal to the flow direction

z_0: bottom of the suspension layer

z_r: distance above bed in Rouse formula

z_s: scour depth downstream of an apron

z_{smax}: maximum scour depth downstream of an apron

Upper case roman letter

A: wave amplitude

B: Bagnold number

C: wave celerity

C_L: lift coefficient

C_M: added mass coefficient

$C_{\varepsilon 1}$, $C_{\varepsilon 2}$, $C_{\varepsilon 20}$, $C_{\varepsilon 3}$: coefficients in turbulence dissipation rate equation

C_μ: coefficient in k_ε model

D_{50}: sediment median diameter

$D_\star$: sediment non-dimensional diameter

D_{ij}^f: fluid phase strain rate tensor

D_p: two-phase flow term in fluid turbulence balance equations

$E = \rho_f(1-\bar{c})\varepsilon_f$

E_{rms}: root mean square error

G: measure of stress in *Bagnold* (1954)'s experiments

$G_0 \equiv \bar{c}g_0(\bar{c})$

$G_0^\star \equiv \bar{c}g_0^\star(\bar{c})$

I_i: i^{th} component of the interphase momentum transfer

I_i^d: i^{th} component of the interphase momentum transfer due to the drag forces

I_i^{am}: i^{th} component of the interphase momentum transfer due to the added mass force

I_i^l: i^{th} component of the interphase momentum transfer due to the lift force

$K = \rho_f(1-\bar{c})k_f$

K_f: mean kinetic energy of fluid

$\tilde{K}_f$: kinetic energy of concentration weighted averaged velocity

K_s: bed roughness

K_{s0}: bed roughness of the apron

$K^s = \bar{c}k_s$

M^{df}:part of M^f due to all forces on the interface but the force due to the interfacial pressure.

M^{ds}: part of M^s due to all forces on the interface but the force due to the interfacial pressure.

M^f: rate of momentum generation for the fluid phase

M^s: rate of momentum generation for the sediment phase

P^c: sediment phase pressure due to the particle-particle interaction

P^f: fluid pressure

$\bar{P}^f$: averaged fluid pressure

$P^{f'}$: fluid pressure fluctuation

P^{fi}: interfacial pressure of the fluid phase

P^s: sediment phase pressure

P^{si}: interfacial pressure of the sediment phase

Q_B: bed load sediment transport rate

Q_S: suspended load sediment transport rate

Q_T: total sediment transport rate

Q_j^f: fluid turbulent kinetic energy flux

$Re_\star$: friction velocity Reynolds number

Re_p: particle Reynolds number

R_{ij}^f: fluid phase "Reynolds" stress tensor

R_p: fall parameter

Ro: Rouse parameter

R_{ij}^s: sediment phase "Reynolds" stress tensor

S: non-dimensional parameter representing the influence of the period for periodic flows

S_0: slope of open channel flow

T: period for periodic flows

T_{ij}^f: fluid stress tensor

T_j^k: transport term in turbulent kinetic energy balance equation

T_j^ε: transport term in turbulence dissipation rate equation

T_{ij}^s: sediment stress tensor

T_c: time scale between collisions

T_F: turbulence time scale

T_p: particle response time

T_s: time at which $z_{smax} = h_0$

U: fluid velocity scale

U_0: fluid free stream velocity

U_c: current part of the free stream velocity

U_{osc}: amplitude of the oscillatory part of the free stream velocity

U_1, U_2: velocity amplitudes used to define a 2nd order Stokes wave

U_r: magnitude of the relative velocity of the sediment respect to the fluid

$U^s = \bar{c}\tilde{u}^s$

W_s: sediment fall velocity

$W^s = \bar{c}\tilde{w}^s$

X_{rbc}: location of the downstream boundary condition for the two-dimensional simulations

Calligraphic letters

$\mathcal{P}_k$: stress production of turbulent kinetic energy

$\mathcal{Q}_j$: j^{th} component of the flux of sediment fluctuation energy

CHAPTER 1

INTRODUCTION

1.1 Coastal management

Throughout history humans have naturally settled on coastlines or near rivers. Such coastal and fluvial environments are attractive because of transport, food and ecological benefits. This trend is still true nowadays as nearly 40 % of the world population (53 % of the United States population) lives in coastal zones (*Small and Cohen*, 2004; *Crossett et al.*, 2004). In addition to accounting for a large part of the population, coastal and fluvial areas are also the most densely populated (*Small and Cohen*, 2004). Such crowdedness coupled with continual coastward migration and recent increasing tourism add up to the strain on the environment. Interactions between humans and coastal and fluvial zones then require appropriate management. One of the main issues pertinent to such management of coastal and fluvial areas is sediment transport, the importance of which is emphasized by the fact that a vast majority of the world sandy beaches are already eroding and that this process will increases with sea level rise (e.g., *Leatherman et al.*, 2003).

1.2 Studying sediment transport

Sediment transport in coastal and fluvial environments can be seen as studying the motions of particles and of an ambient fluid flow, as well as their interactions. As such it is already a complex, multidimensional and dynamic process. In addition, studies in coastal environments will need to consider the effect of waves on both the fluid and particles motions. Man made structures are also common both in fluvial and coastal areas and lead to another level of complexity as their interactions with fluid and particles are considered.

Early works on sediment transport were achieved following simple theoretical assumptions or empirical results and focused on open channel flows. *Rouse* (1937) derived a concentration profile for sediment in steady open channel flows by equating the upward transfer of sediment due to the mixing process to the particle settling. *Bagnold* (1966) obtained expressions for the sediment transport rate by following energetic considerations. *Meyer-Peter and Müller* (1948) and *Wilson* (1966) provided empirical formulation of the bed load sediment transport rate in open channel flows from experimental results obtained using bed load traps. Scouring in river engineering were also investigated experimentally early on (e.g., *Breusers*, 1966, 1967; *Dietz*, 1969). However, more complex flow situations such as sediment transport in wave-current boundary layers first required a better understanding of the hydrodynamics, which was achieved through analytical studies (e.g., *Grant and Madsen*, 1979; *Fredsøe*, 1984), experimental studies (e.g., *Jensen et al.*, 1989) and numerical studies (e.g., *Davies et al.*, 1988).

1.2.1 Models for hydrodynamic conditions and sediment transport

Sediment transport models can generally first be divided into single phase models and two-phase models. The former assume that the presence of sediment has no influence on the hydrodynamics (fluid velocity and pressure), while the later consider equations of motion for a fluid phase and a sediment phase and inter-phase interactions (*Drew*, 1983). In single phase models, the sediment concentration is commonly obtained using an advection diffusion equation. The interaction between the presence of sediment particles and the fluid turbulence can be neglected (e.g., *Savioli and Justesen*, 1996) or accounted for, to some extent, through a "buoyant energy production" term that is similar to that of density stratified flows (*Hagatun*

and Eidsvik, 1986). Most two-dimensional models are still using this single phase approach where clear fluid Navier-Stokes equations are solved to determine the fluid flow and an advection-diffusion equation is solved to obtain the sediment concentration (*Zhang et al.*, 1999; *Harris and Wiberg*, 2001). In order to consider some near bed effects, a mass balance equation for the bed load can be considered (*Minh Duc et al.*, 2004; *Wu*, 2004). Finally, in such two-dimensional models, the bathymetric changes are calculated by solving an "erosion equation", which is the conservation of sediment mass between the water column and the sediment bed (*Harris and Wiberg*, 2001; *Hsu et al.*, 2006; *Hatton et al.*, 2007). Models developed to study scouring around structure also usually follow the same approach (*Brørs*, 1999). Only recently have two-phase approaches been pursued in scour numerical models (*Zhao and Fernando*, 2007).

For one-dimensional flows such as sediment transport under sheet flow conditions, the two-phase flow approach is becoming increasingly popular (e.g., *Kobayashi and Seo* (1985); *Asano* (1990); *Dong and Zhang* (1999); *Greimann et al.* (1999); *Hsu* (2002) and *Hsu et al.* (2003b); *Jiang et al.* (2004); *Longo* (2005); *Liu and Sato* (2005, 2006) more recently). As mentioned previously, this approach solves equations of motion (conservation of mass and momentum) for two phases. Momentum transfer between the two phases is taken into account and is usually specified by considering the forces of the fluid on the sediment particles (*Drew et al.*, 1979; *Drew and Lahey*, 1979). The turbulent fluid stress can be obtained by using a variety of fluid turbulence closures. Most of them are based on the turbulent viscosity hypothesis and the eddy viscosity can then be calculated by a specified profile (e.g., *Kobayashi and Seo*, 1985; *Greimann and Holly*, 2001; *Jiang et al.*, 2004), by using the mixing-length concept (e,g, *Asano*, 1990; *Dong and Zhang*, 1999; *Liu and Sato*, 2005, 2006), by using a length scale and solving a bal-

ance equation for the turbulent kinetic equation (one-equation model), or lastly by using complete two-equations turbulence closures such as $k - \varepsilon$ models (e.g., *Hsu, Jenkins, and Liu*, 2003a; *Hsu, Chang, and Hsieh*, 2003b; *Longo*, 2005). The effect of sediment particles on the carrier fluid turbulence also has to be considered and has been studied in chemical and mechanical engineering (e.g., *Gore and Crowe*, 1989; *Hetsroni*, 1989; *Rashidi et al.*, 1990; *Elghobashi*, 1994; *Squires and Eaton*, 1994; *Crowe et al.*, 1996). These studies show that the presence of particles does impact the carrier fluid turbulence and can increase or decrease its intensity. Very importantly, sediment stresses also need to be appropriately specified if not neglected. Pioneering experimental work on the sediment stresses was done by *Bagnold* (1954) (briefly reviewed in chapter 2). Another empirical expression was introduced later by *Savage and McKeown* (1983) following similar experiments. Both observe a regime for which the particle inertia is the dominant mechanism and a regime for which the viscous effects of the interstitial fluid dominate. Both focused on neutrally buoyant particles and further experiments on the shearing of a suspension of buoyant spherical particles were conducted (*Hanes and Inman*, 1985a,b). Theoretical formulations of the sediment stresses have also been derived and can be used instead of the empirical relationships. For example, *Jenkins and Savage* (1983) and *Jenkins* (1998) express the constitutive relations of the sediment stress for frictionless spheres in a collisional regime (where particle inertia dominates) as a function of the sphere properties, concentration and fluctuation energy. When the viscosity dominates other constitutive relations for the stresses can be used (e.g., *Carpen and Brady*, 2002).

1.2.2 Experiments on sediment transport

Experimental data on sediment transport are crucial to further understanding of the processes involved, first by helping develop empirical models and then by validating theoretical and numerical models. Early on, sediment transport experiments focused on concentration and velocity measurements respectively using suction samplers and pitot tubes. Measurements close to the bed were not possible and bed load measurements consisted on calculating the bed load transport using bed load traps.

For sheet flows, the near bed region is crucial but measurements are difficult due to the small size (the near bed region is usually less than about 1 to 2 cm) and the relatively high sediment concentration. In particular, the presence of sediment renders most acoustic and optical methods (Acoustic Doppler Velocimetry and Laser Doppler Velocimetry for example) inaccurate. Still, recent improvements in measurement techniques have allowed experimental data to be collected close to the bed. *Horikawa et al.* (1982) conducted some of the earliest experiments on sheet flows in oscillating water tunnels. The concentration was obtained using a photographic technique in the dilute region and using a conductivity technique in the concentrated region. The velocity was also measured with the photographic technique and extrapolated in the concentrated region. More recently, Concentration-Conductivity Meters (CCM) have been used to measure near bed sediment concentration for various sheet flows in oscillating water tunnels (e.g., *Katopodi et al.*, 1994b; *Ribberink and Al-Salem*, 1995; *Janssen*, 1999; *O'Donoghue and Wright*, 2004). Near bed sediment velocities have also been calculated using CCMs by correlating the concentration measurements between two probes (e.g., *McLean et al.*, 2001; *Hassan and Ribberink*, 2005), but a clear drawback of this method is that CCMs are intrusive and using two probes to obtain velocity mea-

surements necessarily means that one is downstream of the other (in its wake). A boroscopic technique has also been developed recently (*Dudley*, 2007) to measure near bed sediment velocity following a concept similar to that of Particle-Image Velocimetry. This technique, although also intrusive, only uses one probe to measure the velocity, but near bed concentration have not been measured yet with it.

Two-dimensional experimental data of concentration and velocity is very rare, which is due to most experimental techniques providing point measurements and being intrusive. In scouring problems the focus has usually not been on the near bed processes but rather on the bathymetry, which is easier to measure, and the general fluid flow patterns. Such experimental data has thus been less restricted by measurement techniques. *Breusers* (1966), *Breusers* (1967) and *Dietz* (1969) conducted experiments on scouring downstream of structures and reported several key parameters representative of the scour hole geometry as well as velocity vertical profiles at different locations. Scour below pipelines has also been studied experimentally by focusing on the scour hole characteristics, both in the case of currents (many of these experimental studies are summarized in *Sumer and Fredsøe* (2002)) and in the case of waves (e.g., *Sumer and Fredsøe*, 1990). The flow patterns for scour below pipelines in a current have also been investigated using Laser Doppler Velocimetry by *Jensen et al.* (1990). For two-dimensional cases other than scour most of the available two-dimensional data still remains focused on the bathymetry. For example, even though *Ribberink and Al-Salem* (1994) did measure concentration vertical profile in cases of rippled beds (which are two-dimensional) they performed a "bed-averaging" by moving the suction probe slowly over a number of ripples and therefore do not really obtain two-dimensional concentration data. Another example of two-dimensional bathymetry experimen-

tal data concerns the study of sand bar evolution under partially-standing and standing waves (e.g., *O'Hare and Davies*, 1990, 1993; *Landry et al.*, 2007).

1.3 Scope of the dissertation

Sediment is defined as any granular material that will settle in water by the action of gravity. The mechanical behavior of sediment depends greatly on the particle size distribution and the material composition. We will focus in this thesis on non-cohesive sediment. The main difference between cohesive sediments and non-cohesive sediments is flocculation (the formation and break-up of flocs of sediment), and cohesive sediment usually consists of a mixture of clay, silt, and fine sand (amongst others) (*Winterwerp and van Kesteren*, 2004). As such cohesive sediment is smaller than non-cohesive sediment, and we choose to differentiate these two types of sediment purely based on their particle size. Although it is difficult to define a precise particle diameter threshold between cohesive and non-cohesive behavior, clay is smaller than silt which is usually classified as having a diameter smaller than about $60\mu m$, while fine sand has a particle diameter smaller than 0.2 mm. Any sediment particle with a particle diameter larger than 0.2 mm will then be considered non-cohesive. Finally, we are typically interested in sand transport for which the specific gravity is 2.65.

We present in this thesis a two-phase model for non-cohesive sediment transport. This model accounts for the interphase momentum transfer by only considering drag forces. A two-equation closure ($k - \varepsilon$) is employed to model the fluid turbulence and constitutive relations derived for collisional flows are used to model the sediment stresses.

In chapter 2, we will provide an introduction to the study of sediment transport by presenting appropriate parameterization and classification of the processes

involved. We also review some basic empirical models for sediment transport for steady and oscillatory flows.

In chapter 3, we present the two-phase flow approach used here to model sediment transport. Equations of motions for both a fluid and a sediment phase are introduced and averaged. Closure for the momentum transfer between the two phases, the fluid turbulence (i.e. the fluid phase stresses), the sediment phase stresses and turbulent suspension are also discussed.

In chapter 4, we simplify the model by assuming a dilute concentration and study the remaining model's closure issues. In dilute flow models, sediment stresses are neglected and near-bed processes occurring in the concentrated region are then modeled through appropriate bottom boundary condition. Two different approaches for the boundary condition are implemented and studied. The turbulent suspension closure is also discussed and a concentration dependent sediment diffusivity is considered.

In chapter 5, the full model presented in chapter 3 including the sediment stress closure is implemented for sheet flows (i.e., one-dimensional case). Improvements on the traditional $k - \varepsilon$ fluid turbulence model are sought by considering a better representation of the sediment particle fluid turbulence interaction. The model is then validated using experimental data of sediment velocity in an open channel flow, and of sediment concentration and sediment flux data of sheet flows in oscillating water tunnels.

In chapter 6, we further study results obtained using the one-dimensional model for steady sheet flows, oscillating sheet flows and a pulsating sheet flow. In all three cases, important features of sheet flows are discussed.

In chapter 7, the two-phase model is implemented for two-dimensional situations. We review there the governing equations as well as the numerical implemen-

tation of the model. In particular, the bottom boundary conditions, bed treatment, discretization scheme, cycle algorithm and numerical stability are all discussed.

In chapter 8, an example of a two-dimensional situation is studied. We use there the model introduced and described in chapters 3 and 7 for simulate scouring downstream of a rough apron.

CHAPTER 2

BASIC CONCEPTS OF SEDIMENT TRANSPORT

In this chapter, we will provide some insight on usual parameterization and classification of sediment transport. The main quantity of interest in sediment transport studies being the sediment transport rate, we then present several common, simple and widely used models that provide the transport rate as a function of flow parameters both for steady and unsteady flows. We will then discuss on the necessity to pursue more advanced models.

2.1 Dimensionless expression of sediment transport

Steady sediment transport can usually be parameterized in terms of four dimensionless quantities, the choice of which is not unique (*Yalin*, 1977). Both the specific gravity of the sediment material $s = \rho_s/\rho_f$ (ρ_s and ρ_f being the sediment and fluid mass densities) and the Shields parameter

$$\theta = \frac{u_\star^2}{(s-1)gD_{50}} = \frac{\tau_b}{\rho_f(s-1)gD_{50}}, \tag{2.1}$$

where $u_\star = \sqrt{\tau_b/\rho_f}$ is the friction velocity, τ_b the fluid flow bed shear stress and D_{50} the median sediment diameter, are widely used. A third dimensionless parameter usually involves the fluid depth h (h/d or a Froude number such as $u_\star/\sqrt{gh}$ for example). The fourth parameter reflects the effect of the fluid viscosity and a Reynolds number is appropriate. Several choices for the velocity scale are possible. The simplest is to use the friction velocity as a velocity scale and define

$$Re_\star = \frac{u_\star D_{50}}{\nu} \tag{2.2}$$

as the Reynolds number, where ν is the fluid kinematic viscosity. It is also possible to develop a Reynolds number that only depends on the sediment grains and fluid

properties:

$$R_p = \frac{D_{50}\sqrt{(s-1)gD_{50}}}{\nu}. \tag{2.3}$$

Such a parameter shows the relative importance of the gravity and the viscosity of the fluid, and has been called fall parameter (*Jenkins and Hanes*, 1998). These two Reynolds numbers are related

$$Re_\star = R_p\sqrt{\theta} \tag{2.4}$$

Even though both $Re_\star$ and R_p have been used, we choose here to use R_p because it has the advantage of being independent of the flow stage ($u_\star$). Several other parameters similar to the fall parameter have also been developed and used in previous studies (e.g., $D_\star = R_p^{2/3}$ in *van Rijn* (1984a,b,c)).

Still, such non-dimensional expression of sediment transport does not take into account the period for oscillatory flows. *Sleath* (1994) introduced a parameter that can be viewed as a relative measure of pressure gradient and gravitational forces:

$$S = \frac{U_0\omega}{(s-1)g} \tag{2.5}$$

where U_0 is the amplitude of the oscillatory velocity just above the boundary layer and ω the angular frequency. At low S values, the effect of the pressure gradient is negligible, the mobile layer of sediment is thin and the flow is driven by the shear exerted by the fluid above he sediment. Such a situation is referred to as a quasi-steady regime (e.g., *Sleath*, 1994; *Zala Flores and Sleath*, 1998). The limit of the steady regime corresponds to the limit of zero angular frequency and thus $S = 0$. For large values of S the effects of the pressure gradient are important, and this situation has been referred to as the "pressure gradient" regime (*Sleath*, 1994; *Zala Flores and Sleath*, 1998)

2.2 Sediment transport classification

2.2.1 Sediment transport modes

Sediment transport of non-cohesive particles is usually split into two modes based on the mechanisms of transport: bed load and suspended load. Bed load is usually defined as the region where sediment particles roll, slide and jump while staying mostly in contact with the bed. In other words, it corresponds to the region where interparticle interactions play a dominating role. It occurs in a relatively thin region of high concentration where sediment transport responds instantly to bed shear stress. Above the bed load, the suspended load is the part that results from the fluid turbulence agitation. Although mathematical models for sediment transport commonly assume by necessity a sharp interface between bed load and suspended load, such an interface does not actually exist. Moving away from the bed and as the concentration decreases, fluid turbulence becomes stronger while intergranular interactions diminish and the transition between bed load and suspended load is gradual.

A third mode of sediment transport is also referred to: the wash load. Contrary to the the bed load and suspended load, which are differentiated by the transport mechanisms, the wash load does not correspond to a third transport mechanism, and, in that sense, it is part of the "suspended load". However, the wash load is the transport of very fine particles usually not represented in the bed, and thus does not transport bed material. A more precise terminology for the different modes of transport would then be: bed material bed load, bed material suspended load and wash load. It is nevertheless common to associate the term sediment transport to bed material transport and to neglect wash load.

For a steady flow over a bed of non-cohesive sediment, the grains will not

move for very small flow velocities. There exists a velocity critical value for the initiation of motion of the sediment particles. For flow velocities higher than the critical value, sediment particles start to move and interact with each other in a bed load regime. *Shields* (1936) provided a solution to the problem of the threshold for sediment motion and related the critical Shields parameter θ_c to $Re_\star$ through an experimental curve. Several mathematical relationships have since been derived to approximate the Shields curve $\theta_c = f(Re_\star)$. Because θ, $Re_\star$ and R_p are not independent, the Shields curve can also be approximated by functions of the form $\theta_c = f(Re_p)$, such as the one introduced by *van Rijn* (1984a):

$$\theta_c = \begin{cases} 0.24 D_\star^{-1} & D_\star \leq 4 \\ 0.14 D_\star^{-0.64} & 4 < D_\star \leq 10 \\ 0.04 D_\star^{-0.10} & 10 < D_\star \leq 20 \\ 0.013 D_\star^{0.29} & 20 < D_\star \leq 150 \\ 0.055 & D_\star > 150 \end{cases} \tag{2.6}$$

where $D_\star = R_p^{2/3}$.

For increasing flow velocities, the fluid turbulence intensity increases until it is strong enough to entrain particles into suspension. In a way similar to the initiation of sediment motion, there exists a threshold for sediment suspension. For still higher flow velocities, sediment is transported both in bed load and suspended load. Several threshold formulae have been introduced for the initiation of suspended load (e.g., *Bagnold*, 1966; *van Rijn*, 1984c). *Bagnold* (1966) argued that sediment particles can remain suspended only if the vertical velocity of the turbulent eddies exceeds the sediment particles fall velocity and expressed this suspension criterion as

$$\theta_s = 0.64 \frac{W_s^2}{(s-1)gd} \tag{2.7}$$

where W_s is the sediment fall velocity. *van Rijn* (1984c) represented experimental

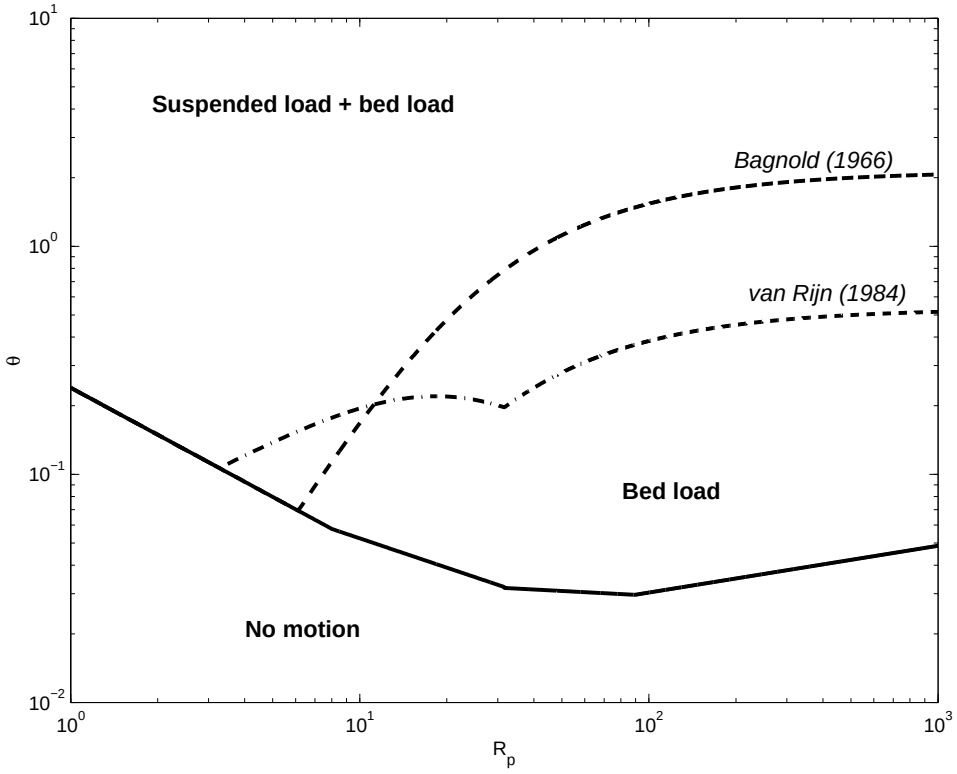

Figure 2.1: Sediment motion and sediment suspension thresholds. The solid line represents the Shields curve approximated by equation 2.6, the dashed line represents the Bagnold suspension criterion (equation 2.7) and the dash-dotted line the van Rijn experimental suspension criterion (equation 2.8).

results by the following criterion:

$$\theta_s = \begin{cases} \frac{16W_s^2}{D_\star^2(s-1)gd} & 1 < D_\star \leq 10 \\ \frac{0.4^2W_s^2}{(s-1)gd} & D_\star > 10 \end{cases} \tag{2.8}$$

Both the sediment motion and the sediment suspension thresholds can be plotted in a R_p - θ plane (figure 2.1) to illustrate the range of bed load and suspended load. For given fluid viscosity and sediment specific gravity, a range of fall parameters corresponds to a range of sediment diameters. For sand in water, we have $s = 2.65$ and $\nu \approx 1.0 \times 10^{-6} m^2/s$, so that the range of fall parameters in figure 2.1 corresponds to grains of diameters from about 40 μm to 4 mm. For small flow velocities (small θ), sediment does not move for all values of R_p. As the flow velocity (θ) increases, sediment transport behavior differ depending on the value

of the fall parameter. For small values (R_p less than about 5), sediment is always transported both in bed load and in suspended load and the "pure" bed load mode does not exist. For higher fall parameters, sediment first moves in bed load and then is suspended as the flow velocity (θ) increases.

2.2.2 Bedform regimes

Different bedform regimes are encountered in coastal and fluvial environments and they mainly depend on the strength of the flow, which is usually represented by the Shields parameter. When the flow is too weak to induce sediment motion ($\theta < \theta_c$), bedforms will usually be determined by previous stronger events (*Nielsen*, 1992). For flows such that $\theta_c < \theta < 0.8$, bedforms such as vortex ripples will be be present. For more intense flows ($\theta > 0.8$), bedforms disappear and flat beds are observed in a regime usually called sheet flow (see figure 2.2). We use here the criterion of *Wilson* (1989) for sheet flow inception ($\theta > 0.8$), however other criteria and formulae exist. It is also important to notice that the sediment transport modes and the bedform regimes do not coincide when the flow is strong enough to induce motion. For example, sheet flow can be dominated by bedload (for large R_p and moderate θ), or can have contribution from both bed load and suspended load (smaller R_p).

2.2.3 Sediment interactions regimes

Bagnold (1954) measured the stress-strain relationship in a mixture of fluid (water) and neutrally buoyant particles under uniform shear and expressed such a relationship in term of two dimensionless parameters:

$$B = \sqrt{\lambda}\frac{sd^2}{\nu}\frac{du}{dz}, \tag{2.9}$$

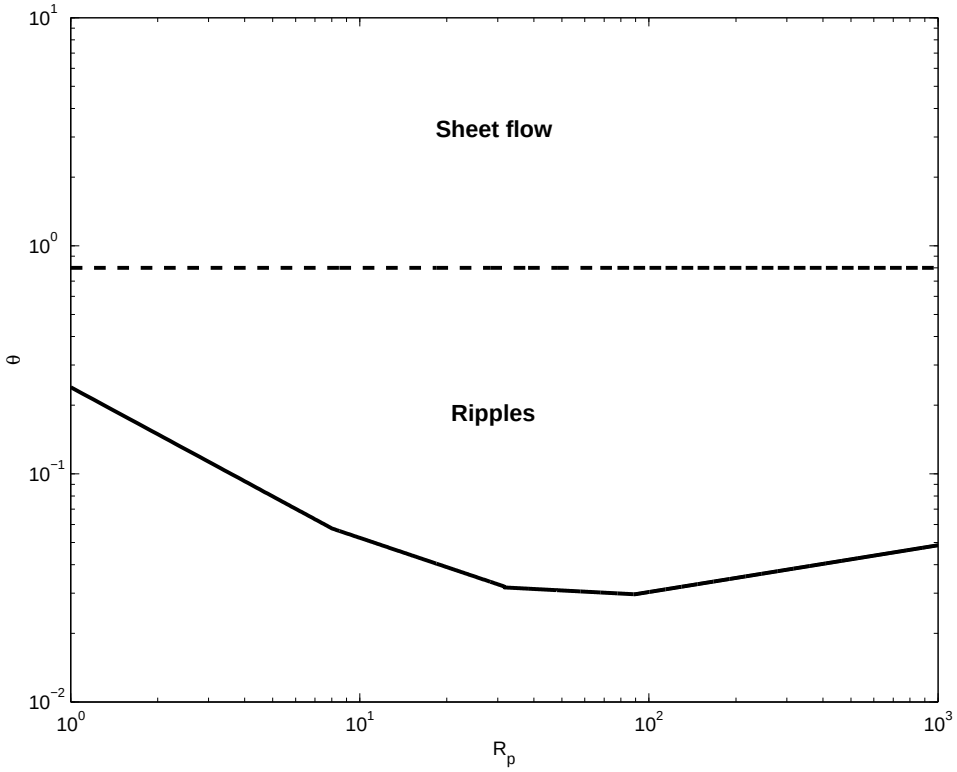

Figure 2.2: Bedforms for different Shields parameter and fall parameters. The dashed line corresponds to $\theta = 0.8$.

which is a measure of the shear in the flow and has been since called the Bagnold number, and

$$G = \frac{d}{\nu}\sqrt{\frac{s}{\lambda}\frac{\tau}{\rho}} \tag{2.10}$$

which is a measure of the stress τ (normal stress or shear stress) and is a kind of Reynolds number for the particles (the square root term has dimensions of a velocity). In both definition, λ is the "linear concentration" linked to the volume concentration through

$$c = \frac{c_\star}{(1 + 1/\lambda)^3} \tag{2.11}$$

with $c_\star = 0.635$ the maximum possible concentration, and du/dz is the uniform shear strain. Results were consistent with theory both in the case of dominant effects of grains inertia for sufficiently high strain ($G \propto B$ and called grain-inertia region) and in the case of dominant effect of interstitial fluid viscosity for small strain ($G^2 \propto B$ and called the macro-viscous region). It was also found that the grain-inertia region occurred for $B > 450$, $G^2 > 3000$ while the macro-viscous region occurred for $B < 40$, $G^2 < 100$. However, for sediment transport, the fluid shear is not uniform and the use of the Bagnold number is not very convenient. The different regimes limits were also related to values of the Reynolds number $Re_\star$: the grain-inertia region happens for $Re_\star > 55$ and the macro-viscous region for $Re_\star < 10$. It is then possible to easily represent both regions in a $\theta - R_p$ diagram using equation 2.4 (see figure 2.3).

2.2.4 Sediment transport "map"

Figure 2.4 combines figures 2.1, 2.2 and 2.3. Conditions for several experimental studies are also included. The figure is divided in several regions which correspond to different combinations of transport modes, bedform regimes and particle interactions regimes. The suspension criterion plotted is however slightly different than

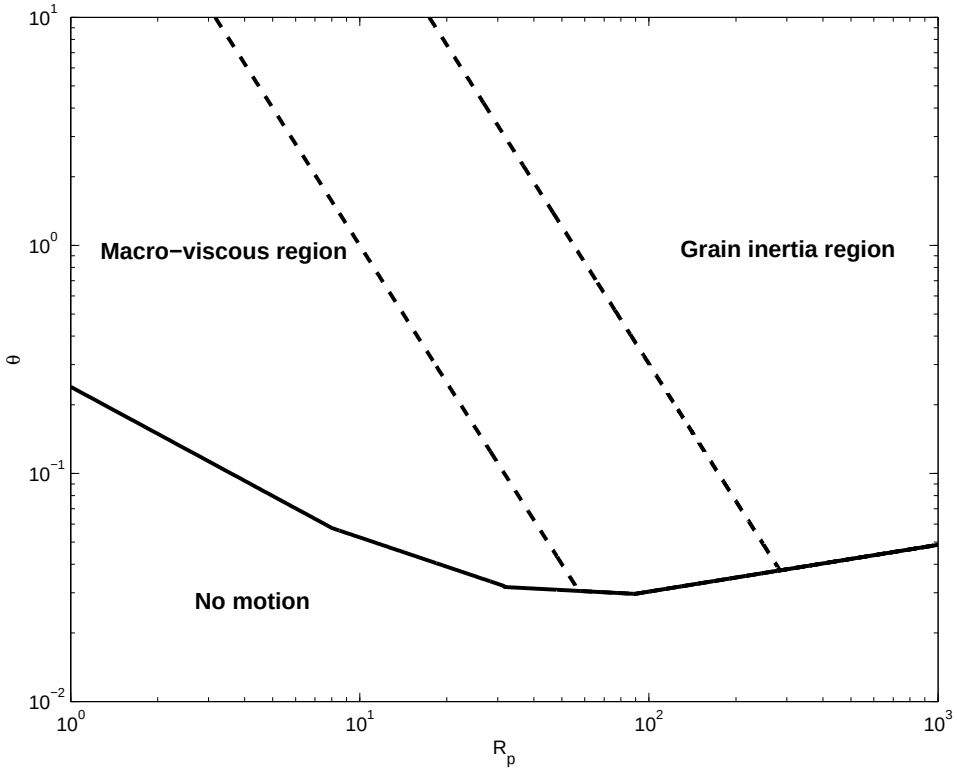

Figure 2.3: Sediment interactions regions. The dashed lines correspond to $Re_\star = R_p\sqrt{\theta} = 10$ and $Re_\star = R_p\sqrt{\theta} = 55$.

those previously introduced. We use here $u_\star = W_s$, which is similar to the *Bagnold* (1966) criterion, to provide an estimate of the relative importance of the fluid turbulence respect to the grain inertia. It is also used to define massive particles: massive particles are such that their fall velocity exceeds the friction velocity of the flow and will be located under the $u_\star = W_s$ curve in figure 2.4.

The naming of the different regions (in grey in figure 2.4) follows the following convention, to the exception of region NM which corresponds to no sediment motion:

- for the first letter: S corresponds to the sheet flow regime while R corresponds to the bedform regime.
- for the second letter: V corresponds to the macro-viscous regime, T to the inter-particle interaction transition region and C to the grain inertia regime.
- for the third letter, M corresponds to massive particles and L to non-massive particle ("light"). When only two letters are used, no distinction based on the transport modes is necessary (i.e., for SV and RC).

2.3 Sediment transport rate for steady flows

Accurately calculating the sediment discharge is probably the most important objective of sediment transport research. The total sediment transport rate Q_T is the integral of the sediment concentration multiplied by the sediment particles velocity over the entire water column. Since we commonly distinguish bed load and suspended load, the total transport rate will be the sum of the bed load transport rate Q_B and of the suspended load transport rate Q_S. Such sediment transport rates are often calculated using dimensionless relationships, where the non-dimensional

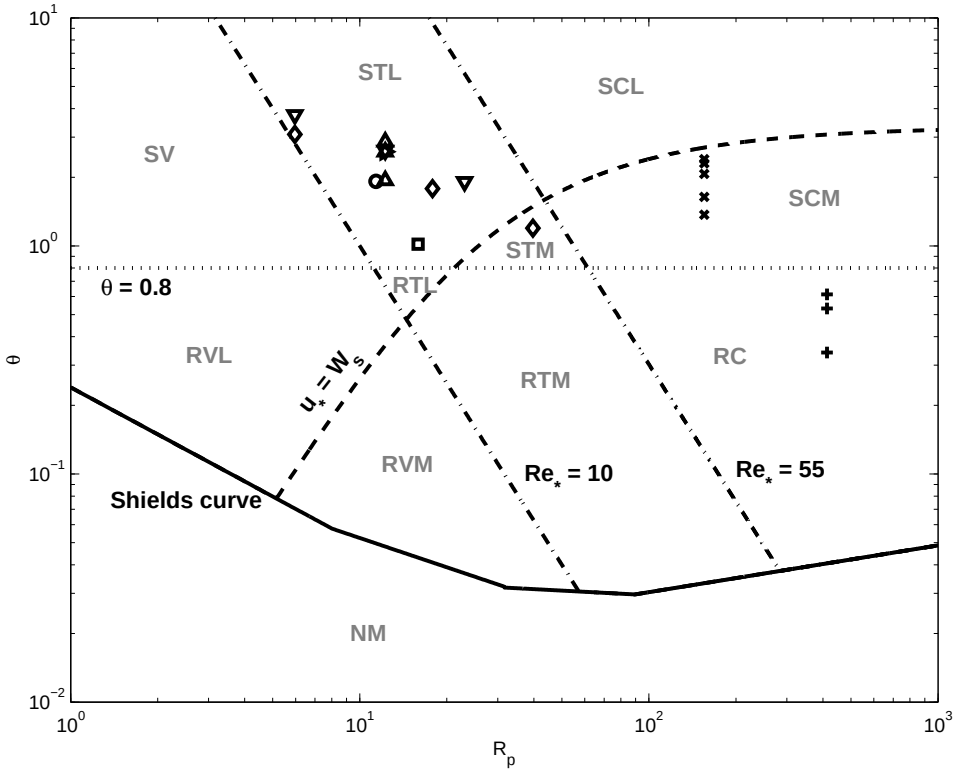

Figure 2.4: Sediment transport regimes as determined by the Shields curve (solid line), $u_\star = W_s$ (dashed line), $\theta = 0.8$ (dotted line), $Re_\star = 10$ and $Re_\star = 55$ (dot-dashed lines). The symbols represent the conditions for some experimental data. $+$: *Asano* (1995). $\times$: *Sumer et al.* (1996) (sediment 2). $\circ$: *Horikawa et al.* (1982). $\triangleright$: *Ribberink and Al-Salem* (1995). $\triangle$: *Katopodi et al.* (1994b). $\triangledown$: *Janssen* (1999). $\Diamond$: *O'Donoghue and Wright* (2004). $\square$: *Dudley* (2007).

transport rates are defined as

$$\Phi_{T,B,S} = \frac{Q_{T,B,S}}{D_{50}\sqrt{(s-1)gD_{50}}} \tag{2.12}$$

2.3.1 Bed load discharge

The bed load transport rate has been measured directly in many experimental studies using bed load traps and empirical formulas have then been introduced in the literature (e.g., *Meyer-Peter and Müller*, 1948; *Wilson*, 1966). For steady flows, the transport formulae can be summarized by:

$$\Phi_B = \begin{cases} m\left(\theta - \theta_c\right)^{3/2} & \theta \geq \theta_c \\ 0 & \theta < \theta_c \end{cases} \tag{2.13}$$

where $m = 8$ in *Meyer-Peter and Müller* (1948) and $m = 12$ in *Wilson* (1966). Wilson's experiments were carried at higher shear-stresses ($\theta > 1$) and thus seem more apt to describe the bed load transport rate under sheet flow conditions.

The previous expression introduced for the bed load sediment transport neglects the dependence of Φ_B on the other dimensionless parameters s, h/d and R_p. Even though the water depth probably does not influence the bed load transport since it is a near bed process and the specific gravity is fixed for sand transport in water, a relationship of the form $\Phi_B = f(\theta, R_p)$ should still be considered. In addition to the bed load transport being related to the fall parameter through the critical Shields parameter ($\theta_c = f(R_p)$), *van Rijn* (1984c) considered an explicit dependence of the bed load transport rate and found that

$$\Phi_B \sim \frac{1}{R_p^{0.2}}. \tag{2.14}$$

Such a dependence is rather weak and equation 2.13 will thus be considered to describe sufficiently accurately the bed load transport rate.

2.3.2 *Bagnold* (1966) model

While the bed load transport rate can be measured directly using bed load traps, measurements of the suspended load transport rate are more complicated and indirect in that they usually rely on concentration and velocity measurements. The suspended transport rate is then found by integrating the product of the concentration and the velocity:

$$Q_s = \int_{z_0}^{h} c(z)u(z)dz \tag{2.15}$$

where z_0 is the lower limit of the suspension layer and h the water depth. It is obvious that the specification of z_0 has an important influence on the results and is thus a crucial part of the suspended transport rate modeling. Unfortunately, because of the definitions of bed load and suspended load (see section 2.2.1), accurate and universal specifications of both the top of the bed load layer and the bottom suspended load layer are difficult to obtain.

Like the bed load transport, the suspended load transport will depend on both the Shields parameter and the fall parameter and it will also depend on the water depth. Few models predict the suspended load transport as a direct function of the necessary parameters $Q_s = f(\theta, R_p, \Pi_h)$ where Π_h is a dimensionless parameters reflecting the influence of the water depth. Different approaches for calculating the suspended load and then the total load have been used. Using considerations of energy balance and mechanical equilibrium, *Bagnold* (1966) derived equations relating bed load, suspended load and total load to the stream power for steady stream flows. Another approach for the suspended load consists in using simple models for the concentration (e.g., *Rouse*, 1937) and velocity profiles in equation 2.15.

The total load following *Bagnold* (1966) is given by

$$Q_T = \frac{1}{(s-1)} \left(\frac{\varepsilon_B}{\tan \psi} + \varepsilon_S \frac{\bar{u}}{W_s} \right) D_{50} S_0 \bar{u} \tag{2.16}$$

where S_0 is the gravity slope and $\bar{u}$ the mean flow velocity. ψ is the angle of friction of the sediment and is such that $\tan \psi = 0.63$. For stream flows, *Bagnold* (1966) found that $\varepsilon_B \approx 0.13$ and $\varepsilon_S \approx 0.01$.

2.3.3 Suspended load discharge by integration of concentration and velocity profiles

Concentration and velocity vertical profiles

A classical approach to calculating the concentration profile of suspended sediment was first introduced by *Rouse* (1937). The solution relates the concentration profile to the concentration at a given elevation above the bed:

$$c(z) = c_{z_r} \left(\frac{h-z}{z} \frac{z_r}{h-z_r} \right)^{Ro} \tag{2.17}$$

where c_{z_r} is the concentration of suspended sediment at a distance z_r above the bed and $Ro = W_s/(\kappa u_\star)$ is called the Rouse parameter with κ the von Karman constant. Since equation 2.17 describes sediment suspensions, z_r has to be higher than (or equal to) the lower limit of the suspension layer z_0. In order to calculate the suspended load transport, both the concentration and the velocity profiles have to be specified for all elevation higher than z_0 and z_r is then chosen to be equal to z_0. For the vertical profile of the concentration to be fully determined, expressions for both $c_{z_r} = c_{z_0}$ and $z_r = z_0$ are necessary and have been the focus of significant research in past decades. A number of different models (seven of which are summarized in *Garcia and Parker* (1991)) have been introduced and

they usually provide both c_{z_r} and z_r. We choose here to use the simple model of *Engelund and Fredsøe* (1976) for which:

$$z_r = z_0 = 2D_{50} \tag{2.18}$$

and

$$c_{z_r} = c_{z_0} = \frac{c_\star}{(1 + 1/\lambda)^3} \tag{2.19}$$

where the linear concentration λ is obtained using

$$\lambda^2 = \frac{\theta - \theta_c - \frac{\pi}{6}\mu_d p}{\frac{0.013}{4\kappa^2} s\theta} \tag{2.20}$$

with p in turn given by

$$p = \left[1 + \left(\frac{\frac{\pi}{6}\mu_d}{\theta - \theta_c}\right)^4\right]^{-1/4}. \tag{2.21}$$

For for small θ values, the predicted concentration depends strongly on the parameter μ_d, which is taken to be $\mu_d = 0.65$ (*Fredsoe and Deigaard*, 1992). In spite of the sensitivity of the reference concentration, we believe that the impact on the total sediment discharge will be limited because the region of strong dependence on μ_d (small θ) corresponds to the region for which the bed load transport should dominate.

Even though the presence of sediment will modify the velocity profile, it is common to assume that the velocity vertical profile follows a logarithmic law. We choose here to describe the velocity using a rough wall log-law:

$$u(z) = \frac{u_\star}{\kappa} \log \frac{30z}{K_s} \tag{2.22}$$

where K_s is the equivalent roughness of the bed.

Both the Rouse profile and the velocity profile are shown in figure 2.5 for different values of the Shields parameter.

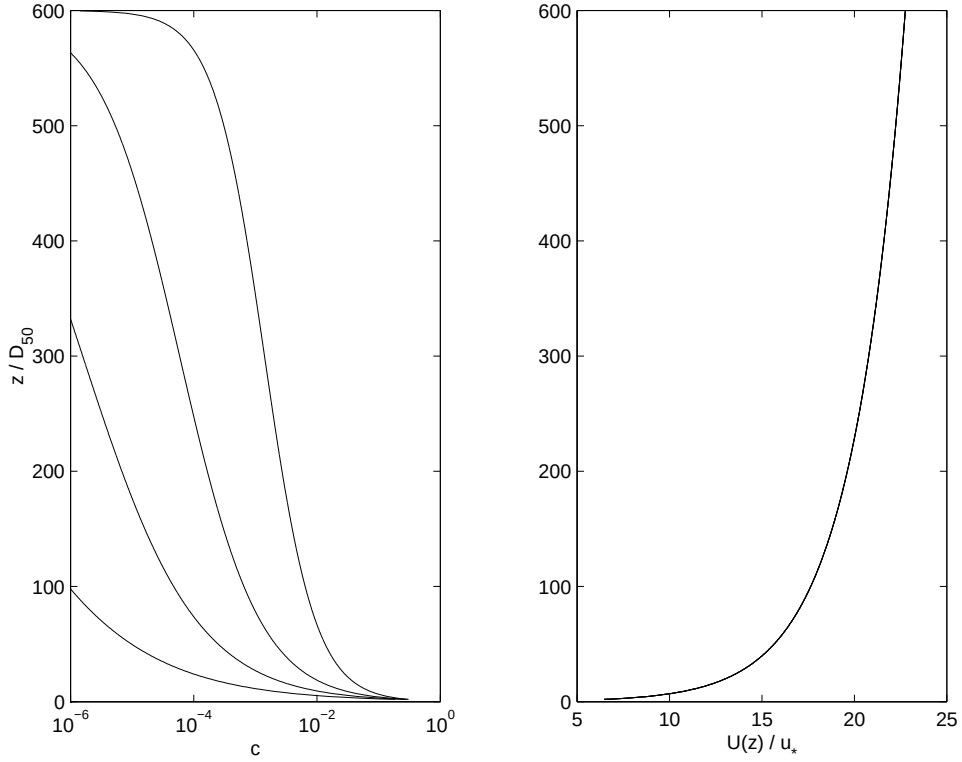

Figure 2.5: Vertical concentration (left panel) and velocity (right panel) profiles as described by the Rouse formula and the rough wall log-law. Profiles for different θ values are plotted: $\theta = 0.5$, $\theta = 1.0$, $\theta = 2.0$ and $\theta = 5.0$ from bottom left to top right in the left panel.

Table 2.1: Figure panel, sediment diameter and fall parameter correspondence for figures 2.6, 2.7 and 2.8.

Figure panel	D_{50} (mm)	R_p
a	0.05	1.42
b	0.1	4.02
c	0.2	11.38
d	0.3	20.91
e	0.4	32.19
f	0.5	44.98
g	1.0	127.2
h	3.0	667.1

Suspended sediment transport

The product of the concentration and the velocity profiles given by equations 2.17 and 2.22 and represented in figure 2.5, can then be numerically integrated to obtain the suspended load transport.

Figure 2.6 represents both the bed load transport and the suspended load transport as functions of the Shields parameter for eight different fall parameters (summarized in table 2.1) and for three different water depths ($h = 0.1m$, $h = 1m$ and $h = 10m$). Figure 2.7 shows the total sediment transport, which is the sum of the suspended load and the bed load, for the same eight fall parameters and the same three water depths and figure 2.8 illustrates the repartition of the total load between bed load and suspended load. While the bed load transport does not depend on the water depth (equation 2.13), the suspended load transport does and more sediment is transported for bigger water depths. It follows that both the total sediment transport and the repartition between the two modes will also depend on the water depth. In both figures 2.6 and 2.7, bigger water depths lead to higher curves in the chosen coordinate system. In figure 2.8, bigger water depths increase the proportion of sediment transported in suspension respect to bed load

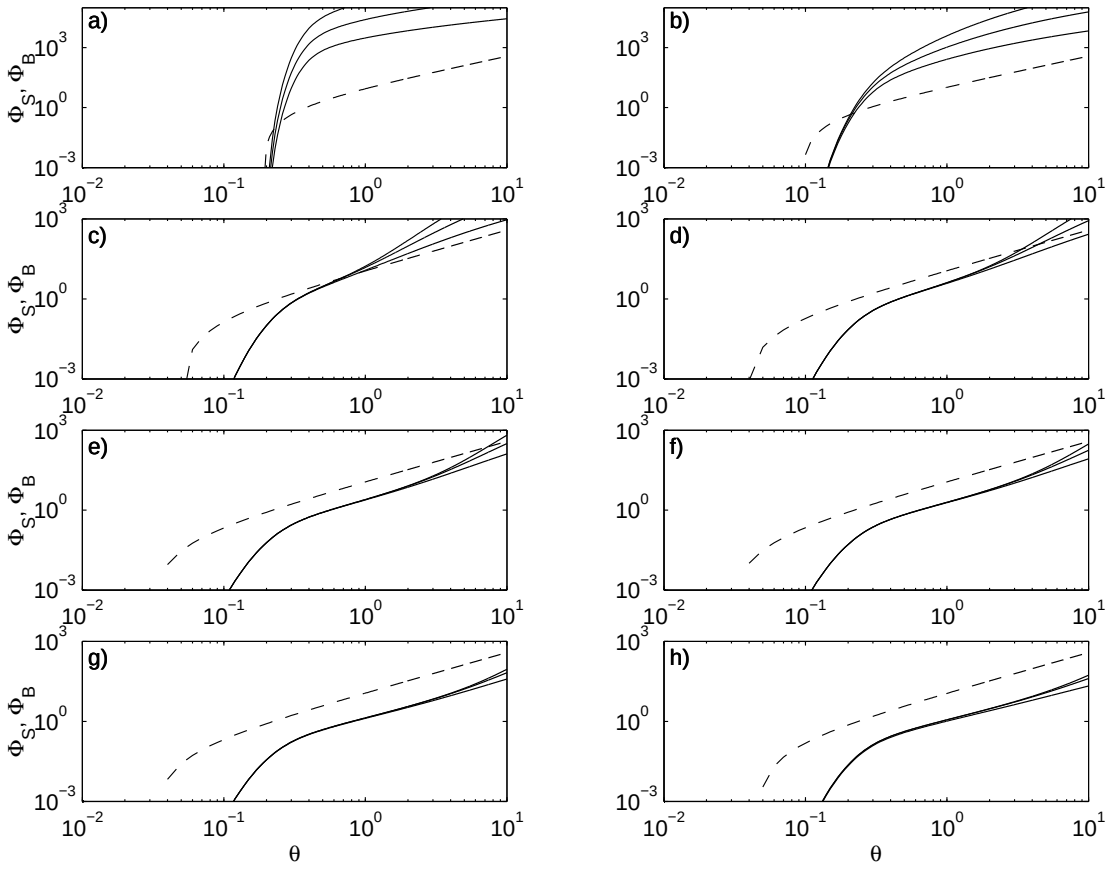

Figure 2.6: Bed load transport (dashed line) and suspended transport (solid lines) as functions of the Shields parameter for different fall parameters (see table 2.1) and different water depth: $h = 0.1m$ (lower curve), $h = 1m$ (middle curve) and $h = 10m$ (upper curve).

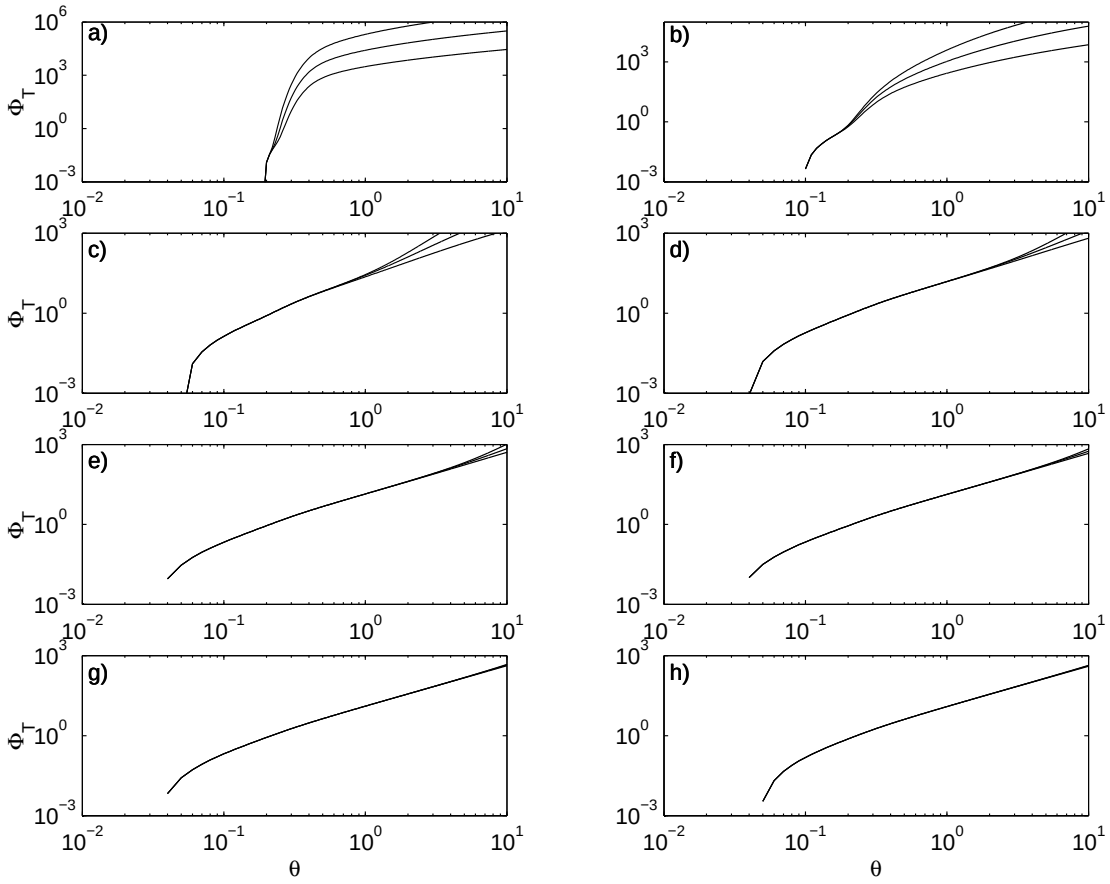

Figure 2.7: Total load transport as function of the Shields parameter for different fall parameters (see table 2.1) and different water depth: $h = 0.1m$ (lower curve), $h = 1m$ (middle curve) and $h = 10m$ (upper curve).

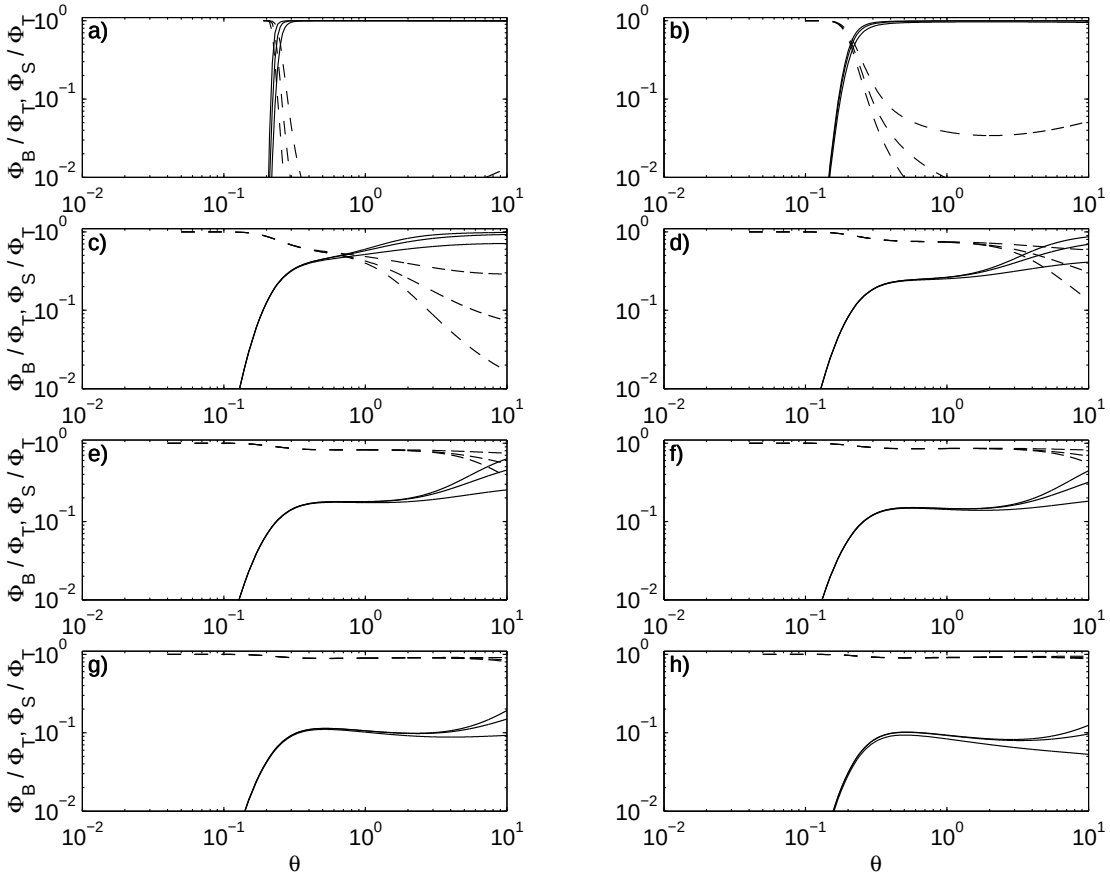

Figure 2.8: Fraction of the total load transported as bed load (dashed line) and as suspended load (solid lines) for different fall parameters (see table 2.1) and different water depth: $h = 0.1m$ (lower solid and upper dashed curves), $h = 1m$ (middle solid and dashed curves), $h = 10m$ (upper solid and lower dashed curves).

and thus will lead to higher curves for Φ_S/Φ_T (solid curves) and lower curves for Φ_B/Φ_T (dashed curves).

Several sediment transport behaviors are distinguishable in figures 2.6, 2.7 and 2.8. For small particles (panels a and b), the suspended load is highly dependent on the water depth and, as the Shields parameter increases, quickly becomes dominant for all water depths. For larger grains (panels c to h), the suspended transport dependence on the bottom shear stress can be divided into three regions. First, for small Shields parameter values (θ less than about $0.4 - 0.5$), suspended load transport increases drastically with θ and does not depend on the water depth. In the second region, for intermediate θ values, the suspended load still does not depend on the water depth and the plots in figure 2.6 become linear, which indicates a power-law relationship between Q_S and θ. Finally, for large values of θ, the suspended sediment transport depends on the water depth and the suspended sediment transport for larger depth deviates positively from the power law profile observed in the intermediate region. Both the Shields parameter value at which the water depth starts to affect the suspended transport and the slope of the linear portion of the curves depend on the fall parameter R_p. The former increases with increasing fall parameters while the later decreases with increasing fall parameters. Such dependence of the suspended load on the water depth is not always reflected in the total load as the bed load becomes dominant for larger particles. In figure 2.8, bed load and suspended load are of comparable magnitude only for panels c and d.

2.4 Time dependent sediment transport rate

In the previous section, we introduced expressions for the sediment transport rate in term of the free stream velocity or of the Shields parameter. For time depen-

dent cases, the same expressions would be valid if the sediment transport reacted instantaneously to changes in velocity. The sediment response can usually be considered instantaneous when the sediment response time is small compared to the time scale on which the velocity varies (i.e. period for oscillatory cases). Many sediment transport rate models have been based on this assumption and relate the instantaneous sediment transport rate ($Q_T(t)$ or $Q_B(t)$) to the instantaneous bed shear stress ($\tau_b(t)$), which in turn can be expressed in terms of the free stream velocity (e.g. *Madsen and Grant*, 1976; *Sleath*, 1978; *Trowbridge and Young*, 1989; *Ribberink*, 1998). These models are based on experimental data and are similar to equation 2.13 by giving $Q_T(t)$ (or $Q_B(t)$) to be proportional to some power (greater than or equal to 1) of $\tau_b(t)$.

In particular, *Ribberink* (1998) introduced the following relationship for oscillatory flows:

$$\Phi_B(t) = \begin{cases} m\left(|\theta(t)| - \theta_c\right)^n \frac{\theta(t)}{|\theta(t)|} & |\theta| \geq \theta_c \\ 0 & \theta < \theta_c \end{cases} \tag{2.23}$$

where $m = 11$ and $n = 1.65$. The time-dependent Shields parameter is then found following:

$$\tau_b(t) = \frac{1}{2}\rho_f f_w |U_0(t)| U_0(t) \tag{2.24}$$

where $U_0(t)$ is the time dependent free-stream velocity and f_w the wave friction factor. In oscillatory flows, the wave friction factor depends on the Reynolds number $A^2\omega/\nu$ (A being the wave free stream amplitude and ω the angular frequency) and on the relative bed roughness K_s/A (*Jonsson*, 1966). In *Ribberink* (1998), f_w is calculated using the formula of *Swart* (1974), which is an explicit approximation of the implicit semi-empirical formula of *Jonsson* (1966).

Bailard (1981) also obtained a time-dependent model for sediment transport by following theoretical energy considerations (extension of the work of *Bagnold*

(1966) to time-varying cases):

$$Q_T = \frac{1}{(s-1)g}\frac{1}{2}f_w\left[\frac{\varepsilon_B}{\tan\psi}|U_0(t)|^2U_0(t) + \frac{\varepsilon_S}{W_s}|U_0(t)|^3U_0(t)\right]. \tag{2.25}$$

An important consequence of the two models explicitly introduced is that all three quantities (free stream velocity, bed shear stress and sediment transport rate) are in phase. This is also the case for the models of *Madsen and Grant* (1976) and *Trowbridge and Young* (1989). Only *Sleath* (1978) introduces a phase lag for the sediment transport rate.

These models, as well as others (e.g. *Watanabe et al.*, 1980; *Shibayama and Horikawa*, 1982; *Dibajnia and Wanatabe*, 1992), also predict the net sediment transport over, either the half cycle for purely sinusoidal cases or over the total cycle for asymmetric cases. It is usually found to be proportional to a power of the maximum Shields parameter.

2.5 On the necessity of more advanced models

In addition to a classification of sediment transport depending on some non-dimensional parameters, we presented in this chapter several simple models that are used to predict the sediment transport rate. However the use of these model presents several shortcomings. First, these models are either empirical (e.g., *Meyer-Peter and Müller* (1948) and *Wilson* (1966) for bed load in steady flows, *Ribberink* (1998) for bed load in oscillatory flows) or are based on simple assumptions on the physics involved (e.g., *Rouse*, 1937; *Bagnold*, 1966; *Bailard*, 1981). As such they provide from no to a limited description of the physics involved in sediment transport. Another issue of the models presented is that most of them do not provide information on both the bed load transport and the suspended load transport (only the *Bagnold* (1966) and the *Bailard* (1981) do). The last deficiency is

that sediment transport models have mainly been developed for simple flow situations such as steady state flows, oscillatory flows and wave-current flows, whereas natural conditions can be a lot more diverse. It follows that most sediment transport discussed previously, although simple and widely used, only provide a partial description of sediment transport and have a limited range of applicability. Improving such issues will require developing and using more complete and complex models.

As the hydrodynamic models become more mature, more and more studies address the sediment responses to nearshore waves and currents due to for example, higher-order wave statistics (e.g., skewness, asymmetry and acceleration), nonlinear (wave-current) boundary layer processes and breaking wave induced turbulence. Some small-scale studies include measurements of sediment transport within the wave boundary layer (e.g., *Ribberink and Al-Salem*, 1995; *Dohmen-Janssen et al.*, 2001; *McLean et al.*, 2001; *Dohmen-Janssen and Hanes*, 2002; *O'Donoghue and Wright*, 2004; *Hassan and Ribberink*, 2005) and the development of various detailed models to capture intermittent turbulence (e.g., *Zedler and Street*, 2006; *Chang and Scotti*, 2006), two-phase fluid-sediment interaction (*Dong and Zhang*, 2002; *Hsu et al.*, 2004), granular flow dynamics (*Jenkins and Hanes*, 1998; *Drake and Calantoni*, 2001; *Hsu et al.*, 2004) and heterogeneity of discrete sediment particles (*Calantoni et al.*, 2004).

Several approaches have been employed to model sediment transport, amongst which the two-phase flow models have become increasingly popular. In two-phase models, continuity and momentum conservation equations are established for both sediment and fluid phases. Consequently, closure problems arise not only in the fluid turbulent stresses, but also in the sediment stresses and the interaction between the two phases. Turbulent fluid stress closures range from using specified

eddy viscosity profiles (e.g., *Kobayashi and Seo*, 1985; *Greimann and Holly*, 2001) to using complete two-equations turbulence closures such as $k - \varepsilon$ models (e.g., *Hsu, Jenkins, and Liu*, 2003a; *Hsu, Chang, and Hsieh*, 2003b; *Longo*, 2005). Sediment stress closures can be divided in two main categories: formulations based on phenomenological equations (that of *Bagnold* (1954) in *Kobayashi and Seo* (1985) or that of *Savage and McKeown* (1983) in *Dong and Zhang* (1999) for example) and formulations based on a collisional granular flow theory (*Greimann and Holly*, 2001; *Hsu et al.*, 2004; *Longo*, 2005). Only recently have models started to combine the higher levels of complexity as presented herein for both fluid and sediment stresses (e.g., *Hsu et al.*, 2004; *Longo*, 2005).

CHAPTER 3

TWO-PHASE FLOW EQUATIONS

Models that are based on multi-phase flow theory are becoming increasingly popular to study sediment transport. Such models usually employ a two-phase mixture flow concept, for which two-phases that are separate and yet form interpenetrating continua are considered. Such continuum hypothesis is common and widely used in fluid mechanics (for small Knudsen number flows). This hypothesis is based on not considering the motions of each molecule or sediment particle, but instead working with average properties. It implies that an average is already applied to the properties of both phases. For the fluid, this average has to be done on a scale larger than the mean free pass of molecules. For the sediment phase, the average has to be done on a scale larger than the sediment diameter. The continuum assumption for the two-phase flow thus introduces two scales: the molecular scale (related to the fluid phase continuum) and a scale related to the sediment phase continuum that we shall refer to as "small-scale".

In a similar way to turbulent flows for which the flow properties fluctuate on a scale larger than the molecular scale and a (second) average is introduced, we will introduce a (second) average to account for the turbulent fluctuation of the properties of both phases. Such an average will be done on a scale larger than that of the continuum hypothesis and then defines a third scale that we shall refer to as "large-scale". Since all averages introduce residual stresses, both small-scale and large-scale residual stresses will be present in the flow governing equations and appropriate modeling of such stresses will be crucial and further discussed.

In this chapter, we will first introduce the equations of motions for a fluid phase and a sediment phase (that are separate and yet form interpenetrating continua). We will then specify the inter-phase momentum transfer which is the coupling

term between the momentum equations of each phase. The (second) average that accounts for the turbulent fluctuations is chosen to be a concentration-weighted average and is then presented, as well as the averaged equations of motion. Finally, closures for the residual stresses and other fluctuation correlation terms are discussed. A brief discussion on the relevance of the commonly used one-dimensional assumption (negligible variations in the flow direction) to sediment transport processes in coastal and fluvial environments acts as a conclusion to the chapter.

3.1 Two-phase equations of motion

For each phase, the equations of motion are given by the conservation of mass and the conservation of linear momentum. In two-phase flows, only one independent concentration is needed since the sum of all volumetric concentrations is 1. The resulting fluid-phase and sediment-phase conservation of mass equations can thus be written as (*Drew and Lahey*, 1979; *Drew*, 1983):

$$\frac{\partial \rho^f (1-c)}{\partial t} + \frac{\partial \rho^f (1-c) u_i^f}{\partial x_i} = 0 \tag{3.1}$$

$$\frac{\partial \rho^s c}{\partial t} + \frac{\partial \rho^s c u_i^s}{\partial x_i} = 0, \tag{3.2}$$

where c is the sediment phase volumetric concentration, ρ^f the fluid density and u denotes the velocity with the f superscript referring to the fluid phase and the s superscript referring to the sediment phase. The conservation of linear momentum

equations for both phases can be written as (*Drew and Lahey*, 1979; *Drew*, 1983):

$$\begin{aligned}\frac{\partial \rho^f (1-c) u_i^f}{\partial t} + \frac{\partial \rho^f (1-c) u_i^f u_j^f}{\partial x_j} &= \rho^f (1-c) g_i - \frac{\partial (1-c) P^f}{\partial x_i} + M_i^f \\ &\quad + \frac{\partial (1-c) T_{ji}^f}{\partial x_j} \qquad (3.3)\\ \frac{\partial \rho^s c u_i^s}{\partial t} + \frac{\partial \rho^s c u_i^s u_j^s}{\partial x_j} &= \rho^s c g_i - \frac{\partial c P^s}{\partial x_i} + M_i^s \\ &\quad + \frac{\partial c T_{ji}^s}{\partial x_j} \qquad (3.4)\end{aligned}$$

where g_i represents the gravitational acceleration, P^f and P^s the pressures of the fluid phase and the sediment phase, T_{ij}^f and T_{ij}^s are the stress tensors for the fluid phase and the sediment phase (containing the viscous stress and the residual stress due the averaging of the continuum hypothesis). M^f and M^s are the rate of momentum generation for the fluid phase and for the sediment phase at the interphase and their sum equals the mixture momentum source at the interphase due to surface tension. These two terms are expressed as

$$M_i^f = P^{fi} \frac{\partial (1-c)}{\partial x_i} + M_i^{df} \qquad (3.5)$$

and

$$M_i^s = P^{si} \frac{\partial c}{\partial x_i} + M_i^{ds} \qquad (3.6)$$

where P^{fi} and P^{si} are the interfacial pressures respectively for the fluid phase and the sediment phase and the corresponding terms are due to the average pressure at the interface. M_i^{df} and M_i^{ds} contain the forces on the fluid phase and the sediment phase due to viscous and form drag, virtual added mass and lift. A third term accounting for phase change can also be accounted for in M^f and M^s, but it is taken to be zero here. Assuming that the surface tension is negligible, we have that both interfacial pressures are equal ($P^{fi} = P^{si}$), which results in $M_i^{df} + M_i^{ds} = 0$. Following *Drew* (1983), we also assume that for the fluid phase $P^f = P^{fi}$, while we

will have in the sediment phase a pressure due to the particle-particle interactions P^c. We can then write

$$P^s = P^f + P^c \tag{3.7}$$

Using these pressure relationships and choosing $I_i \equiv M_i^{ds} = -M_i^{df}$, we can rewrite the fluid phase momentum equation as follow

$$\begin{aligned} \frac{\partial \rho^f (1-c) u_i^f}{\partial t} + \frac{\partial \rho^f (1-c) u_i^f u_j^f}{\partial x_j} &= \rho^f (1-c) g_i - (1-c)\frac{\partial P^f}{\partial x_i} - I_i \\ &\quad + \frac{\partial (1-c) T_{ji}^f}{\partial x_j} \end{aligned} \tag{3.8}$$

$$\tag{3.9}$$

and the sediment phase momentum equation as

$$\frac{\partial \rho^s c u_i^s}{\partial t} + \frac{\partial \rho^s c u_i^s u_j^s}{\partial x_j} = \rho^s c g_i - c\frac{\partial P^f}{\partial x_i} + I_i - \frac{\partial c\left(P^s - P^f\right)}{\partial x_i} + \frac{\partial c T_{ji}^s}{\partial x_j} \tag{3.10}$$

where $c\left(P^s - P^f\right)$ is the effective normal sediment stress.

3.2 Inter-phase momentum transfer

The inter-phase momentum transfer couples the two momentum equations and needs to be modeled appropriately. In general, drag, added-mass and lift forces due to the presence of particles are considered (e.g., *Drew*, 1983; *Longo*, 2005). The drag force can be expressed as:

$$I_i^d = c\beta\left(u_i^f - u_i^s\right), \tag{3.11}$$

where β is a drag coefficient. For sand particles the particle Reynolds number $Re_p = U_r d/\nu^f$ where U_r is the magnitude of the relative velocity between the two phases

$$U_r = \sqrt{\sum\left(u_i^f - u_i^s\right)^2} \tag{3.12}$$

will remain limited. The drag coefficient is thus chosen so that it satisfies the Stokes law for small particle Reynolds number and reaches the constant drag regime for higher particle Reynolds numbers. Furthermore, in the case of many particles moving simultaneously, the drag observed is higher than the one for one single particle and depends on the concentration of particles. We then use the following relationship to describe the drag coefficient:

$$\beta = \frac{\rho^f U_r}{d}\left(\frac{18.0}{Re_p} + 0.3\right)\frac{1}{(1-c)^n} = \frac{\mu^f}{d^2}\left(18.0 + 0.3Re_p\right)\frac{1}{(1-c)^n} \tag{3.13}$$

in which d is the diameter of the particles. The concentration dependence is taken from the experimental data of *Richardson and Zaki* (1954) where n depends on the particle Reynolds number:

$$n = \begin{cases} 4.35{Re_p}^{-0.03} - 1, & 0.2 \leq Re_p \leq 1.0 \\ 4.45{Re_p}^{-0.1} - 1, & 1.0 \leq Re_p \leq 500 \\ 1.39, & 500 \leq Re_p \end{cases} \tag{3.14}$$

The added-mass and lift forces are introduced as follow in *Drew* (1983):

$$\begin{aligned} I_i^{am} + I_i^l &= \rho^f c C_M \left(\frac{\partial u_i^f}{\partial t} + u_j^s \frac{\partial u_i^f}{\partial x_j} - \frac{\partial u_i^s}{\partial t}\ u_j^f \frac{\partial u_i^s}{\partial x_j}\right) \\ &\quad + \rho^f c C_M (1-\lambda_{fs})\left(u_j^f - u_j^s\right)\frac{\partial\left(u_i^f - u_i^s\right)}{\partial x_j} \\ &\quad + \rho^f c C_L\left(u_j^f - u_j^s\right) D_{ij}^f \end{aligned} \tag{3.15}$$

where C_M and C_L are respectively an added-mass coefficient and a lift coefficient, λ_{fs} is a parameter (*Drew et al.*, 1979) and D_{ij}^f is the fluid phase strain rate tensor

$$D_{ij}^f = \frac{1}{2}\left(\frac{\partial u_i^f}{\partial x_j} + \frac{\partial u_j^f}{\partial x_i}\right) \tag{3.16}$$

Another formulation regroups all terms that can be seen as convective accelerations, introduces Ω_{ij}^f as the fluid phase rate of rotation tensor

$$\Omega_{ij}^f = \frac{1}{2}\left(\frac{\partial u_i^f}{\partial x_j} - \frac{\partial u_j^f}{\partial x_i}\right) \tag{3.17}$$

and leads to the following expression for the total interphase momentum transfer:

$$\begin{aligned} I_i &= \frac{\mu^f}{d^2}\left(18.0+0.3Re_p\right)\frac{c}{(1-c)^n}u_i^r \\ &\quad +\rho^f c C_M\left[\frac{\partial u_i^r}{\partial t}+(1-\lambda_{fs})u_j^r\frac{\partial u_i^r}{\partial x_j}+u_j^f\frac{\partial u_i^r}{\partial x_j}+\left(\frac{C_L}{C_M}-1\right)u_i^r\frac{\partial u_i^f}{\partial x_j}\right] \\ &\quad -\rho^f c C_L u_i^r \Omega_{ij}^f \end{aligned} \tag{3.18}$$

with $u_i^r = u_i^f - u_i^s$. The last term can then clearly be identified with a lift force, that is a force perpendicular to the relative velocity and the vorticity of the flow ($\mathbf{I}^l \propto \mathbf{u}^r \times \omega^f$ where $\omega^f = \nabla \times \mathbf{u}^f$). In most practical cases however, only the drag term is of importance. This can easily be seen by scaling the different terms in the previous equation. For the added mass term to be on the same order of magnitude than the drag, the time scale involved in the acceleration has to be on the order of τ_M, where

$$\tau_M = \frac{C_M d^2 (1-c)^n}{\nu(18.0+0.3Re_p)} \tag{3.19}$$

and the rate of strain has to be on the order $1/\tau_M$. Similarly for the lift force to be on the same order of magnitude than the drag force the rate of rotation has to be on the order of $1/\tau_L$, where

$$\tau_L = \frac{C_L d^2 (1-c)^n}{\nu(18.0+0.3Re_p)} \tag{3.20}$$

For both terms such restrictions imply that the time scales τ_M and τ_L will have to be smaller than $0.01s$ for sediment sizes around $0.4mm$ and $\nu = 10^{-6}m^2/s$, which is unrealistic both for the time scale and the velocity gradients scale. The added mass term and the lift force term are then negligible respect to the drag term for sand transport in water and the interphase momentum transfer can then reasonably be taken as:

$$I_i = c\beta\left(u_i^f - u_i^s\right), \tag{3.21}$$

The same simplification has also been used in other models, for example in some bed load models calculating the particle trajectory (e.g., *Sekine and Kikkawa*, 1990; *McEwan et al.*, 1999).

3.3 Averaged two phase flow equations

As mentioned previously, the flow properties can fluctuate on a scale larger than that of the continuum hypothesis. In order to account for such fluctuations as well as turbulence, another average needs to be performed on the two phase flow equations. We choose here to apply a concentration weighted average to equations 3.1, 3.2, 3.8 and 3.10.

3.3.1 Concentration-weighted average

In the Favre average (*Favre*, 1965), the average is applied to the momentum per unit mass of each phase rather than to the velocity per se. We choose to follow a similar approach and the concentration weighted mean velocities of each phase are thus defined by

$$\tilde{u}_i^f = \frac{\overline{(1-c)u_i^f}}{1-\bar{c}}, \tag{3.22}$$

and

$$\tilde{u}_i^s = \frac{\overline{cu_i^s}}{\bar{c}}, \tag{3.23}$$

where the overbar denotes the average. Corresponding fluctuations for the concentration and velocities are

$$c' = c - \bar{c} \tag{3.24}$$

$$\Delta u_i^f = u_i^f - \tilde{u}_i^f \tag{3.25}$$

$$\Delta u_i^s = u_i^s - \tilde{u}_i^s \tag{3.26}$$

Following from the definition of the concentration-weighted average we have that

$$\overline{\Delta u_i^f} \neq 0 \text{ and } \overline{\Delta u_i^s} \neq 0 \tag{3.27}$$

but

$$\overline{(1-c)\Delta u_i^f} = 0 \text{ and } \overline{c\Delta u_i^s} = 0 \tag{3.28}$$

The concentration-weighted averaging is based on a different concept than that of the traditional method for which the average is directly applied to the velocities of both phases. These two averaging techniques are not equals and their difference can be calculated:

$$\delta\tilde{u}_i^f = \bar{u}_i^f - \tilde{u}_i^f \tag{3.29}$$

$$\delta\tilde{u}_i^s = \bar{u}_i^s - \tilde{u}_i^s \tag{3.30}$$

Expressions for these differences between the two averages can be deduced from the concentration-weighted average definition:

$$\delta\tilde{u}_i^f = \frac{\overline{c' u_i^{f'}}}{1-\bar{c}} = \overline{c\Delta u_i^f} = \overline{\Delta u_i^f}, \tag{3.31}$$

$$\delta\tilde{u}_i^s = -\frac{\overline{c' u_i^{s'}}}{\bar{c}} = \overline{\Delta u_i^f} \tag{3.32}$$

They are thus related to the correlation between concentration fluctuations and velocity fluctuations, which are not known a priori. This issue of estimating the difference between concentration-weighted averages and traditional methods is of notable importance when performing model-data comparisons on the velocities. Experimentally, the velocities are usually not averaged using a concentration-weighted average and we then need to estimate $\delta\tilde{u}_i^f$ and $\delta\tilde{u}_i^s$ to be able to compare experimental data with numerical results. Fortunately, such correlation terms are commonly modeled using a gradient diffusion approach and therefore the differences between the two methods can be related to concentration gradients. In particular, for horizontal velocities in one-dimensional cases the two averages are equivalent for there is no horizontal concentration gradient.

3.3.2 Concentration-weighted averaged interphase momentum transfer

The drag coefficient in the momentum equations is a function of both the relative velocity magnitude and the concentration and will therefore also fluctuate. Applying the concentration-weighted average to the interphase momentum transfer leads to

$$\overline{I_i} = \left(\bar{\beta}\bar{c} + \overline{\beta' c'}\right)\left(\tilde{u}_i^f - \tilde{u}_i^s\right) + \bar{\beta}\overline{c\Delta u_i^f} + \overline{\beta' c\left(\Delta u_i^f - \Delta u_i^s\right)} \tag{3.33}$$

For simplicity we will neglect all correlations involving the drag coefficient fluctuation (equivalent to assuming $\beta' = 0$) and we will approximate the concentration-weighted averaged interphase momentum transfer by

$$\overline{I_i} = \beta\bar{c}\left(\tilde{u}_i^f - \tilde{u}_i^s\right) + \beta\overline{c\Delta u_i^f}. \tag{3.34}$$

where β is the averaged drag coefficient

$$\beta = \frac{\rho^f \widetilde{U}_r}{d}\left(\frac{18.0}{\widetilde{Re}_p} + 0.3\right)\frac{1}{(1-\bar{c})^n} = \frac{\mu^f}{d^2}\left(18.0 + 0.3\widetilde{Re}_p\right)\frac{1}{(1-\bar{c})^n}, \tag{3.35}$$

with

$$\widetilde{U}_r = \sqrt{\sum\left(\tilde{u}_i^f - \tilde{u}_i^s\right)^2}, \tag{3.36}$$

and

$$\widetilde{Re}_p = \frac{\widetilde{U}_r d}{\nu}. \tag{3.37}$$

3.3.3 Concentration-weighted averaged two-phase equations

The continuity equations after concentration-weighted averaging become

$$\frac{\partial \rho^f(1-\bar{c})}{\partial t} + \frac{\partial \rho^f(1-\bar{c})\tilde{u}_i^f}{\partial x_i} = 0, \tag{3.38}$$

for the fluid phase and

$$\frac{\partial \rho^s \bar{c}}{\partial t} + \frac{\partial \rho^s \bar{c} \tilde{u}_i^s}{\partial x_i} = 0 \tag{3.39}$$

for the sediment phase.

The momentum equations become

$$\begin{aligned} \frac{\partial \rho^f (1-\bar{c}) \tilde{u}_i^f}{\partial t} + \frac{\partial \rho^f (1-\bar{c}) \tilde{u}_i^f \tilde{u}_j^f}{\partial x_j} &= \rho^f (1-\bar{c}) g_i - (1-\bar{c}) \frac{\partial \bar{P}^f}{\partial x_i} + \overline{c' \frac{\partial P^{f'}}{\partial x_i}} \\ &\quad -\beta \bar{c} \left(\tilde{u}_i^f - \tilde{u}_i^s \right) - \beta \overline{c \Delta u_i^f} \\ &\quad + \frac{\partial}{\partial x_j} \left(R_{ji}^f + \overline{(1-c) T_{ji}^f} \right) \end{aligned} \tag{3.40}$$

for the fluid phase and

$$\begin{aligned} \frac{\partial \rho^s \bar{c} \tilde{u}_i^s}{\partial t} + \frac{\partial \rho^s \bar{c} \tilde{u}_i^s \tilde{u}_j^s}{\partial x_j} &= \rho^s \bar{c} g_i - \bar{c} \frac{\partial \bar{P}^f}{\partial x_i} + \overline{c' \frac{\partial P^{f'}}{\partial x_i}} + \beta \bar{c} \left(\tilde{u}_i^f - \tilde{u}_i^s \right) + \beta \overline{c \Delta \tilde{u}_i^f} \\ &\quad + \frac{\partial}{\partial x_j} \left(R_{ji}^s + \overline{c(P^s - P^f)} \delta_{ij} + \overline{c T_{ji}^s} \right) \end{aligned} \tag{3.41}$$

for the sediment phase. In both momentum equations, $\bar{P}^f$ is the averaged fluid pressure and $P^{f'} \equiv P^f - \bar{P}^f$ the corresponding fluid pressure fluctuation. The notations R_{ij}^f and R_{ij}^s denote the large-scale Reynolds stresses for the fluid phase and the sediment phase respectively

$$R_{ij}^f = -\rho^f \overline{(1-c) \Delta u_i^f \Delta u_j^f} \tag{3.42}$$

$$R_{ij}^s = -\rho^s \overline{c \Delta u_i^s \Delta u_j^s} \tag{3.43}$$

In a way similar to the Reynolds stresses in the Reynolds Averaged Navier-Stokes equations, several terms in the concentration-weighted Averaged Two-Phase Flow equations require further modeling and discussion:

- The correlation between the concentration fluctuation and the pressure fluctuation gradient $\overline{c' \frac{\partial P^{f'}}{\partial x_i}}$. This term will be neglected mainly due to lack of information.

- The correlation between concentration and fluid velocity fluctuation $\beta\overline{c\Delta u_i^f}$ (see section 3.5.1).
- The total fluid phase stresses $\tau_{ij}^f = \overline{(1-c)T_{ij}^f} + R_{ij}^f$ (see sections 3.4 and 5.1.2).
- The total sediment phase stresses $\tau_{ij}^s = \overline{c(P^s - P^f)}\delta_{ij} + \overline{cT_{ij}^s} + R_{ij}^s$ (see section 3.5.2).

3.4 Two-phase fluid turbulence modeling

3.4.1 Total fluid stresses

The total fluid stresses consist of three terms: the concentration-weighted Averaged Fluid Reynolds Stresses, small-scale averaged Reynolds stresses and the viscous stresses. The concentration-weighted Averaged Fluid Reynolds Stresses will be modeled using the turbulent viscosity hypothesis:

$$R_{ij}^f = \rho^f \nu_T \left[\frac{\partial \tilde{u}_i^f}{\partial x_j} + \frac{\partial \tilde{u}_j^f}{\partial x_i} - \frac{2}{3}\frac{\partial \tilde{u}_k^f}{\partial x_k}\delta_{ij} \right] - \frac{2}{3}\rho^f(1-\bar{c})k_f\delta_{ij} \tag{3.44}$$

where ν_T is the turbulent eddy viscosity and k_f the fluid turbulent kinetic energy

$$k_f = \frac{1}{2(1-\bar{c})}\overline{(1-c)\Delta u_i^f \Delta u_i^f} \tag{3.45}$$

The small-scale Reynolds stresses are the stresses resulting from the continuum hypothesis average. Taking them into account would introduce another turbulent eddy viscosity ν_t, which would be specified based on the mechanisms causing such small-scale turbulence. The two major mechanisms involved there are, first, the turbulence generated by the flow of the interstitial fluid around the sediment particles and, second, the turbulence induced by the small-scale particle velocity

fluctuations. In the dilute region, the particles are scarce and the small-scale turbulence effect will thus be negligible on the mean flow quantities. Elsewhere, ν_t is characterized by a length scale and a velocity scale. For the first mechanism, the characteristic length scale is on the order of the particle diameter and the characteristic velocity scale the relative velocity U_r. The second mechanism has the mean free path as length scale and a velocity scale based on the sediment fluctuation energy. In the concentrated region, the mean free path is small and the length scale for the first mechanism will be smaller than the diameter due to the small distance between particle. Even though this leads to a small value for ν_t, it should still be compared to ν_T to evaluate the relative importance of the small-scale and large-scale stresses. ν_T can be characterized by the mixing length and the square root of the turbulent kinetic energy. Further assuming that the turbulent kinetic energy and the sediment fluctuation energy are of the same order, the turbulence due to the small-scale particle fluctuations can be neglected when the fluid turbulence mixing length is much bigger than the particles mean free path, which should be the case. Even though scaling argumentation does not lead to a satisfactory conclusion for the other mechanism, the turbulence generated by the flow of the interstitial fluid around the sediment particles will be neglected (mainly for simplicity purposes). The total fluid stresses can therefore be expressed as

$$\tau_{ij}^f = \rho^f \left(\nu_T + \nu\right) \left[\frac{\partial \tilde{u}_i^f}{\partial x_j} + \frac{\partial \tilde{u}_j^f}{\partial x_i} - \frac{2}{3}\frac{\partial \tilde{u}_k^f}{\partial x_k}\delta_{ij}\right] - \frac{2}{3}\rho^f(1-\bar{c})k_f\delta_{ij} \tag{3.46}$$

3.4.2 Two-phase $k-\varepsilon$ model

Using the eddy viscosity hypothesis to model the fluid Reynolds stresses requires specification of the eddy viscosity ν_T. Different approaches of various complexity have been used for sediment transport. Algebraic models specify the eddy viscosity either directly or through the use of a mixing length (e.g., *Dong and Zhang*, 1999;

Asano, 1990). The eddy viscosity can also be calculated using the balance equation of turbulent kinetic energy and an empirical length scale (i.e., one-equation model). The use of two-equation models for which two turbulence quantities, such as the fluid turbulent kinetic energy k_f and the fluid turbulent dissipation rate ε_f for example, are found by solving respective balance equations makes the closure model complete (*Pope*, 2000). We scale here the eddy viscosity using k_f, ε_f and the concentration:

$$\nu_T = C_\mu \frac{(1-\bar{c})k_f^2}{\varepsilon_f}. \tag{3.47}$$

Balance equations for both k_f and ε_f have been shown in the literature (e.g., *Elghobashi and Abou-Arab*, 1983) and can be summarized as follows:

$$\frac{\partial K}{\partial t} + \frac{\partial K\tilde{u}_j^f}{\partial x_j} = \mathcal{P}_k + \frac{\partial T_j^k}{\partial x_j} - E - D_p, \tag{3.48}$$

$$\frac{\partial E}{\partial t} + \frac{\partial E\tilde{u}_i^f}{\partial x_i} = C_{\varepsilon 1}\frac{\varepsilon_f}{k_f}\mathcal{P}_k + \frac{\partial T_j^\varepsilon}{\partial x_j} - C_{\varepsilon 2}\frac{\varepsilon_f}{k_f}E - C_{\varepsilon 3}\frac{\varepsilon_f}{k_f}D_p, \tag{3.49}$$

where

$$K = \rho^f(1-\bar{c})k_f, \tag{3.50}$$

$$E = \rho^f(1-\bar{c})\varepsilon_f. \tag{3.51}$$

In the balance equations, $\mathcal{P}_k$ is the production of kinetic energy, T^k and T^ε are transport terms modeled following a gradient diffusion assumption:

$$T_j^k = \left(\nu + \frac{\nu_T}{\sigma_k}\right)\frac{\partial K}{\partial x_j}, \tag{3.52}$$

$$T_j^\varepsilon = \left(\nu + \frac{\nu_T}{\sigma_\varepsilon}\right)\frac{\partial E}{\partial x_j}. \tag{3.53}$$

The last term D_p is due to the phase interaction drag term in the fluid momentum equation. It is added here as an additional dissipative term for the turbulent energy, however, it can also be a productive term (i.e., $D_p < 0$). Detailed expressions of the fluid turbulence governing equations are presented in appendix A.

Table 3.1: Common values for numerical coefficients in the model.

σ_c	C_μ	$C_{\varepsilon 1}$	$C_{\varepsilon 2}$	$C_{\varepsilon 3}$	σ_k	σ_ε
1.0	0.09	1.44	1.92	1.2	1.0	1.3

Complete closure of the model requires the specification of several parameters related to the fluid turbulence modeling: C_μ, $C_{\varepsilon 1}$, $C_{\varepsilon 2}$, $C_{\varepsilon 3}$, σ_k and σ_ε. Common values for these coefficients (e.g., *Hsu et al.*, 2004; *Longo*, 2005) are presented in table 3.1. C_μ, $C_{\varepsilon 1}$, $C_{\varepsilon 2}$, σ_k and σ_ε are chosen to be the same as those values usually used in $k-\varepsilon$ models for clear fluids, while $C_{\varepsilon 3}$ is chosen based on sediment laden jets results (*Elghobashi and Abou-Arab*, 1983). This particular set of coefficients will be later referred to as the dilute flow turbulence assumption.

3.5 Sediment transport modeling

Sediment particles can be suspended by mainly two mechanisms: fluid turbulence and particle collisions, both of which need to be modeled accurately and are specific to sediment transport modeling. Each one of these processes corresponds to a term in the sediment phase momentum equation, $\beta\overline{c\Delta u_i^f}$ for the sediment suspension due to the fluid turbulence and $\partial\tau_{ji}^s/\partial x_j$ for the sediment suspension due to inter-particle interactions, and will be discussed in more details in the following sections.

3.5.1 Turbulent suspension

The correlation between concentration and fluid velocity fluctuations is usually called turbulent suspension. It represents the turbulent sediment mass flux generated by the interaction of the sediment with the large-scale fluid turbulence and

is commonly modeled using a gradient diffusion hypothesis (e.g., *McTigue*, 1981):

$$\overline{c\Delta u_i^f} = -\frac{\nu_T}{\sigma_c}\frac{\partial \bar{c}}{\partial x_i}, \tag{3.54}$$

where σ_c is the ratio of the sediment turbulent diffusivity over the fluid eddy viscosity, also called Schmidt number. More details on the specification of this parameter will be provided in chapter 4 for the dilute flow model and in chapter 5 for the model that includes the sediment stress closure.

3.5.2 Sediment phase stresses

The last term to be modeled in equations 3.38 to 3.41 is the sediment phase stress gradient that represents the transfer of momentum due to the particle-particle interactions. At the bed, bottom friction caused by a near-bed shear flow dislodges sediment particles. Such particles are then accelerated by the ambient flow and in turn dislodge other particles upon rebound. As this process repeats itself, bed particles lose contact, start to move and interact with each other.

It has been common in the literature to divide sand transport into bed load and suspended load. Although no precise definition for both terms exists, bed load occurs in a relatively thin region of high concentration where sediment transport responds instantly to bed shear stress. Above the bed load, the suspended load is of dilute concentration and particle movement is mostly the result of fluid turbulence agitation. Near the bottom of the bed load, fluid turbulence is small and the dominant mechanism for suspension and transport is particle intergranular interaction. At the upper end of the bed load region, as the concentration decreases, fluid turbulence becomes stronger while intergranular interactions diminish. Sediment particles are then entrained by turbulent fluid eddies, as turbulent suspension becomes the dominant transport mechanism.

Several approaches of different complexity are usually employed to model particle intergranular interactions. One can assume that the flow is dilute and then neglect the sediment stresses. In such an approach, the bed load is actually modeled though the use of appropriate boundary conditions (see section 4.2). In the case where diluteness is not assumed, expressions for the sediment stresses have to be used. Sediment stresses closures can usually be based on phenomenological equations (*Bagnold* (1954), *Savage and McKeown* (1983) for example) or on a collisional granular flow theory (*Jenkins and Savage*, 1983; *Jenkins*, 1998).

The closure scheme for the sediment stresses in the present sediment transport model is based on different descriptions of the inter-particle interactions throughout the water column (figure 3.1). Below the bed, which is defined as the location where particles can first be sheared, the particles are stationary and have solid-like behavior in that they are able to sustain compression and shear. Some distance above the bed (a few grain diameters), as sediment concentration becomes lower, each particle moves independently of other particles and behaves analogously to molecules in the kinetic theory of gases. However, the rigid structure of the solid-like region is not broken at once to give rise to the fluid-like region but rather follows a transition (*Zhang and Campbell*, 1992). The particles will first move while staying in contact and interacting frictionally with their neighbors. This is the quasi-static regime of enduring contact, which we will take to be for concentrations between the random close-packing value ($c^\star = 0.635$) and the random loose-packing value ($c_\star = 0.57$). Once the particle motion is rapid enough, sufficient energy is available to break the frictional bonds and particles enter the collisional regime. Further away from the bed, sediment particles become dilute and the particle-particle interactions can be neglected.

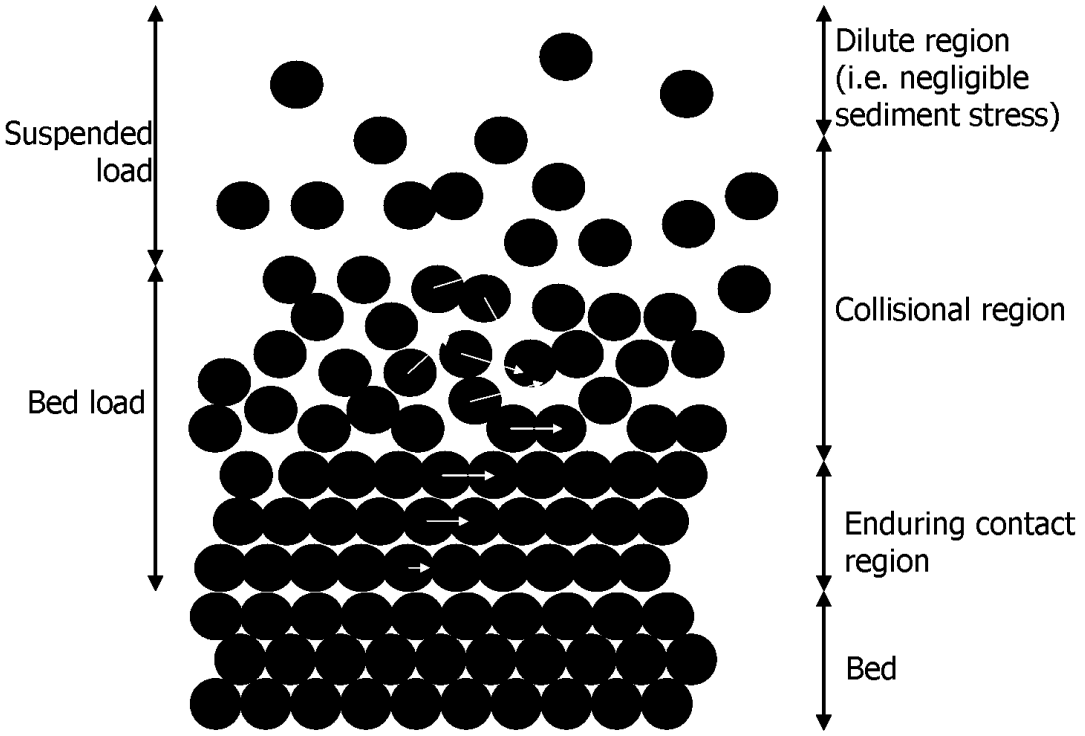

Figure 3.1: Sediment stress diagram throughout the water column. To the right are labelled the different regions corresponding to different sediment stress formulation. To the left are labelled the bed load and the suspended load regions.

Collisional region

Balance laws, constitutive relations and boundary conditions for systems of colliding grains (e.g., *Jenkins and Savage*, 1983; *Jenkins*, 1998) have been derived using an analogy to the kinetic theory of dense gases (*Chapman and Cowling*, 1970). In the collisional region, the sediment stresses are calculated using the constitutive relations derived for collisional flows of identical, frictionless, nearly elastic spheres (*Jenkins*, 1998) and a balance equation for the particle fluctuating energy k_s derived from the particle-phase momentum equations (e.g., *Zhang and Reese*, 2003; *Hsu et al.*, 2004),

$$k_s = \frac{1}{2\bar{c}}\overline{c\Delta u_i^s \Delta u_i^s}. \tag{3.55}$$

The balance equation for k_s is

$$\frac{\partial \rho^s \bar{c} k_s}{\partial t} + \frac{\partial \rho^s \bar{c} k_s \tilde{u}_j^s}{\partial x_j} = \tau_{ij}^s \frac{\partial \tilde{u}_i^s}{\partial x_j} - \frac{\partial \mathcal{Q}_j}{\partial x_j} - \gamma + 2\beta\bar{c}\left(\alpha k_f - k_s\right) \tag{3.56}$$

where both the energy flux $\mathcal{Q}_j$ and the dissipation γ are also calculated using constitutive relations derived for collisional flows of identical, frictionless, nearly elastic spheres.

The collisional stress tensor is

$$\tau_{ij}^{sc} = \left(-p_c + \omega_c \frac{\partial \tilde{u}_k^s}{\partial x_k}\right)\delta_{ij} + \mu_c\left(\frac{\partial \tilde{u}_i^s}{\partial x_j} + \frac{\partial \tilde{u}_j^s}{\partial x_i} - \frac{2}{3}\frac{\partial \tilde{u}_k^s}{\partial x_k}\delta_{ij}\right) \tag{3.57}$$

where the collisional pressure p_c, the bulk viscosity ω, and the shear viscosity μ_c are

$$p_c = \frac{2}{3}\rho^s\left(1 + 4G_0\right)\bar{c}k_s \tag{3.58}$$

$$\omega = \frac{8}{3\sqrt{\pi}}\rho^s d\bar{c}G_0\left(\frac{2}{3}k_s\right)^{1/2} \tag{3.59}$$

$$\mu_c = \frac{8}{5\sqrt{\pi}}\rho^s d\bar{c}G_0^\star\left(\frac{2}{3}k_s\right)^{1/2}\left[1 + \frac{\pi}{12}\left(1 + \frac{5}{8G_0^\star}\right)^2\right] \tag{3.60}$$

G_0 is related to the radial distribution function for contacting identical particles $g_0(\bar{c})$ by $G_0 \equiv \bar{c} g_0(\bar{c})$, where following *Torquato* (1995)

$$g_0(\bar{c}) = \begin{cases} \frac{2-\bar{c}}{2(1-\bar{c})^3} & \text{for } \bar{c} < 0.49 \\ \frac{2-0.49}{2(1-0.49)^3} \frac{0.64-0.49}{(0.64-\bar{c})} & \text{for } 0.49 \leq \bar{c} < 0.64 \end{cases} \tag{3.61}$$

$G_0^\star$ is similarly related to a radial distribution function that is modified for concentrations between the random loose packing value ($c_\star = 0.57$) and the random close packing value ($c^\star = 0.635$) (*Hsu et al.*, 2004)

$$g_0^\star(\bar{c}) = \begin{cases} \frac{2-\bar{c}}{2(1-\bar{c})^3} & \text{for } \bar{c} < 0.49 \\ \frac{2-0.49}{2(1-0.49)^3} \frac{0.64-0.49}{(0.64-\bar{c})} & \text{for } 0.49 \leq \bar{c} < 0.57 \\ \frac{2-0.49}{2(1-0.49)^3} \frac{0.64-0.49}{(0.64-\bar{c})^{1.75}} & \text{for } 0.57 \leq \bar{c} < 0.64 \end{cases} \tag{3.62}$$

The sediment fluctuation energy flux is

$$\mathcal{Q}_j = -\frac{2}{3} \kappa_c \frac{\partial k_s}{\partial x_j} \tag{3.63}$$

where

$$\kappa_c = \frac{4}{\sqrt{\pi}} \rho^s d \bar{c} G_0 \left(\frac{2}{3} k_s \right)^{1/2} \left[1 + \frac{9\pi}{32} \left(1 + \frac{5}{12 G_0} \right)^2 \right] \tag{3.64}$$

The collisional dissipation is associated with the inelasticity of the particles

$$\gamma = \left[\frac{16 \rho^s G_0}{\sqrt{\pi} d} \left(\frac{2}{3} k_s \right)^{1/2} - 4 \rho^s G_0 \frac{\partial \tilde{u}_k^s}{\partial x_k} \right] (1-e) \bar{c} k_s \tag{3.65}$$

Enduring contact region

For concentration bigger than the random loose packing value ($c_\star = 0.57$), particles interact less through collision and are more in contact. In such a region, stresses arising from enduring contacts become important and need to be included. We then have contributions from collisions and enduring contacts in the total sediment stresses

$$\tau_{ij}^s = \tau_{ij}^{sc} + \tau_{ij}^{se} \tag{3.66}$$

where τ_{ij}^{se} represent the stresses from enduring contacts. *Bocquet et al.* (2001) suggest that for concentrations greater than the random loose-packing concentration the collisional shear viscosity should be greatly increased. Such an increase of the shear viscosity is incorporated in the model through the use of the modified radial distribution function $g_0^{\star}(\bar{c})$ instead of $g_0(\bar{c})$. Furthermore, an extra normal stress component due to homogeneously packed identical spheres in Hertzian contact is added to the total sediment stress (*Hsu et al.*, 2004). We will then take the enduring contacts stress tensor to be

$$\tau_{ij}^{se} = \begin{cases} 0, & \bar{c} < c_{\star} \\ \frac{2}{9\pi\sqrt{3}} \frac{\mu_e}{1-\upsilon} K(\bar{c}) \bar{c} \left(\bar{c} - c_{\star}\right)^5 \delta_{ij}, & c_{\star} \leq \bar{c} \leq c^{\star} \end{cases} \tag{3.67}$$

where μ_e is the shear modulus, υ is Poisson's ratio and $K(\bar{c})$ is a function of concentration

$$K(\bar{c}) = 3 + 3\sin\frac{\pi}{2}\left(2\frac{\bar{c} - c_{\star}}{c^{\star} - c_{\star}} - 1\right), \quad c_{\star} \leq \bar{c} \leq c^{\star} \tag{3.68}$$

For concentrations greater than the random-close packed concentration, the sediment particles are fixed and the sediment stress does not need to be calculated.

From a theoretical point of view, such a specification for the sediment stresses is more complete than other existing models in several aspects. First, the intergranular stress closure in the energetic regime of sediment transport is based on the kinetic theory of granular flow, which is more general than phenomenological expressions such as the Bagnold's rheological relation developed from simple shear flow for example. Secondly, sediment stresses in the quasi-static regime of enduring contact (*Zhang and Campbell*, 1992) are incorporated separately from that of the kinetic theory, providing a more complete description for the granular rheology.

3.6 One-dimensional assumption for waves

So far, most sheet flow sediment transport models assume flow uniformity in the flow direction (denoted by x thereafter), which means that all changes in the x direction are neglected to the exception of the pressure gradient $\partial P^f/\partial x$. While this is reasonable for comparisons with laboratory experiments conducted in oscillatory tunnels and for open-channel flows, it might not be the case for real waves. It is common when studying waves to use the wavelength λ as the length scale in the flow direction and the wave period T as the time scale. Using U and W as the velocity scales respectively in the x direction and in the z direction (normal to x), and δ as the length scale in the vertical direction, it is possible to deduce conditions required to satisfy the flow uniformity.

For clear fluids in absence of turbulence, $\partial/\partial x$ terms are only present in the convective acceleration and in the viscous stress term. The term in the convective acceleration can be neglected when

$$\frac{U}{C} << 1, \tag{3.69}$$

which actually implies that both convective terms can be neglected respect to the time derivative of the velocity. The $\partial/\partial x$ term in the viscous stress can be neglected when

$$\frac{\delta^2}{\lambda^2} << 1. \tag{3.70}$$

When turbulence is accounted for in clear fluids, additional terms are present in the Reynolds Averaged Navier-Stokes equations. The mean flow momentum equation can be written as:

$$\frac{\partial \bar{u}_j}{\partial t} + \bar{u}_i \frac{\partial \bar{u}_j}{\partial x_i} = \frac{\partial}{\partial x_i}\left[\nu_e \left(\frac{\partial \bar{u}_i}{\partial x_j} + \frac{\partial \bar{u}_j}{\partial x_i}\right)\right] - \frac{1}{\rho}\frac{\partial}{\partial x_j}\left(P + \frac{2}{3}\rho k\right) \tag{3.71}$$

where $\nu_e = \nu_T + \nu$ is the effective viscosity. The condition for negligible convective term remains unchanged. The condition for the right hand side (to the exception

of the pressure gradient) has to deal with an extra term and a different stress formulation. For the horizontal momentum equation, the right hand side term consist of the horizontal pressure gradient and of

$$2\frac{\partial}{\partial x}\left(\nu_e\frac{\partial \bar{u}}{\partial x}\right)+\frac{\partial}{\partial z}\left(\nu_e\frac{\partial \bar{w}}{\partial x}\right)+\frac{\partial}{\partial z}\left(\nu_e\frac{\partial \bar{u}}{\partial z}\right)-\frac{2}{3}\frac{\partial k}{\partial x} \tag{3.72}$$

In order to compare the relative importance of the different terms we then have to estimate the effective viscosity and k. Assuming that $\nu_T >> \nu$, we get $\nu_e \sim \nu_T$ and the eddy viscosity can be written as the product of a length and of a velocity. Following the mixing length model for simple shear flows, we have

$$\nu_T = l_m^2\left|\frac{d\bar{u}}{dz}\right| \tag{3.73}$$

and then

$$\nu_e \sim l_m^2\frac{U}{\delta} \tag{3.74}$$

Using the mixing-length as the length and $\sqrt{k}$ as the velocity, the effective viscosity will also scale as $\nu_e \sim l_m\sqrt{k}$ or

$$\sqrt{k} \sim l_m\frac{U}{\delta} \tag{3.75}$$

Using the continuity equation ($U/\lambda = W/\delta$), the different terms in the horizontal momentum equation right hand side then scale as

$$\frac{\partial}{\partial x}\left(\nu_e\frac{\partial \bar{u}}{\partial x}\right) \sim l_m^2\frac{U}{\delta}\frac{U}{\lambda^2}, \tag{3.76}$$

$$\frac{\partial}{\partial z}\left(\nu_e\frac{\partial \bar{u}}{\partial z}\right) \sim l_m^2\frac{U}{\delta}\frac{U}{\delta^2}, \tag{3.77}$$

$$\frac{\partial}{\partial z}\left(\nu_e\frac{\partial \bar{w}}{\partial x}\right) \sim l_m^2\frac{U}{\delta}\frac{W}{\lambda\delta} = -l_m^2\frac{U}{\delta}\frac{U}{\lambda^2} \tag{3.78}$$

and

$$\frac{\partial k}{\partial x} \sim l_m^2\frac{U^2}{\lambda\delta^2}. \tag{3.79}$$

The most restrictive condition arises from neglecting the last term ($\partial k/\partial x$), and the flow uniformity is then assured when the following condition is satisfied

$$\frac{\delta}{\lambda} << 1. \tag{3.80}$$

Uniformity in two-phase flow will require that more conditions are satisfied. First, the "turbulent suspension" term in the horizontal direction has to be negligible. Then, a similar approach comparing the relative importance of the different terms has to be done for the sediment phase equations. Negligible "turbulent suspension" in the horizontal momentum equation requires that

$$\frac{\beta}{\rho_f}\frac{\nu_T}{\sigma_c}\frac{\partial \bar{c}}{\partial x} << \nu_e \frac{U}{\delta^2} \tag{3.81}$$

which leads to

$$\frac{\delta}{\lambda} << \frac{\rho_f}{\beta}\frac{U}{\delta}. \tag{3.82}$$

From equation 3.13 and taking that Re_p will not be very large, we get that

$$\frac{\beta}{\rho_f} \sim 20\frac{\nu}{d^2} \tag{3.83}$$

and then

$$\frac{\delta}{\lambda} << 20\frac{d}{\delta}\frac{Ud}{\nu}. \tag{3.84}$$

For typical sheet flow sand transport condition that $d^2 \sim 10^{-7}m$, $\delta \sim 10cm$, $U \sim 1m/s$ and the right hand side will be bigger than 1. The condition stated in equation 3.80 remains the critical one, and sediment laden flows will satisfy uniformity the same way as clear fluid flow as far as the fluid phase in concerned.

For the sediment phase, a similar approach can be taken and similar terms will have to be compared. However, for the sediment phase, the collisional viscosity and k_s should be considered instead of the effective fluid viscosity and the fluid turbulent kinetic energy. We will have $\nu_c = \mu_c/\rho_s \sim \sqrt{(}k_s)$, and we will approximate that $k_s \sim k_f \sim k$. We will also keep the same velocity scales for both the fluid phase and the sediment phase velocities. Following the same steps as for the clear fluid turbulent case and the horizontal "turbulent suspension" leads to the following three conditions:

$$\frac{U}{C} << 1. \tag{3.85}$$

for negligible convective acceleration,

$$\frac{\delta l_m}{\lambda d} << 1 \tag{3.86}$$

for a negligible $\partial/\partial x$ term in the sediment stress, and

$$\frac{\delta l_m}{\lambda d} << 20\frac{d}{\delta}\frac{Ud}{\nu} \tag{3.87}$$

for a negligible horizontal "turbulent suspension". Again, the third condition will be less restrictive than the second. Altogether, a criterion on uniformity can be formulated in terms of the three conditions expressed in equations 3.69, 3.80, 3.86. However, since the mixing length will be bigger than the particle diameter, equation 3.86 is more restrictive than equation 3.80 and satisfying equations 3.69 and 3.86 are sufficient to have uniform flows. The last condition means than waves are (very) long, and the first condition can then be approximated by a small amplitude condition.

CHAPTER 4

ONE-DIMENSIONAL DILUTE FLOW MODEL

Detailed two-phase models that incorporate proper sediment stress closures are computationally demanding and at present are still not suitable for modeling sediment transport of, for example, the entire surfzone. Often, sediment transport models in the surfzone assume dilute transport, focus on suspended load and parameterize the concentrated region through near-bed boundary conditions (e.g. *Hagatun and Eidsvik*, 1986; *Savioli and Justesen*, 1996; *Hsu and Liu*, 2004). However, several modeling difficulties are not completely resolved in these dilute models. The intergranular stress is neglected and therefore the bedload effects need to be included through bottom boundary conditions. Several choices of boundary conditions are possible, but their accuracies are still not clear. Moreover, the turbulent suspension is commonly modeled using a gradient transport hypothesis but the specification of the particle diffusion coefficient is not completely understood yet.

In this chapter, we will use the sediment transport model presented in chapter 3 with the dilute concentration assumption and for one-dimensional flows in order to investigate dilute models' closure issues (i.e., the choice of the bottom boundary condition and the specification of the particle diffusion coefficient). After a brief review of the of the dilute one-dimensional model, we will present the bottom boundary conditions implemented in this model. We will then investigate the particle diffusion coefficient and assess the performance of two sediment near-bed boundary conditions: an empirical formula (*van Rijn*, 1984a) and an approach based on simple bed load modeling (*Engelund and Fredsøe*, 1976).

4.1 Summary of the governing equations

In the dilute flow assumption, the sediment stresses are neglected in the momentum conservation equations. In the one dimensional model, the flow is also assumed to be uniform in the flow direction. Setting x as the flow direction and z the as the vertical direction, the horizontal velocities (in the flow direction) are denoted by u and the vertical velocities by w. The two continuity equations (equations 3.38 and 3.39)can then be summarized as

$$\frac{\partial \rho^f (1-\bar{c})}{\partial t} + \frac{\partial \rho^f (1-\bar{c}) \tilde{w}^f}{\partial z} = 0 \tag{4.1}$$

for the fluid phase continuity,

$$\frac{\partial \rho^s \bar{c}}{\partial t} + \frac{\partial \rho^s \bar{c} \tilde{w}^s}{\partial z} = 0 \tag{4.2}$$

for the sediment phase continuity. The momentum conservation (equations 3.40 and 3.41) yields two equations per phase:

$$\begin{aligned} \frac{\partial \rho^f (1-\bar{c}) \tilde{u}^f}{\partial t} + \frac{\partial \rho^f (1-\bar{c}) \tilde{u}^f \tilde{w}^f}{\partial z} &= \rho^f (1-\bar{c}) g_x - (1-\bar{c}) \frac{\partial \bar{P}^f}{\partial x} + \frac{\partial \tau_{xz}^f}{\partial z} \\ &\quad -\beta \bar{c} \left(\tilde{u}^f - \tilde{u}^s \right) \end{aligned} \tag{4.3}$$

and

$$\begin{aligned} \frac{\partial \rho^f (1-\bar{c}) \tilde{w}^f}{\partial t} + \frac{\partial \rho^f (1-\bar{c}) \tilde{w}^f \tilde{w}^f}{\partial z} &= \rho^f (1-\bar{c}) g_z - (1-\bar{c}) \frac{\partial \bar{P}^f}{\partial z} + \frac{\partial \tau_{zz}^f}{\partial z} \\ &\quad -\beta \bar{c} \left(\tilde{w}^f - \tilde{w}^s \right) + \beta \frac{\nu_T}{\sigma_c} \frac{\partial \bar{c}}{\partial z} \end{aligned} \tag{4.4}$$

for the fluid phase momentum conservation;

$$\frac{\partial \rho^s \bar{c} \tilde{u}^s}{\partial t} + \frac{\partial \rho^s \bar{c} \tilde{u}^s \tilde{w}^s}{\partial z} = \rho^s \bar{c} g_x - \bar{c} \frac{\partial \bar{P}^f}{\partial x} + \beta \bar{c} \left(\tilde{u}^f - \tilde{u}^s \right) \tag{4.5}$$

and

$$\frac{\partial \rho^s \bar{c} \tilde{w}^s}{\partial t} + \frac{\partial \rho^s \bar{c} \tilde{w}^s \tilde{w}^s}{\partial z} = \rho^s \bar{c} g_z - \bar{c} \frac{\partial \bar{P}^f}{\partial z} + \beta \bar{c} \left(\tilde{w}^f - \tilde{w}^s \right) - \beta \frac{\nu_T}{\sigma_c} \frac{\partial \bar{c}}{\partial z} \tag{4.6}$$

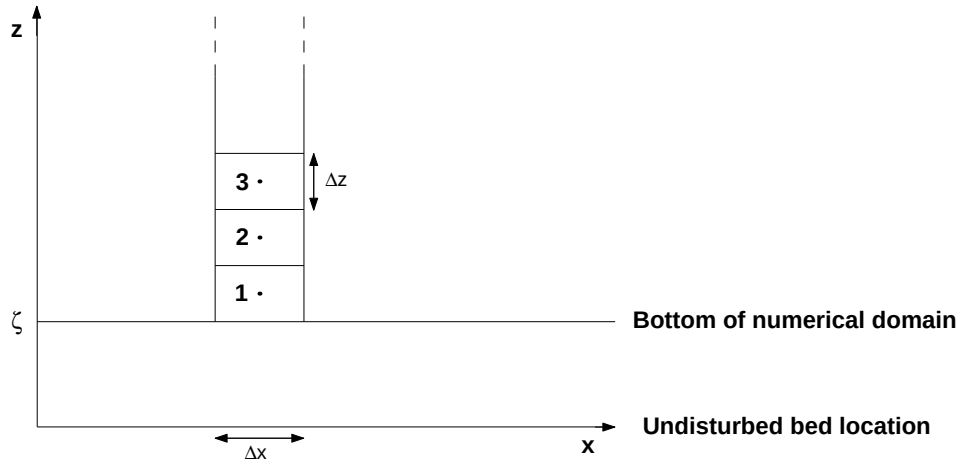

Figure 4.1: Near-bed boundary representation.

for the sediment phase momentum conservation. τ_{xz}^f and τ_{zz}^f respectively represent the total fluid shear and normal stresses, and are modeled using the dilute flow fluid turbulence closure previously introduced (see section 3.4).

Because of the gradient transport assumption for the fluid turbulent suspension, the Schmidt number σ_c is a free parameter to be specified in the model and its closure will be discussed in a following section (section 4.4).

4.2 Near-bed boundary conditions

Because of the dilute assumption, the location of the "bed" in this numerical model is the interface between the concentrated region and the dilute region. Since the concentrated region is not resolved, complete knowledge of the location of such an interface can not be obtained in the present dilute model. Therefore, it is approximated by specifying the lower boundary of the numerical model at a certain constant elevation ζ above the initially undisturbed bed (figure 4.1) and appropriate boundary conditions for both the fluid phase and the sediment phase need to be implemented at this bottom boundary ($z = \zeta$).

Both the sediment behavior in the high concentration region and the near-bed

boundary conditions are commonly parameterized using the Shields parameter and the sediment phase boundary conditions will thus be expressed as functions of the Shields parameter.

4.2.1 Fluid turbulence boundary conditions

Based on the analysis of the measured fluid velocity profile above a mobile sand bed under uniform and steady flow conditions, *Sumer et al.* (1996) suggested that the velocity profile follows a logarithmic law near the bed. Since the Favre averaging used in the model's balance equations reduces to a typical ensemble averaging in the dilute limit (*Hsu et al.*, 2003a) and for the horizontal velocity in one-dimensional flows (see chapter 3), we can use a rough wall logarithmic law to determine the bottom shear stress. However, for oscillatory flows, both the turbulent kinetic energy and the sediment pick-up may not be zero at flow reversal. We thus calculate the bottom shear stress using:

$$\theta = \frac{\sqrt{C_\mu} k_f}{(s-1)gd}, \tag{4.7}$$

and we use a no-flux boundary condition for the turbulent kinetic energy (e.g. *Hagatun and Eidsvik*, 1986):

$$\frac{\partial k_f}{\partial z} = 0. \tag{4.8}$$

Finally, the boundary condition for the turbulent dissipation rate is given as (e.g., *Pope*, 2000):

$$\varepsilon_f = \frac{C_\mu^{3/4} k_f^{3/2}}{\kappa z}, \tag{4.9}$$

where κ is the von Karman constant. It has been repeatedly reported that the presence of sediment reduces the value of the von Karman constant (e.g., *Vanoni*, 1975). In our case, the von Karman constant is only used at the bottom boundary to determine the turbulent dissipation rate. We would thus need to compute the

modified κ value at the elevation $z = \zeta$. Although *Hsu et al.* (2003a) provided a modified κ that is a function of the elevation, we choose for simplicity to keep the typical value of $\kappa = 0.41$.

4.2.2 Sediment phase boundary conditions

In dilute flow models, we neglect the particle-particle interactions and do not resolve the highly concentrated region close to the bed. Therefore, we need to parameterize the concentrated region of transport which provides information on the amount of sediment that is entrained into the dilute region. This is achieved through specifying appropriate near-bed boundary conditions for the total sediment flux. Assuming a local equilibrium, we write the total vertical sediment flux as the sum of an upward flux (also called pick-up) and of a downward flux due to the immersed weight of the sediment particles (deposition rate).

$$\bar{c}\tilde{w}_s = \Psi_p(\theta) - \frac{\rho_s - \rho_f}{\beta} g\bar{c}. \tag{4.10}$$

Hence, complete knowledge of the total vertical flux requires information on both the pick-up and the sediment concentration near the bed, which can be provided in different ways. Here, we examine two commonly used approaches: describing the pick-up by using an empirical formula and by specifying the concentration at a reference location above the bed.

Empirical pick-up approach

The pick-up can be specified as an empirical function of the flow parameters and sediment properties. In this paper, we adopt the pick-up formula suggested by *van Rijn* (1984a):

$$\frac{\Psi_p(\theta)}{\sqrt{(s-1)gD_{50}}} = 3.3 \times 10^{-4} \left[\frac{\theta - \theta_c}{\theta_c}\right]^{1.5} \left[\frac{(s-1)gD_{50}^3}{\nu^2}\right]^{0.1}, \quad \text{for} \quad \theta > \theta_c, \tag{4.11}$$

where $\theta_c = 0.05$ is the critical Shields parameter, which corresponds to the bottom shear stress necessary to initiate particle motion. The experiments used to obtain this pick-up formula were done by a series of steady flow experiments of mean flow velocities in the range 0.5–1.0 m/s (Shields parameters less than 0.9). Rigorously speaking, we can only use this expression within the range of the experiments. For our purposes and for simplicity, we will assume that this relation still holds quasi-steadily under unsteady forcing (e.g. oscillatory flows with a mean current). We further assume that van Rijn's formula still holds when the Shields parameter is greater than 0.9. Finally, we will follow *Hsu and Liu* (2004) and set ζ equal to the roughness K_s.

Reference concentration approach

In this approach, we take the reference location to be the bottom boundary of the computational domain and specify the concentration there as a function of the Shields parameter. Following the argument that for equilibrium suspension the total vertical flux must vanish (e.g., *Garcia and Parker*, 1991), we approximate the pick-up by:

$$\Psi_p(\theta) = \frac{\rho_s - \rho_f}{\beta} g c_{ref}(\theta). \tag{4.12}$$

Once again, this is true only for equilibrium flow conditions, and we assume that near the bed, the disequilibrium introduced by unsteady forcing is mild.

We adopt an explicit parameterization for reference concentration suggested by *Engelund and Fredsøe* (1976). Such a relationship is not solely empirical, but based on theoretical bedload model (e.g., *Einstein*, 1950):

$$c_{ref}(\theta) = \begin{cases} 0 & \text{for} \quad \theta < \theta_c \\ c_{max} \frac{\theta - \theta_c}{\theta_l - \theta_c} & \text{for} \quad \theta_c < \theta < \theta_l \\ c_{max} & \text{for} \quad \theta_l < \theta \end{cases}, \tag{4.13}$$

where $c_{max} = 0.3$ and $\theta_l = 1.5$ give a reasonable approximation of the Engelund-Fredsøe formula. This formula specifies the reference concentration at a distance of two particle diameters above the bed. We thus choose to have the numerical bottom boundary at $\zeta = 2d$.

Deposition rate

As explained previously, we also need information on the sediment concentration near the bed to calculate the deposition rate (downward flux in equation 4.10) and thus the total vertical flux. In our numerical model, this requires to explicitly know the concentration at the bottom boundary. Different treatments are possible. We choose in the current study to extrapolate the concentration at the boundary from the interior concentration field (see below).

4.3 Numerical implementation

The proposed two-phase equations have been incorporated into a wave-hydrodynamic model called COBRAS (*Lin and Liu*, 1998a,b) and are solved by a finite difference scheme on a staggered grid system (see appendix B for more details). The sediment phase equations are solved at the beginning of the computational cycle using a predictor-corrector scheme. After the sediment concentration and velocities are found, the two-step projection method (modified for two-phase equations) is used to solve for the fluid pressure and velocities. The $k-\varepsilon$ equations for fluid turbulence are updated at the end of the computational cycle.

The sediment phase boundary conditions are implemented in the numerical model as follows. Information on the pick-up at $z = \zeta$ is found by using equation (4.11) or equations (4.12) and (4.13) in which the Shields parameter is obtained by evaluating equation (4.7) at the the first grid point above the bottom boundary

Table 4.1: Experimental flow conditions for the dilute flow model model-data comparison. U_c is the mean current velocity, U_{osc} the oscillatory velocity amplitude, T the period and D_{50} the median sediment diameter.

Data set	$U_c(m/s)$	$U_{osc}(m/s)$	$T(s)$	$D_{50}(mm)$
Horikawa et al. (1982)	0	1.27	3.6	0.2
Ribberink and Al-Salem (1995)	0	1.7	7.2	0.21
Katopodi et al. (1994a) - case E1	0.15	1.65	7.2	0.21
Katopodi et al. (1994a) - case E2	0.20	1.50	7.2	0.21
Katopodi et al. (1994a) - case E3	0.29	1.15	7.2	0.21
Janssen (1999) - case H6	0.24	1.47	7.2	0.13

(center of cell 1 in figure 4.1). Finally, the concentration for downward flux in (4.10) at $z = \zeta$ is found by extrapolation. That is, we linearly extrapolate the values calculated for cells 1 and 2 to find the value at the numerical bottom boundary ($z = \zeta$).

We test the proposed model and boundary conditions with laboratory measurements in a U-tube. Both pure oscillatory flows (*Horikawa et al.*, 1982; *Ribberink and Al-Salem*, 1995) and oscillatory flows superposed on a mean current (*Katopodi et al.*, 1994a; *Janssen*, 1999) are considered. The flow conditions of all experiments are summarized in table 4.1, in which the specific gravity of sediment is $s = 2.65$. In all cases we ensure that our numerical solutions reached the quasi-steady state and then we use the last twenty-five periods for the time-averaging.

4.4 Turbulent suspension closure

Although the issue concerning the value of the sediment diffusivity has been investigated (e.g., *Lees*, 1981; *van Rijn*, 1984b; *Whitehouse*, 1995; *Rose and Thorne*, 2001), it is still not very well understood and a satisfactory specification may depend on model equations and boundary conditions used. We will first try to

appreciate the influence of the Schmidt number on the numerical results and then introduce a new concentration dependent description.

4.4.1 Results sensitivity

Following *van Rijn* (1984b), we estimate that a reasonable range for possible values of the Schmidt number is from 0.3 to 1.0. The variation on the time-averaged concentration introduced by a change of the Schmidt number (figure 4.2 (a)) grows with the distance to the bed rapidly to an order of magnitude (note that a decrease in the Schmidt number leads to more suspension). The effect of σ_c on the magnitude of concentration time histories (figure 4.2 (b)) is also quite dramatic and depends on the specified boundary condition, even though the phase is almost insensitive to σ_c.

4.4.2 Constant Schmidt number

Adopting a constant value of σ_c and van Rijn pick-up function, *Hsu and Liu* (2004) calibrate the Schmidt number using the experimental results of *Ribberink and Al-Salem* (1995). Here we conduct similar calibration using reference concentration as near-bed boundary condition. Again, *Ribberink and Al-Salem* (1995) data is tested because it is more complete than Horikawa's data set and shows less scattering than the data sets of *Katopodi et al.* (1994a) and *Janssen* (1999). Consistent with *Hsu and Liu* (2004), the value of the Schmidt number we find depends on the region we consider for the best-fit: $\sigma_c = 0.7$ is found close to the bed ($z/D_{50} < 50$) whereas $\sigma_c = 0.52$ is found far ($50 < z/D_{50} < 175$) from the bed (see figure 4.4). Hence, describing the Schmidt number as a constant value might not be appropriate and improved results may be predicted by considering a concentration dependent closure.

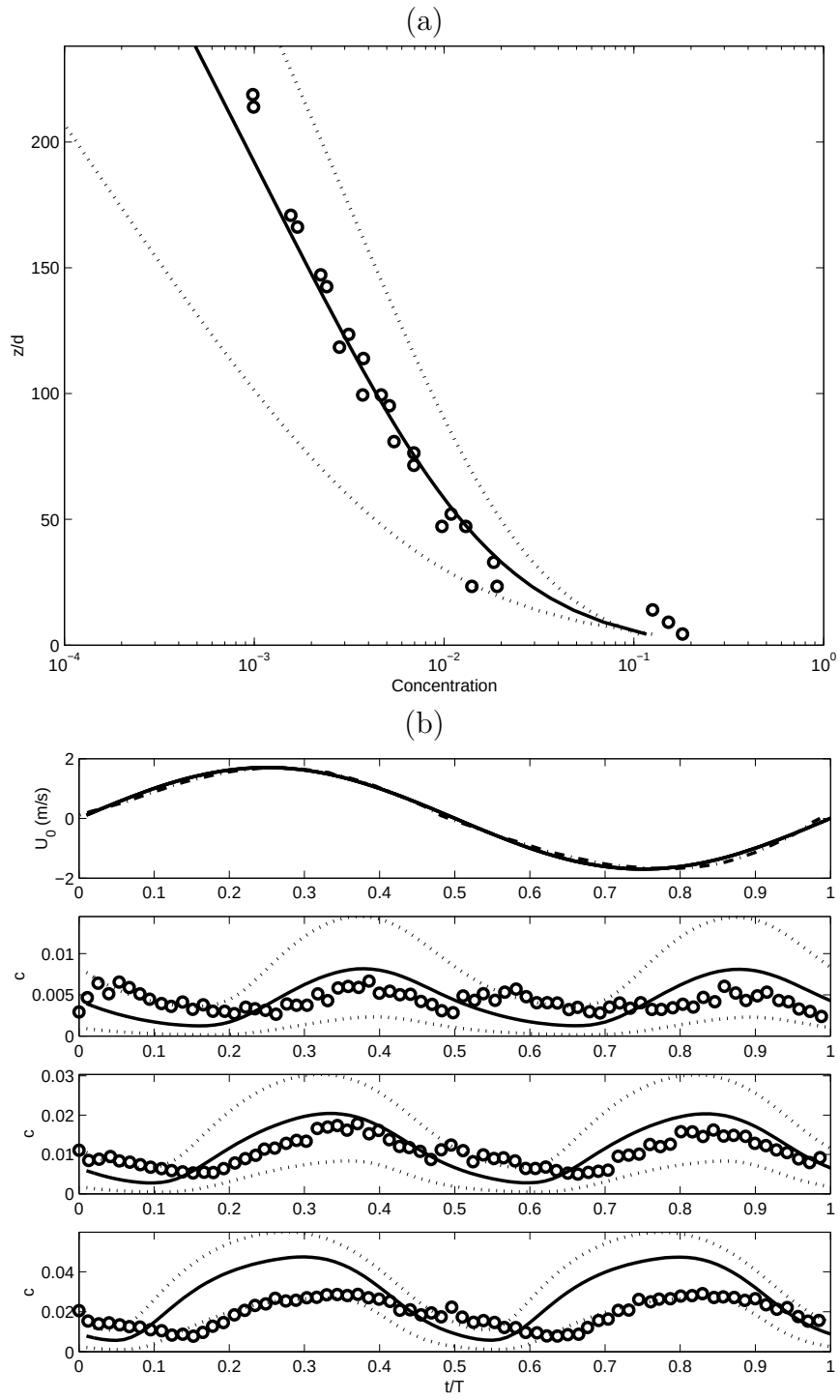

Figure 4.2: Influence of the Schmidt number on (a) the time-averaged concentration profile and (b) on the concentration time histories at different elevations using the reference concentration approach. The solid line is for $\sigma_c = 0.52$ and the dotted lines for $\sigma_c = 1.0$ and $\sigma_c = 0.3$. The symbols represent the measured data of *Ribberink and Al-Salem* (1995). For (b), from top to bottom are the time histories of the free stream velocity and of the concentration at $z/D_{50} = 100$, $z/D_{50} = 52$ and $z/D_{50} = 24$.

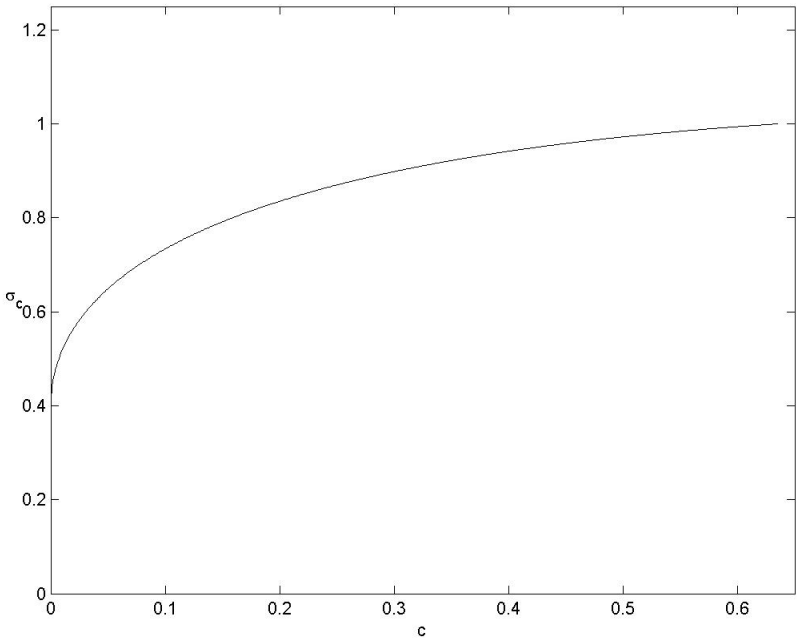

Figure 4.3: Schmidt number as a function of the concentration (equation 4.15) with $\sigma_{c0} = 0.40$ and $n_\sigma = 0.5$.

4.4.3 Concentration dependent Schmidt number

Despite model-data comparisons for constant Schmidt number that suggest a direct dependence of σ_c on the elevation above the bed, we believe it is more physically justified to assume that σ_c depends on the concentration, which in general gives the expected dependence on the elevation:

$$\sigma_c = f(\frac{\bar{c}}{c^\star}), \tag{4.14}$$

where $c^\star = 0.635$ is the maximum possible sediment concentration (close-packing concentration).

As argued in *van Rijn* (1984b), centrifugal forces on the sediment particles cause the sediment particles to be thrown to the outside of the fluid eddies. This implies a greater turbulent diffusion for the particles than for the fluid momentum, and σ_c is thus typically less than unity. Dynamic effects of the sediment on itself will also

limit the turbulent diffusion for high concentration. The Schmidt number is then expected to increase with the concentration, which is confirmed experimentally by *Lees* (1981). In addition, the experimental data of *Lees* (1981) suggests a power law to relate Schmidt number and sediment concentration. Finally, because an infinite sediment diffusivity is physically impossible, we force the Schmidt number to asymptotically approach a non-zero value as the concentration approaches zero. Consequently, the following function for σ_c is assumed:

$$\sigma_c = \sigma_{c0}\left(1 - \frac{\bar{c}}{c^\star}\right) + \left(\frac{\bar{c}}{c^\star}\right)^{n_\sigma}, \tag{4.15}$$

where σ_{c0} and n_σ are empirical constants. That σ_c is typically less than unity ensures that $n_\sigma > 0$. The Schmidt number derivative respect to the concentration also has to be positive, which leads to $1 \geq n_\sigma \geq \sigma_{c0}$. We fully determine this function empirically by performing model-data comparisons. In our case, using the *Ribberink and Al-Salem* (1995) data, we find: $n_\sigma = 0.5$ and $\sigma_{c0} = 0.39$ for the reference concentration approach, $n_\sigma = 0.5$ and $\sigma_{c0} = 0.40$ for the empirical pick-up approach of van Rijn.

We further test the proposed Schmidt number description with experimental conditions (table 4.1) sharing a constant particle diameter (*Ribberink and Al-Salem*, 1995; *Katopodi et al.*, 1994a). In all cases, the time averaged concentration profiles (figures 4.4, 4.5 and 4.6 (a)) are clearly better described by (4.15). The numerical results calculated by the new concentration dependent σ_c tend to follows those for $\sigma_c = 0.7$ close to the bed, and those for $\sigma_c = 0.52$ away from the bed. Moreover, unlike the predictions made by using a constant Schmidt number, the time-averaged concentration far from the bed is not underpredicted (compare dashed and solid curves for $z/D_{50} > 175$). The time history predictions (figures 4.4, 4.5 and 4.6 (b)) are quite good for the case without mean current, but are less satisfactory for the other cases with mean current. However, even for cases

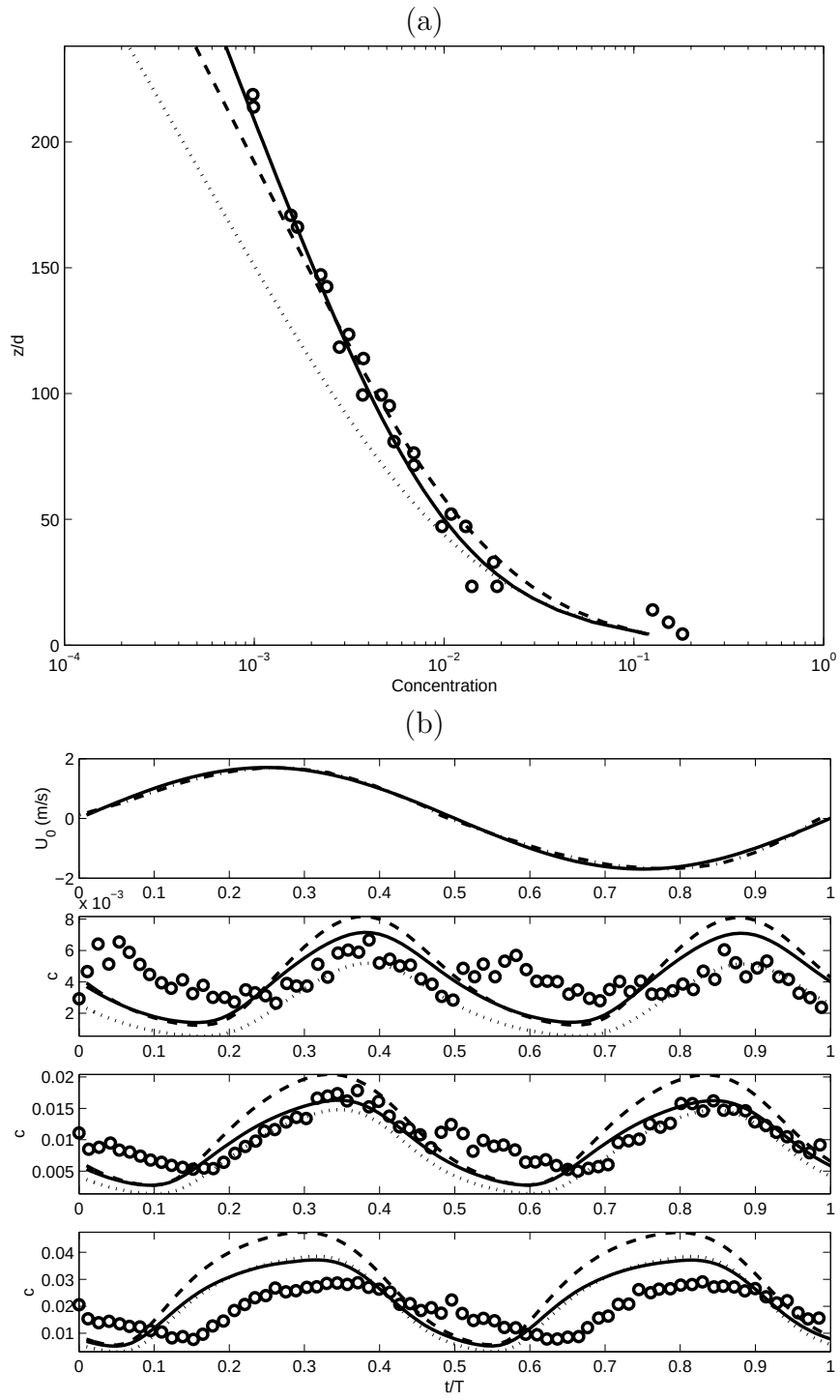

Figure 4.4: Comparison of (a) the time-averaged concentration profiles and (b) the concentration time histories at different elevations for the reference concentration approach for $\sigma_c = f(\bar{c}/c^\star)$ (solid line), $\sigma_c = 0.52$ (dashed line) and $\sigma_c = 0.7$ (dotted line) with the measured data of *Ribberink and Al-Salem* (1995) (symbols). For (b), from top to bottom are the time histories of the free stream velocity and of the concentration at $z/D_{50} = 100$, $z/D_{50} = 52$ and $z/D_{50} = 24$.

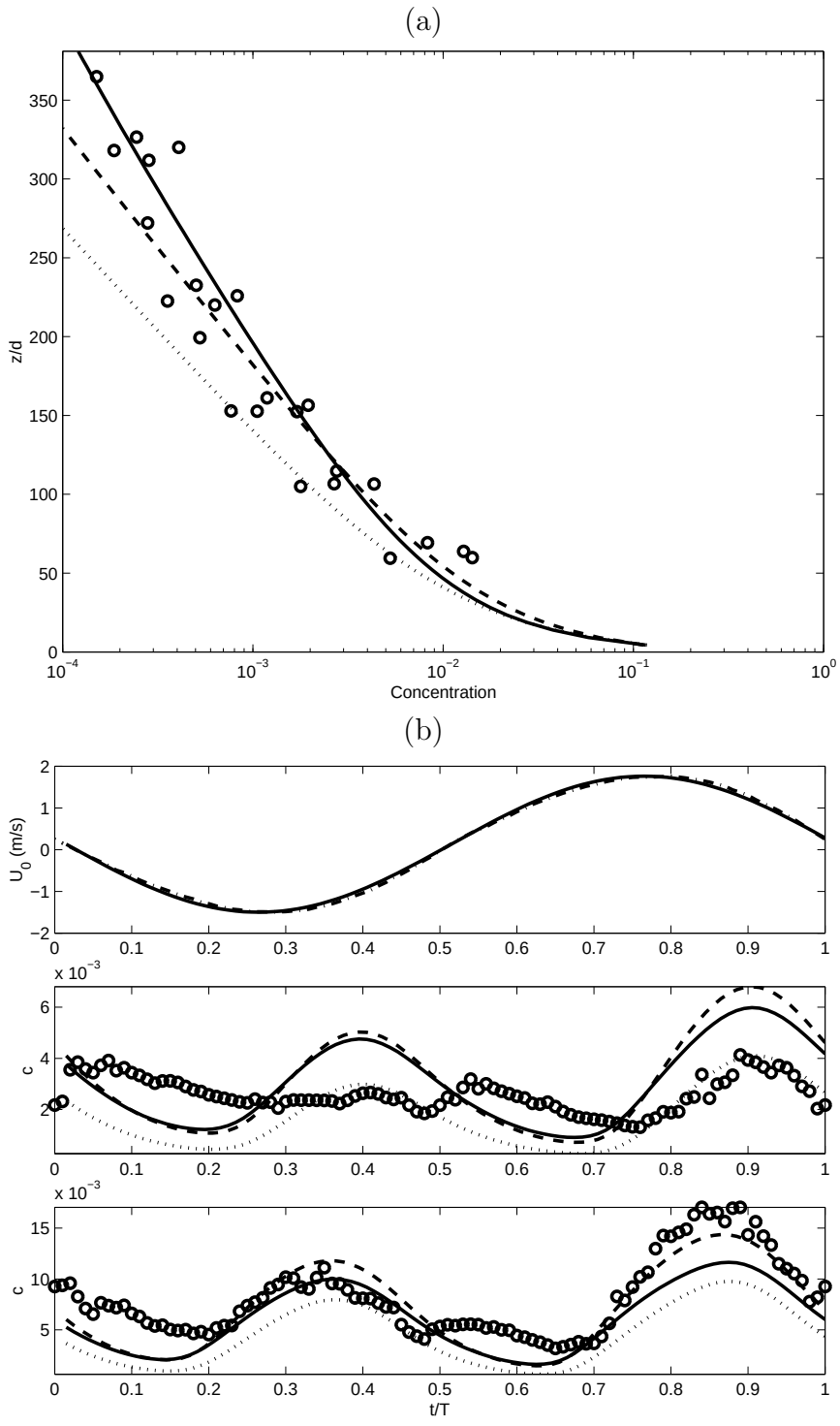

Figure 4.5: Comparison of (a) the time-averaged concentration profiles and (b) the concentration time histories at different elevations for the reference concentration approach for $\sigma_c = f(\bar{c}/c^\star)$ (solid line), $\sigma_c = 0.52$ (dashed line) and $\sigma_c = 0.7$ (dotted line) with the measured data of *Katopodi et al.* (1994a) - case E1 (symbols). For (b), from top to bottom are the time histories of the free stream velocity and of the concentration at $z/D_{50} = 112$ and $z/D_{50} = 69$.

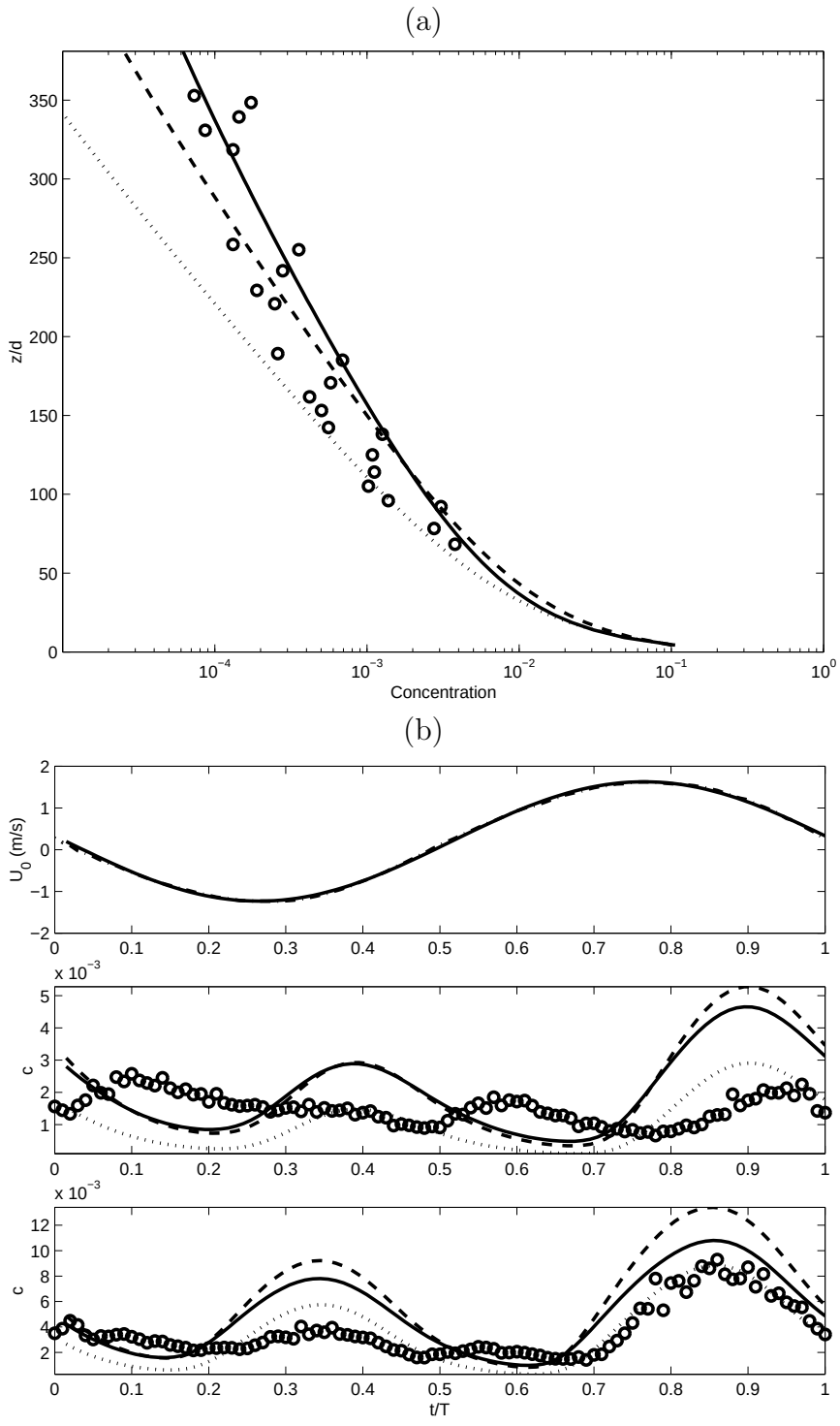

Figure 4.6: Comparison of (a) the time-averaged concentration profiles and (b) the concentration time histories at different elevations for the reference concentration approach for $\sigma_c = f(\bar{c}/c^\star)$ (solid line), $\sigma_c = 0.52$ (dashed line) and $\sigma_c = 0.7$ (dotted line) with the measured data of *Katopodi et al.* (1994a) - case E2 (symbols). For (b), from top to bottom are the time histories of the free stream velocity and of the concentration at $z/D_{50} = 110$ and $z/D_{50} = 62$.

with mean current, we believe that using the Schmidt number prescribed by equation (4.15) provides a better compromise for the concentration time histories at different elevations.

4.5 Effects of sediment bottom boundary condition

We further study the effect of the two sediment flux bottom boundary conditions introduced in section 4.2.2 on the model results. All the experimental conditions reported in table 4.1 are simulated by the model. We assume that the influence on Schmidt number due to slight difference in particle diameter is negligible for *Horikawa et al.* (1982). The case of *Janssen* (1999) for fine sand ($D_{50} = 0.13$mm) is discussed separately.

Both the reference concentration and empirical pick-up approaches predict similar time-averaged sediment concentration profiles with reasonable accuracy (figures 4.7, 4.8, 4.9 and 4.10 (a)). However, results for concentration time histories (figures 4.7, 4.8, 4.9, and 4.10 (b)) are less satisfactory. In general, both boundary conditions lead to an overprediction of the concentration peaks and amplitudes, which may be a consequence of approximating boundary conditions of a unsteady problem by a steady-state formulation (*Hsu and Liu*, 2004). Nevertheless, the overall results predicted by the reference concentration approach are in better agreement with the measured data, especially in terms of the phase of the concentration time series.

More quantitative evaluation on the model performance on time-dependent concentration is presented in tables 4.2, 4.3 and 4.4 using three parameters. For practical sediment transport applications, accurate predictions for the magnitude and phase lag (e.g., between the concentration and the external flow velocity) of concentration time histories are crucial to estimate net suspended transport rates

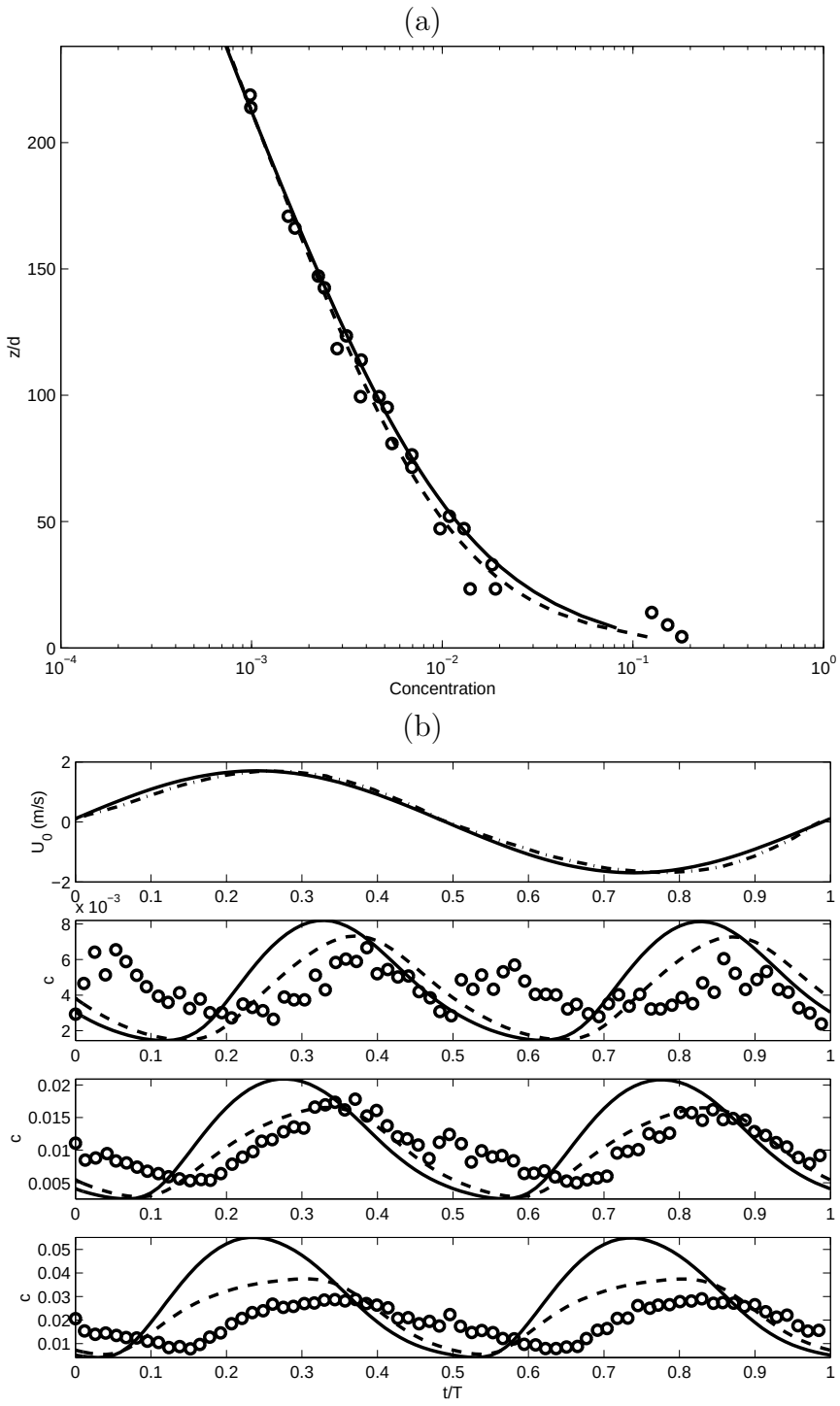

Figure 4.7: Comparison of (a) the time-averaged concentration profiles and (b) the concentration time histories at different elevations, for $\sigma_c = f(\bar{c}/c^{\star})$, using van Rijn's pick-up (solid line) and the reference concentration approach (dashed line), with the measured data of *Ribberink and Al-Salem* (1995) (symbols). For (b), from top to bottom are the time histories of the free stream velocity and of the concentration at $z/D_{50} = 100$, $z/D_{50} = 52$ and $z/D_{50} = 24$.

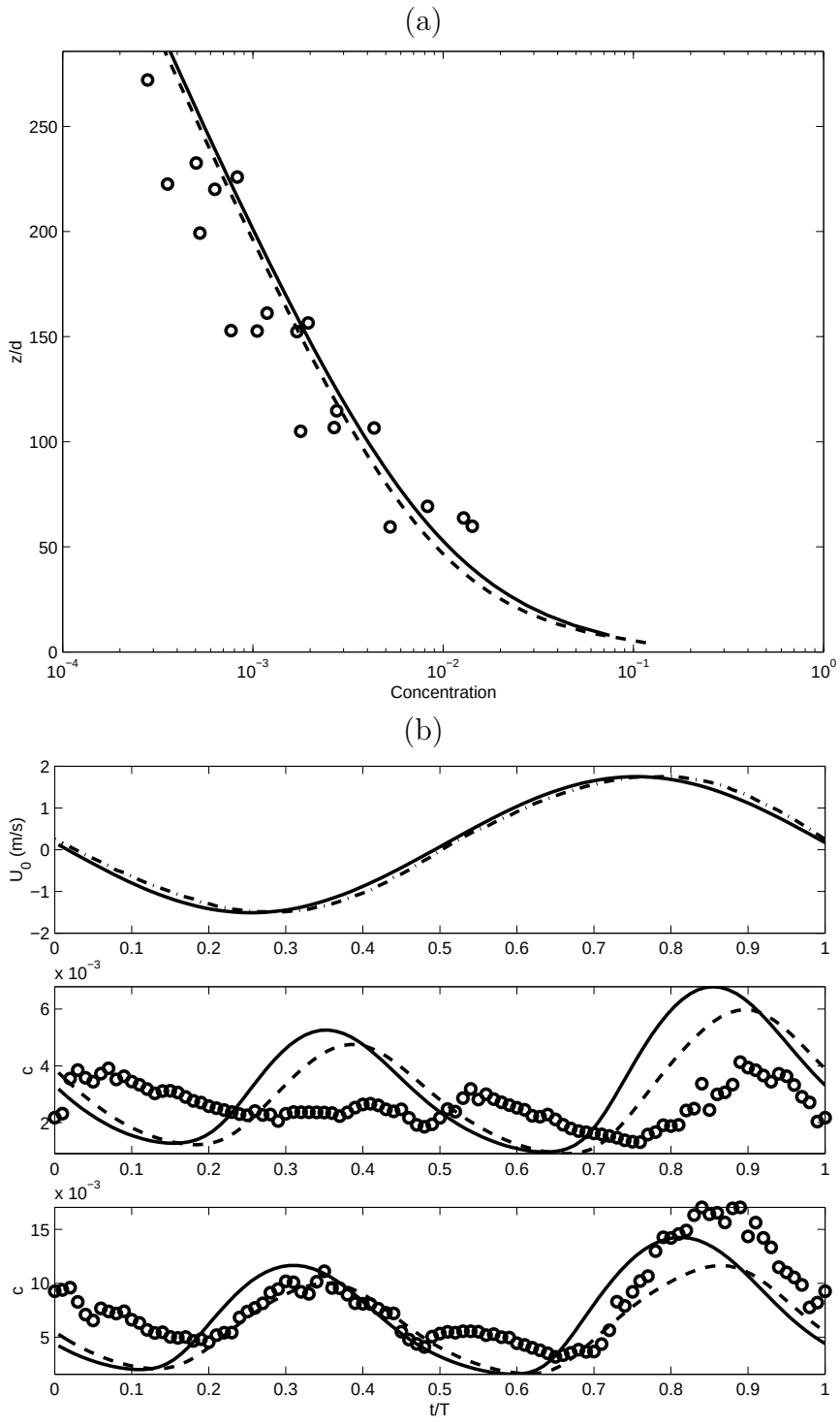

Figure 4.8: Comparison of (a) the time averaged concentration profiles and (b) the concentration time histories at different elevations, for $\sigma_c = f(\bar{c}/c^{\star})$, using van Rijn's pick-up (solid line) and the reference concentration approach (dashed line), with the measured data of *Katopodi et al.* (1994a) - case E1 (symbols). For (b), from top to bottom are the time histories of the free stream velocity and of the concentration at $z/D_{50} = 112$ and $z/D_{50} = 69$.

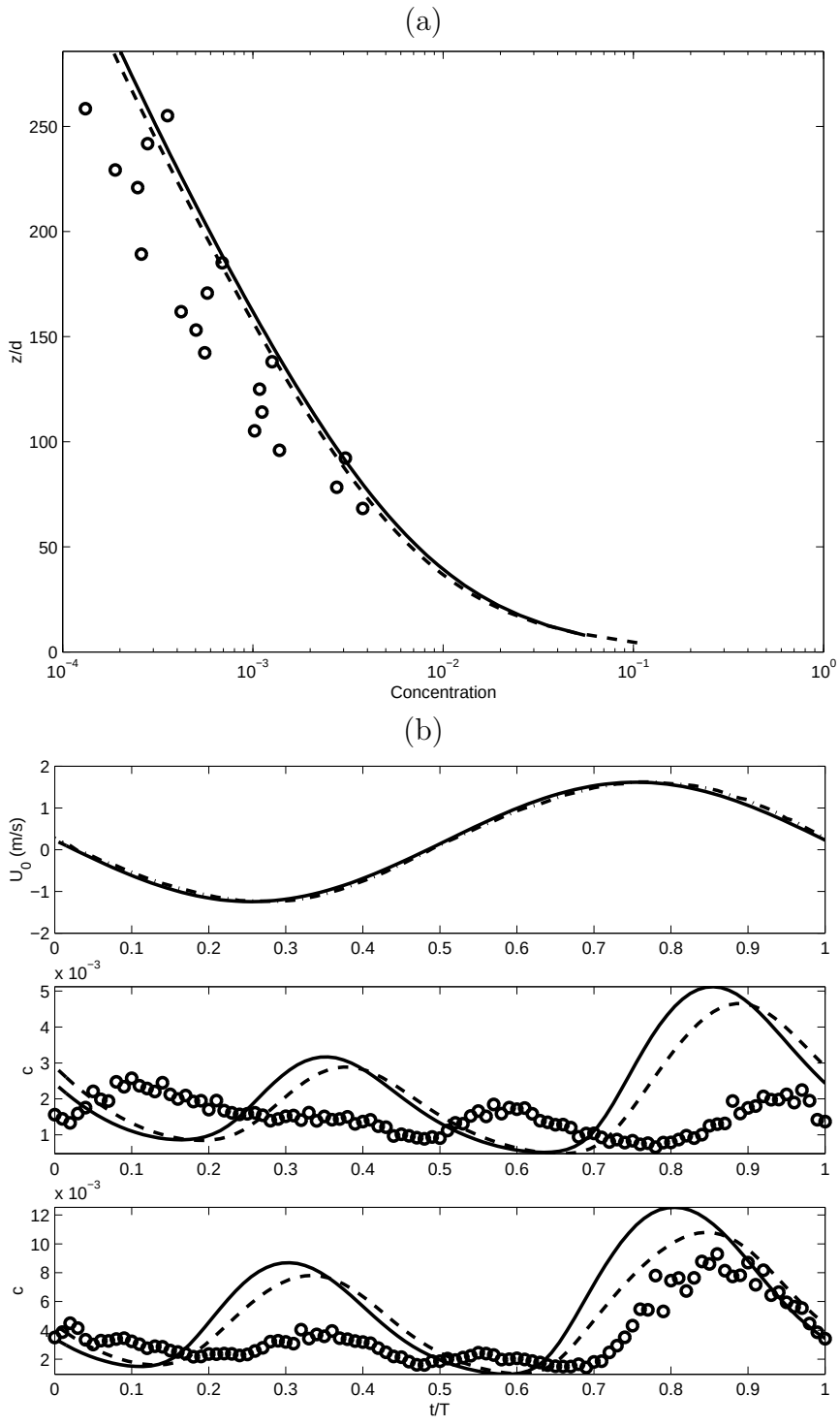

Figure 4.9: Comparison of (a) the time averaged concentration profiles and (b) the concentration time histories at different elevations, for $\sigma_c = f(\bar{c}/c^{\star})$, using van Rijn's pick-up (solid line) and the reference concentration approach (dashed line), with the measured data of *Katopodi et al.* (1994a) - case E2 (symbols). For (b), from top to bottom are the time histories of the free stream velocity and of the concentration at $z/D_{50} = 110$ and $z/D_{50} = 62$.

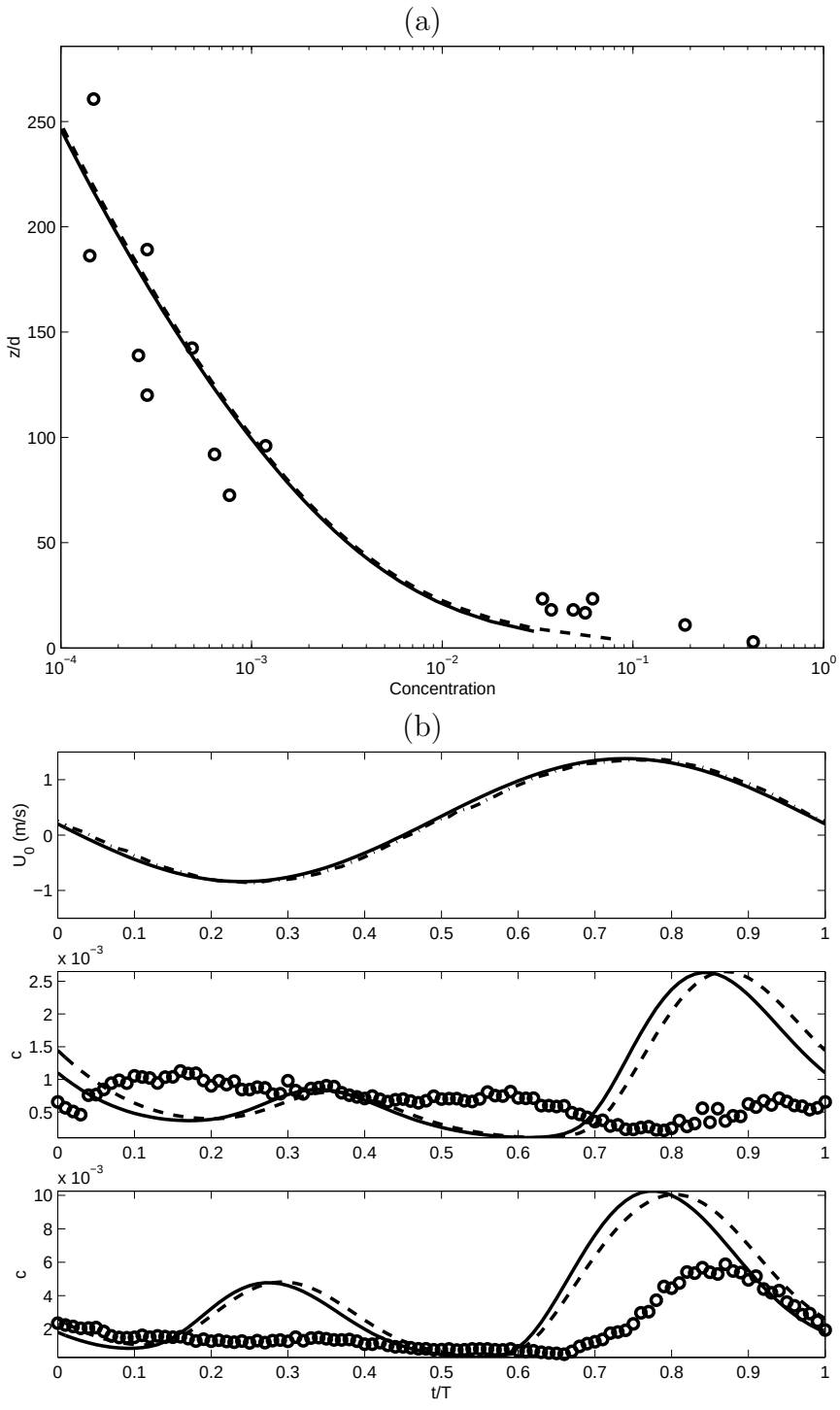

Figure 4.10: Comparison of (a) the time averaged concentration profiles and (b) the concentration time histories at different elevations, for $\sigma_c = f(\bar{c}/c^\star)$, using van Rijn's pick-up (solid line) and the reference concentration approach (dashed line), with the measured data of *Katopodi et al.* (1994a) - case E3 (symbols). For (b), from top to bottom are the time histories of the free stream velocity and of the concentration at $z/D_{50} = 105$ and $z/D_{50} = 45$.

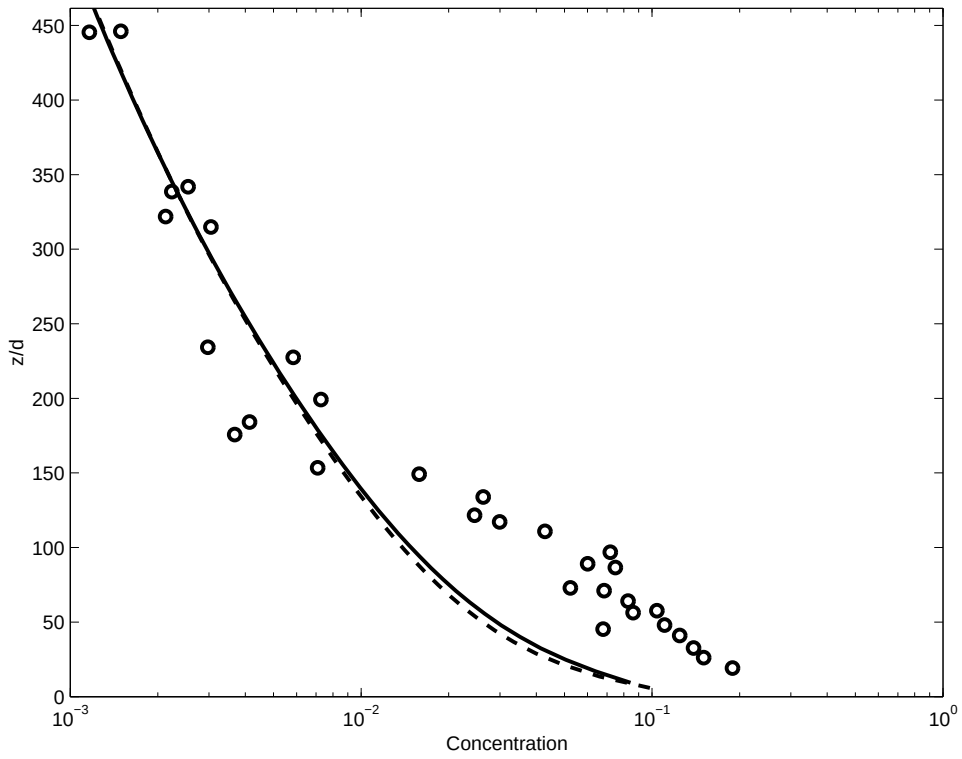

Figure 4.11: Comparison of time averaged concentration profiles for $\sigma_c = 0.52$, using van Rijn's pick-up (solid line) and the reference concentration approach (dashed line), with the measured data of *Janssen* (1999) - case H6 (symbols).

Table 4.2: Numerical predictions for the mean concentration $\langle \bar{c} \rangle$ between the concentration and the external flow velocity. In each case, the left column shows the values predicted using van Rijn's pick-up, the middle column the values predicted using the reference concentration approach and the right column the experimental values.

		$\langle \bar{c} \rangle$ $(*10^{-2})$		
Horikawa et al. (1982)	$z/d = 50$	0.564	0.490	0.393
	$z/d = 75$	0.255	0.220	0.180
Ribberink and Al-Salem (1995)	$z/d = 24$	2.82	2.29	1.92
	$z/d = 52$	1.12	0.965	1.04
	$z/d = 100$	0.452	0.417	0.422
Katopodi et al. (1994a) - E1	$z/d = 69$	0.698	0.613	0.816
	$z/d = 112$	0.334	0.304	0.259
Katopodi et al. (1994a) - E2	$z/d = 62$	0.550	0.507	0.367
Katopodi et al. (1994a) - E3	$z/d = 45$	0.369	0.385	0.201
	$z/d = 105$	0.0902	0.0929	0.068
Janssen (1999) - H6	$z/d = 162$	0.821	0.792	0.698

Table 4.3: Numerical predictions for the maximum concentration $\bar{c}_{max}$ between the concentration and the external flow velocity. In each case, the left column shows the values predicted using van Rijn's pick-up, the middle column the values predicted using the reference concentration approach and the right column the experimental values.

		$\bar{c}_{max}$ $(*10^{-2})$		
Horikawa et al. (1982)	$z/d = 50$	1.02	0.851	0.617
	$z/d = 75$	0.442	0.377	0.285
Ribberink and Al-Salem (1995)	$z/d = 24$	5.51	3.75	2.91
	$z/d = 52$	2.09	1.66	1.78
	$z/d = 100$	0.820	0.732	0.667
Katopodi et al. (1994a) - E1	$z/d = 69$	1.16	0.998	1.11
		1.43	1.16	1.70
	$z/d = 112$	0.679	0.598	0.413
Katopodi et al. (1994a) - E2	$z/d = 62$	1.25	1.08	0.929
	$z/d = 110$	0.512	0.465	0.257
Katopodi et al. (1994a) - E3	$z/d = 45$	1.03	1.00	0.588
	$z/d = 105$	0.263	0.265	0.113
Janssen (1999) - H6	$z/d = 162$	1.36	1.31	1.16

Table 4.4: Numerical predictions for the phase lag ϕ_c between the concentration and the external flow velocity. In each case, the left column shows the values predicted using van Rijn's pick-up, the middle column the values predicted using the reference concentration approach and the right column the experimental values.

		ϕ_c/T		
Horikawa et al. (1982)	$z/d = 50$	0.09	0.13	0.11
	$z/d = 75$	0.14	0.18	0.14
Ribberink and Al-Salem (1995)	$z/d = 24$	0.01	0.04	0.095
	$z/d = 52$	0.05	0.08	0.11
	$z/d = 100$	0.10	0.14	0.19
Katopodi et al. (1994a) - E1	$z/d = 69$	0.075	0.115	0.12
		0.075	0.105	0.10
	$z/d = 112$	0.115	0.145	0.20
Katopodi et al. (1994a) - E2	$z/d = 62$	0.065	0.095	0.10
	$z/d = 110$			
Katopodi et al. (1994a) - E3	$z/d = 45$	0.05	0.07	0.11
	$z/d = 105$			
Janssen (1999) - H6	$z/d = 162$	0.205	0.225	0.23

(e.g., *Dohmen-Janssen et al.*, 2002). Therefore, we choose to summarize model performance based on the mean concentration $\langle\bar{c}\rangle$, the maximum concentration $\bar{c}_{max}$ and a normalized time-lag (ϕ_c/T).

Both boundary conditions give similar results for the mean concentration and for the maximum concentration "far" from the bed. Close to the bed, the reference concentration approach generally gives more accurate predictions for the mean and maximum concentration. The phase lag presented is calculated by a cross-correlation technique, and the reference concentration predictions are clearly more accurate.

Dohmen-Janssen et al. (2001, 2002) observe very different sheet flow characteristics for fine sand of $D_{50} = 0.13$mm as compared to coarser ($D_{50} = 0.21 \sim 0.32$mm) sand. If defining $\bar{c} = 8\%$ as a critical concentration dividing the concentrated and dilute transports, according to *Janssen* (1999), the observed upper bound for concentrated region (or lower bound for dilute region) for $D_{50} = 0.13$mm sand is at about $z/D_{50} = 80$ ($z = 10$mm) above the initially undisturbed bed level. Such critical location for 0.21mm sand is no more than $z/D_{50} = 5$ ($z = 1$mm) (*Katopodi et al.*, 1994a), which is much closer to the bed. Because the validity of the dilute model depends on such critical concentration, predicting dilute transport of fine sand ($D_{50} = 0.13$mm) poses a challenge for the present dilute formulation. The predicted time-averaged suspended sediment concentration is poor as compared with measured data (figure 4.11). Although the comparison presented here is based on constant Schmidt number (σ_c=0.52), no significant improvement is observed using concentration dependent Schmidt number. Using commonly used value of $z = 2D_{50}$ as the lower boundary, a correct solution requires the dilute model to calculate a significant portion of transport ($z/D_{50} = 2$ to 70) that is highly concentrated (8% to 20%, see figure 4.11 symbols) where the particle in-

tergranular interaction may be important. To follow the dilute assumption, an appropriate value for lower boundary of fine sand needs to be elevated to $z \approx 1$cm. However, the thickness of the wave boundary layer is only about a few cm and hence it is difficult to accommodate the requirements of both diluteness and resolution for accurate modeling of the wave boundary layer.

4.6 Summary / Conclusion

We presented in this chapter one use of the two-phase sediment transport model presented in chapter 3. In this case, the concentration is assumed to remain dilute and the sediment phase stress is neglected. In dilute models, sediment is suspended mainly through its interaction with fluid turbulence (turbulent suspension) and the closure of this term is crucial. The other traditional suspension mechanism due to the inter-particle interactions in the concentrated region is modeled through a sediment flux bottom boundary condition. We investigated both issues in this chapter by numerically simulating dilute sediment transport and testing with experimental data.

We found that the turbulent suspension closure (value of the Schmidt number) only affected the magnitude of the suspended sediment and not its phase lag respect to the free stream velocity. Furthermore, a concentration dependent Schmidt number has been introduced through model-data comparisons. Although this new closure of the sediment diffusivity may provide a better description of the physical processes involved, it is determined empirically using available experimental data and more comprehensive studies on the sediment diffusivity are needed.

We also investigated the issue of modeling the near bed processes through the bottom boundary condition by comparing two approaches. We considered here an alternative to the van Rijn pick-up function, a reference concentration approach

based on on the bed load modeling of *Engelund and Fredsøe* (1976). Choosing between these two boundary conditions depends on, amongst other criteria, the predicted phase of concentration near the bed. The reference concentration approach gives results that are in better agreement with the experimental data tested here. In addition to better agreements with the data, the reference concentration approach may present at least an additional theoretical advantage. The reference concentration approach uses the concept of locally saturated condition and hence is bounded by a maximum concentration of about 30% under high Shields parameter flow. On the other hand, the empirical pick-up formula used in this study is not bounded for high Shields parameters. Consequently it limits the validity of extending van Rijn's formula to more intense flow and may be the cause of the overprediction on the magnitude of suspended sediment concentration.

Although using the same fluid turbulence boundary condition does highlight the differences between the two sediment boundary condition approaches, we used $\kappa = 0.41$ at the boundary. Such a value might not be appropriate in presence of sediment, in particular at the bottom boundary of the dilute model where the sediment concentration could be significant. A lower value would then have to be implemented, for example by relating κ to the concentration and the elevation above the bed (*Hsu et al.*, 2003a). Since κ only appears in the calculation of the boundary value of the fluid turbulence dissipation rate, we can expect a lower κ value to result in an increase of the turbulence dissipation rate at the bottom boundary. In turn, this would reduce the turbulent kinetic energy, the Shields parameter and finally the amount of sediment picked-up.

CHAPTER 5

ONE-DIMENSIONAL SHEET FLOW MODEL

We have seen in chapter 2 that it is common to parameterize sediment transport regimes using the Shields parameter, $\theta = \tau_b/(\rho_f - \rho_s)gd$, and the fall parameter, $R_p = D_{50}\sqrt{(s-1)gD_{50}}/\nu$. We also saw that different sediment transport regimes and modes map different regions in a $R_p - \theta$ plane (figure 5.1). Figure 5.1 represents the different regimes of sediment transport for non-cohesive grains that correspond to different physical processes with a focus on the sheet flow regime. Once again, the solid line is an approximation of the Shields curve characterizing incipient motion, under which sediment is motionless. The dashed line corresponds to the friction velocity of the flow $u_\star$ and the sediment fall velocity W_s being equal. The dotted curve represents the sheet flow inception criterion following *Wilson* (1989). Finally, the dot-dashed lines correspond to the regimes of interparticle interactions as introduced by *Bagnold* (1954). In addition to such division, the same experimental conditions than in figure 2.4 are included. for the oscillatory flow cases, the Shields parameter value is obtained using the maximum bed shear stress value. The experiments of *Asano* (1995) and *Sumer et al.* (1996) are included here because they were the ones used to validate *Hsu et al.* (2004)'s model and provide examples for massive particles. The other experimental conditions all give examples of beach sand transport under sheet flow conditions.

Sheet flows correspond to the region above the dotted line ($\theta = 0.8$) in figure 5.1 and can be divided in five sub regions (named A, B, C, D and E in figure 5.1). They correspond respectively to (A) the macro viscous region for non-massive particles, (B) the inter-particle interaction transition region for non-massive particles, (C) the inter-particle interaction transition region for massive particles, (D) the grain-inertia region for non-massive particles and (E) the grain-inertia region for massive

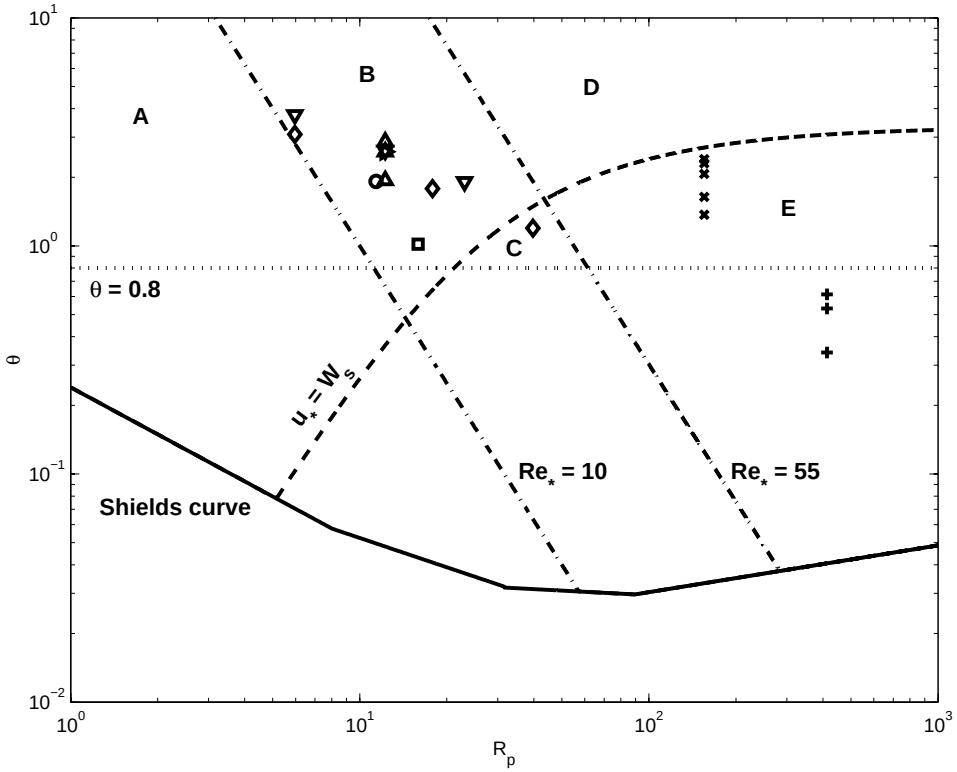

Figure 5.1: Sediment transport regimes as determined by the Shields curve (solid line), $u_\star = W_s$ (dashed line), $\theta = 0.8$ (dotted line), $Re_\star = 10$ and $Re_\star = 55$ (dot-dashed lines). The symbols represent the conditions for some experimental data. $+$: *Asano* (1995). $\times$: *Sumer et al.* (1996) (sediment 2). $\circ$: *Horikawa et al.* (1982). $\triangleright$: *Ribberink and Al-Salem* (1995). $\triangle$: *Katopodi et al.* (1994b). $\triangledown$: *Janssen* (1999). $\Diamond$: *O'Donoghue and Wright* (2004). $\square$: *Dudley* (2007).

particles. As mentioned previously, the model developed by *Hsu et al.* (2004) is for massive particles under collisional interactions and thus should only be used when the flow and sediment properties correspond to region E. More typical conditions for beach sand under sheet flow conditions will lie in region B (see the experimental data in figure 5.1). Modifications to the interparticle interaction closure that would account for some of the effects of the transition and the macro-viscous region should then be included. However, such a modification was experimented using the theory developed by *Carpen and Brady* (2002) and changes observed were small. The other main difference between zone E and zone B concerns the "massiveness" of the particles considered, which is an estimation of the relative importance of the fluid turbulence respect to the grain-inertia. It follows that efforts to better describe the processes involved with the fluid turbulence are necessary.

We present such an attempt at a better description of the sediment transport under sheet flow conditions by improving the fluid turbulence closure. After a review of the governing equations for the one-dimensional model, we will discuss the fluid turbulence closure and in particular how to better incorporate the sediment particle fluid turbulence two-way interactions. The newer sheet flow model is then validated using concentration, sediment flux, and sediment velocity experimental data. More detailed discussions on the sediment transport and flow characteristics are presented in chapter 6.

5.1 Model formulation

5.1.1 Two-phase flow governing equations

Similarly to the one-dimensional dilute model, the flow is assumed to be uniform in the flow direction. Using the same coordinate system (x is the flow direction, z the normal to the flow direction), the two-phase concentration-weighted averaged

governing equations for the sheet flow model (equations 3.38, 3.39, 3.40 and 3.41) can be summarized as follow:

$$\frac{\partial \rho^f (1-\bar{c})}{\partial t} + \frac{\partial \rho^f (1-\bar{c})\tilde{w}^f}{\partial z} = 0 \tag{5.1}$$

for the fluid phase continuity,

$$\frac{\partial \rho^s \bar{c}}{\partial t} + \frac{\partial \rho^s \bar{c}\tilde{w}^s}{\partial z} = 0 \tag{5.2}$$

for the sediment phase continuity,

$$\begin{aligned} \frac{\partial \rho^f (1-\bar{c})\tilde{u}^f}{\partial t} + \frac{\partial \rho^f (1-\bar{c})\tilde{u}^f\tilde{w}^f}{\partial z} &= \rho^f (1-\bar{c}) g_x - (1-\bar{c})\frac{\partial \bar{P}^f}{\partial x} + \frac{\partial \tau^f_{xz}}{\partial z} \\ &\quad -\beta\bar{c}\left(\tilde{u}^f - \tilde{u}^s\right) \end{aligned} \tag{5.3}$$

for the fluid phase momentum conservation in the x-direction,

$$\begin{aligned} \frac{\partial \rho^f (1-\bar{c})\tilde{w}^f}{\partial t} + \frac{\partial \rho^f (1-\bar{c})\tilde{w}^f\tilde{w}^f}{\partial z} &= \rho^f (1-\bar{c}) g_z - (1-\bar{c})\frac{\partial \bar{P}^f}{\partial z} + \frac{\partial \tau^f_{zz}}{\partial z} \\ &\quad -\beta\bar{c}\left(\tilde{w}^f - \tilde{w}^s\right) + \beta\frac{\nu_T}{\sigma_c}\frac{\partial \bar{c}}{\partial z} \end{aligned} \tag{5.4}$$

for the fluid phase momentum conservation in the z-direction;

$$\frac{\partial \rho^s \bar{c}\tilde{u}^s}{\partial t} + \frac{\partial \rho^s \bar{c}\tilde{u}^s\tilde{w}^s}{\partial z} = \rho^s \bar{c} g_x - \bar{c}\frac{\partial \bar{P}^f}{\partial x} + \frac{\partial \tau^s_{xz}}{\partial z} + \beta\bar{c}\left(\tilde{u}^f - \tilde{u}^s\right) \tag{5.5}$$

for the sediment phase momentum conservation in the x-direction

$$\frac{\partial \rho^s \bar{c}\tilde{w}^s}{\partial t} + \frac{\partial \rho^s \bar{c}\tilde{w}^s\tilde{w}^s}{\partial z} = \rho^s \bar{c} g_z - \bar{c}\frac{\partial \bar{P}^f}{\partial z} + \frac{\partial \tau^s_{zz}}{\partial z} + \beta\bar{c}\left(\tilde{w}^f - \tilde{w}^s\right) - \beta\frac{\nu_T}{\sigma_c}\frac{\partial \bar{c}}{\partial z} \tag{5.6}$$

for the sediment phase momentum conservation in the z-direction. In the momentum equations, τ^f_{xz} and τ^s_{xz} are the fluid and sediment shear stresses, τ^f_{zz} and τ^s_{zz} the fluid and sediment normal stresses. Their respective closures have already been discussed in sections 3.4 and 3.5.2 and the fluid turbulence modeling is further discussed in the following section.

5.1.2 Fluid turbulence closure for sheet flow model

The fluid stresses and the fluid turbulence are modeled following the approach presented in section 3.4.

Dilute flow turbulence assumption

Using the coefficients given in table 3.1 and $\sigma_c = 1.0$, *Hsu et al.* (2004) have tested their model for massive particles (particles whose fall velocity exceeds the friction velocity of the flow). However this model fails to accurately reproduce experimental data for typical sand grains (diameter of about 0.2 mm), as shown in model-data comparisons for two types of ambient oscillatory flows and different sediment diameters (summarized in table 5.1). In figures 5.2 and 5.3 numerical results obtained from the model developed by *Hsu et al.* (2004) are presented with the dashed line. Although the model-data comparison for the time averaged concentration profiles is satisfactory (figure 5.2), the comparisons for time histories of concentration are not. Since in sheet flow regime most of the sediment is transported in the sheet layer, the concentration time histories in the sheet layer (figure 5.3) are essential for estimating the sediment flux and therefore are important physical quantities for assessing the quality of the numerical model.

In the model-data comparisons all elevations are non-dimensionalized by the median sand diameter D_{50}, and the vertical origin is taken to be the undisturbed bed (bed location without ambient flow). For the concentration time histories in the sheet layer, the plots show the free stream velocity on the top panel and the concentration time histories at the elevations specified to the right in the other panels. Some of the discrepancies between Janssen's experimental data and numerical results for the time averaged concentration and for the maximum concentration in the time histories under the undisturbed bed (respectively figures 5.2 and 5.3 (a)

Table 5.1: Summary of experimental data used for the sheet flow model-data comparisons.

Case	Data set	D_{50} (mm)	Flow type
1	*Janssen* (1999)	0.21	$T = 7.2$ s, $U_{osc} = 1.47$ m/s, $U_c = 0.26$ m/s. (†)
2	*O'Donoghue and Wright* (2004)	0.27	$T = 7.5$ s, $U_1 = 1.19$ m/s, $U_2 = 0.31$ m/s. (‡)
3	*Janssen* (1999)	0.32	$T = 7.2$ s, $U_{osc} = 1.47$ m/s, $U_c = 0.26$ m/s. (†)
4	*McLean et al.* (2001)	0.32	$T = 7.2$ s, $U_{osc} = 1.52$ m/s, $U_c = 0.33$ m/s. (†)
5	*McLean et al.* (2001)	0.32	$T = 7.2$ s, $U_{osc} = 1.51$ m/s, $U_c = 0.55$ m/s. (†)
6	*O'Donoghue and Wright* (2004)	0.46	$T = 7.5$ s, $U_1 = 1.19$ m/s, $U_2 = 0.31$ m/s. (‡)
7	*Dudley* (2007)	0.25	$u_\star = 6.42$ cm/s, $h = 0.15$ m (#)

(†) $U_0(t) = U_{osc} \cos 2\pi t/T + U_c$.
(‡) $U_0(t) = U_1 \cos 2\pi t/T + U_2 \cos 2\pi t/T$.
(#) Steady flow, h is the water depth.

and (b)) can be partly explained by the lower than expected concentration measurements, which should be closer to the theoretical closed packed concentration ($c^\star = 0.635$) (Dohmen-Janssen, personal communication).

The experimental concentration time histories in the sheet layer show rather clearly the effect of pick-up through the concentration variations within one period. When the flow intensity increases, particles are picked-up and suspended, which is represented by a decrease of the concentration below the undisturbed bed ($z/D_{50} < 0$) and an increase of the concentration above the undisturbed bed. On the other hand, when the flow intensity decreases, settling occurs and particles are deposited leading to an increase of the concentration under the undisturbed bed and a decrease of the concentration above the undisturbed bed. The failure to correctly represent the concentration variations within a wave period suggests that the predictive ability of the pick-up and suspension of particles in the sheet layer in the model developed by *Hsu et al.* (2004) needs to be improved for small sand grains.

Modification of turbulence for concentrated flow

Sediment pick-up is commonly related to the bottom shear stress. It seems natural to attribute unsatisfactory results for pick-up predictions to inaccurate time dependent bottom shear stress. Both the turbulence and the granular flow models affect the bottom stress calculations. For massive particles, the granular flow contribution is dominant and inaccuracies in the fluid turbulence closure are not critical to the overall model's performance. On the other hand, for smaller sediment particles, the relative importance of fluid turbulence is greater and inaccuracies in the fluid turbulence closure will impact the overall results more significantly. Since the model by *Hsu et al.* (2004) has been validated for massive particles, it suggests that the granular flow contribution has been modeled adequately. We conjecture

here that the poor numerical results observed for the concentration time histories in the sheet layer are thus mainly due to an inadequate turbulence closure to model the concentrated near-bed physical processes of small sand grains.

Even though the assumption that the sediment diffusivity is the same as the eddy viscosity might not always be valid (see chapter 4), it is found that the effect of changing the Schmidt number is minimal on the sheet layer concentration predictions. This is not surprising: if bed shear stress is responsible for poor predictions, the modeling deficiency concerns mainly the eddy viscosity near the bed, not the sediment diffusivity. Hence, the discussion should focus on the values of C_μ and the constants in the ε equation. For clear fluid wall turbulence, it is well known that the standard eddy viscosity specification (similar to equation 3.47) yields a viscosity that is too large in the near-wall region, and damping functions are required (e.g., *Pope*, 2000). In the two-phase flow model, the concentration dependence is also acting as a damping function near the bed where the concentration is high. However, in the model of *Hsu et al.* (2004) the turbulent kinetic energy and the turbulence dissipation rate are calculated using clear fluid constants for the productive and dissipative terms and therefore the effects of particles on turbulence are not fully incorporated. In the sheet layer, the concentration is high and effects of sediment particles on fluid turbulence can be significant.

The effects of sediment particles on fluid turbulence have been studied both experimentally for boundary layers (e.g., *Rashidi et al.*, 1990; *Rogers and Eaton*, 1991) and numerically for wall turbulence (e.g., *Pan and Banerjee*, 1996). Particles will either enhance or suppress turbulence depending on their size. The enhanced turbulence in turn corresponds to larger Reynolds stresses values that would increase the pick-up. *Hetsroni* (1989) attributes enhanced turbulence to vortex shedding. More precisely, *Rashidi et al.* (1990) and *Pan and Banerjee* (1996)

attribute the turbulence modulation to changes in the wall turbulence events: large particles increase ejections and sweeps while small particles decrease such events.

The relative size of sediment particles is usually determined using a characteristic length scale of fluid turbulence. Using the integral turbulent length scale l_e, *Gore and Crowe* (1989) showed that turbulence is enhanced for particles with $d/l_e > 0.1$. Near the bed in a boundary layer the integral turbulent length scale can be approximated by the mixing length that is proportional to the distance to the bed. It follows that very close to the bed the ratio d/l_e will become larger than 0.1, and the turbulence is enhanced. On the other hand, using the Kolmogorov length scale η, *Pan and Banerjee* (1996) showed that particles smaller than η reduce the energy production and increase the dissipation leading to suppressed turbulence while particles larger than η increase both the production and dissipation with a larger increase for the production leading to enhanced turbulence. Taking $u_\star$ as the turbulent flow friction velocity, we can relate the Kolmogorov length scale, which is on the order of $\nu/u_\star$, to the sediment diameter and the Shields parameter

$$\frac{\eta}{d} \sim \frac{\nu}{\sqrt{\theta}\sqrt{(s-1)gd^3}} \tag{5.7}$$

For sand grains ($s = 2.65$ and $d > 0.1$ mm) in sheet flow regime ($\theta > 0.8$), the particles are much bigger than the Kolmogorov scale and should then enhance turbulence. Both analyses lead to the same conclusion that the fluid turbulence is enhanced by sand grains in the high concentration region of sheet flows. Including these effects of particles on fluid turbulence in the model should increase both the turbulence intensity and the Reynolds stresses near the bed and thus should provide additional pick-up.

To account for the effects of particles on turbulence in the model will require the modification of the coefficients introduced in the ε equation. Using their DNS results, *Squires and Eaton* (1994) investigated the effects of turbulence modification

by particles on $k-\varepsilon$ models for homogeneous isotropic turbulence. Unfortunately, the homogeneous isotropic turbulent flow study does not provide information concerning modifications to $C_{\varepsilon 1}$, the coefficient in front of the production term. Even though this coefficient might be modified by the presence of particles, we have no other solution but to set $C_{\varepsilon 1}$ to be the same as that for clear fluid turbulence. *Squires and Eaton* (1994)'s results show that $C_{\varepsilon 2}$ is a function of the particle concentration and the particle inertia, which has also been observed by *Ahmed and Elghobashi* (2000) for shear flows. The proposed modification can be expressed as follows

$$C_{\varepsilon 2} = C_{\varepsilon 20}\left[1 + \max\left(c_1 \ln\left(c_2 \frac{T_F}{T_p}\right), 0\right)\frac{\bar{c}}{c^\star}\right], \tag{5.8}$$

where $C_{\varepsilon 20} = 1.92$ is the clear fluid value, T_F is the time scale of fluid turbulence and T_p the particle response time. This formulation causes a decrease in dissipation, which is consistent with enhancing turbulence and follows the trend observed in the DNS data of *Squires and Eaton* (1994). The ratio T_p/T_F is a measure of the particle inertia (massive particles correspond to large values) and the maximum function in equation 5.8 is included so that we recover the clear fluid value (when $T_p > c_2 T_F$) previously tested for massive particles. c_2 is an indication on the inertia of the particles that will enhance turbulence and is usually believed to be of order 1. Both constants c_1 and c_2 can be chosen for each case studied based on best fitting to specific experimental data (concentration and/or sediment flux for example). When taking into account all the cases summarized in table 5.1, $c_1 = 2.4$ and $c_2 = 2$ provide the best results.

The last model coefficient is $C_{\varepsilon 3}$. Its presence in the ε equation is due to the phase interaction term. The term D_p in the turbulence transport equations is (see appendix A):

$$D_p = 2\beta(1-\alpha)\bar{c}k_f - \beta\frac{\nu_T}{\sigma_c}\frac{\partial \bar{c}}{\partial z}\left(\tilde{w}^f - \tilde{w}^s\right) \tag{5.9}$$

where α is a parameter that measures the degree of correlation between the fluid velocity fluctuations and the sediment velocity fluctuations and is a function of the time scales involved (*Hsu et al.*, 2004): particle response time, time between collisions and the fluid turbulence time scale. As such, this term is already a function of the concentration and the particle inertia. Furthermore, the value chosen for $C_{\varepsilon 3}$ is based on work done on sediment laden jets. We therefore believe that there is already an account of the effect of the particles in this additional term.

5.2 Numerical implementation

Details of the numerical implementation of the sheet flow model are presented in appendix B and in *Hsu* (2002). In particular, it has to be noted that the current model can not accurately describe the initiation of sediment motion. An artificial initial condition is thus specified. A linear profile of sediment concentration that decreases from $c^\star$ at the bed is prescribed as the initial concentration profile. The sediment and fluid velocities are initially set to zero. The flow is then first calculated with the vertical sediment velocity remaining zero (*Hsu*, 2002). After this initial process, the numerical model is driven by a horizontal pressure gradient determined so that the numerical and experimental free stream velocities match.

5.3 Model validation

5.3.1 Concentration in oscillatory flows

The proposed modification for the $k-\varepsilon$ fluid turbulence model is implemented and model-data comparisons using the experimental data of table 5.1 are performed to

assess the performance of the new model. A moving vertical averaging technique is applied to the numerical results. At each elevation, the time dependent concentration is spatially averaged over a height corresponding to that of the sampling volume of the CCM probe. The results using the turbulence modification are presented in solid lines in figure 5.2 for the time-averaged concentration profiles and figure 5.3 for the concentration time histories in the sheet layer. Both the time-averaged concentration profiles and the concentration time histories in the sheet layer are improved. In particular, the concentration variations within a period are better predicted when some of the influence of the particles on fluid turbulence is included in the model. We also observe that the difference between the numerical results using *Hsu et al.* (2004)'s model and the present model diminishes as the sediment diameter increases (difference between the dashed and solid curve in figure 5.2 (a) and (d), figure 5.3 (a) and (d) for example). This confirms that the turbulence modification we introduced vanishes for larger particles.

It is also possible to quantify the accuracy of the numerical predictions respect to the experimental data. One way to do this is to calculate the Root Mean Square Error made when approximating the experimental time histories by the numerical time histories. The RMS Error is defined as:

$$E_{rms} = \sqrt{\frac{1}{N}\sum (c_{num} - c_{exp})^2}, \tag{5.10}$$

where N is the number of data points included, c_{num} and c_{exp} are respectively the numerical and experimental values of the concentration. The results for the four cases are summarized in table 5.2 and confirm the improvement made by considering $C_{\varepsilon 2} = C_{\varepsilon 2}(c)$.

However, some discrepancies in the model-data comparisons still remain. The modeling of sand transport here is based on three major assumptions: first, the interphase momentum transfer is supposed to be caused only by drag forces; sec-

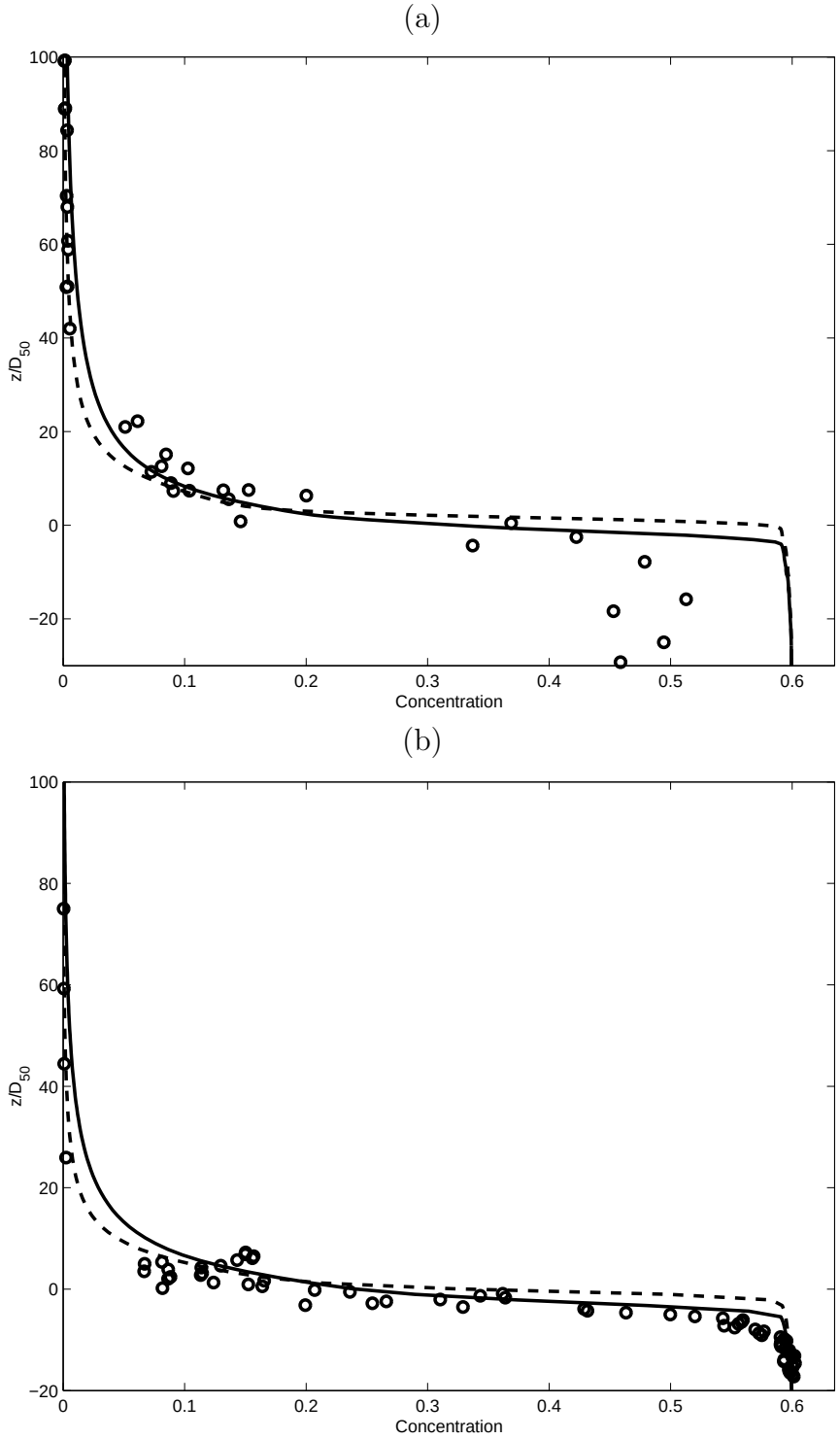

Figure 5.2: Time-averaged concentration profile for (a) case 1, (b) case 2, (c) case 3, (d) case 6. Dashed line: numerical results following *Hsu et al.* (2004). Solid line: numerical results using the proposed turbulence modification. Symbols: experimental data.

Figure 5.2 (continued).

(c)

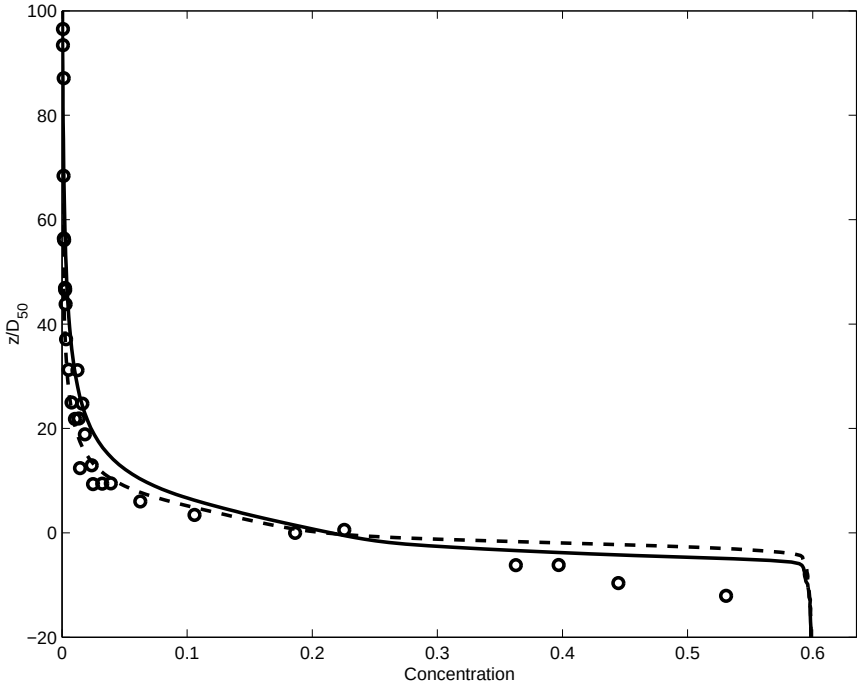

(d)

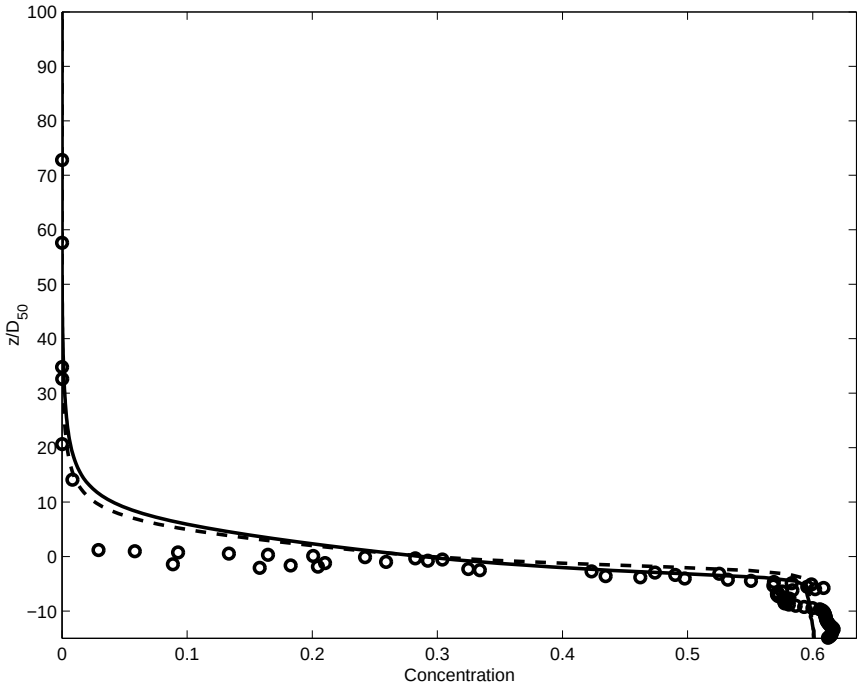

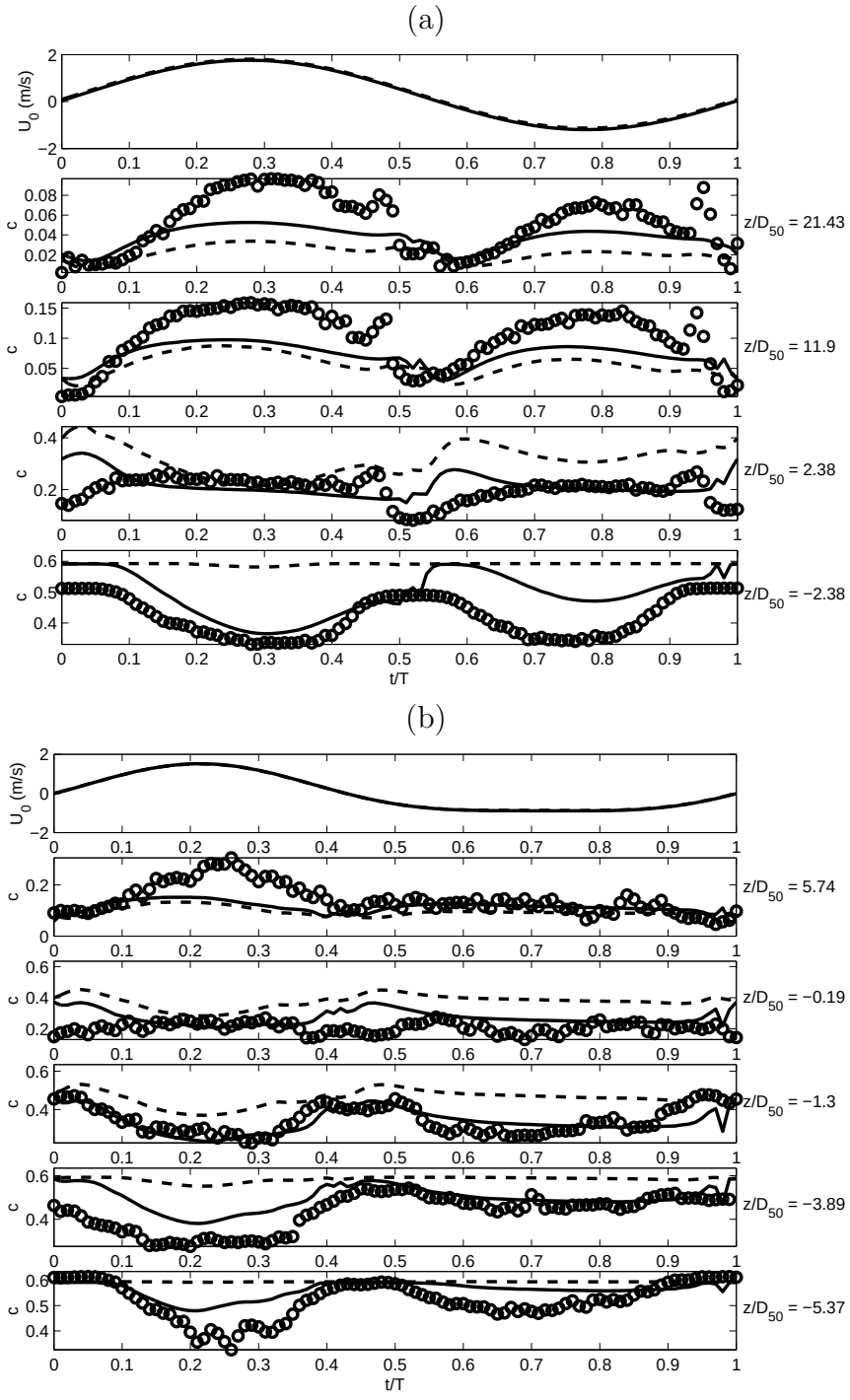

Figure 5.3: Concentration time histories in the sheet layer for (a) case 1, (b) case 2, (c) case 3, (d) case 6. Dashed line: numerical results following *Hsu et al.* (2004). Solid line: numerical results using the proposed turbulence modification. Symbols: experimental data.

Figure 5.3 (continued).

(c)

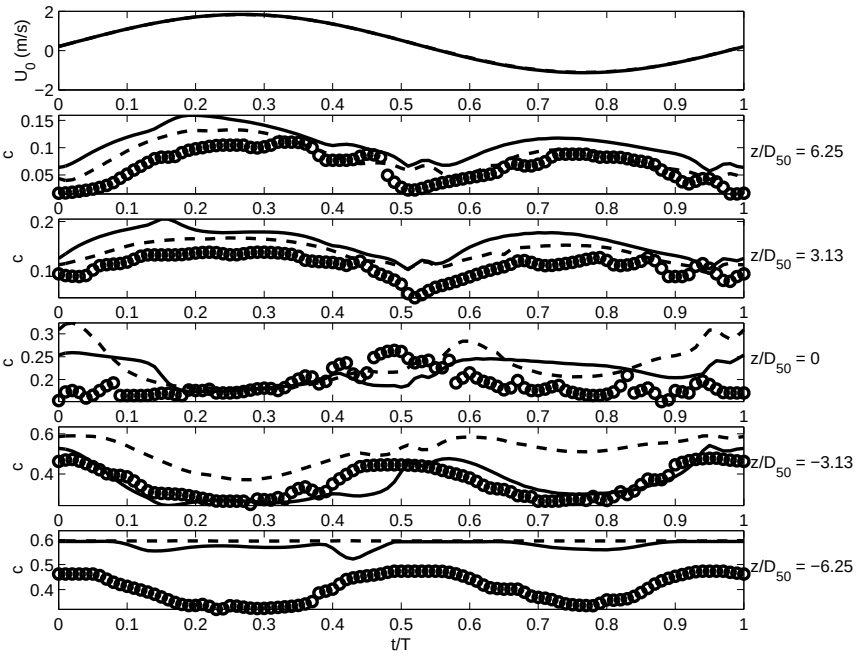

(d)

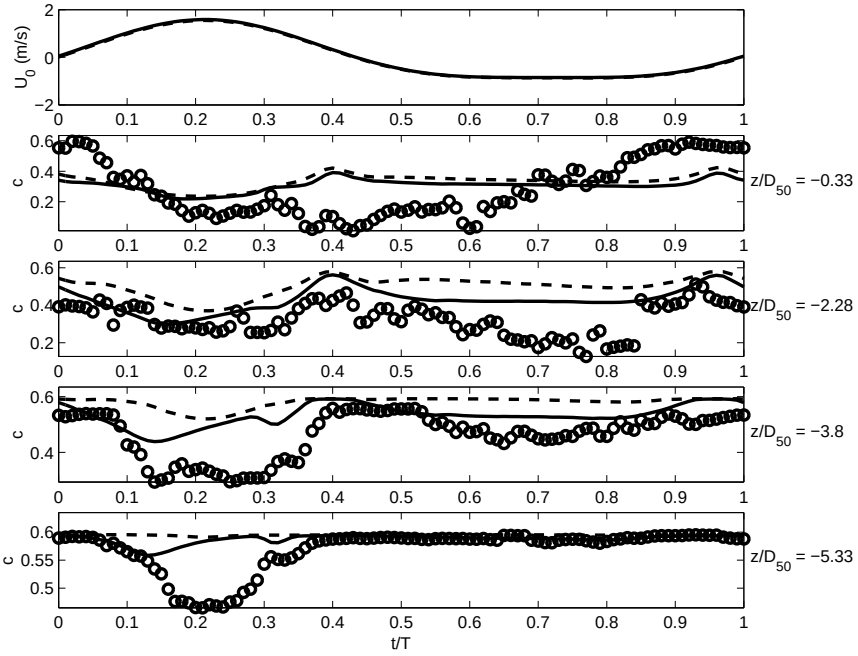

Table 5.2: Root Mean Square Error between the numerical and experimental time-dependent concentration profiles.

Case	z/D_{50}	E_{rms} ($C_{\varepsilon 2} = 1.92$)	E_{rms} ($C_{\varepsilon 2} = C_{\varepsilon 2}(c)$)
1	21.43	3.80	2.43
	11.9	5.65	4.29
	2.38	14.4	7.24
	-2.38	18.3	9.65
2	5.74	4.23	3.92
	-0.19	18.66	9.40
	-2.04	16.05	8.60
	-3.89	20.60	13.74
	-5.74	4.14	5.24
3	6.25	2.36	4.35
	3.13	3.04	4.93
	0	6.35	5.03
	-3.13	16.41	5.48
	-6.25	19.73	17.89
6	-0.33	18.90	20.13
	-2.28	13.41	8.50
	-3.8	11.58	9.78
	-5.33	2.24	2.13

ond, we assume that a collisional granular flow theory is sufficient to describe the particle-particle interactions; finally, the fluid turbulence and its interaction with the sediment particle is modeled using a modified $k - \varepsilon$ model. In its full form the interphase momentum transfer contains an added-mass term and a lift force term (*Drew*, 1983). However, we showed in chapter 3 that both these terms are small for sand grains in water. This simplification corresponds exactly to the simplification based on numerical experiments made in some bed load models that calculate the particle trajectory (e.g., *Sekine and Kikkawa*, 1990; *McEwan et al.*, 1999). Although we believe, as mentioned previously, that the collisional granular flow theory is sufficient to model sediment transport of most sand grains, the error introduced by making this assumption will increase with decreasing grain sizes. In particular, the "very fine" sand used in some experiments usually lies at the limit of the macro-viscous region in figure 5.1 and it is then probable that a different theory for the interparticle interactions should be used. The fluid turbulence closure is also a known source of discrepancies. The $k - \varepsilon$ model is known to perform poorly in presence of strong pressure gradients (see the discussion on the model accuracy in *Pope* (2000) for example), and other approaches can perform better for oscillatory boundary layers. Furthermore, the modification introduced is based on results obtained for homogeneous isotropic turbulence, which is far from being the case in sediment transport.

We also observe that our model is not able to accurately simulate experiments conducted with "very fine" sand ($D_{50} \approx 0.1$ mm). In addition of such cases being at the limit of the macro-viscous regime, laboratory observation for fine sands suggest that there is a strong suspension event during the flow reversal. Such suspension event has been demonstrated to be related to sediment suspension interacting with intermittent turbulent burst. Currently, our model is based on an

ensemble-averaged approach and such intermittent turbulent burst is not resolved. Consequently, the instantaneous nonlinear interaction between the turbulent burst and sediment particles is also not well parameterized in the existing eddy-viscosity type gradient diffusion formulation.

5.3.2 Sediment flux in oscillatory flows

Comparisons with time dependent velocity and sediment flux measurements in the sheet layer are presented for cases 4 and 5 in figures 5.4 and 5.5 respectively. The legend is similar to that of figures 5.2 and 5.3. Even though the improvement made by the turbulence modification is less pronounced for the sediment velocity than for the concentration, the results below the undisturbed bed level are better and some improvements are also observed for the sediment flux in the sheet layer.

We visually observe that the quality of sediment flux predictions is not even throughout the period. In particular, the negative fluxes seem to be worse than the positive ones. This is important when calculating the net sediment flux over a period, which is the integral of the curves shown in figures 5.4b and 5.5b. We choose to divide the net flux q in a positive component q^+ and a negative component q^- as a way to estimate the quality of the numerical results. All three quantities at different elevations close to the bed are estimated by numerical trapezoidal integration of the sediment flux time histories and the results are presented in table 5.3. Although the net flux is not better predicted by the present model, both positive and negative components are. The results in table 5.3 confirm that the positive component (and thus the positive fluxes in figure figures 5.4b and 5.5b) tends to be better predicted than the negative component, which explains the overprediction of the net flux. Also, the improvement made by the new model is greater for the positive fluxes, which explains why the net sediment flux is worse

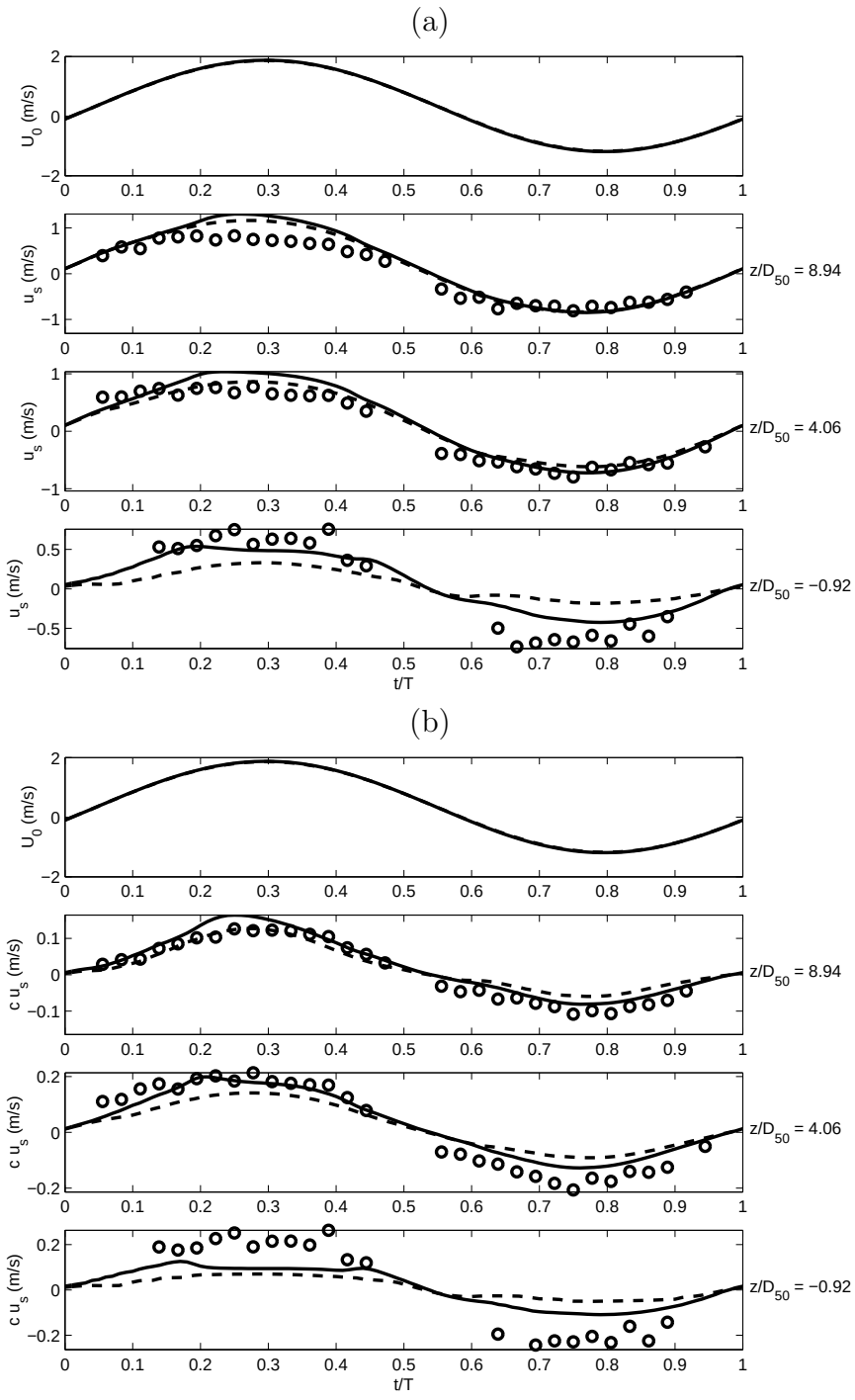

Figure 5.4: (a) Sediment velocity and (b) sediment horizontal flux time histories in the sheet layer for case 4. Dashed line: numerical results following *Hsu et al.* (2004). Solid line: numerical results using the proposed turbulence modification. Symbols: experimental data.

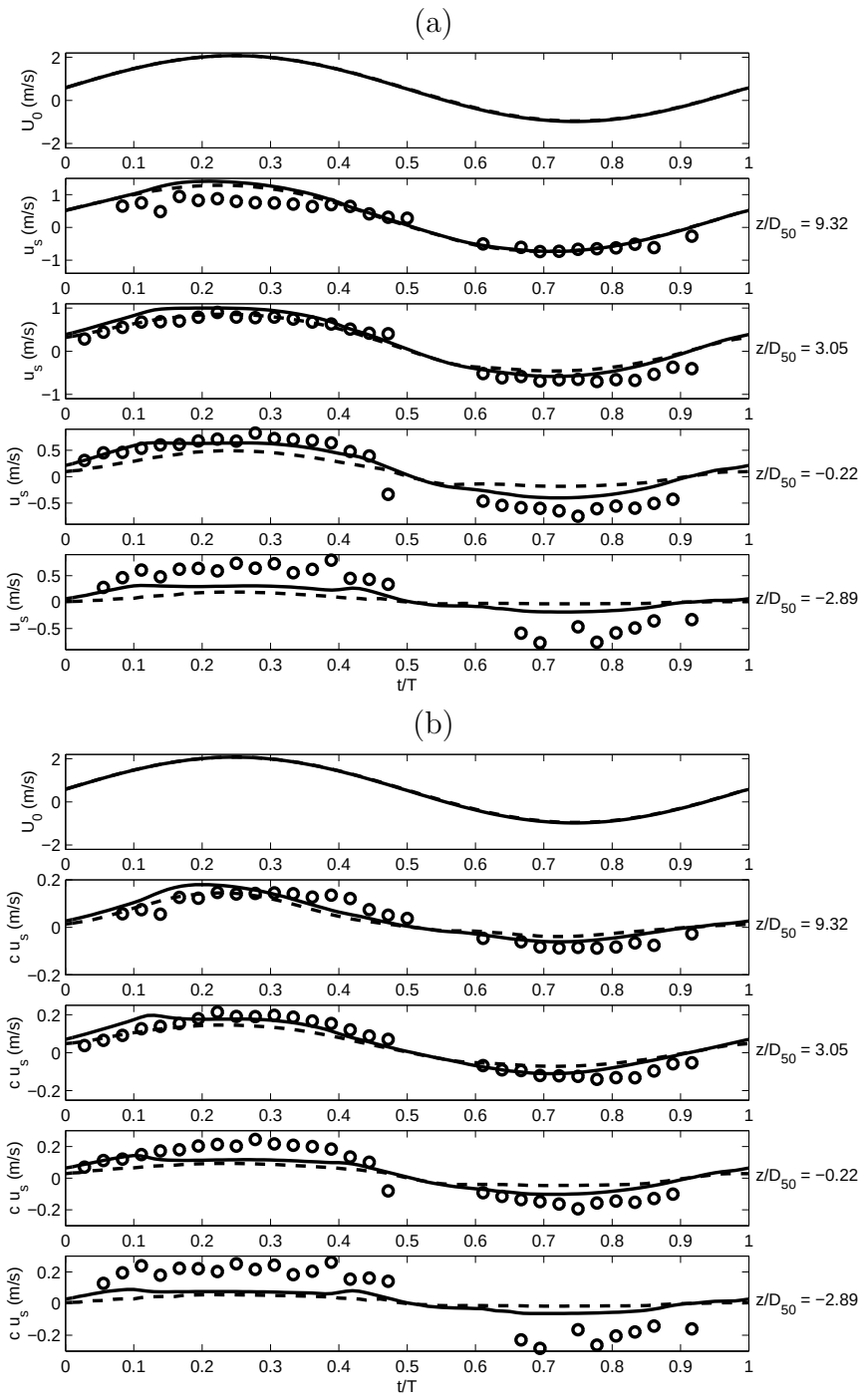

Figure 5.5: (a) Sediment velocity and (b) sediment horizontal flux time histories in the sheet layer for case 5. Dashed line: numerical results following *Hsu et al.* (2004). Solid line: numerical results using the proposed turbulence modification. Symbols: experimental data.

Table 5.3: Net sediment flux q for the experimental data q_{exp}, using *Hsu et al.* (2004) model q_o and the present model q_n (all $\times 10^{-2}$ m/s). The + superscript corresponds to the positive part of the net flux, and the − superscript to the negative part.

Case	z/D_{50}	q_{exp}	q_o	q_n	q^+_{exp}	q^+_o	q^+_n	q^-_{exp}	q^-_o	q^-_n
4	-0.92	0.55	1.04	1.18	7.93	2.55	4.35	-7.38	-1.51	-3.17
4	4.06	1.58	2.10	2.93	7.08	4.59	6.26	-5.50	-2.49	-3.33
4	8.94	0.83	1.98	2.50	3.80	3.39	4.54	-2.97	-1.41	-2.04
4	17.54	0.52	0.68	0.96	2.68	1.08	1.84	2.16	0.40	0.88
5	-2.89	1.94	1.43	1.82	9.43	1.91	3.49	-7.49	-0.49	-1.67
5	-0.22	1.91	2.09	2.64	7.56	3.54	5.37	-5.64	-1.44	-2.73
5	3.05	3.12	3.27	4.34	6.77	5.21	7.06	-3.65	-1.93	-2.73
5	9.32	2.63	3.21	3.88	4.99	4.08	5.31	-2.36	-0.87	-1.43

for the new model even though both the positive and negative contributions are better predicted.

5.3.3 Horizontal sediment velocity for a steady and uniform flow.

The modified model is also used to simulate experiments conducted for a uniform, steady flow (*Dudley*, 2007). Figure 5.6 compares the experimental data obtained for the sediment horizontal velocity and the numerical predictions. Experimentally, the velocity is measured with a fiberscope close to the bed and with an ADV in the water column (*Dudley*, 2007). In both figures, the elevation is non-dimensionalized by the median particle diameter and the velocity is non-dimensionalized by its maximum value which is also the free stream velocity (measured or calculated at 10 cm above the bed). Figure 5.6 (a) presents the model-data comparison for the entire water column while figure 5.6 (b) presents the model-data comparison for the fiberscope data only. In both figures the elevation origin is taken to be the actual

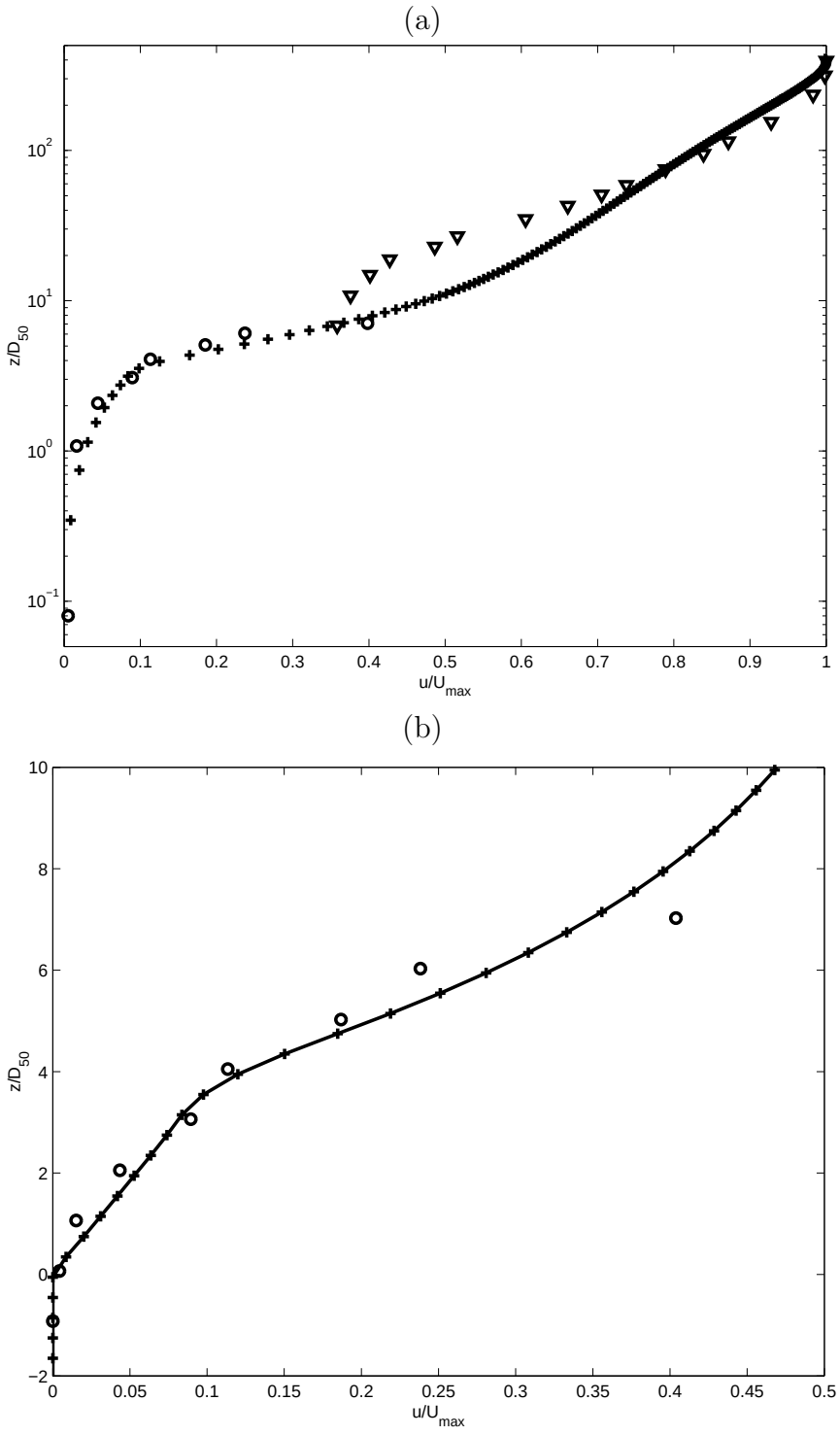

Figure 5.6: Vertical profile of the horizontal sediment velocity (a) in the entre water column and (b) in the near bed region. +: numerical data. ∘: experimental data (Fiberscope); ▽: experimental data (ADV).

stationary bed determined from the numerical model results. Both figures show reasonable agreement between experimental and numerical data. The main discrepancy occurs in the region ten to forty diameters above the bed. In this region, the sediment velocity is measured using the ADV but the small distance from the bed may affect the accuracy of the experimental results. Overall, we believe that this region lies at (or past) the experimental limits for both measurement methods used (fiberscope and ADV, see *Dudley* (2007)).

CHAPTER 6

SHEET FLOW SEDIMENT TRANSPORT

The one-dimensional sheet flow model introduced and validated in chapter 5 can be used to study sediment transport under a multitude of conditions as along as the model's assumptions remain valid. All the assumptions introduced in previous chapters have a certain given range of validity function of governing parameters such as the Shields parameter, the fall parameter R_p and S (see chapter 2). However, some of these assumption will remain valid for the entire range of parameters that we are interested in. The three main assumption limiting the use of the model are:

- uniformity in the flow direction
- the particles interact between each other in a collisional regime
- such a collisional regime can be described statistically.

The uniformity in the flow direction has been discussed at the end of chapter 3. Here we will reduce it to satisfying a sheet flow inception criterion (the flow parameters are such that the bed will be plane). In previous chapters, we used a simple criterion ($\theta > 0.8$). While the use of such a criterion is straightforward for steady flows, the bed shear stress is a function of time for oscillatory flows and the definition of a single (constant) parameter describing the intensity of the flow is less evident. Often, the maximum Shields parameter absolute value is chosen (i.e., $\max(|\theta|) > 0.8$). Other more complicated sheet flow inception criteria are also available (e.g., *You*, 1999).

The second assumption can be evaluated using $Re_\star$ and has been discussed in the previous chapter. For oscillatory flows, the bed shear stress varies with time which is equivalent to moving up and down in figure 5.1 or 2.3 at a constant given fall parameter. For high fall parameters ($R_p > 300$), the interparticle interactions

will always be collisional. For smaller fall parameters, the interparticle interactions are not necessarily always collisional (they can be be in the transition regime or even in the macro-viscous regime). Again we will use the maximum Shields parameter absolute value to evaluate the validity of this assumption. It has to be noted that the choice of the maximum Shields parameter value is consistent with better predictions at the flow maxima, which are crucial since the amount of sediment transported depends non-linearly (see chapter 2) on the flow intensity.

The last assumption that the collision are numerous enough has not been discussed yet even though it is linked to the initial condition implemented. First, the current model and its artificial initial condition require that the results do not depend on the initial condition. This will be the case if the sediment transport processes modeled reach at least a quasi-steady state. For steady flows, a steady state is indeed reached. For oscillatory flows, a quasi-steady state will be reached for low S values ($S < 0.2$) (*Zala Flores and Sleath*, 1998). All cases simulated so far (see table 5.1) do satisfy this criterion. Aside from the initial condition, the profusion of collisions is difficult to quantify and the appreciation is also different for steady flows and oscillatory flows. For steady flows, collisions will always be considered to be numerous enough when the flow intensity is strong enough to ensure sheet flow (uniformity in the flow direction). For oscillatory flows, while collisions may be numerous at the flow extrema, they could be scarce at flow reversal when the forcing intensity is small. It seems logical to assume that if the flow remains small for a long time, collisions will rarefy and the model's validity will break down. Such a situation can occur in mainly two different ways for oscillatory flows: the flow maximum (or minimum) is not strong enough, or the flow period is too long. Following the same argumentation as for steady flows, the first condition will be satisfied if both flow extrema satisfy the sheet flow condition. The second

condition can be expressed in terms of the parameter S introduced in chapter 2: the model will not be valid for very small S values.

Discussions on the sediment transport and flow characteristics under sheet flow conditions are presented in this chapter for three different types of flows: steady flow, oscillatory and wave-current boundary layers and positive triangular flows. In particular, the numerical results for the cases summarized in table 5.1 are used to illustrate such discussions for steady flows and for oscillatory and wave-current boundary layers.

6.1 Steady sheet flow characteristics

6.1.1 Characteristics out of the sheet layer

The linear profile (for $z/D_{50} > 10$) in figure 5.6 (a) indicates that the velocity follows a logarithmic law. For clear fluid boundary layers, the rough-wall log-law is commonly expressed as follows:

$$u^+ = \frac{\tilde{u}^f}{u_\star} = \frac{1}{\kappa} \ln\left(\frac{30z}{K_s}\right), \tag{6.1}$$

where $\kappa = 0.41$ is the von Karman constant for clear fluid and K_s is the equivalent sand roughness. For sediment laden flows, it is found that the velocity satisfies a similar law. However, for sediment laden flows the slope of the velocity profile does not correspond to a value of 0.41 for κ. Historically, a number of authors in the 50s and 60s suggested that the presence of sediment leads to a reduction of the value of the von Karman constant (reviewed in *Vanoni* (1975)). The complete determination of the log-law requires to evaluate the friction velocity (in particular κ and $u_\star$ are not independent). In the early work reviewed in *Vanoni* (1975), the friction velocity (or bottom shear stress $\tau_b = \rho u_\star^2$) is evaluated using a force balance

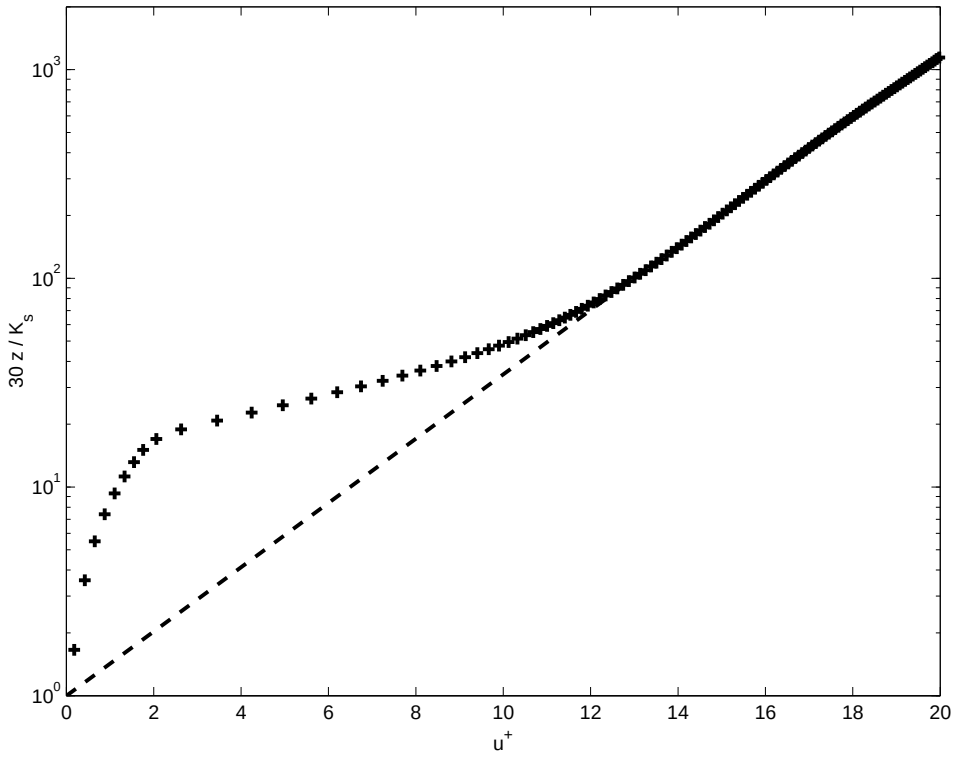

Figure 6.1: Logarithmic law for the fluid velocity. The numerical results are plotted in pluses and the rough wall logarithmic-law is plotted as a dashed line.

$\tau_b = \rho g h S_0$ where h is the flow depth, and S_0 the slope of the channel. A similar approach in the case of a steady, fully developed flow driven by a pressure gradient leads to $d\tau/dz = dP/dx$ where the pressure is a function only of x and the stress is a function only of z (see *Pope* (2000) for details). Solutions for this equation can then be explicitly written in term of the wall shear stress. Such solutions provide means to evaluate the wall shear stress, and therefore the friction velocity.

The numerical simulations performed here lead to the log-law shown in figure 6.1. Close to the bed ($30z/K_s < 20$), the velocity follows a linear profile similar to the viscous sublayer of clear fluid turbulent boundary layers. Further away from the bed ($30z/K_s > 80$), the velocity follows the rough boundary log-law and we obtain $\kappa = 0.355$ and $K_s/D_{50} = 6.27$. Both the von Karman constant and the roughness values are consistent with values previously reported. *Longo* (2005) found von

Karman constants in the range 0.33 to 0.38 for sand; *Bennett et al.* (1998) found $\kappa = 0.33$ and K_s/D_{50} in the range 8.7 to 17.4 for a similar case. Although such roughness values are bigger than our results, models for the roughness such as those of *Wiberg and Rubin* (1989) and *Sumer et al.* (1996) predict respectively $K_s/D_{50} = 5.68$ and $K_s/D_{50} = 6.76$.

Our model's results suggest that the van Karmam constant is smaller than that in clear fluid, which can be interpreted as reduced turbulence in the diluted region due to the presence of sediment (e.g., *Dohmen-Janssen et al.*, 2001; *Hsu et al.*, 2003a). Given the same roughness, smaller von Karman constant gives larger slope in the plot shown in figure 6.1 and a larger flow velocity in the logarithmic layer. This is known as the "drag reduction" phenomenon that the presence of sediment reduced the flow turbulence (compared with that of no sediment) and hence increases the mean flow rate. This is actually not contradictory with the turbulence modification introduced previously. The argument was that large particles relative to a turbulence length scale would increase fluid turbulence while small particles would decrease the turbulence. Following the *Gore and Crowe* (1989) approach, we showed that turbulence should be increased close to the bed. Far way from the bed, the turbulence length scale is much bigger, particles will then become relatively small and thus reduce the turbulence. Our model's results further suggest that with a mobile sediment bed, the resulting roughness height K_s is greater than that typically obtained for fixed bed condition ($K_s \sim 2.5D_{50}$, *Jensen et al.* (1989)). The larger roughness results from processes occurring in the concentrated region ($0 < 30z/K_s < 20$) of sediment transport, such as intergranular interactions. Overall, the turbulent boundary layer velocity in sediment-laden condition is rather complex but can be explained by the multiphase flow theory. Far from the bed, the presence of sediment reduces the flow turbulence, the von Karman

constant and hence increases the flow rate. On the other hand, the presence of concentrated sediment transport regime (mobile bed effects) gives a larger roughness for the overlaying turbulent flow. These two mechanisms have competing effects to the overall magnitude of the flow velocity and flow rate in the boundary layer.

6.1.2 Shear stresses vertical profiles and distribution

As an illustration of the stress closures we present in figure 6.2 the vertical profiles and distribution of the sediment and the fluid shear stresses for the open channel flow case. The elevation is made dimensionless by the median particle diameter, and the origin is taken to be the stationary bed. The shear stresses are non-dimensionalized by the bottom shear stress. As expected for open channels flows, the total shear stress for the mixture follows a linear profile. The region very close to the bed where the fluid shear stress is small and constant corresponds to the enduring contact region. The major suspension mechanism in this layer is sediment stress due to enduring contact. Going away from the bed, the fluid stress increases while the sediment stress decreases to reach the dilute approximation of negligible sediment stress.

6.1.3 Bed load sediment transport

In our model, sediment is suspended through two terms in the vertical sediment phase momentum equation (equation 5.6): the sediment stress gradient, which is due to the interparticle interactions, and the turbulent suspension (concentration gradient term) due to the agitation of the fluid turbulence. In a way similar to the shear stress profiles, the sediment stress gradient dominates close to the bed and decreases with increasing elevation from the bed while the turbulent suspension increases with elevation from the bed to be dominant away from the bed. We

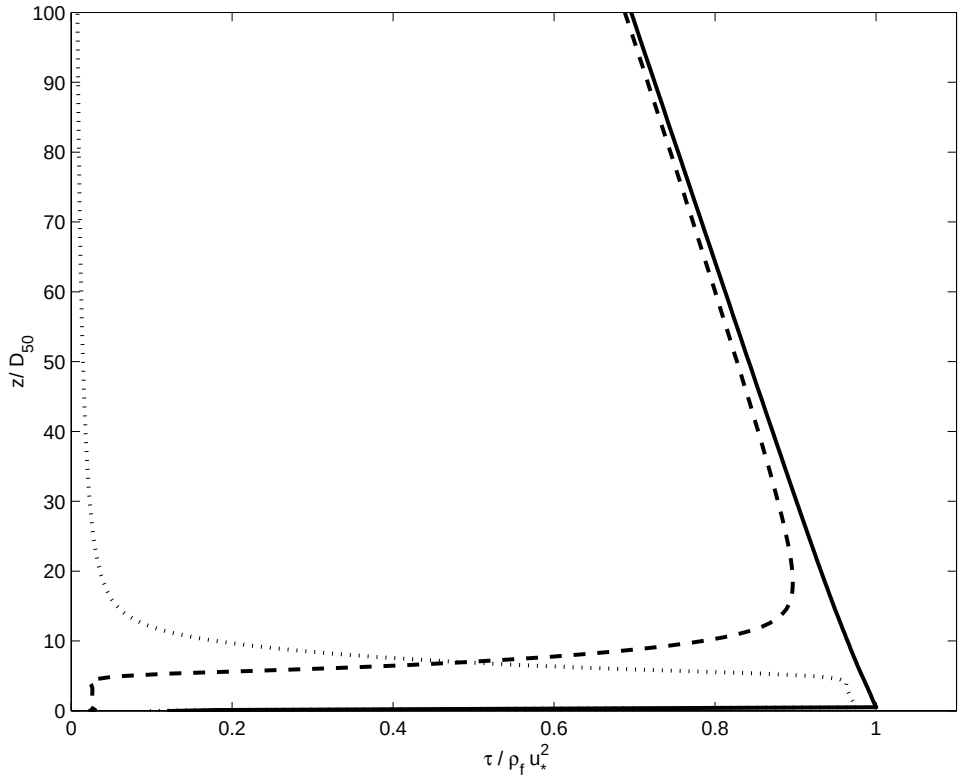

Figure 6.2: Vertical profile for the sediment shear stress (dotted line), fluid shear stress (dashed line), total shear stress (solid line).

can then define two layers corresponding to the dominance of each term, which we believe reflect the bed load / suspended load distinction. Since bed load is the part supported by the interparticle interactions, it corresponds to the region of dominant sediment stress gradient. Similarly, the suspended load corresponds to the region where the turbulent suspension term is dominant.

It is thus possible using our model to determine quantitatively the bed load layer by calculating both the sediment stress gradient and the turbulent suspension term and comparing them: the location for which the sediment stress gradient profile and the turbulent suspension profile cross represents the top of the bed load layer. We can then also estimate the bed load sediment transport rate by integrating the sediment flux only up to the top of the bed load layer. Performing such calculations for the steady flow case of table 5.1 leads to the following bed load layer thickness $\delta_s = 10.9D_{50}$ and the following dimensionless bed load transport rate $\Phi_B = 9.4$ ($\Phi_B = Q_B/\sqrt{(s-1)gD_{50}^3}$). Such values compare well with results obtained by using the bed load thickness and transport formulae of *Wilson* (1987) ($\delta_s = 10D_{50}$ and $\Phi_B = 11.5$). The bed load transport numerical value compares even better with *Ribberink* (1998)'s formula ($\Phi_B = 9.97$) which is determined by doing a more extensive comparison to experimental data. Interestingly, the numerical total load transport rate for this case is $\Phi_T = 23.97$ and the bed load therefore only accounts for about 40% of the total load.

6.1.4 Flow characteristics in the sheet layer

We will now present and discuss some of the sheet flow model characteristics in the near-bed region (within the bed load layer as defined in the previous section), and although only results for steady flows are presented, the discussion and the flow features are also relevant to the other cases. Figure 6.3 shows the sediment

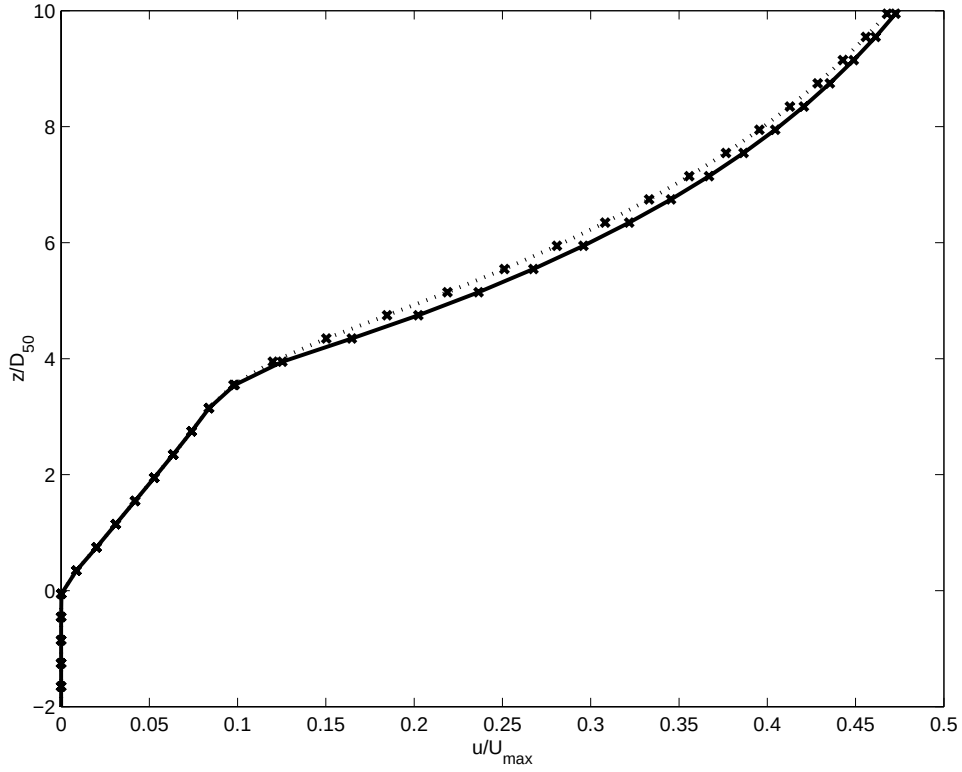

Figure 6.3: Horizontal velocities profiles for both the sediment (dotted line) and fluid (solid line) phases in the near-bed region.

phase and the fluid phase velocities in the sheet layer. The axes are the same as those in figure 5.6 (b) (again the origin of the vertical axis is taken to be the actual stationary bed determined from the numerical model results). Three distinct regions are clearly discernable on this graph. Below the bed, the particles are in contact and immobile, the sediment velocity is zero for $z/D_{50} < 0$. However, the fluid velocity has a very small value in the porous bed. In the region a few particle diameters above the stationary bed ($0 < z/D_{50} < 4$), both fluid and sediment velocities follow a linear profile and are almost identical. Then, for higher elevations, the velocities follow "power-law type" profiles, and a small difference between fluid and sediment velocities is induced by drag on the particles.

Figure 6.4 presents profiles of the concentration, horizontal sediment flux, fluid turbulent kinetic energy and sediment phase fluctuation energy, k_s, in addition to

the sediment velocity. Below the bed, the concentration is close to the random close packing value ($c^\star = 0.635$), while all of the sediment phase quantities quantities are zero since there is no particle motion and the turbulent kinetic energy is extremely small. In the "linear velocity" layer ($0 < z/D_{50} < 4$), the concentration remains higher than the random loose packing value ($c_\star = 0.57$) and somewhat constant. The sediment horizontal flux increases linearly with distance from the bed because of the linear profile of the sediment velocity. Finally, both the fluid turbulent kinetic energy and the particle fluctuation energy, although non zero, stay small. At the top of this layer ($z/D_{50} \simeq 4$), the rapid decrease in concentration leads to a locally constant flux. If the concentration gradient is strong enough, it can even cause a local decrease in the sediment flux. This sudden drop in concentration often occurs at $\bar{c} \approx c_\star$ when enduring contact stress diminishes.

Such profiles for the sediment concentration, velocities, sediment flux and particle fluctuation energy are a feature of the sediment stress closure in the near-bed region as described previously. The region just above the stationary bed corresponds to the quasi-static regime of enduring contact. Even though for the velocity profiles this region is analogous to the viscous sublayer of boundary layers (linear profile), the physics involved are different as attests the fluid turbulent kinetic energy profile. In this region, the particles move in a layered structure: a layer of particles slides on top of another layer of particles (*Zhang and Campbell*, 1992). In addition, the fluid is trapped between the particles and is thus forced to follow the motions of the sediment particles. Such a structure explains both the linear profile for the sediment and fluid velocities and the absence of drag. The layered structure also limits the mobility and possible intermittent collisions that one particle can endure, explaining the small particle fluctuation energy values.

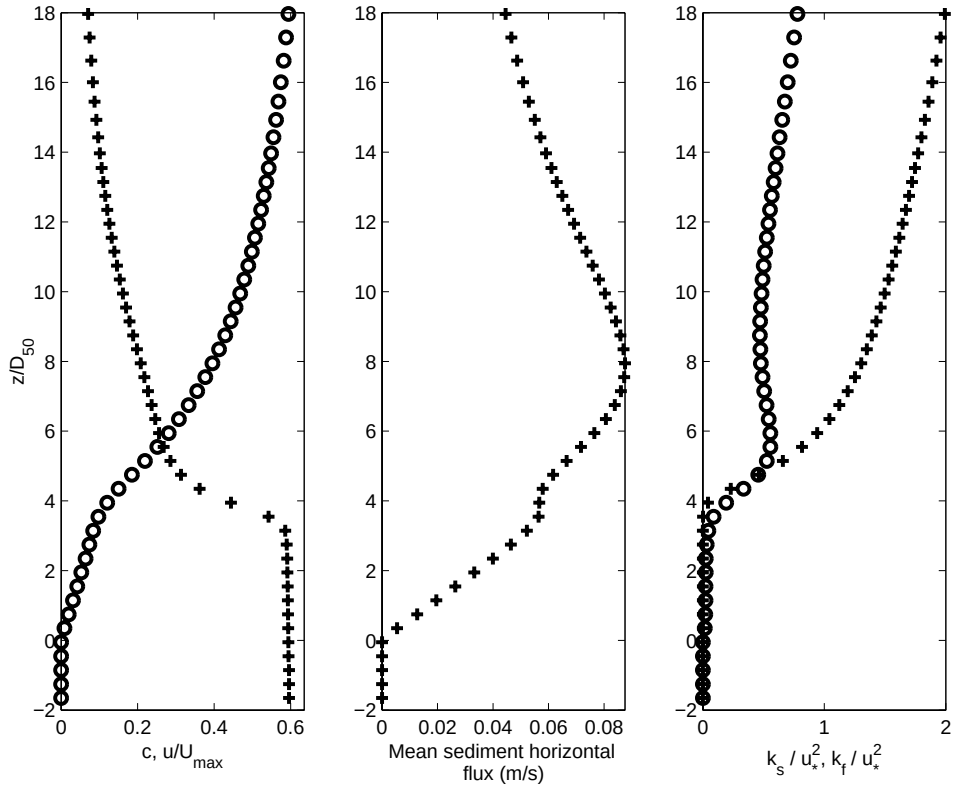

Figure 6.4: Vertical profiles for the concentration (pluses, left panel), sediment horizontal velocity (circles, left panel), sediment horizontal flux (middle panel), fluid turbulence kinetic energy (pluses, right panel) and sediment particle fluctuation energy (circles, right panel).

6.2 Sheet flow characteristics in oscillatory boundary layers

We will now discuss results obtained for oscillatory and wave-current flows and we will focus on the cases summarized in table 5.1. In such periodic cases, results are function of the phase and we choose to set $\phi = 0$ when the free stream velocity is zero and the acceleration positive ($dU_0/dt > 0$). The numerical model that we use allows us to calculate all desirable quantities.

6.2.1 Horizontal velocities profiles

Vertical profiles for both the fluid and sediment velocities can be obtained for all cases. We choose to focus here on case 1, which superposes a current in the positive direction to a purely sinusoidal wave, because of the relevance of the wave-current conditions to natural occurrences. For this case, the second flow reversal happens for $\phi = 0.56$ while the maximum free stream velocity is at at $\phi = 0.28$ and the minimum at $\phi = 0.78$. The other cases present in table 5.1 would present similar features than that observed for case 1.

Vertical profiles for both the fluid and sediment velocities are presented at several phases in figure 6.5. Figure 6.5 (a) shows the profiles at the free stream velocity extrema and flow reversals while figure 6.5 (b) shows the profiles during the acceleration and deceleration stages of the positive free stream velocity. In both figures the profiles are plotted for the entire water column up to the free stream condition and the elevation origin is taken to be the undisturbed bed location.

Several features of wave-current boundary layers are noticeable in the velocity profiles. The profiles at flow reversal (figure 6.5 (a)) show a phase lead of the velocity in the boundary layer compared to the free stream velocity. Also, close

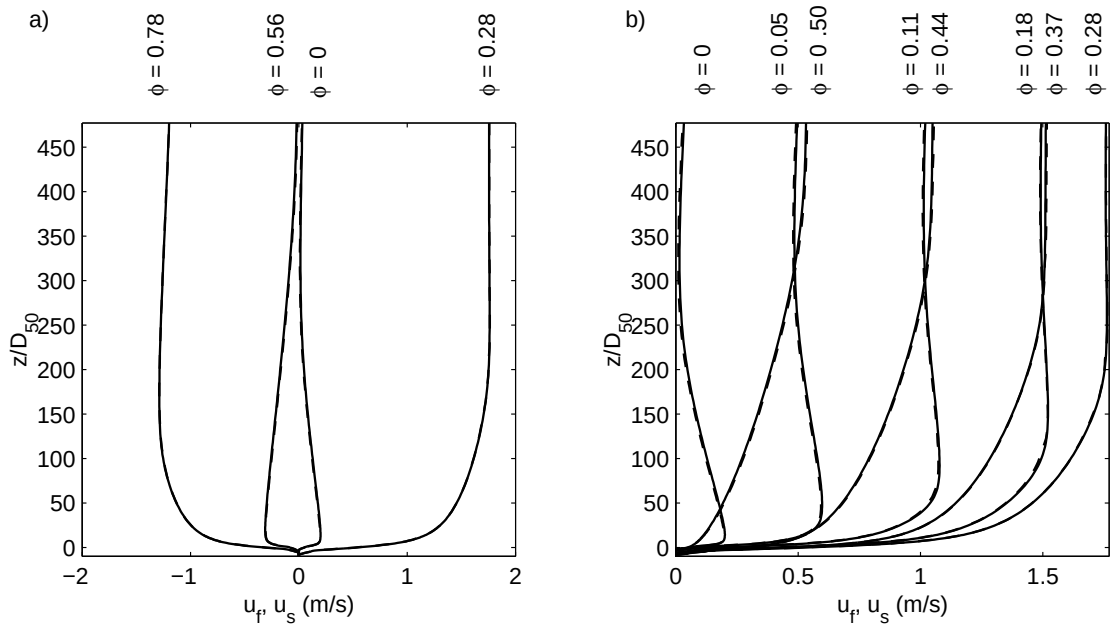

Figure 6.5: Horizontal fluid and sediment velocity profiles (a) at the flow reversals and free stream velocity extrema and (b)during the accelerating and decelerating stages. The fluid velocity is the solid line, the sediment velocity the dashed line.

to the bed, the velocity gradients are steeper during the accelerating stages than during the decelerating stages and there is an overshoot of the velocity during the acceleration stage (figure 6.5 (b)). All these features are typical of oscillatory wave-current boundary layers and have been observed in clear fluids both experimentally (e.g., *Jensen et al.*, 1989) and numerically (e.g., *Guizien et al.*, 2003). For clear fluid oscillatory boundary layers, such features on the horizontal velocity profiles are related to the phase lead of the bottom shear stress on the free stream velocity. Here, the bottom shear stress is the total shear stress (sum of the fluid and sediment stresses) at the bed. It is discussed in more details in a later section but also presents a phase lead respect to the free stream velocity (about 21.5 degrees).

Similar to the uniform and steady flow case, we are also interested in the velocity profiles close to the bed in the sheet layer both for the sediment and fluid velocities. Figure 6.6 is the enlargement of figure 6.5 close to the bed. The velocity

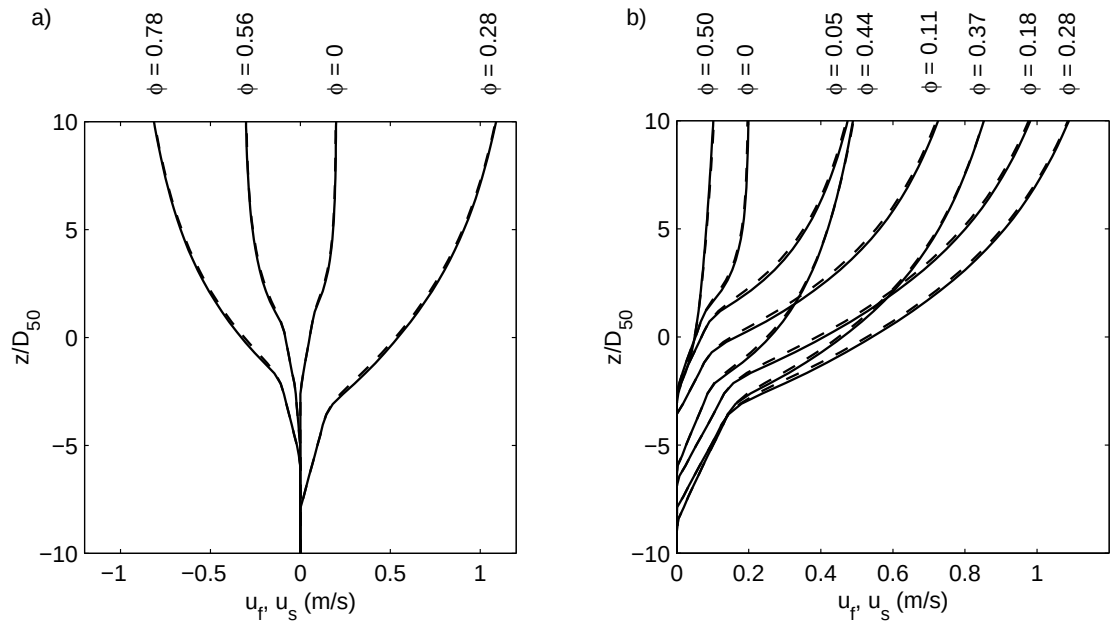

Figure 6.6: Horizontal fluid and sediment velocity profiles in the sheet layer (a) at the flow reversals and free stream velocity extrema and (b) during the accelerating and decelerating stages. The fluid velocity is the solid line and the sediment velocity the dashed line.

profiles are found to be similar to those of the uniform steady case. Three regions are also observed at any given instance. In particular the enduring contact region where both sediment and fluid velocities are almost identical and increase linearly with elevation from the bed is again present. The location of the stationary bed and the thickness of the transition layer vary in time. The stationary bed moves downwards during the acceleration phase because particles are picked up and the enduring contact layer thickness also increases.

We observe from both figures 6.5 and 6.6 that the sediment and fluid velocities are almost identical for all phases. The biggest difference occurs in the region where collisions are important, just above the enduring contact region. Figure 6.7 presents the envelope of the velocity difference normalized by the fall velocity for the entire water column. Close to the bed, the envelope is representative of the difference for the flow maxima, while far from the bed it is representative of

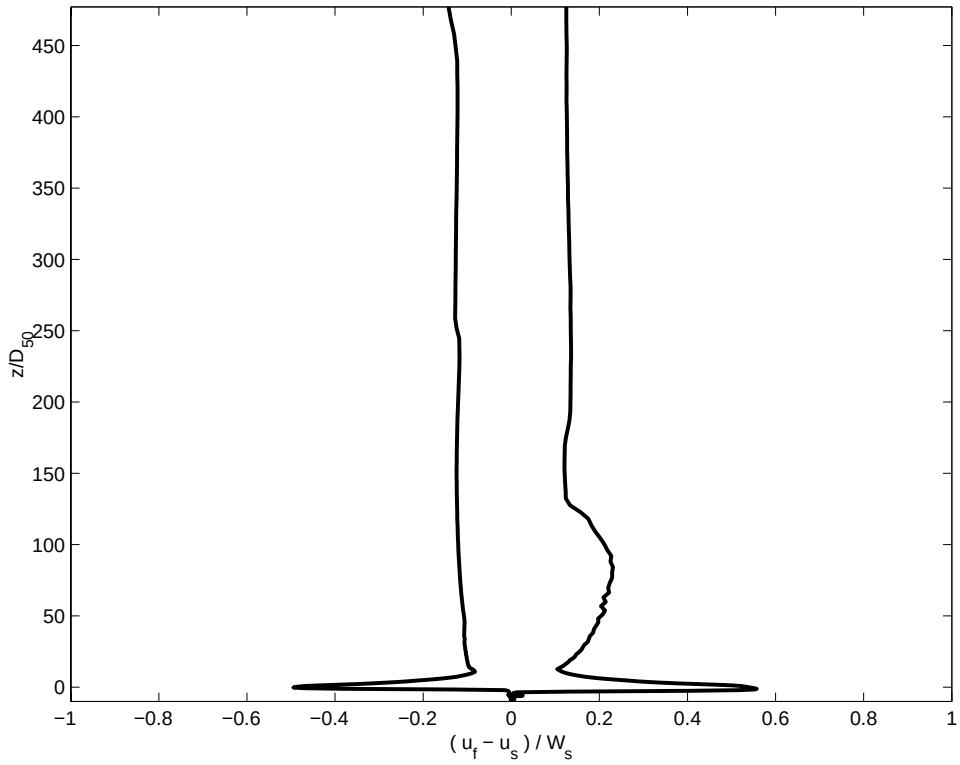

Figure 6.7: Envelope of the horizontal velocity difference normalized by the fall velocity for the entire water column.

the difference at flow reversals. In the literature, the velocity difference has been approximated by the fall velocity (e.g., *Kobayashi and Johnson*, 2001). Our numerical results show that this assumption may over-predict the velocity difference. This is of particular importance close to the bed where the concentration is still significant and most of the sediment is transported.

6.2.2 Fluid turbulence

Turbulence quantities are also part of the solution of the numerical model and a turbulent kinetic energy balance can be calculated. Figure 6.8 presents the turbulent kinetic energy as function of time in the near bed region as well as a simplified balance: the third panel from the top presents the sum of the production $\mathcal{P}$, dissipation ε and additional term D_p while the bottom panel shows the sum of the

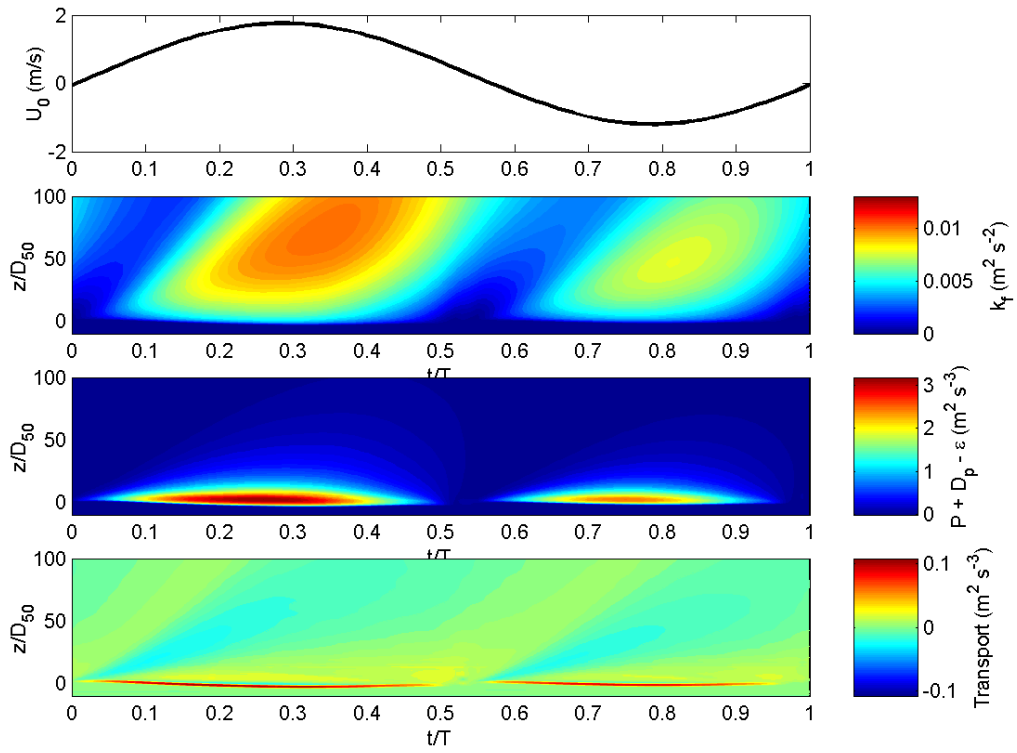

Figure 6.8: From top to bottom: Free stream velocity, turbulent kinetic energy, $\mathcal{P} - \varepsilon + D_p$, sum of transport and convection terms for case 1.

transport and the convection terms. All quantities are plotted in dimensional form and in SI units. The major interest of figure 6.8 lies in the comparison of the magnitudes of the two bottom panels and as expected the production/dissipation largely dominates the turbulent kinetic energy balance. Only very close to the bed is the transport term significant due to the kinetic energy vertical gradient. Negative values in the bottom panel (blue color) mean that kinetic energy is transported away from these locations, and this term is consistent with a "gradient reducing" action on the turbulent kinetic energy vertical profile.

Figure 6.9 focuses on the dominant terms in the turbulent kinetic energy balance (i.e., the production, dissipation and additional term D_p). These terms are plotted in figure 6.9 in the same way than in figure 6.8. Once again, the most

interesting information concerns the magnitude of the different terms rather than their evolution within a period which is expected. We find that the additional term D_p is almost always a productive term and that it is the strongest contributor to the turbulent kinetic energy balance. Furthermore, while the stress production is on the same order of magnitude as D_p, the dissipation is about five times smaller than both productive terms. This is actually important respect to the turbulence modification which is destined to improve sediment transport predictions. The three terms plotted in figure 6.9 correspond to the terms containing the parameters $C_{\varepsilon 1}$, $C_{\varepsilon 2}$ and $C_{\varepsilon 3}$ in the ε equation (respectively to the stress production, dissipation, and D_p). Our approach was to modify these parameters in order to increase the fluid turbulence near the bed. We see from the respective magnitudes of these three terms that changing $C_{\varepsilon 2}$ would actually be the least effective way to increase the near bed turbulence intensity. Even if we are satisfied with our argument stating that D_p is sufficiently well described as is (see chapter 5 section 5.1.2), changing $C_{\varepsilon 1}$ would still induce a bigger change a priori.

6.2.3 Sediment flux

Time averaged sediment horizontal flux

The sediment flux is the product of the sediment velocity and the concentration. Figure 6.10 shows the vertical profile of the time averaged horizontal sediment flux. Moving away for a few particle diameters from the actual stationary bed ($z/D_{50} \approx -8$) the velocity increases while the concentration remains somewhat constant. Therefore, the sediment flux also increases. Moving farther upwards in the water column the concentration starts to decrease rapidly. If the concentration gradient is sharp enough, it can lead to a slight decrease in sediment flux (as in this case). Farther away from the bed, the sediment flux increases again due to

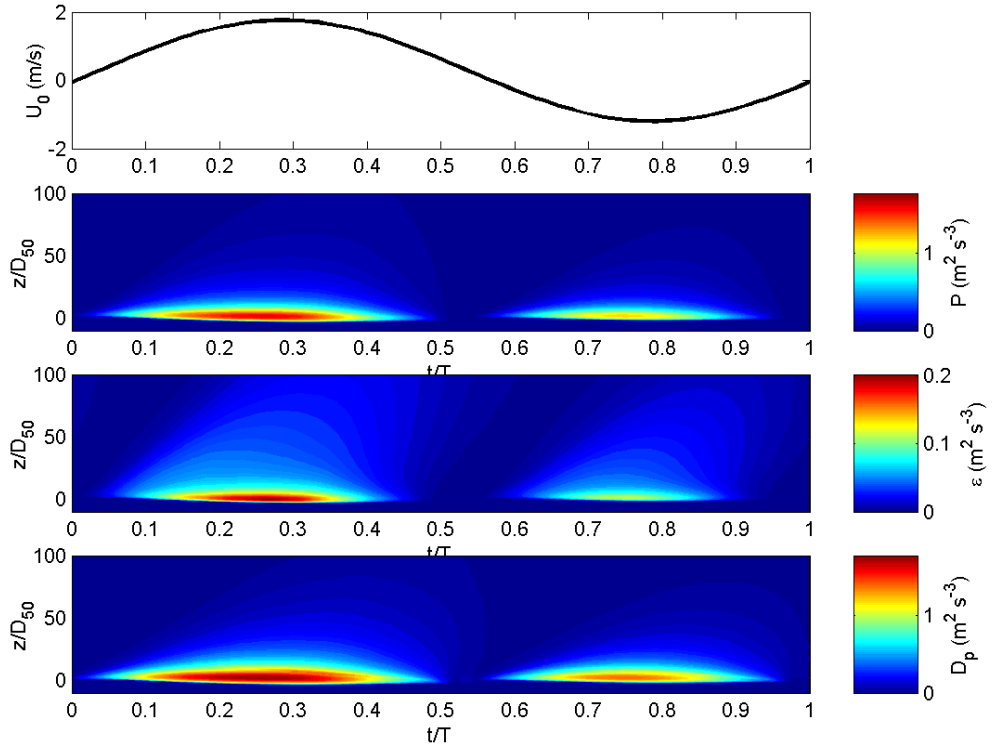

Figure 6.9: From top to bottom: Free stream velocity, stress production, dissipation and D_p for case 1.

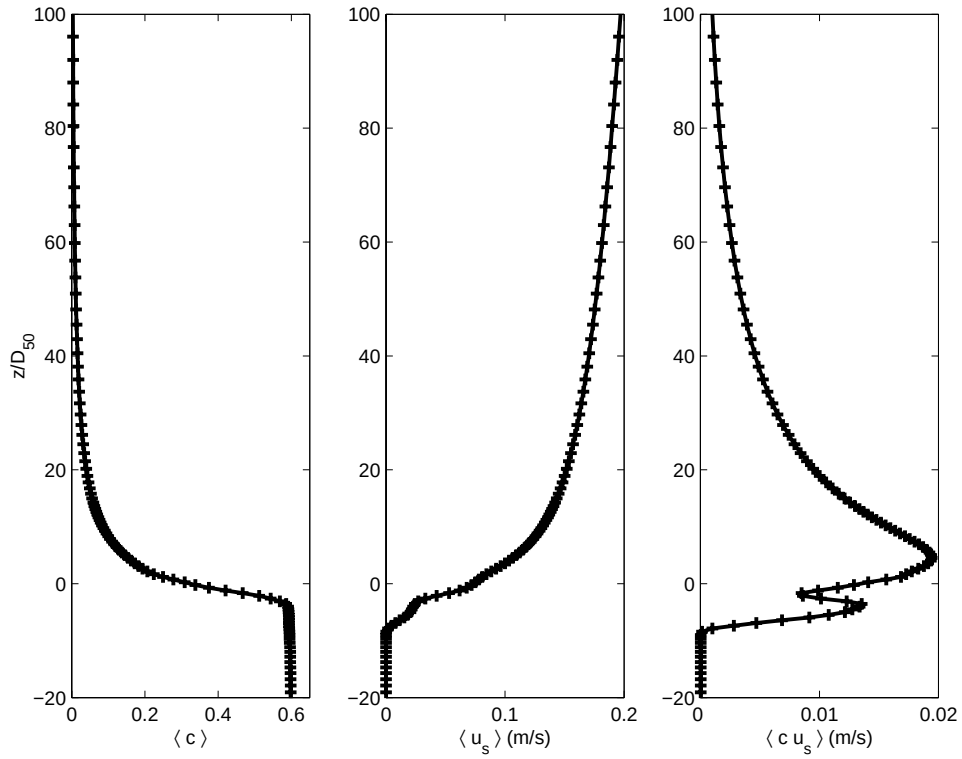

Figure 6.10: Time-averaged vertical profiles for the concentration (left panel), sediment horizontal velocity (middle panel) and horizontal sediment flux (right panel).

increasing velocity, reaches a maximum at $z/D_{50} \approx 5$ and then decreases away from the bed as the velocity increases while the concentration rapidly decreases.

Vertically integrating the sediment flux provides additional information on where the majority of the transport happens. Figure 6.11 plots the amount of the total horizontal flux that is comprised under a given elevation. In particular, we find here in this case that 90% of the sediment fluxes occurs at elevations lower than 70 diameters above the undisturbed bed (i.e., $\sim$ 1.5 cm). The existence of a maximum for this quantity (around $z/D_{50} = 200$) implies that the sediment horizontal flux is negative for elevations higher than a two hundred diameters away from the undisturbed bed. This phenomenon was experimentally observed by *Janssen* (1999). An explanation was provided by looking at the flux due to the wave action and the flux due to the current. For elevation far from the bed,

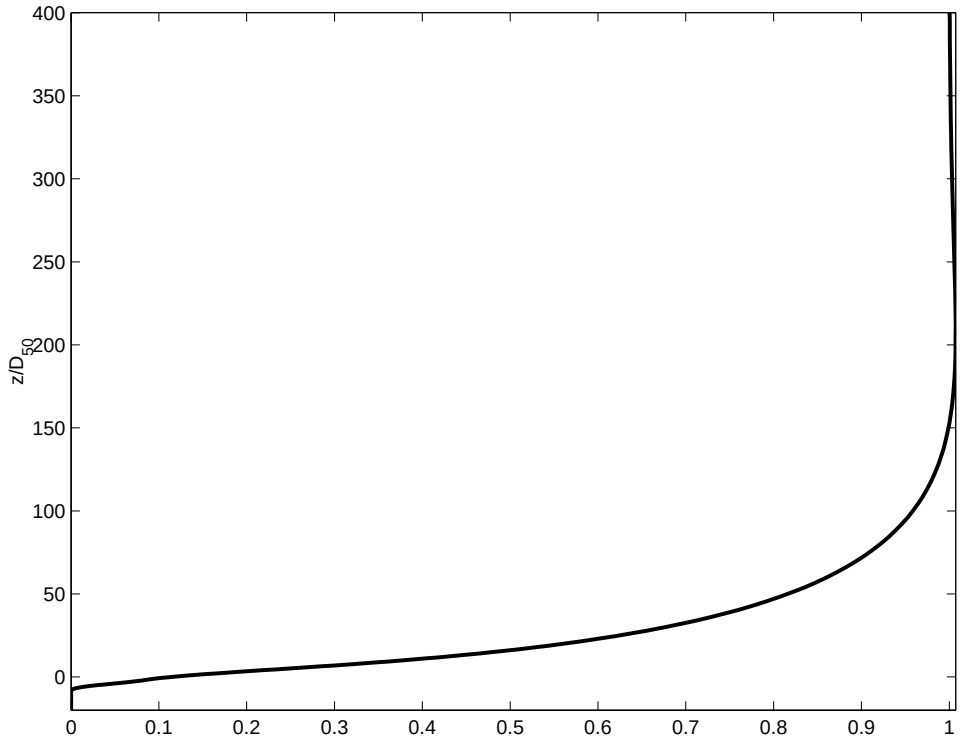

Figure 6.11: Fraction of total horizontal sediment flux comprised below z/D_{50}.

the negative flux due to the wave was stronger than the positive flux due to the current alone.

Time dependent sediment flux

The sediment flux is presented for all non-steady cases of table 5.1 in figures 6.12 to 6.17. In these figures, the top panel shows the time history of the free stream velocity $U_0(t)$ in the solid line and of the non-dimensional bed shear stress $\theta(t)$, both during one period of the oscillatory flow. Although $\theta(t)$ is plotted here and a phase lag between the bed shear stress and the free stream velocity is obvious, further discussion on the bed shear stress and the phase lags will await until sections 6.2.4 and 6.2.5 and this section will focus on the time dependent sediment fluxes. Both components of the sediment flux ($\bar{c}\tilde{u}_s$ and $\bar{c}\tilde{w}_s$) are then plotted in a non dimensional time-elevation map. Since most of the sediment transport happens

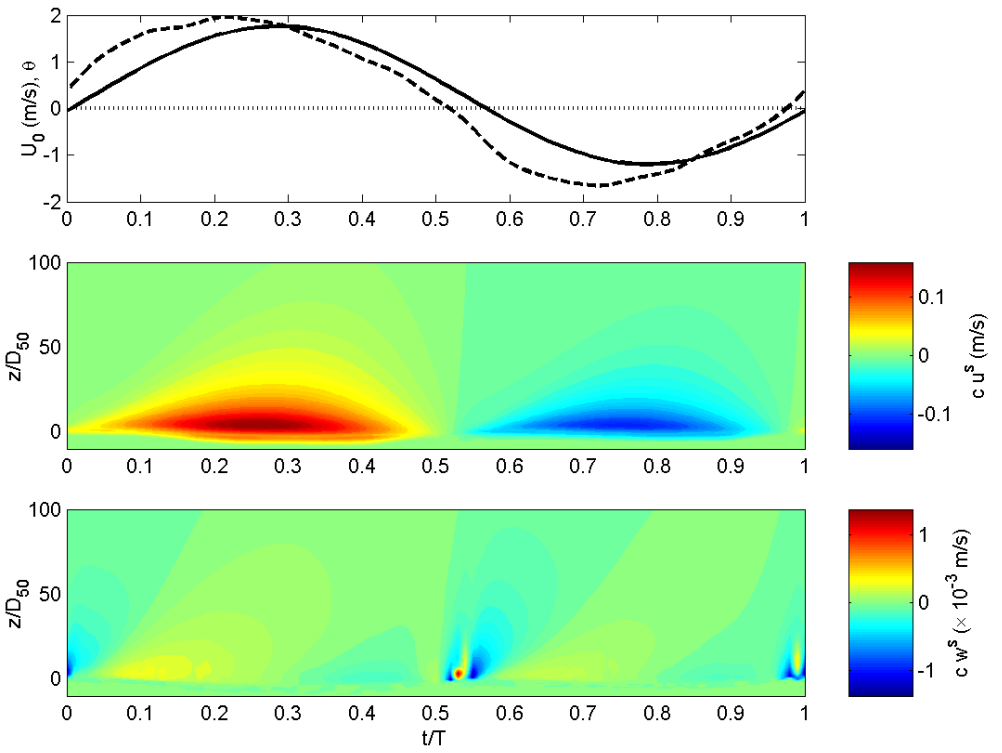

Figure 6.12: Free stream velocity (top), horizontal sediment flux $\bar{c}\tilde{u}_s$ (middle) and vertical sediment flux $\bar{c}\tilde{w}_s$ (bottom) for case 1.

close to the bed the elevation range is limited to the near bed region ($z/D_{50} < 100$). The values of the flux component are color coded and referenced in the color scale to the right of the map. The vertical sediment flux magnitude is on the order of one hundred times smaller than the magnitude of the horizontal sediment flux, and such a difference implies that a vector representation of the sediment flux would not display the vertical component.

As expected, the sediment flux quickly vanishes with increasing elevation above the undisturbed bed. For both components, most of the flux is actually contained within the first fifty diameters above the undisturbed bed. As expected given the definition of the flux as the product of the concentration by the velocity, positive horizontal fluxes are observed for positive horizontal velocity and negative fluxes

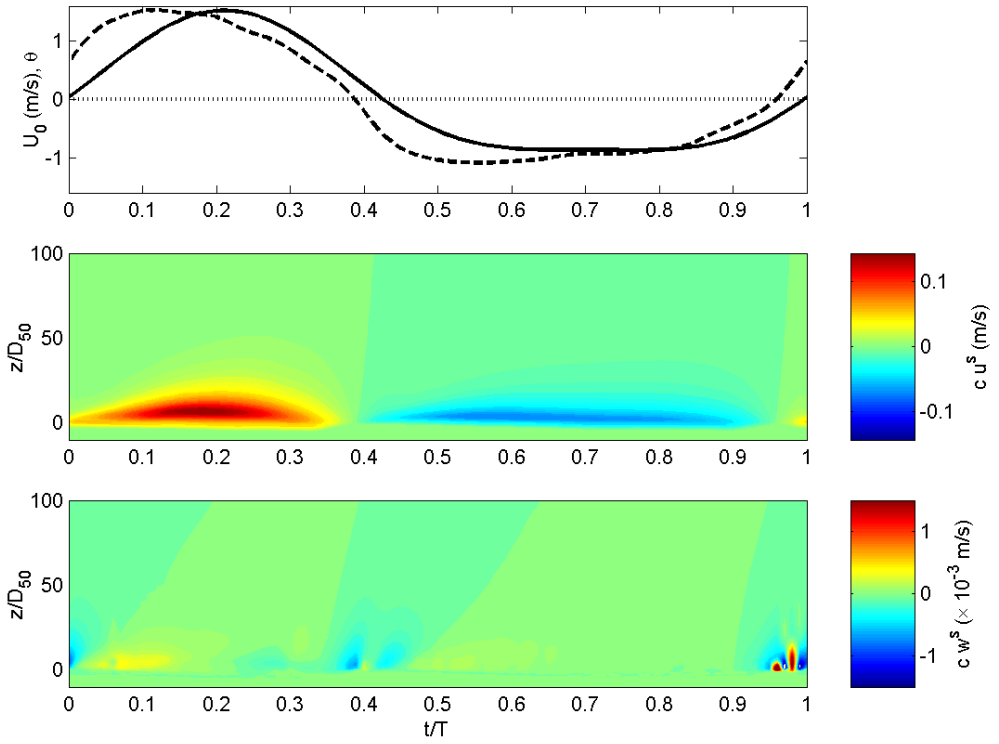

Figure 6.13: Free stream velocity (top), horizontal sediment flux $\bar{c}\tilde{u}_s$ (middle) and vertical sediment flux $\bar{c}\tilde{w}_s$ (bottom) for case 2. The color scale for the vertical sediment flux is compressed to increase contrast, the maximum vertical flux (at $t/T \approx 0.95$) is 0.0025 m/s.

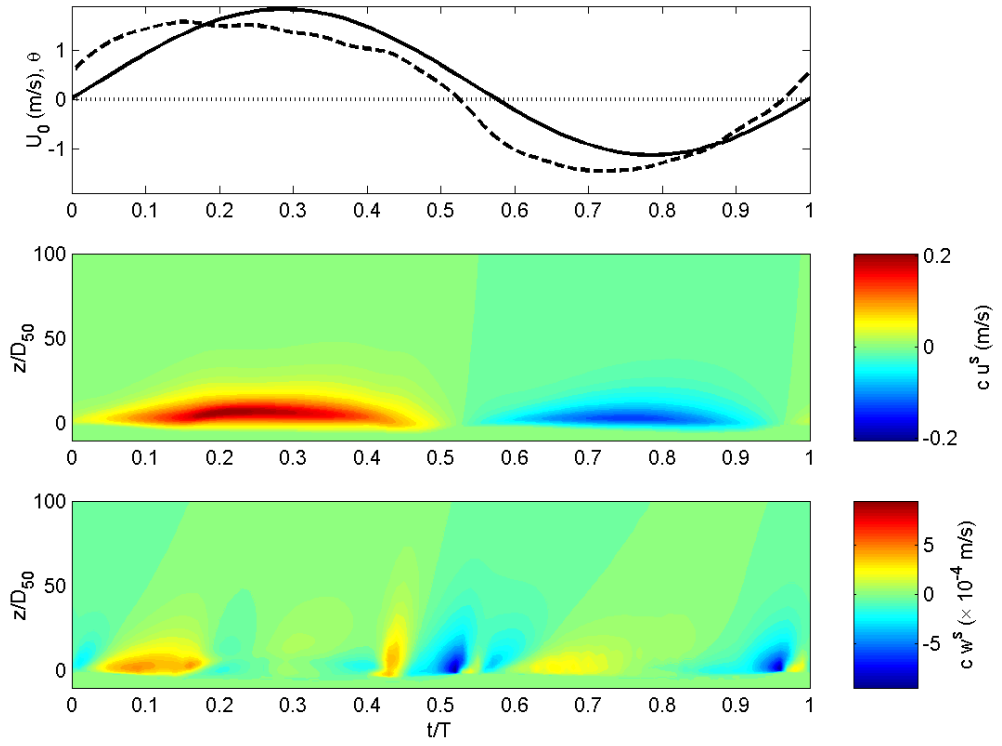

Figure 6.14: Free stream velocity (top), horizontal sediment flux $\bar{c}\tilde{u}_s$ (middle) and vertical sediment flux $\bar{c}\tilde{w}_s$ (bottom) for case 3.

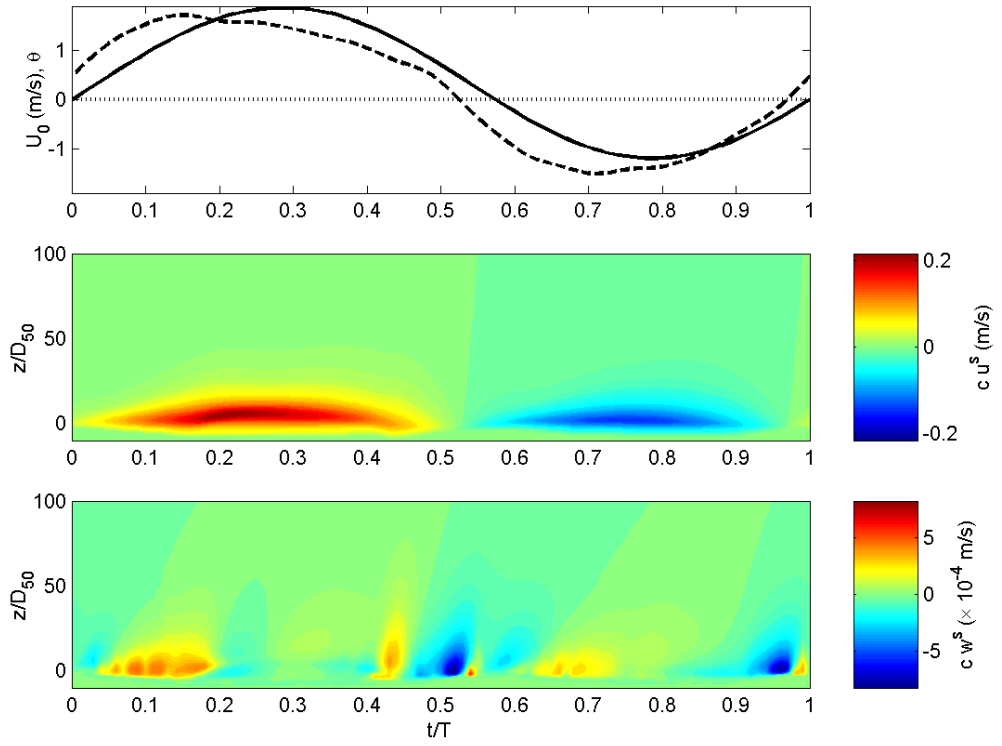

Figure 6.15: Free stream velocity (top), horizontal sediment flux $\bar{c}\tilde{u}_s$ (middle) and vertical sediment flux $\bar{c}\tilde{w}_s$ (bottom) for case 4.

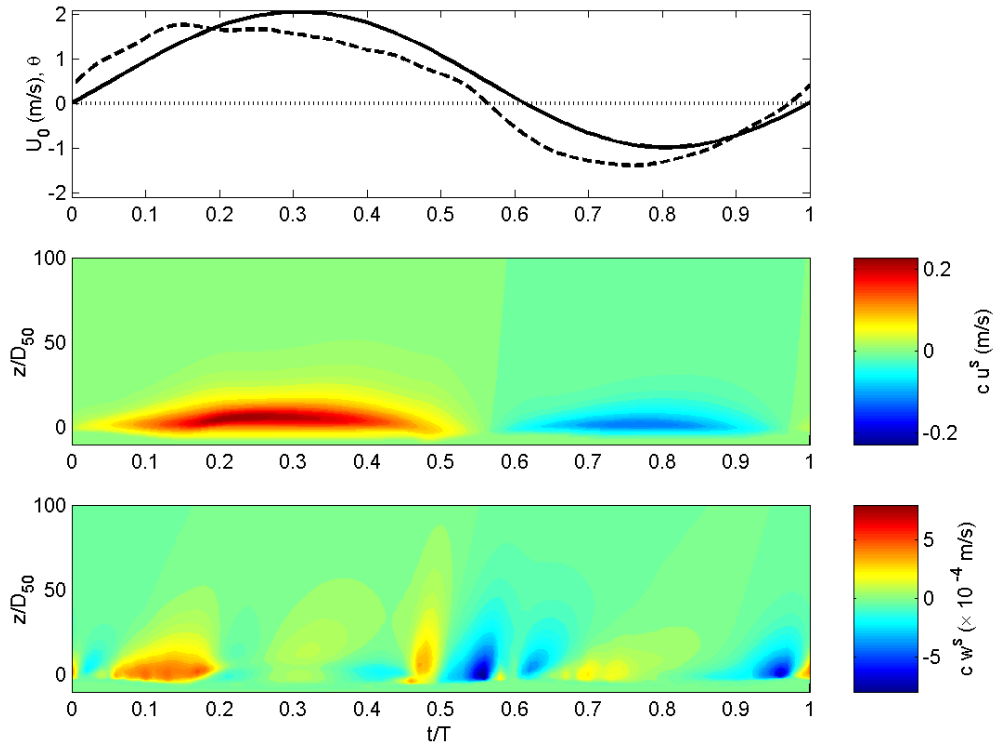

Figure 6.16: Free stream velocity (top), horizontal sediment flux $\bar{c}\tilde{u}_s$ (middle) and vertical sediment flux $\bar{c}\tilde{w}_s$ (bottom) for case 5.

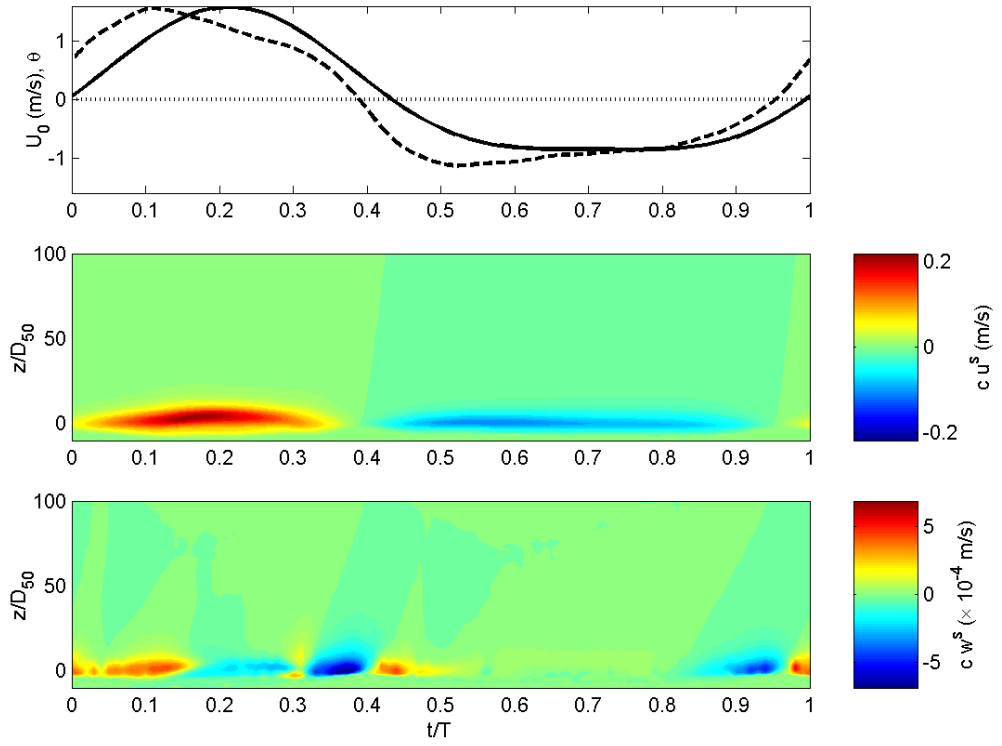

Figure 6.17: Free stream velocity (top), horizontal sediment flux $\bar{c}\tilde{u}_s$ (middle) and vertical sediment flux $\bar{c}\tilde{w}_s$ (bottom) for case 6.

for negative velocities. At a given elevation (along a horizontal line in the figures), the horizontal flux evolves in a way similar to the free stream velocity and already observed in the previous chapter (figures 5.4 b and 5.5 b). At a given instant (along a vertical line in the figures), the flux profile is similar to the profile shown in figure 6.10. The maps do provide more information, in particular concerning the phase of the flux. Close to the bed, the horizontal flux is early respect to the free stream velocity and seems to be in phase with the bed shear stress. Far away from the bed (out of the elevation range of the figures), the sediment is dilute and follows the fluid thus being in phase with the free stream velocity. In between, the sediment flux gets delayed with increasing elevation (because of the time needed for sediment to be suspended) until it is in phase with the free stream velocity. This explains the shape of the iso-flux contours being skewed to the right. Finally, at elevations under the undisturbed bed location, sediment starts to be transported as the bed shear stress increases and sediment is eroded at the start of each "half-cycle" (iso-flux contours going downwards). At the end of these half-cycles, sediment ceases to be transported and is deposited (iso-flux contours going upwards).

The vertical sediment flux is consistent with the horizontal flux contours under the undisturbed bed: when the contour for $\bar{c}\tilde{u}_s$ goes down, sediment is eroded and $\bar{c}\tilde{w}_s$ is positive (upwards); inversely, when the contour for $\bar{c}\tilde{u}_s$ goes up , sediment is deposited and $\bar{c}\tilde{w}_s$ is negative (downwards). While a dependence of the horizontal flux on the bed shear stress seems appropriate, the patterns observed for the vertical sediment are more complicated. In particular the vertical flux's sign (upward flux or downward flux) does not seem to depend on the sign of the bed shear stress as is the case for the horizontal sediment flux, but rather on the bed shear stress time derivative (slope of the dashed plot in the top panels of figures 6.12 to 6.17). Upward vertical fluxes occur when the bed shear stress absolute value is increasing

and downward vertical fluxes occur when the bed shear stress absolute value in decreasing. Similarly to the horizontal flux, the vertical flux is also delayed with increasing elevation. Such a dependence on the shear stress derivative is consistent with the intuition of particles in an accelerating flow gaining energy, thus interacting more strongly with other particles, and in turn increasing the suspension mechanism. It also explains most of the observed pattern in figures 6.12 to 6.17 to the exception of strong fluxes around the near bed flow reversals for the finer particles (figures 6.12 to 6.13). On the one hand, strong suspension events have been observed experimentally around flow reversals for the finer particles (*Janssen*, 1999; *O'Donoghue and Wright*, 2004) (see the concentration peaks at flow reversal in figure 5.3 a). On the other hand, such events (as mentioned in chapter 5) are due to the interaction of the sediment with turbulent burst which can not be resolved by the present approach.

Influence of flow forcing on the sediment flux

It is also interesting to compare the results obtained for the three cases sharing a common particle diameter (i.e., cases 3, 4, 5). The difference between those three cases is the flow forcing (see table 5.1). Cases 4 and 5 have almost the same sinusoidal component but a different added current. Although case 3 has both different sinusoidal component and different added current, the ratio of mean flow to wave velocity is close to that of case 4, which leads to the free stream velocity time histories of case 3 and 4 being different mainly through the flow amplitude. The free stream flow reversal for cases 3 and 4 happen at approximately the same phase, while that of case 5 is significantly later.

Comparing cases 3 and 4 (figures 6.14 and 6.15), the horizontal flux is stronger in both directions for case 4. In addition, a vertical shift of the iso-flux contours in the middle panels implies that more sediment is eroded in case 4. As expected,

no horizontal shift of these contour is observed. Similarly the vertical flux differs in strength: the same events are observed at the same times but are stronger for case 4, which can be explained by bigger absolute values of the bed shear stress derivatives in turn due to bigger flow amplitude.

Comparing cases 4 and 5 (figure 6.15 and 6.16), the horizontal flux differences are consistent with the dependence of the flux with the velocity: the positive flux for case 5 is stronger and lasts longer, while the negative flux is both weaker and shorter. For the sediment vertical flux, we observe in case 5 a stronger upward flux for the positive flow and a weaker upward flux for the negative flow. Both are consistent with a dependence on the bed shear stress derivative. The downwards fluxes intensity does not change much between the two cases, but neither do the corresponding negative bed shear stress derivative (negative slope of the dashed line in the top panel).

Overall, the behavior of both components of the sediment flux is fairly consistent with a dependence on the bed shear stress for the horizontal flux and on the bed shear stress derivative for the vertical flux. A change in the flow amplitude (such as that from case 3 to case 4) will lead to a change in the bed shear stress amplitude, no phase shift and, in the end, stronger fluxes in both directions for both components result. A change in the current will lead to different relative magnitudes of the bed shear stress for the positive flow and for the negative flow. It also seems to change the positive derivative of the bed shear stress to greater extent than the negative derivative.

6.2.4 Sediment transport rates

The volume sediment transport rate is calculated by integrating the horizontal sediment flux across the water column depth h:

$$Q_T(t) = \int_{-\infty}^{h} \bar{c}(t)\tilde{u}^s(t)dz \tag{6.2}$$

and is commonly used in non-dimensional form:

$$\Phi_T = \frac{Q_T}{\sqrt{(s-1)gD_{50}^3}}. \tag{6.3}$$

In the same way than for the steady state case, both the sediment normal stress gradient and the turbulent suspension can be calculated at each instant and the total load can then be split into bed load (where the sediment normal stress gradient dominates) and suspended load (where turbulent suspension dominates). In addition, the bed load layer thickness can also be calculated as a function of time.

Bed shear stress and sediment transport rates

Figure 6.18 presents the time dependent response to the flow forcing of the cases summarized in table 5.1 during a period. The bed shear stresses (middle panels) and the different sediment transport rates (bottom panels) are plotted along with the free stream velocity (top panels). In the present cases, the definition of the bed shear stress and its calculation are slightly different than in typical boundary layers because of the movable bed. In typical boundary layer flows, the bed is fixed and the bed shear stress is then defined and calculated at a fixed location. In our model, the bed location changes with time. We defined and calculate the bed shear stress as the shear stress at the (movable) bed location. Is has to be noted that a "bottom shear stress" could also be defined and calculated at a fixed location (the undisturbed bed for example). Numerically, the bed shear stress results present

some unwanted fluctuations, and the raw results are filtered using a low pass filter to obtain the data that is plotted in figure 6.18. All of the bed load transport rate, the suspended load transport rate and the total load transport rate are also plotted in the bottom panels using respectively dashed lines, dotted lines, and solid lines.

Figure 6.18 provides a good indication on the phase leads or lags between the free stream velocity, the bed shear stress and the sediment transport rates and they will be discussed in more details in the next section. We can also see from figure 6.18 that the relative importance of the bed load transport and the suspended load transport depends on the sediment particle diameter. The suspended load importance increases with decreasing particle diameter, which can be linked to figure 2.1 showing the different modes of transport and how bed load is more important for larger particles. The suspended load transport is also found to be relatively more important during the two deceleration portions of the cycle.

Bed load layer thickness

The bed load layer thickness is plotted in figure 6.19. In addition to the numerical results (solid line), the thickness given by an extension of *Wilson* (1987)'s model (i.e., $\delta_s(t)/D_{50} = 10\theta(t)$) is also plotted in dashed lines.

There is a reasonable agreement between the numerical values of the bed load layer thickness and the values found by extrapolating the formula of *Wilson* (1987). Both numerical and model thickness time histories are in phase. However, the numerical thickness time histories are skewed and the numerical results predict thicknesses that grow slower than what Wilson's model predicts. This can be caused by a "response time" of the particles. In other words, because of their inertia particles do not respond instantaneously to changes in the bed shear stress. The maximum thickness during the positive velocity portion of the cycle matches well, however the numerical thickness during the negative velocity is constantly

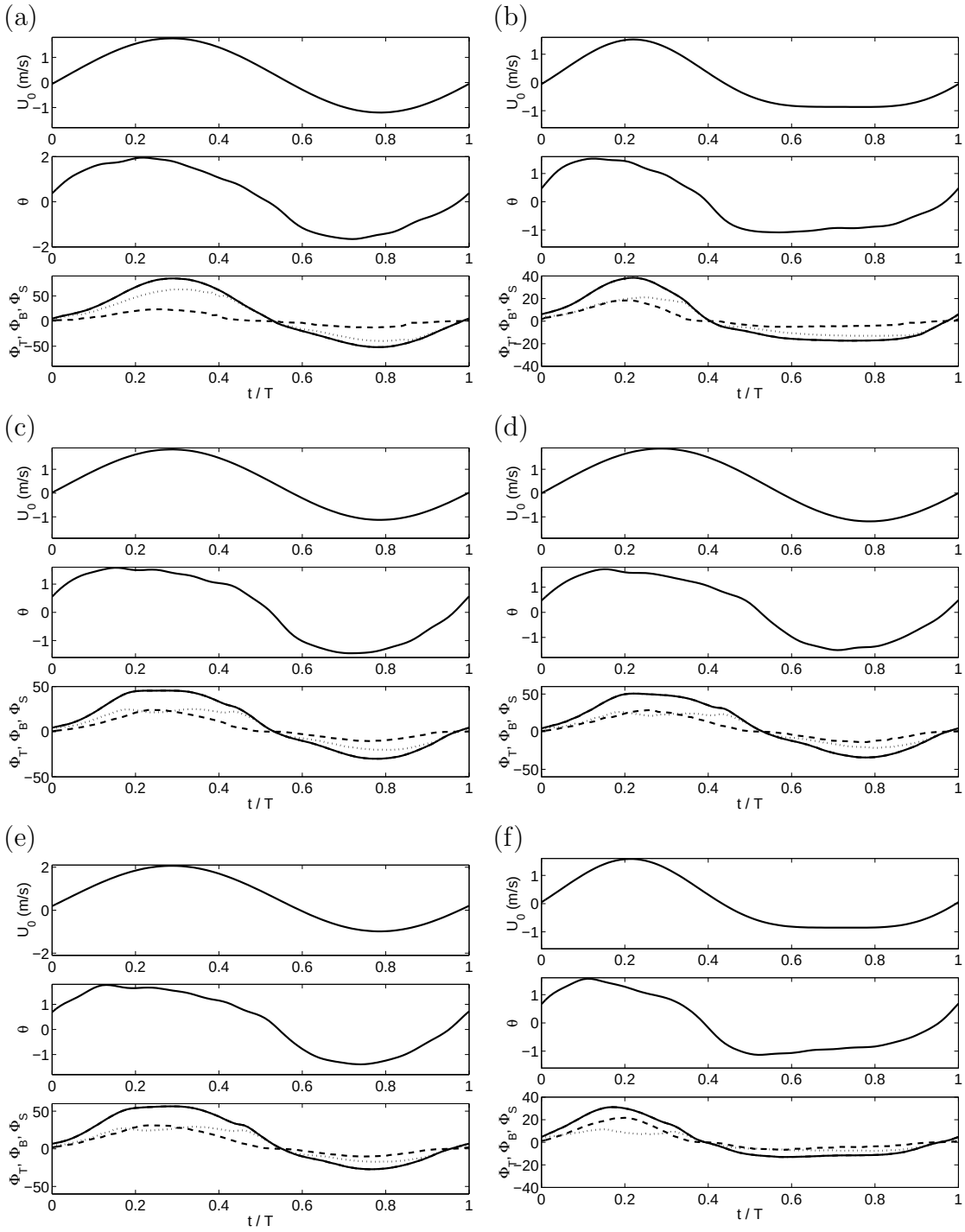

Figure 6.18: Free stream velocity (top panels), Shields parameter (middle panels) and sediment transport rates (bottom panels): total load (solid line), bed load (dashed line) and suspended load (dotted line) for cases 1 to 6 respectively from (a) to (f).

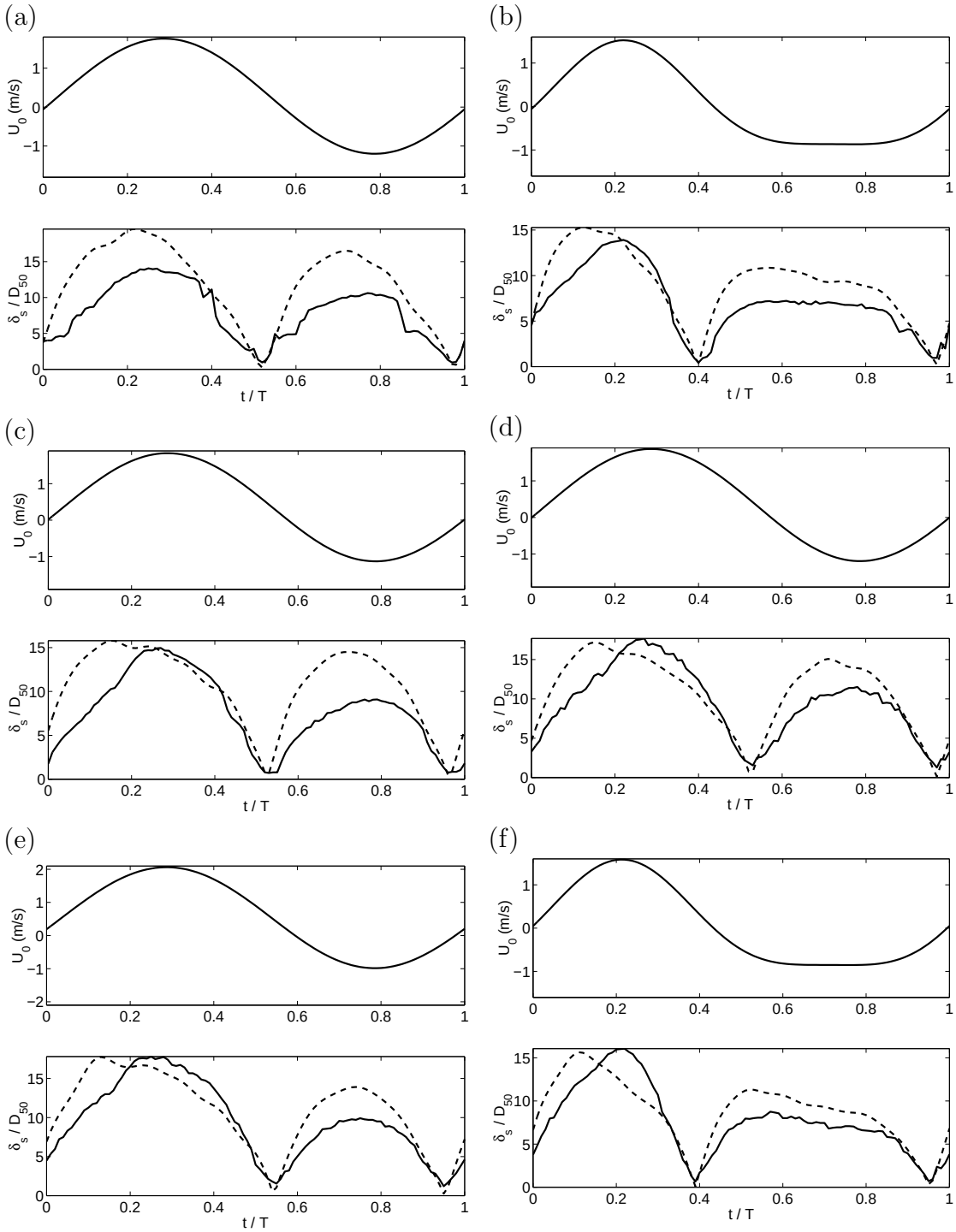

Figure 6.19: Free stream velocity (top panels) and bed load layer thickness (bottom panels) given by the present model and $\delta_s(t)/D_{50} = 10\theta(t)$ (extension of *Wilson* (1987)'s formula to oscillatory cases) for cases 1 to 6 respectively from (a) to (f).

Table 6.1: Phase lag analysis for the bottom shear stress and the sediment transport rate. The phase lag is given in degrees. Positive values mean that the first subscript is late respect to the second subscript. Negative values mean that the first subscript is early respect to the second subscript.

Case	ϕ_{θ/U_0}	ϕ_{Φ_T/U_0}	$\phi_{\Phi_T/\theta}$	ϕ_{Φ_B/U_0}	$\phi_{\Phi_B/\theta}$	ϕ_{Φ_S/U_0}	$\phi_{\Phi_S/\theta}$
1	-20	-3	18	-13	9	0	22
2	-20	-5	17	-12	8	-2	24
3	-20	-6	15	-10	12	-2	18
4	-20	-6	14	-11	11	-2	18
5	-19	-5	15	-11	11	0	18
6	-21	-12	10	-12	11	-12	8

lower than Wilson's predictions.

6.2.5 Phase lag for sediment transport in oscillatory flow

Several different techniques can be used to obtain the time lag between two periodic signals. The time lag between the two signals can be taken to be the time lag between the maximum (minimum) values of the signals. It can also be taken to be the time lag between the instants at which the periodic signal equals its mean (which we will call mean crossing). In our case, the quantities we are interested in have both a positive and negative part and a "zero crossing" method could be used. Finally, the time lag can be calculated using a cross-correlation technique: the time lag is the lag at which the cross-correlation of the two periodic signals is maximized. All these different methods may not lead to the same result.

The results obtained by the cross-correlation technique for the phase lag between the free stream velocity, the bottom shear stress an the different sediment transport rates are reported in table 6.1. The bed shear stress is found to be rather consistently about 20 degrees early respect to the free stream velocity.

In general, the sediment transport rates are late respect to the bed shear stress,

but still early respect to the free stream velocity. However, the phase lags presented in table 6.1 are not sufficient to completely describe the processes involved. In particular, computing the time lags between the sediment transport rates and the bed shear stress by the "zero crossing" method leads to different results: both the suspended and total sediment transport rates are only a few (2 to 3) degrees late respect to the bed shear stress while the bed load transport rate is in phase with the bed shear stress. Since the transport rates and the bed shear stress reverse at approximately the same times within a period, the phase lags reported in table 6.1 are due to the transport rates time histories being skewed late (in a similar way than the bed load layer thickness is). All three transport rates are, but we see that the suspended transport rate is skewed later than the bed load transport rate, which is confirmed both by the results in table 6.1 and the visual observation of figure 6.18.

We mentioned in the previous section that this shifting of the maximum (minimum) within the cycle was due to the sediment not responding instantaneously to changes in the bed shear stress. The behavior of the sediment transport rates in also linked to the observations made on the sediment flux components. The whole cycle can be split in two parts corresponding to the positive flow and the negative flow. Each of these two parts can also be split in an accelerating part and a decelerating part. During the accelerating part, the sediment responds late to changes in the bed shear stress because of its response time, and all of the bed load layer thickness and the sediment transport rates are late respect to the bed shear stress. In addition, sediment is picked up from the bed and suspended as indicated by the positive vertical flux, which explains the relative importance of the suspended transport rate during the decelerating stage.

6.3 Positive triangular flow

The model developed and introduced in previous chapters has also been used to simulate a very specific flow for which the free stream velocity follows a positive triangular form. Even though such a flow would rarely be naturally found, it presents interesting characteristics in terms of sediment transport modeling. A positive triangular flow is a succession of constant accelerating and decelerating stages, it also is such that the free stream velocity does not experience a flow reversal. Still, a near bed flow reversal is expected.

We simulate the positive triangular flow by representing it by the first five terms of its Fourier series. The period is taken to be $T = 2.6s$, and the maximum free stream velocity is taken to be $U_{osc} = 1.5m/s$. The sediment considered in this case is sand ($s = 2.65$) of median diameter $D_{50} = 0.25mm$.

6.3.1 Horizontal velocity

Both the fluid and sediment velocity vectors are presented in figure 6.20 in which the top panel represents the free stream velocity and the middle and bottom panels respectively the fluid and sediment velocity vectors at different times. As mentioned for oscillatory flows the vertical component of the velocity is much smaller than the horizontal component and is thus hardly discernable in a vector plot. Also the difference between the sediment velocity and the fluid velocity is small. As expected, the flow is reversed in the near bed region when the free stream velocity is small. In figure 6.20, the near bed reversals happen slightly before $t/T = 0.1$ and $t/T = 0.9$.

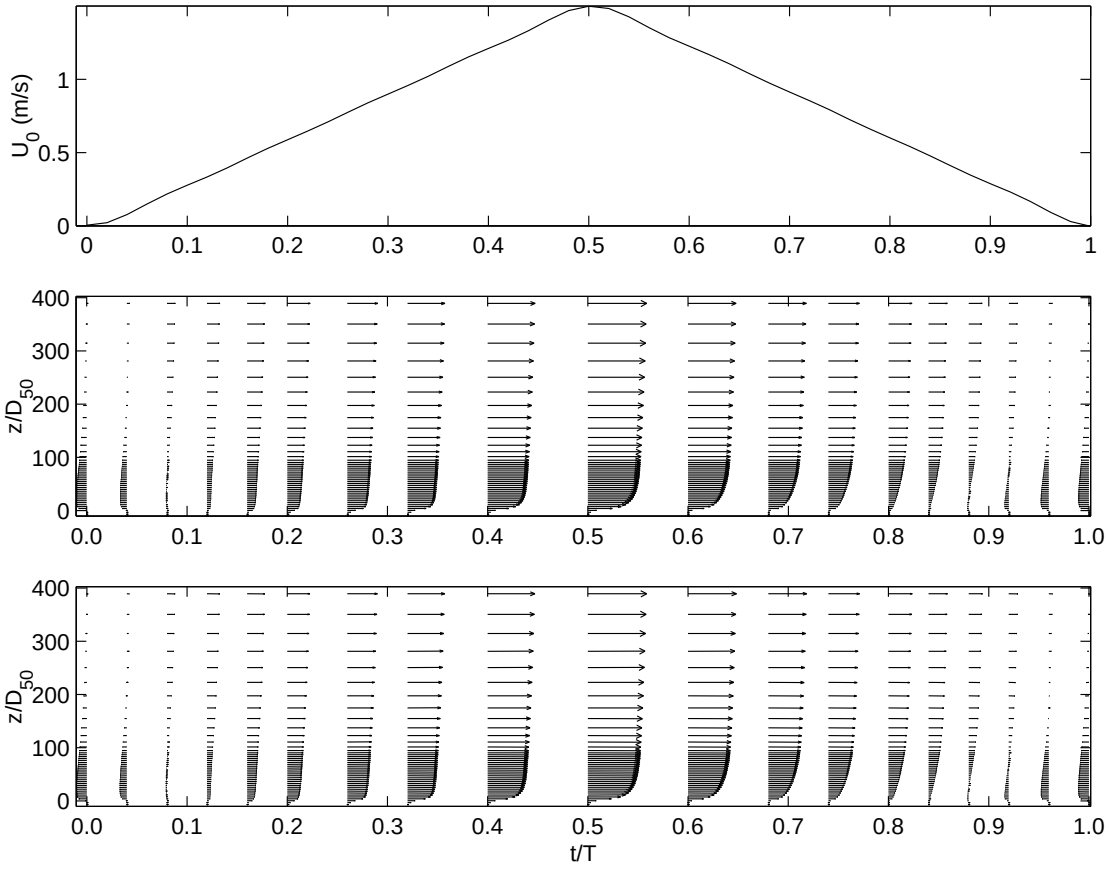

Figure 6.20: Free stream velocity (top), fluid velocity (middle) and sediment velocity (bottom) for the positive triangular flow.

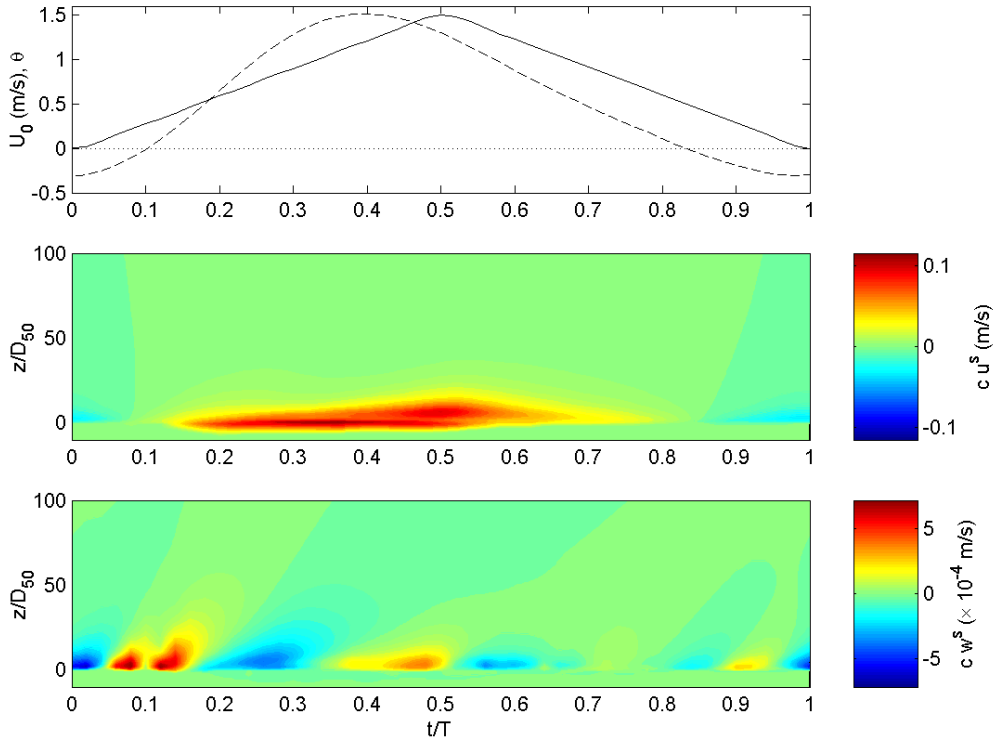

Figure 6.21: Free stream velocity (top), horizontal sediment flux $\bar{c}\tilde{u}_s$ (middle) and vertical sediment flux $\bar{c}\tilde{w}_s$ (bottom) for the positive triangular flow.

6.3.2 Sediment flux

Figure 6.21 presents the sediment flux in the near bed region. Again the top plot shows the time histories of the free stream velocity in the solid line and of the bed shear stress in the dashed line. The middle and bottom panels present respectively the horizontal and vertical sediment fluxes in non-dimensional elevation-time maps and the magnitude of the fluxes is color coded to the right of the panels. Similar to oscillatory flows, the vertical flux is much smaller than the horizontal flux.

Even though the free stream velocity is always positive, we do observe a negative horizontal flux at some instants, which is consistent with the near bed flow reversal observed in figure 6.20. The sign of the horizontal flux close to the bed again coincides with that of the bed shear stress, while the sediment flux tends to recover

a behavior similar to that of the free stream velocity (always positive) far away from the bed.

Again, the vertical sediment flux is more complex. For oscillatory cases, we argued that its evolution was related to the time derivative of the bed shear stress and to near bed flow reversals. In this case, a relationship between the vertical sediment flux and the bed shear stress derivative is far less obvious. Strong fluxes due to near-bed flow reversals could still be present but they are harder to distinguish than for oscillatory flows.

6.3.3 Sediment transport rate

Figure 6.22 presents the bed shear stress and the sediment transport rate. Similarly to figure 6.18, the top panel shows the free stream velocity during one period, while the middle and bottom panels show respectively the bed shear stress and the total sediment transport rate. In the bottom panel, the sediment transport rate predicted by a model that relates ψ to some power of the free stream velocity (*Bailard* (1981) here) is also plotted.

As expected from the near bed flow reversal observed previously, the bed shear stress has negative values during the cycle ($t/T < 0.1$ and $t/T > 0.83$) even though the free stream velocity remains positive at all times. We also observe that the shape of the bed shear stress is modified respect to that of the free stream velocity. In addition of not keeping a triangular time evolution, the maximum bed shear stress happens for $t/T \approx 0.4$ while the minimum remains close to $t/T = 0$. The bed shear stress is thus significantly skewed to the early phases.

Like the bed shear stress, the numerical sediment transport rate exhibits negative values during the cycle. This behavior is not predicted by models that relate the sediment transport rate to some power of the free stream velocity such as

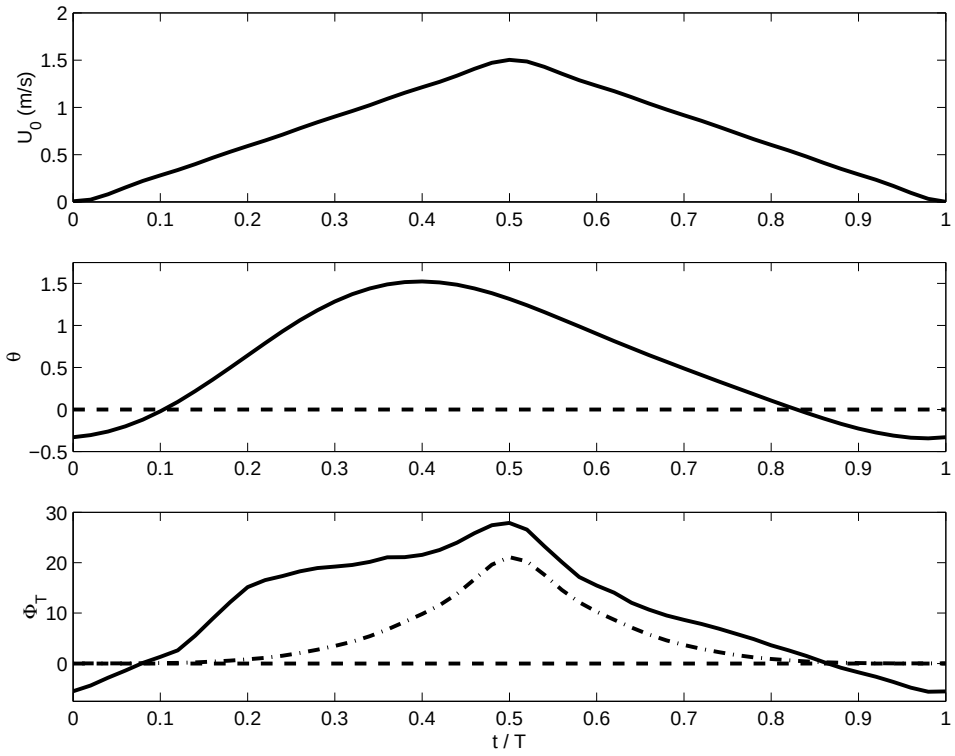

Figure 6.22: Free stream velocity (top), bed shear stress (middle) and total load sediment transport (bottom) for the triangular flow case. The numerical results are in the solid line, while the total sediment transport predicted by the *Bailard* (1981) model is in the dot-dashed line in the bottom panel.

Bailard (1981). Although negative transport rates could be predicted by models relating the sediment transport rate to the bed shear stress (provided that the bed shear stress is predicted adequately), we observe that the reversals for the bed shear stress and the sediment transport rate do not happen at the same instants. During the accelerating stage the sediment transport rate becomes positive before the bed shear stress and during the decelerating stage the sediment transport rate becomes negative after the bed shea stress. These observations lead to infer that we can not relate the total transport rate to some power of the bed shear stress and that the total transport rate is not constantly lagged respect to the bed shear stress. The sediment transport rate also exhibits a peak at $t/T = 0.5$. Such a peak can not be linked to the bed shear stress, but is probably related to the free stream velocity maximum. The fact that the transport rate predicted by *Bailard* (1981) has the same behavior at $t/T = 0.5$ is indeed a confirmation. It then seems like the sediment transport rate evolution during a period can be partly explained by a contribution that is related to the bed shear stress and a contribution related to the free stream velocity. This is not surprising considering that the total load is usually split into bed load (commonly considered to be related to the bed shear stress) and suspended load (that we can consider to be related to the free stream velocity).

6.4 Summary

We investigated in this chapter sediment transport under sheet flow condition using the model developed in chapters 3 and 5 and validated in chapter 5. Three different types of flows have been looked at: steady flows, oscillatory and wave-current boundary layers and a pulsating flow. The use of the model enabled us to observe all quantities relevant to the fluid flow, the fluid turbulence and the

sediment transport and to thus provide descriptions of the flow characteristics throughout the water column and in particular in the (very) near-bed region. Such a resolution of the near-bed region is quite important for two reasons. The first is that most of the transport happens close to the bed; the second is that this near-bed region has been lacking in experimental data until recently and the use of newer techniques such as CCM (e.g., *Ribberink and Al-Salem*, 1995) and boroscopes (*Dudley*, 2007). Even now, experimental data in the near-bed region provides information on few of the flow quantities (concentration, velocity, and sediment flux at best). In addition to a full description of the flow, this models also enables us to distinguish bed load from suspended load by determining the dominant suspension mechanism and thus to compute the bed load layer thickness. The result was found to be in good agreement with an earlier model for the bed load layer thickness. Finally, phase lags between sediment transport, bed shear stress and free stream velocity can be obtained for periodic flows.

We found that, as expected, for steady flows under sheet flow conditions the fluid phase velocity follows closely the law of wall in which the von Karman constant is reduced and the equivalent roughness is increased, compared to the clear fluid flow conditions. The fluid phase velocity both for the oscillatory boundary layers and the pulsating flow were also found to satisfy expectations based on the knowledge of clear fluid flows: for example, the phase lead of the near-bed velocity respect to the free stream velocity in oscillatory boundary layers and the presence of a near bed flow reversal for the particular pulsating flow considered. For the oscillatory boundary layers, the bed shear stress is about 20 degrees early respect to the free stream velocity. For the pulsating flow, the existence of flow reversal and of negative values of the bed shear stress provide a counter-example to the common approach that relates the bed shear stress to the free stream velocity

through a friction factor (equation 2.24).

An investigation of the fluid turbulence for oscillatory boundary layers lead us to conclude that further more dramatic improvements on the fluid turbulence modification could be achieved.

Numerical results for the sediment flux showed that the horizontal and the vertical sediment flux had different behaviors. The horizontal flux is in phase with the bed shear stress close to the bed, is delayed with increasing elevation until it is in phase with the free stream velocity far away from the bed and its magnitude seems to depend on the bed shear value. The vertical sediment flux seems to depend on the time derivative of the bed shear stress $d\theta(t)/dt$ rather than on $\theta(t)$ directly for wave-current boundary layers. Even though most applications seek to model the sediment transported (i. e. the integral of the horizontal sediment flux), results on and modeling of the vertical flux and transport can be useful. For example, dilute models depend on a sediment vertical flux bottom boundary condition (see chapter 4 and *Hsu and Liu* (2004)). We used in chapter 4 two different approaches to specify the vertical sediment flux, both of which expressed the upward sediment flux (pick-up) as a function of the Shields parameter. Even though the numerical results presented in this chapter pertain to the total vertical sediment flux and not just the upward part, they indicate that the vertical flux should be expressed as a function of the Shields parameter time derivative instead of the Shields parameter directly. Aside from implication on the amount of sediment suspended, this should have a clear repercussion on the phase of the numerical results, which was one of the main concern in chapter 4.

CHAPTER 7

TWO-DIMENSIONAL MODEL

In addition to studying sediment transport in one dimensional sheet flows, the model that we introduced in chapters 3 and 5 can also be used to address numerically sediment transport issues in multidimensional flows. We will focus here on two dimensional flows for which uniformity in the flow direction is not assumed (i.e. we do not enforce that $\partial/\partial x = 0$). This chapter will focus on the model formulation and the general numerical implementation. A summary of the two-phase model formulation in the two-dimensional case is first presented. In a way similar to the sheet flow model, the bed treatment is an important part of the numerical model and will then be discussed with the bottom boundary conditions. Finally, we will discuss in more details some numerical implementation issues of the two-dimensional model such as the spatial discretization, the cycle algorithm and the numerical stability.

7.1 Summary of the governing equations

We will here summarize the governing equations for the two-dimensional model in terms of Cartesian coordinates (x, z). The continuity equations for the fluid phase (equation 3.38) and the sediment phase (equation 3.39) can be respectively rewritten for two-dimensional flows as

$$\frac{\partial \rho^f (1-\bar{c})}{\partial t} + \frac{\partial \rho^f (1-\bar{c})\tilde{u}^f}{\partial x} + \frac{\partial \rho^f (1-\bar{c})\tilde{w}^f}{\partial z} = 0 \tag{7.1}$$

and

$$\frac{\partial \rho^s \bar{c}}{\partial t} + \frac{\partial \rho^s \bar{c}\tilde{u}^s}{\partial x} + \frac{\partial \rho^s \bar{c}\tilde{w}^s}{\partial z} = 0. \tag{7.2}$$

The momentum conservation yields two equations for each phase. For the fluid phase momentum conservation (equation 3.40), both the horizontal and vertical

momentum equations can be rewritten using the fluid phase continuity equation, and respectively lead to:

$$\begin{aligned}\frac{\partial \tilde{u}^f}{\partial t} &= -\tilde{u}^f\frac{\partial \tilde{u}^f}{\partial x} - \tilde{w}^f\frac{\partial \tilde{u}^f}{\partial z} - \frac{1}{\rho^f}\frac{\partial \bar{P}^f}{\partial x} - \frac{\beta}{\rho^f(1-\bar{c})}\bar{c}\tilde{u}^f + \frac{\beta}{\rho^f(1-\bar{c})}\bar{c}\tilde{u}^s \\ &\quad + \frac{\beta}{\rho^f(1-\bar{c})}\frac{\nu_T}{\sigma_c}\frac{\partial \bar{c}}{\partial x} + \frac{1}{\rho^f(1-\bar{c})}\left[\frac{\partial \tau^f_{xx}}{\partial x} + \frac{\partial \tau^f_{xz}}{\partial z}\right], \end{aligned} \tag{7.3}$$

and

$$\begin{aligned}\frac{\partial \tilde{w}^f}{\partial t} &= -\tilde{u}^f\frac{\partial \tilde{w}^f}{\partial x} - \tilde{w}^f\frac{\partial \tilde{w}^f}{\partial z} - g - \frac{1}{\rho^f}\frac{\partial \bar{P}^f}{\partial z} - \frac{\beta}{\rho^f(1-\bar{c})}\bar{c}\tilde{w}^f + \frac{\beta}{\rho^f(1-\bar{c})}\bar{c}\tilde{w}^s \\ &\quad + \frac{\beta}{\rho^f(1-\bar{c})}\frac{\nu_T}{\sigma_c}\frac{\partial \bar{c}}{\partial z} + \frac{1}{\rho^f(1-\bar{c})}\left[\frac{\partial \tau^f_{zx}}{\partial x} + \frac{\partial \tau^f_{zz}}{\partial z}\right]. \end{aligned} \tag{7.4}$$

For the sediment phase, the horizontal and vertical momentum equations are obtained from equation 3.41:

$$\begin{aligned}\frac{\partial \rho^s\bar{c}\tilde{u}^s}{\partial t} &= -\frac{\partial \rho^s\bar{c}\tilde{u}^s\tilde{u}^s}{\partial x} - \frac{\partial \rho^s\bar{c}\tilde{u}^s\tilde{w}^s}{\partial z} - \bar{c}\frac{\partial \bar{P}^f}{\partial x} + \beta\bar{c}\tilde{u}^f - \beta\bar{c}\tilde{u}^s \\ &\quad -\beta\frac{\nu_T}{\sigma_c}\frac{\partial \bar{c}}{\partial x} + \left[\frac{\partial \tau^s_{xx}}{\partial x} + \frac{\partial \tau^s_{xz}}{\partial z}\right] \end{aligned} \tag{7.5}$$

and

$$\begin{aligned}\frac{\partial \rho^s\bar{c}\tilde{w}^s}{\partial t} &= -\frac{\partial \rho^s\bar{c}\tilde{w}^s\tilde{u}^s}{\partial x} - \frac{\partial \rho^s\bar{c}\tilde{w}^s\tilde{w}^s}{\partial z} - \rho^s\bar{c}g - \bar{c}\frac{\partial \bar{P}^f}{\partial z} + \beta\bar{c}\tilde{w}^f - \beta\bar{c}\tilde{w}^s \\ &\quad -\beta\frac{\nu_T}{\sigma_c}\frac{\partial \bar{c}}{\partial z} + \left[\frac{\partial \tau^s_{zx}}{\partial x} + \frac{\partial \tau^s_{zz}}{\partial z}\right] \end{aligned} \tag{7.6}$$

In the fluid momentum equations, the fluid stresses are given by the turbulent viscosity hypothesis (equation 3.44):

$$\tau^f_{xx} = 2\rho^f\left(\nu_T + \nu\right)\left[\frac{2}{3}\frac{\partial \tilde{u}^f}{\partial x} - \frac{1}{3}\frac{\partial \tilde{w}^f}{\partial z}\right] - \frac{2}{3}\rho^f(1-\bar{c})k_f \tag{7.7}$$

$$\tau^f_{zz} = 2\rho^f\left(\nu_T + \nu\right)\left[\frac{2}{3}\frac{\partial \tilde{w}^f}{\partial z} - \frac{1}{3}\frac{\partial \tilde{u}^f}{\partial x}\right] - \frac{2}{3}\rho^f(1-\bar{c})k_f \tag{7.8}$$

$$\tau^f_{xz} = \tau^f_{zx} = \rho^f\left(\nu_T + \nu\right)\left(\frac{\partial \tilde{u}^f}{\partial z} + \frac{\partial \tilde{w}^f}{\partial x}\right). \tag{7.9}$$

The turbulent kinetic energy k_f and the turbulent eddy viscosity ν_T are in turn found by the $k-\varepsilon$ fluid turbulence model, which introduces balance equations

for both the turbulent kinetic energy (equation 3.48) and turbulence dissipation (equation 3.49). Using again the fluid phase continuity, these equations can be rewritten for two-dimensional flows as

$$\begin{aligned}
\frac{\partial k_f}{\partial t} &= -\tilde{u}^f\frac{\partial k_f}{\partial x} - \tilde{w}^f\frac{\partial k_f}{\partial z} + \frac{\mathcal{P}^f}{\rho^f(1-\bar{c})} - \varepsilon_f \\
&+\frac{1}{\rho^f(1-\bar{c})}\frac{\partial}{\partial x}\left[\left(\nu + \frac{\nu_T}{\sigma_k}\right)\frac{\partial \rho^f(1-\bar{c})k_f}{\partial x}\right] \\
&+\frac{1}{\rho^f(1-\bar{c})}\frac{\partial}{\partial z}\left[\left(\nu + \frac{\nu_T}{\sigma_k}\right)\frac{\partial \rho^f(1-\bar{c})k_f}{\partial z}\right] \\
&+\frac{\beta}{\rho^f(1-\bar{c})}\frac{\nu_T}{\sigma_c}\left[\frac{\partial \bar{c}}{\partial x}\left(\tilde{u}^f - \tilde{u}^s\right) + \frac{\partial \bar{c}}{\partial z}\left(\tilde{w}^f - \tilde{w}^s\right)\right] \\
&-2\frac{\beta}{\rho^f(1-\bar{c})}(1-\alpha)\bar{c}k_f
\end{aligned} \tag{7.10}$$

for the turbulent kinetic energy, and

$$\begin{aligned}
\frac{\partial \varepsilon_f}{\partial t} &= -\tilde{u}^f\frac{\partial \varepsilon_f}{\partial x} - \tilde{w}^f\frac{\partial \varepsilon_f}{\partial z} + C_{\varepsilon 1}\frac{\varepsilon_f}{k_f}\frac{\mathcal{P}^f}{\rho^f(1-\bar{c})} - C_{\varepsilon 2}\frac{\varepsilon_f}{k_f}\varepsilon_f \\
&+\frac{1}{\rho^f(1-\bar{c})}\frac{\partial}{\partial x}\left[\left(\nu + \frac{\nu_T}{\sigma_\varepsilon}\right)\frac{\partial \rho^f(1-\bar{c})\varepsilon_f}{\partial x}\right] \\
&+\frac{1}{\rho^f(1-\bar{c})}\frac{\partial}{\partial z}\left[\left(\nu + \frac{\nu_T}{\sigma_\varepsilon}\right)\frac{\partial \rho^f(1-\bar{c})\varepsilon_f}{\partial z}\right] \\
&+C_{\varepsilon 3}\frac{\varepsilon_f}{k_f}\frac{\beta}{\rho^f(1-\bar{c})}\frac{\nu_T}{\sigma_c}\left[\frac{\partial \bar{c}}{\partial x}\left(\tilde{u}^f - \tilde{u}^s\right) + \frac{\partial \bar{c}}{\partial z}\left(\tilde{w}^f - \tilde{w}^s\right)\right] \\
&-2C_{\varepsilon 3}\frac{\varepsilon_f}{k_f}\frac{\beta}{\rho^f(1-\bar{c})}(1-\alpha)\bar{c}k_f
\end{aligned} \tag{7.11}$$

for the turbulence dissipation.

In the sediment momentum equations, the sediment stresses are given by (see

section 3.5.2):

$$\begin{aligned}
\tau_{xx}^s &= -p_c + \omega\left(\frac{\partial \tilde{u}^s}{\partial x} + \frac{\partial \tilde{w}^s}{\partial z}\right) - \frac{2}{3}\rho^s \bar{c} k_s \\
&\quad +2\mu_c\left(\frac{2}{3}\frac{\partial \tilde{u}^s}{\partial x} - \frac{1}{3}\frac{\partial \tilde{w}^s}{\partial z}\right) + \tau_{xx}^{se} \qquad (7.12)\\
\tau_{zz}^s &= -p_c + \omega\left(\frac{\partial \tilde{u}^s}{\partial x} + \frac{\partial \tilde{w}^s}{\partial z}\right) - \frac{2}{3}\rho^s \bar{c} k_s \\
&\quad +2\mu_c\left(\frac{2}{3}\frac{\partial \tilde{w}^s}{\partial z} - \frac{1}{3}\frac{\partial \tilde{u}^s}{\partial x}\right) + \tau_{zz}^{se} \qquad (7.13)\\
\tau_{xz}^s &= \tau_{zx}^s = \mu_c\left(\frac{\partial \tilde{u}^s}{\partial z} + \frac{\partial \tilde{w}^s}{\partial x}\right) \qquad (7.14)
\end{aligned}$$

where the collisional pressure p_c, the bulk viscosity ω, and the shear viscosity μ_c are explicitly introduced in section 3.5.2. A balance equation for the sediment phase fluctuation energy k_s is also introduced (equation 3.56) and can be rewritten for two-dimensional flows:

$$\frac{\partial \rho^s \bar{c} k^s}{\partial t} + \frac{\partial \rho^s \bar{c} k^s \tilde{u}^s}{\partial x} + \frac{\partial \rho^s \bar{c} k^s \tilde{w}^s}{\partial z} = \mathcal{P}^s + \frac{\partial \mathcal{Q}_x}{\partial x} + \frac{\partial \mathcal{Q}_z}{\partial z} - \gamma + 2\beta\bar{c}\left(\alpha k_f - k_s\right). \quad (7.15)$$

In both sediment and fluid energy equations as well as in the ε_f equation, the stress production term is expressed as the sum of the products of the stress by the velocity gradients:

$$\begin{aligned}
\mathcal{P}^f &= \tau_{xx}^f \frac{\partial \tilde{u}^f}{\partial x} + \tau_{zz}^f \frac{\partial \tilde{w}^f}{\partial z} + \tau_{xz}^f \frac{\partial \tilde{u}^f}{\partial z} + \tau_{zx}^f \frac{\partial \tilde{w}^f}{\partial x} \qquad (7.16)\\
\mathcal{P}^s &= \tau_{xx}^s \frac{\partial \tilde{u}^s}{\partial x} + \tau_{zz}^s \frac{\partial \tilde{w}^s}{\partial z} + \tau_{xz}^s \frac{\partial \tilde{u}^s}{\partial z} + \tau_{zx}^s \frac{\partial \tilde{w}^s}{\partial x} \qquad (7.17)
\end{aligned}$$

7.2 Bed treatment and bottom boundary conditions

To the contrary of the dilute sediment transport model (chapter 4) in which the numerical domain is such that the bottom boundary is above the real sediment bed (see figure 4.1), the numerical domain in both the one dimensional sheet flow model and the present two-dimensional model is such that the bottom boundary is located

within the sediment bed. The two-phase flow within the porous sediment bed is thus calculated. In the sediment bed, both the sediment velocity and the sediment fluctuation energy vanish, leading to $\tilde{u}^s = 0$, $\tilde{w}^s = 0$ and $k_s = 0$. Similarly to the one-dimensional model, numerical bottom boundary conditions are unnecessary for the sediment phase and not important for the fluid phase (see appendix B).

Since sediment particles can be eroded or deposited, the location of the interface between the stationary bed and the region where particles move changes and needs to be calculated by the model. Several approaches have been used to determine the location of such an interface. For example, the interface can be determined to be the location for which the concentration equals a certain arbitrary value (e.g., *Zhao and Fernando*, 2007). In our model, the interface is determined as the location for which the sediment bed can first be sheared. To that end, we follow *Hanes and Inman* (1985a) and *Hanes and Inman* (1985b) and use a Coulomb failure criterion to calculate the failure concentration (concentration at which the sediment bed can first be sheared). Then, the interface location is determined as the location for which the concentration equals the failure concentration.

The Coulomb yield criterion (e.g., *Hanes and Inman*, 1985a,b) relates the normal and tangential components of the sediment stress at the boundary between immobile and mobile sediment particles:

$$\tau_t^s = \tau_n^s \tan\psi \tag{7.18}$$

where ψ is the friction angle of the sediment, τ_t^s the tangential stress (shear stress) and τ_n^s the normal stress. In the one-dimensional case, the tangential and normal directions are respectively x and z, thus leading to:

$$\tau_{xz}^s = \tau_{zz}^s \tan\psi \tag{7.19}$$

In the two-dimensional case, the bed is not necessarily horizontal and locally has an angle α_{bed} with the horizontal direction (see figure 7.1). The tangential and

normal directions are then not x and z, and τ_t^s and τ_n^s need to be expressed in function of τ_{xx}^s, τ_{zz}^s and τ_{xz}^s. The stress force dF on a surface dS is such that $dF_j = \tau_{ij} n_i dS$ where n is the normal to the surface. τ_t^s and τ_n^s can then be seen as the elemental forces tangential and normal to an elemental surface of the bed. Using the same stress tensor force relationship, the two components of the stress force in the cartesian coordinate system (x, z) are

$$dF_x = \left(\tau_{zx}^s \cos\alpha_{bed} - \tau_{xx}^s \sin\alpha_{bed}\right) dS \tag{7.20}$$

and

$$dF_z = \left(\tau_{zz}^s \cos\alpha_{bed} - \tau_{xz}^s \sin\alpha_{bed}\right) dS. \tag{7.21}$$

Finally, projecting on the directions normal and tangential to the bed, and using that the stress tensor is symmetric we obtain that

$$\tau_t^s = \left(\cos^2\alpha_{bed} - \sin^2\alpha_{bed}\right) \tau_{zx}^s + \sin\alpha_{bed}\cos\alpha_{bed}\left(\tau_{zz}^s - \tau_{xx}^s\right) \tag{7.22}$$

and

$$\tau_n^s = \sin^2\alpha_{bed}\tau_{xx}^s + \cos^2\alpha_{bed}\tau_{zz}^s - 2\sin\alpha_{bed}\cos\alpha_{bed}\tau_{zx}^s \tag{7.23}$$

7.3 Spatial discretization

7.3.1 Computational domain

The governing equations summarized previously are solved using a finite difference method. The computational domain is discretized into rectangular cells (see figure 7.1), and ghost cells are added to treat the boundary conditions. The flow variables are defined following a staggered approach, meaning that

- All scalar quantities (e.g., $\bar{c}$, k_f, $\bar{P}_f$ ...) are defined at the cell center (the dot in figure 7.1).

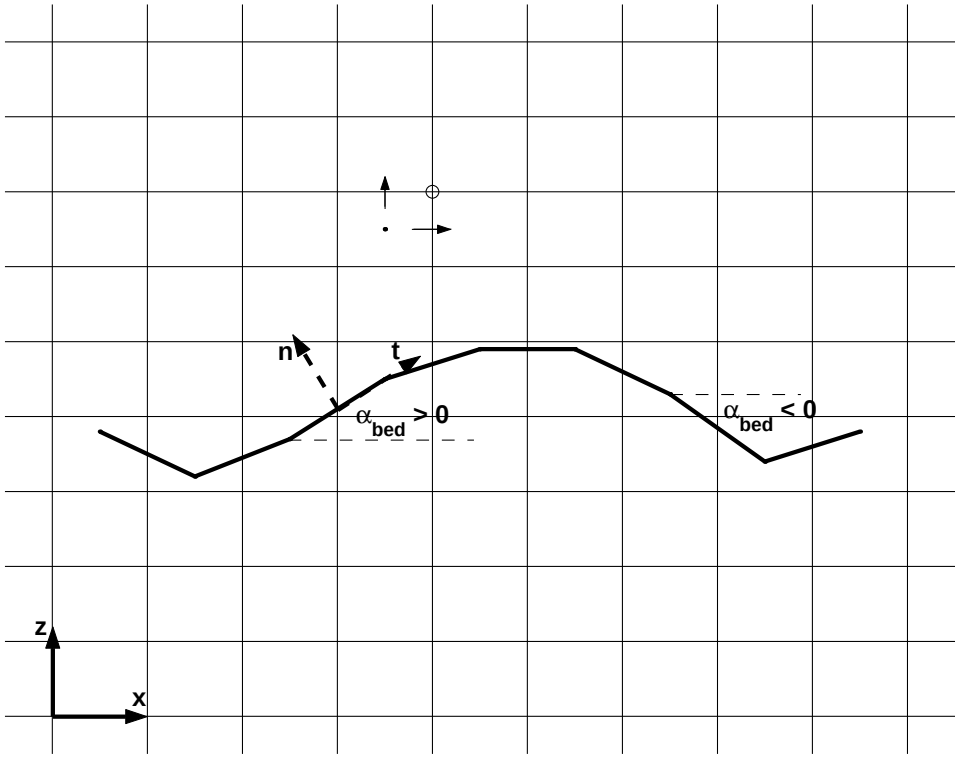

Figure 7.1: Grid for the two-dimensional problem. The bed discretization is represented in the bold solid line, as well as the local angle with the horizontal axis (α_{bed}) and the tangential and normal directions to the bed "surface" in dashed arrows. Also, the staggered approach is illustrated for one cell (above the bed) by the dot (cell center), the two arrows at the cell faces and the circle at the top-right corner of the cell.

- The horizontal velocities and fluxes are defined at the right face of the cell (horizontal arrow in figure 7.1).
- The vertical velocities and fluxes are defined at the top face of the cell (vertical arrow in figure 7.1).
- The normal fluid and sediment stresses are defined at the cell center (again the dot in figure 7.1).
- The shear stresses for both phases are defined at the top-right corner of the cell (the circle in figure 7.1).

Using a staggered grid approach simplifies the discretization of many terms in the governing equations. In particular, velocity/fluxes gradients at the cell center

and the gradients of scalar quantities at the cell faces are easily obtained using this representation. Values for the scalar quantities will need to be computed at cell faces. Several techniques are available and, in general and unless otherwise specified, we will use:

$$\chi_{i^+,j} = \frac{\Delta x_i \chi_{i+1,j} + \Delta x_{i+1} \chi_{i,j}}{\Delta x_i + \Delta x_{i+1}} \tag{7.24}$$

where χ represents any given scalar quantity and i^+ corresponds to the right face of the cell (i, j). Similarly i^-, j^+, j^- will correspond respectively to the left, top and bottom faces of the cell and the value of any given scalar χ there can be found by equations similar to 7.24.

7.3.2 Sediment energy equation

The balance equation for the sediment phase energy (equation 7.15) requires that all of its terms are defined at the cell center. The dissipative and interaction terms are functions of scalars and/or velocity gradients and are therefore easily estimated at the cell center. The other terms require further discussion.

The production term is discretized as follows:

$$\begin{aligned} \mathcal{P}^s)_{i,j} &= \tau^s_{xx} \frac{\partial \tilde{u}^s}{\partial x}\Big)_{i,j} + \tau^s_{zz} \frac{\partial \tilde{w}^s}{\partial z}\Big)_{i,j} \\ &\quad + \frac{1}{4}\left[SP_s)_{i^+,j^+} + SP_s)_{i^-,j^+} + SP_s)_{i^+,j^-} + SP_s)_{i^-,j^-} \right] \end{aligned} \tag{7.25}$$

where

$$SP_s = \tau^s_{xz} \frac{\partial \tilde{u}^s}{\partial z} + \tau^s_{zx} \frac{\partial \tilde{w}^s}{\partial x}. \tag{7.26}$$

The sediment energy transport term is discretized as follows:

$$\begin{aligned} \frac{\partial Q_x}{\partial x}\Big)_{i,j} + \frac{\partial Q_z}{\partial z}\Big)_{i,j} &= \frac{2}{3} \frac{\kappa_{i^+,j} \frac{\partial k_s}{\partial x}\Big)_{i^+,j} - \kappa_{i^-,j} \frac{\partial k_s}{\partial x}\Big)_{i^-,j}}{\Delta x_i} \\ &\quad + \frac{2}{3} \frac{\kappa_{i,j^+} \frac{\partial k_s}{\partial z}\Big)_{i,j^+} - \kappa_{i,j^-} \frac{\partial k_s}{\partial z}\Big)_{i,j^-}}{\Delta z_j} \end{aligned} \tag{7.27}$$

where

$$\frac{\partial k_s}{\partial x}\Big)_{i^+,j} = \frac{k_s)_{i^+,j} - k_s)_{i,j}}{\frac{1}{2}\left(\Delta x_{i+1} + \Delta x_i\right)}. \tag{7.28}$$

The horizontal convective term is estimated using

$$\frac{\partial \rho^s K^s \tilde{u}^s}{\partial x}\Big)_{i,j} = \rho^s \frac{K^s)_{i^+,j}\,\tilde{u}^s)_{i^+,j} - K^s)_{i^-,j}\,\tilde{u}^s)_{i^-,j}}{\Delta x_i} \tag{7.29}$$

where

$$K^s)_{i^+,j} = \frac{1}{2}\left[1 + \xi \mathrm{sgn}\left(\tilde{u}^s)_{i^+,j}\right)\right] K^s)_{i,j} + \frac{1}{2}\left[1 - \xi \mathrm{sgn}\left(\tilde{u}^s)_{i^+,j}\right)\right] K^s)_{i+1,j} \tag{7.30}$$

while the vertical convective term is computed using similar equations for vertical fluxes and velocities.

7.3.3 Sediment momentum equations

The sediment momentum equations necessitate to calculate the different terms at the right face of the cell for the horizontal momentum and at the top face for the vertical momentum. We will only present the equations describing the work done for the right face. The equations for the top face are similar and can be easily derived.

The convective term for the horizontal momentum is discretized following equations 7.31 and 7.34.

$$\frac{\partial \rho^s U^s \tilde{u}^s}{\partial x}\Big)_{i^+,j} = 2\frac{U^s)_{i+1,j}\,\tilde{u}^s)_{i+1,j} - U^s)_{i,j}\,\tilde{u}^s)_{i,j}}{\Delta x_i + \Delta x_{i+1}} \tag{7.31}$$

where

$$U^s)_{i+1,j} = \frac{1}{2}\left[1 + \xi \mathrm{sgn}\left(\tilde{u}^s)_{i+1,j}\right)\right] U^s)_{i^+,j} + \frac{1}{2}\left[1 - \xi \mathrm{sgn}\left(\tilde{u}^s)_{i+1,j}\right)\right] U^s)_{(i+1)^+,j} \tag{7.32}$$

and

$$\tilde{u}^s)_{i,j} = \frac{1}{2}\left(\tilde{u}^s)_{i^+,j} + \tilde{u}^s)_{i^-,j}\right). \tag{7.33}$$

$$\left.\frac{\partial \rho^s U^s \tilde{w}^s}{\partial z}\right)_{i^+,j} = 2\frac{U^s)_{i^+,j^+}\,\tilde{w}^s)_{i^+,j^+} - U^s)_{i^+,j^-}\,\tilde{w}^s)_{i^+,j^-}}{\Delta z_j} \tag{7.34}$$

where

$$U^s)_{i^+,j^+} = \frac{1}{2}\left[1+\xi \mathrm{sgn}\left(\tilde{w}^s)_{i^+,j^+}\right)\right] U^s)_{i^+,j} + \frac{1}{2}\left[1-\xi \mathrm{sgn}\left(\tilde{w}^s)_{i^+,j^+}\right)\right] U^s)_{(i^+)^+,j+1} \tag{7.35}$$

and

$$\tilde{w}^s)_{i^+,j^+} = \frac{\Delta x_i\,\tilde{w}^s)_{i+1,j^+} + \Delta x_{i+1}\,\tilde{w}^s)_{i,j^+}}{\Delta x_i + \Delta x_{i+1}} \tag{7.36}$$

Most of the other terms are discretized trivially from the staggered grid approach. However, the concentration in the interaction term is not calculated using equation 7.24 but rather using:

$$\bar{c}_{i^+,j} = \frac{1}{2}\left[1+\xi \mathrm{sgn}\left(\tilde{u}^s_{i^+,j}\right)\right]\bar{c}_{i,j} + \frac{1}{2}\left[1-\xi \mathrm{sgn}\left(\tilde{u}^s_{i^+,j}\right)\right]\bar{c}_{i+1,j} \tag{7.37}$$

7.4 Computational cycle algorithm

A modified version of the two-step projection method is implemented here to solve "simultaneously" all the governing equations. At the beginning of the cycle, the time step is adjusted dynamically following stability criterions discussed later. The sediment phase equations are solved using a predictor-corrector scheme which has been described in more details in appendix B and in *Hsu* (2002). The fluid phase velocities and the fluid pressure are then solved using the two-step projection method (*Chorin*, 1968). In this method, the fluid continuity is not solved per se, but is used to simplify the momentum equations and to derive an equation for the fluid pressure. In the first step of the two-step projection method, an intermediate velocity $\hat{u}_i^f$ with the correct vorticity is introduced. This intermediate velocity is

found at cycle $(n+1)$ following:

$$\begin{aligned}\frac{\hat{u}_i^{f(n+1)} - u_i^{f(n)}}{\Delta t} + \left(\frac{\beta}{\rho^f(1-c)}\hat{u}_i^f\right)^{(n+1)} &= -\left(u_j^f \frac{\partial u_i^f}{\partial x_j}\right)^{(n)} + \left(\frac{\beta}{\rho^f(1-c)} c u_i^s\right)^{(n)} \\ &\quad + g_i + \left(\frac{\beta}{\rho^f(1-c)}\frac{\nu_T}{\sigma_c}\frac{\partial c}{\partial x_i}\right)^{(n)} \\ &\quad + \left(\frac{1}{\rho^f(1-c)}\frac{\partial \tau_{ij}^f}{\partial x_j}\right)^{(n)} \end{aligned} \tag{7.38}$$

In the second step of the two-step projection method, the pressure is calculated by solving the Poisson Pressure Equation and modifying accordingly the intermediate velocity field to obtain the final velocity.

$$\rho^f \frac{u_i^{f(n+1)} - \hat{u}_i^{f(n+1)}}{\Delta t} = -\frac{\partial P^{f(n+1)}}{\partial x_i} \tag{7.39}$$

The Pressure Poisson Equation is obtained by taking the divergence of equation 7.39 multiplied by $(1-c)$ and applying the fluid phase continuity to the result:

$$\frac{\partial}{\partial x_i}\left[(1-c)^{(n+1)}\frac{\partial P^{f(n+1)}}{\partial x_i}\right] = \frac{\rho^f}{\Delta t}\left[\frac{\partial(1-c)}{\partial t} + \frac{\partial}{\partial x_i}\left((1-c)\hat{u}_i^f\right)^{(n+1)}\right] \tag{7.40}$$

Last, the fluid turbulence equations are solved at the end of the computational cycle. The most "up-to-date" values are used in most terms to the exception of the production of turbulent kinetic energy, the destruction of dissipation and the terms arising from the interphase interaction. In details, the turbulent dissipation

rate at cycle (n+1) is found by the following equation:

$$\begin{aligned}
\frac{\varepsilon_f^{(n+1)}-\varepsilon_f^{(n)}}{\Delta t} &= -\tilde{u}^{f(n+1)}\frac{\partial \varepsilon_f}{\partial x}^{(n)} - \tilde{w}^{f(n+1)}\frac{\partial \varepsilon_f}{\partial z}^{(n)} \\
&+C_{\varepsilon 1}\frac{\varepsilon_f^{(n)}}{k_f^{(n)}}\frac{\mathcal{P}^{f(n+1)}}{\rho^f(1-\bar{c}^{(n+1)})} - C_{\varepsilon 2}\frac{\varepsilon_f^{(n)}}{k_f^{(n)}}\varepsilon_f^{(n+1)} \\
&+\frac{1}{\rho^f(1-\bar{c}^{(n+1)})}\frac{\partial}{\partial x}\left[\left(\nu+\frac{\nu_T^{(n)}}{\sigma_\varepsilon}\right)\frac{\partial \rho^f(1-\bar{c}^{(n+1)})\varepsilon_f^{(n)}}{\partial x}\right] \\
&+\frac{1}{\rho^f(1-\bar{c}^{(n+1)})}\frac{\partial}{\partial z}\left[\left(\nu+\frac{\nu_T^{(n)}}{\sigma_\varepsilon}\right)\frac{\partial \rho^f(1-\bar{c}^{(n+1)})\varepsilon_f^{(n)}}{\partial z}\right] \\
&+\frac{C_{\varepsilon 3}}{\sigma_c}\frac{\varepsilon_f^{(n+1)}}{k_f^{(n)}}\frac{\beta^{(n+1)}\nu_T^{(n)}}{\rho^f(1-\bar{c}^{(n+1)})}\left[\frac{\partial \bar{c}}{\partial x}\left(\tilde{u}^f-\tilde{u}^s\right)+\frac{\partial \bar{c}}{\partial z}\left(\tilde{w}^f-\tilde{w}^s\right)\right]^{(n+1)} \\
&-2C_{\varepsilon 3}\frac{\varepsilon_f^{(n+1)}}{k_f^{(n)}}\frac{\beta^{(n+1)}}{\rho^f(1-\bar{c}^{(n+1)})}(1-\alpha)\bar{c}^{(n+1)}k_f^{(n)} \qquad (7.41)
\end{aligned}$$

and the turbulent kinetic energy by the following

$$\begin{aligned}
\frac{k_f^{(n+1)}-k_f^{(n)}}{\Delta t} &= -\tilde{u}^{f(n+1)}\frac{\partial k_f}{\partial x}^{(n)} - \tilde{w}^{f(n+1)}\frac{\partial k_f}{\partial z}^{(n)} \\
&+\frac{1}{2}\left(\frac{\mathcal{P}^{f(n+1)}+\mathcal{P}^{f(n)}}{\rho^f(1-\bar{c}^{(n+1)})} - \varepsilon_f^{(n+1)} - \varepsilon_f^{(n)}\right) \\
&+\frac{1}{\rho^f(1-\bar{c}^{(n+1)})}\frac{\partial}{\partial x}\left[\left(\nu+\frac{\nu_T^{(n)}}{\sigma_k}\right)\frac{\partial \rho^f(1-\bar{c}^{(n+1)})k_f^{(n)}}{\partial x}\right] \\
&+\frac{1}{\rho^f(1-\bar{c}^{(n+1)})}\frac{\partial}{\partial z}\left[\left(\nu+\frac{\nu_T^{(n)}}{\sigma_k}\right)\frac{\partial \rho^f(1-\bar{c}^{(n+1)})k_f^{(n)}}{\partial z}\right] \\
&+\frac{\beta^{(n+1)}}{\rho^f(1-\bar{c}^{(n+1)})}\frac{\nu_T^{(n)}}{\sigma_c}\left[\frac{\partial \bar{c}}{\partial x}\left(\tilde{u}^f-\tilde{u}^s\right)+\frac{\partial \bar{c}}{\partial z}\left(\tilde{w}^f-\tilde{w}^s\right)\right]^{(n+1)} \\
&-2\frac{\beta^{(n+1)}}{\rho^f(1-\bar{c}^{(n+1)})}(1-\alpha)\bar{c}k_f^{(n+1)} \qquad (7.42)
\end{aligned}$$

7.5 Numerical stability

As mentioned previously, the time step is adjusted dynamically for each cycle. The convective terms in both momentum equations lead to the Courant condition:

$$\Delta t \leq \min\left\{\frac{0.3\Delta x}{\max\left(|u^f|,|u^s|\right)}, \frac{0.3\Delta z}{\max\left(|w^f|,|w^s|\right)}\right\} \qquad (7.43)$$

The diffusion term for both phases lead to the following condition:

$$\Delta t \leq \min \left\{ \frac{1}{2 \max \left(\nu + \nu_T, \mu_c / \rho^s \right)} \frac{(\Delta x)^2 (\Delta z)^2}{(\Delta x)^2 + (\Delta z)^2} \right\}, \tag{7.44}$$

where ν and ν_T are respectively the viscous and turbulent eddy kinematic viscosity of the carrier fluid, ρ_s is the sediment mass density and μ_c the dynamic collisional viscosity for the sediment phase. The phase interaction term also leads to a constraint on the time step value (*Hsu*, 2002):

$$\Delta t \leq 0.1 \frac{T_p}{s}, \tag{7.45}$$

where s is the specific gravity of the sediment and T_p is the particle response time which is a measure of the time needed to accelerate a particle from rest to the velocity of the ambient fluid. For each cycle, the time step is determined by the minimum value found by the three previous conditions. However, such a value can still be too large to avoid negative concentration or negative sediment energy. In this case, the cycle is repeated with a smaller time step (80% of the previous value).

CHAPTER 8

SCOUR DOWNSTREAM OF STRUCTURES

As mentioned in the previous chapter, the sediment transport model that is introduced in chapters 3 and 5 can be used to study more diverse problems than just sediment transport under sheet flow conditions and a numerical model valid in two full dimensions has been introduced in the previous chapter. Once again the use of such a model is restricted by the validity of the assumptions used. Such a discussion was made at the start of chapter 6. The only difference for the two-dimensional model consists in the lack of one-dimensionality. However, the other assumptions and their related constraints remain: the particles still need to interact between each other in a collisional regime and collisions still need to be numerous enough for the collisional regime to be described statistically. Also in the same way that the one-dimensional version, the two-dimensional sediment transport is still not able to accurately describe the sediment motion initiation.

In spite of the different restrictions, there are many sediment transport problems that can be resolved by the model presented in the previous chapter. In particular, two-dimensional scouring presents a two-dimensional sediment transport case for which the main assumptions can be satisfied. In order to allow more diverse scouring problems the presence of obstacles is implemented in the sediment transport model. Obstacles are treated using a partial cell treatment similar to that of the wave hydrodynamics model called COBRAS (*Lin and Liu*, 1998a,b). Other problems that do not involve the three way interaction among fluid flow, sediment transport and structures (i.e. scour) can also be investigated.

One of the major recurring issue for two-dimensional sediment transport numerical simulations is the computational cost of the simulation. The model presented in chapters 3 and 7 requires that the different "layers" such as the enduring contact

region, the collisional region (see figure 3.1) are well resolved numerically, which determines the vertical size of the grid (Δz) used to discretize the numerical domain. In turn, the aspect ratio of the cells has to be limited and thus restricts the horizontal size of the grid (Δx). Unfortunately, many two-dimensional sediment transport problems (to the exception of scour) presents characteristic length scales that are much bigger in the horizontal direction than in the vertical direction, and would then require computational domains with an unrealistic number of cells. In addition to such a physical space restriction, some two dimensional problems have a characteristic time scale that would require an unrealistic number of time steps, the size of which is adjusted dynamically (see chapter 7).

We study in this chapter scouring processes downstream of structures, which are both two-dimensional and time dependent. Since many structures interacting with sediment are designed with a protection in the form of an apron, such an issue can be viewed as studying scour downstream of an apron, or, in other words, scour after a backward facing step. This problem was chosen following the usual habit of using the flow over a backward-facing step as a benchmark test of turbulence modeling. We will first present a brief summary of the process and of relevant experimental work and findings. We will then specify the numerical setup used to perform the scouring simulations and discuss the influence of the initial condition and downstream boundary condition. Finally, we will present the numerical results for one particular example and discuss the influence of the upstream flow conditions.

8.1 A brief overview

Scour is a natural phenomenon that is the result of the interaction of structures (usually man made) with fluid flows and with erodable beds. It is of particular importance because of the possible damage incurring to the structure. Several experiments on scouring downstream of structures were undertaken in the 60s

(e.g., *Breusers*, 1966, 1967; *Dietz*, 1969) and were summarized in *Breusers and Raudkivi* (1991). More recent studies on the subject include work by *Buchko et al.* (1987), *Hoffmans and Booij* (1993) and *Hoffmans and Pilarczyk* (1995). The scour process downstream of structures has commonly been divided in four stages (e.g., *Hoffmans and Pilarczyk*, 1995): an initiation stage, a development stage, a stabilization stage and the equilibrium stage. During the initiation stage, the flow in the scour hole is nearly uniform and erosion is at its most intense. During the development stage, the scour depth increases considerably while the shape of the scour hole remains the same. During the stabilization stage, the scour depth increases less rapidly and the scour hole increases more in the streamwise direction than in the vertical direction. In the equilibrium stage, the dimensions of the scour hole no longer evolve significantly. However, assuming that the solution far downstream should be given by the steady solution of the one-dimensional model, a mass balance argument between the apron ($x = 0$) and a location far downstream will yield that there is always an imbalance between the sediment flux in (at $x = 0$, $Q_T = 0$) and the sediment flux out (far downstream $Q_T \neq 0$). It logically follows that the bathymetry can then not reach a steady state.

Most of the early experiments (e.g., *Breusers*, 1966, 1967; *Dietz*, 1969) pertained to the development stage, even though *Dietz* (1969) did observe a tendency towards equilibrium in some cases. These experiments generally show that the shape of the scour hole is almost independent of the flow velocity and the bed grain size if the flow velocity is large relative to the critical velocity for incipient motion (similar to $\theta >> \theta_c$). For a given flow geometry (see sketch in figure 8.1), the similarity of the scour hole is then expressed by

$$\frac{z_s(x,t)}{h_0} = f\left(\frac{t}{T_s}, \frac{x}{h_0}\right) \tag{8.1}$$

where $z_s(x,t)$ is the depth of the scour hole, h_0 the water depth at the end of the

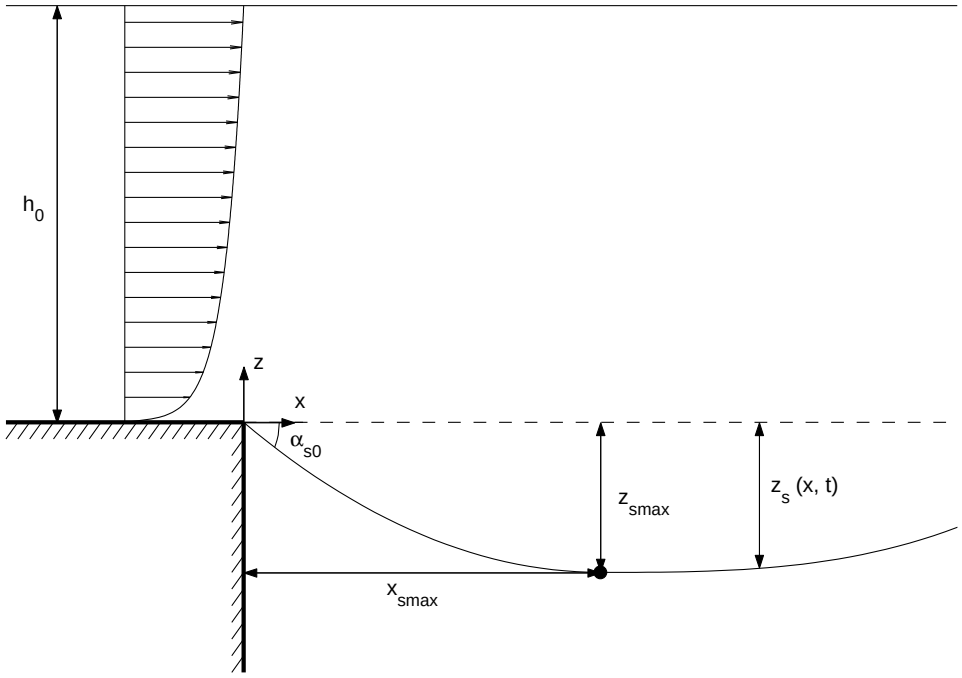

Figure 8.1: Sketch of scour downstream of an apron.

bottom protection, and T_s is the time at which $z_{smax} = h_0$. The time evolution of the maximum scour depth was found to be (*Breusers*, 1967)

$$\frac{z_{smax}}{h_0} = \left(\frac{t}{T_s}\right)^{n_s} \tag{8.2}$$

where $n_s = 0.38$. The time T_s was expressed as a function of the sediment specific gravity, the flow geometry, the upstream flow velocity and the critical velocity for incipient motion.

The slope of the initial part of the scour hole (α_{s0}, and later referred to as the upstream scour slope) was also observed and reported for various flow cases and for different sediment materials (sand, lignite and polystyrene) in *Dietz* (1969). It was found to reach an equilibrium and to be a function of the ratio of the friction velocity divided by the fall velocity and the fall parameter (*Dietz*, 1969). For high upstream velocity flows, the angle was found to more or less reach a constant (e.g. *Dietz*, 1969; *Buchko et al.*, 1987) and some indicative values presented in *Breusers*

and Raudkivi (1991) are such that

$$3.5 < \cot \alpha_{s0} < 6 \tag{8.3}$$

or, expressing α_{s0} in degrees

$$-16^\circ < \alpha_{s0} < -9.5^\circ. \tag{8.4}$$

Furthermore, the equilibrium for the upstream scour slope is already reached early on while the scour depth still increases, and α_{s0} is more or less constant during the development, stabilization and equilibrium stages introduced previously.

8.2 Numerical simulation of scour downstream of an apron

8.2.1 Numerical model setup

We choose to model the simplest flow configuration possible, which is the scouring downstream of a simple apron with no structure upstream. This situation is equivalent to simulating sediment transport downstream of a backward facing step. The computational domain will be chosen to start at the backward facing step (left boundary) and to extend horizontally some distance downstream of the step (right boundary) as shown in figure 8.2. Vertically, the computational domain will include some region below the step level and the boundary layer region above the step. Since the scour hole is expected to increase both in depth and in length with time, the longer the problem is simulated the larger the numerical domain needs to be and in turn the more costly the computation is. A variable grid both in the horizontal and vertical directions is chosen so that the horizontal grid size is small near the backward facing step and increases going away from the step, and so that the vertical grid size is small and constant under the step level (where the sediment bed will be located) and increases going upwards above the apron

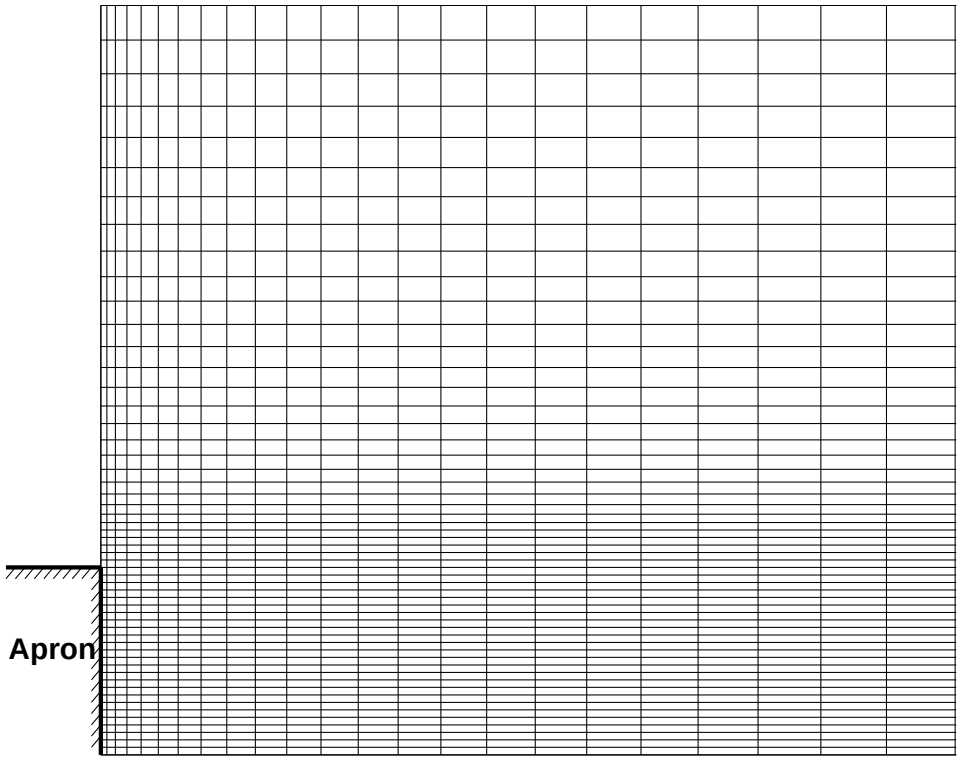

Figure 8.2: Computational domain and grid for scouring downstream of an apron (not to scale). Large grid ($X_{rbc} = 1.0$ m), the small grid would stop halfway through in the horizontal direction. Horizontal lines are plotted every 2 cells and vertical lines are potted every three cells.

level (see figure 8.2). Two different grids (a small domain and a large domain) have been used in the numerical simulations discussed in this chapter. Both are identical in the vertical direction and are such that $\Delta z_{min} = 1$ mm, $\Delta z_{max} = 4.7$ mm, and 110 grid points extend over 0.20 m. The apron is set to be 0.05 m above the bottom of the numerical domain. In the horizontal directions both grids are such that $\Delta x_{min} = 2$ mm. The small grid has 50 points extending over 0.5 m and $\Delta x_{max} = 18.3$ mm while the large grid has 73 point extending over 1 m and $\Delta x_{max} = 25.7$ mm. The larger grid is also chosen so that it almost coincides with the smaller grid for $x < 0.5$ m.

The bottom boundary condition is an integral part of the numerical model and is discussed in chapter 7. The top boundary is assumed to be a symmetry bound-

ary. The left boundary is located at the backward facing step. As such, the left boundary condition is chosen to be a solid no-flux boundary under the step level. Above the step, the fluid flow is set to follow a rough wall logarithmic law specified by its friction velocity $u_{\star 0}$ and the apron's roughness K_{s0}, while no sediment is transported into the computational domain. Several boundary conditions can be implemented at the downstream boundary (right boundary). The most common are Neumann Boundary Conditions (NBC), for which the first derivatives respect to x are specified, or Open Boundary Conditions (OBC), for which we let all quantities be advected freely out of the numerical domain. Mathematically, NBCs are expressed as:

$$\frac{\partial \chi}{\partial x} = C_{nbc} \tag{8.5}$$

where χ represents any quantity and C_{nbc} is a constant, while OBCs can be expressed as

$$\frac{\partial \chi}{\partial t} + c_{obc}\frac{\partial \chi}{\partial x} = 0 \tag{8.6}$$

where c_{obc} is the velocity as which quantities are advected out of the domain. In our case, we choose to set c_{obc} as the local horizontal fluid velocity. We also consider a NBC with $C_{nbc} = 0$ and both boundary condition types are further discussed in the following section.

Since the initiation of sediment motion is not easily simulated by the current model, an artificial initial condition is required. We choose here to base the initial condition on the results of the corresponding one-dimensional model, which is such that the undisturbed bed is at the apron level and the free stream flow velocity is the same as that of the flow on top of the apron. The fluid phase quantities and the concentration are then initialized by setting them equal to the one-dimensional solution. Such an initial condition for the concentration provides a reasonable artificial vertical profile while maintaining the amount of sediment initially in the

numerical model consistent with a still sediment bed at the apron level. The other sediment phase quantities are initialized by setting then equal to a linear combination of the clear fluid solution (at the left boundary) and the one dimensional sediment transport solution (at the right boundary).

8.2.2 Influence of the downstream boundary condition

As mentioned previously, the downstream boundary condition can impact the numerical results and such an influence is further investigated here. This is achieved by simulating an identical problem ($u_{\star 0} = 3.69$ cm/s, $D_{50} = 0.25$ mm and $K_{s0} = 2.5D_{50}$) for the two boundary condition types (NBC and OBC) , each at two locations downstream of the apron, $X_{rbc} = 0.5$ m and $X_{rbc} = 1.0$ m. The computational grid used are those introduced in the previous section. Figure 8.3 shows the sediment bed profiles at several instants for all boundary condition situations. Even though the location of the failure bed is calculated in the numerical simulation and could be plotted, the bed in figure 8.3 is approximated as the location where $\bar{c} = 0.5$. Both a justification and a comparison between the two bed profiles are provided in a later section.

Clearly, both the boundary condition chosen and its location affect the results, and this influence increases with time as attest the increasing differences between the OBC profiles or between the NBC profiles. The NBC also clearly overestimates the scouring at the downstream boundary and thus presents a major flaw. This is due to the no-gradient constraint imposed, and that the profiles in the solid lines remain somewhat close (not too far downstream) is just an indication that the NBC has not yet affected the numerical results. Results obtained using the OBC comparatively seem much better. However, there is a difference between the two OBCs used, which means that the boundary condition still affects the results. For

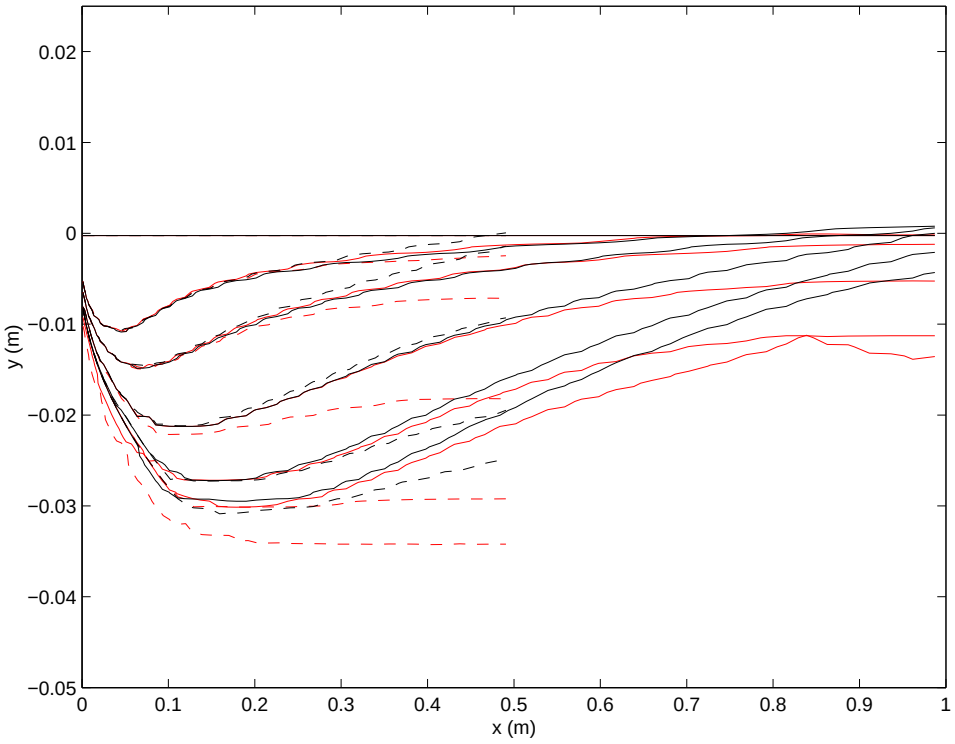

Figure 8.3: Sediment bed profiles at $t = 0s$, $t = 5s$, $t = 10s$, $t = 20s$, $t = 30s$ and $t = 35s$ for all boundary condition situations: $X_{rbc} = 0.5$ m (dashed line) and $X_{rbc} = 1.0$ m (solid line), OBC (back) and NBC (red).

the structural integrity, the most important part of the scour hole is the upstream part (upstream scour slope and maximum scour depth), and both are unaffected by the boundary condition used to the exception of the NBC for the small domain.

The results presented in figure 8.3 show that the Neumann Boundary condition used is inappropriate for the problem considered. Another NBC (second derivative set to zero) has been implemented but such a condition is less stable and is found to result in slower computation. The Open Boundary Condition is better both theoretically by not explicitly specifying gradients downstream and computationally by allowing the use of smaller domains. However, boundary effects remain and will affect the numerical results. The computational domain size thus has to be determined so that numerical results are not affected by the downstream boundary.

8.2.3 Influence of the initial condition

Scouring is a time dependent process and, in addition to effects of the downstream boundary condition, the initial condition can also impact the numerical results. An approach similar to that used for the downstream boundary condition is employed to investigate such an influence. Two cases with different initial conditions are simulated for $u_{\star 0} = 3.69$ cm/s, $D_{50} = 0.25$ mm, $K_{s0} = 2.5D_{50}$ and $X_{rbc} = 0.5$ m with an OBC. One of these two cases is performed with a modified initial condition, which, instead of being based on the corresponding one-dimensional solution, is based on the one-dimensional solution of the problem with $u_{\star 0} = 2.77$ cm/s, $D_{50} = 0.25$ mm, $K_{s0} = 2.5D_{50}$ and $X_{rbc} = 1.0$ m.

Although the two initial conditions are not directly related, we will briefly discuss how they compare. The initial bed profiles and sediment transport rates are shown in figure 8.4 (a). Even though the modified boundary condition presents a different initial concentration profile for which less sediment is "suspended", the

difference between the two concentration profiles mainly occurs at low concentration levels and the total amount of sediment initially in the computational domain is practically unchanged (change of 0.4%) and so is the initial location of the bed. However, all of the other sediment phase variables are significantly different, in particular the sediment flux, and the initial horizontal sediment transport rate at the downstream boundary is about 30% smaller for the modified initial condition.

Figure 8.4 presents both the bed profiles and the sediment transport rates at different instants for the two initial conditions. Numerical results for both initial conditions first converge to the same solution (parts (b) and (c) of figure 8.4), and the time needed to obtain the "same" solution is roughly the time needed to fully advect the initial condition out of the computational domain. We thus conclude that the initial condition should not influence the numerical results. However, observation of figure 8.4 for later times (see part d) shows that the results (in particular the bed location) diverge. Such a behavior is linked to significant differences in the sediment flux at the downstream boundary condition for $t > 10s$. However, this difference happens locally at the downstream boundary and is probably due to other factors than the initial condition, for example effects of the boundary condition or of the spatial discretization.

8.3 Example of scouring downstream of an apron

Scouring downstream of a backward facing step has been simulated for different flow conditions but we will first focus on describing one particular case for which $u_{\star 0} = 3.69$ cm/s, $D_{50} = 0.25$ mm, $K_{s0} = 2.5D_{50}$ and $X_{rbc} = 1.0$ m with an Open Boundary Condition.

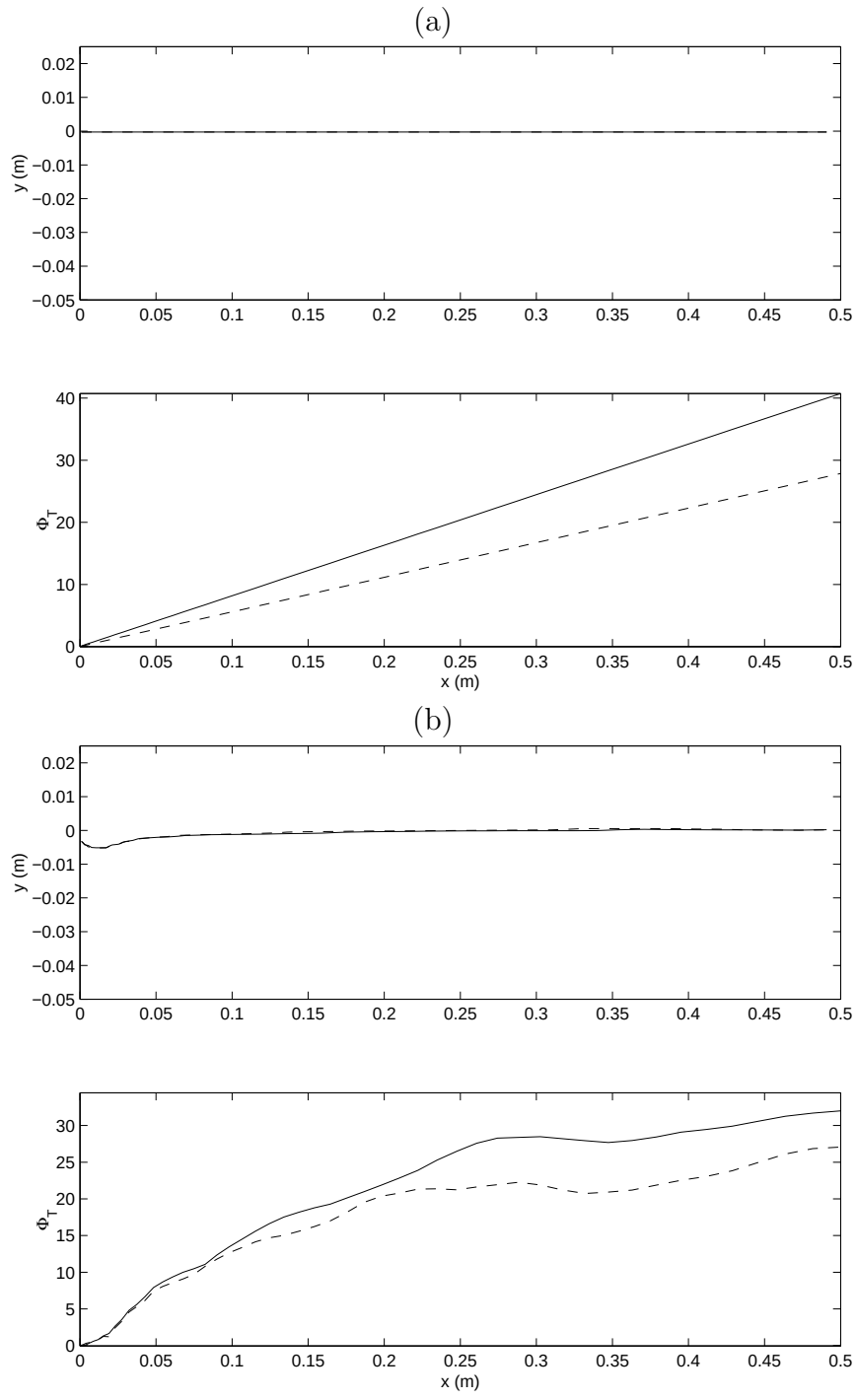

Figure 8.4: Sediment bed profiles (top panel) and sediment transport rate (bottom panel) at (a) $t = 0s$, (b) $t = 0.5s$, (c) $t = 2s$, (d) $t = 20s$ for the original initial condition (solid line) and for the modified initial condition (dashed line).

Figure 8.4 (continued).

(c)

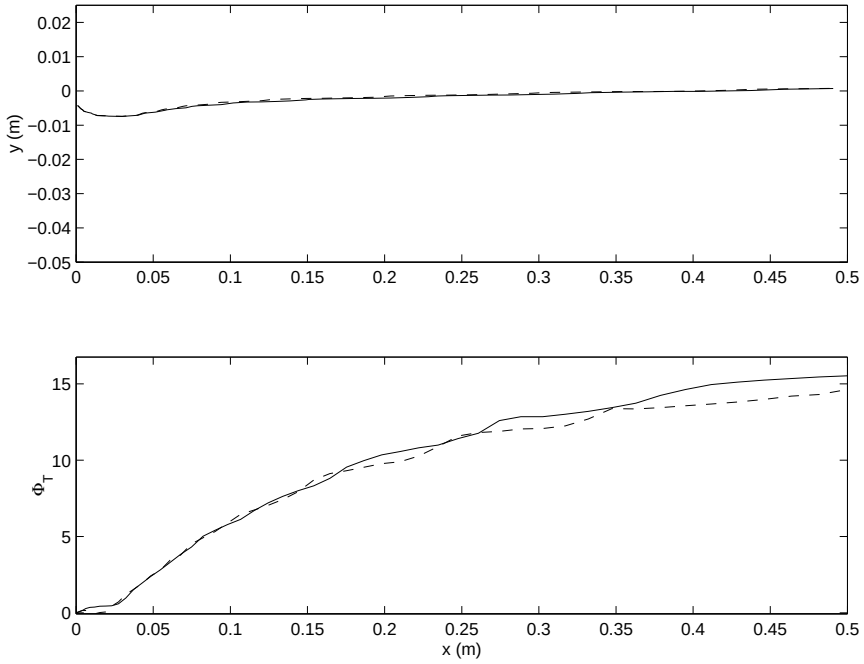

(d)

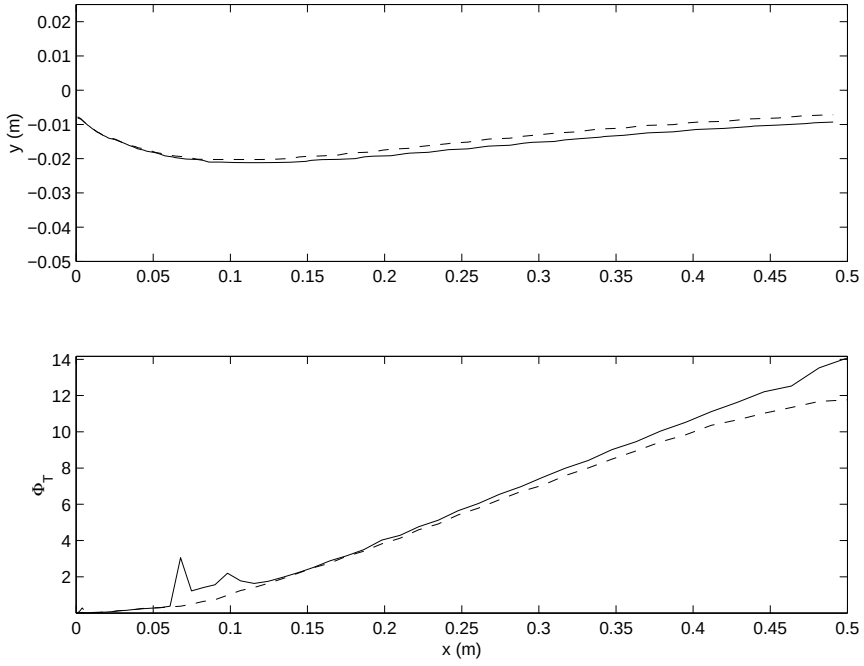

8.3.1 Two-dimensional flow characteristics

Concentration field snapshots and bed profile

Figure 8.5 presents snapshots of the concentration field in the numerical domain at several instants during the simulation. The concentration field is color coded with the map to the right of the snapshots which is in a logarithmic scale. The minimum and maximum of the scale are chosen to match the minimum and maximum values allowed in the numerical simulations ($\bar{c}_{min} = 10^{-7}$ and $\bar{c}_{max} = c^{\star} = 0.635$). The snapshots show clearly that sediment is eroded from the bed and slowly washed out of the numerical domain. The sediment bed can be visually approximated by the top of the dark red region ($\bar{c} > 0.5$).

Bed profiles are more clearly presented in figure 8.6. In this figure both the failure bed and the approximated bed (location where $\bar{c} = 0.5$) are plotted. Although the approximated bed is generally higher than the failure bed it also generally is a fair approximation. In addition, it removes some of the numerical bed fluctuations. Both the scour hole depth and its distance from the apron increase with time and the upstream scour slope doesn't change significantly between the four times shown in figure 8.6.

Velocity profiles

Velocity profiles are presented at different locations downstream of the apron in figures 8.7, 8.8, and 8.9. In all three figures, a close up of the scoured region is provided. While the profiles at $x = 0$ m and far downstream from the bed are representative of the law of the wall for boundary layers, the profiles in the scour hole are rather different. Upstream of the maximum scour depth, we observe a small flow reversal close to the bed (most visible in figure 8.9). Just downstream of the maximum scour depth, the velocity profile seems to increase linearly with

(a)

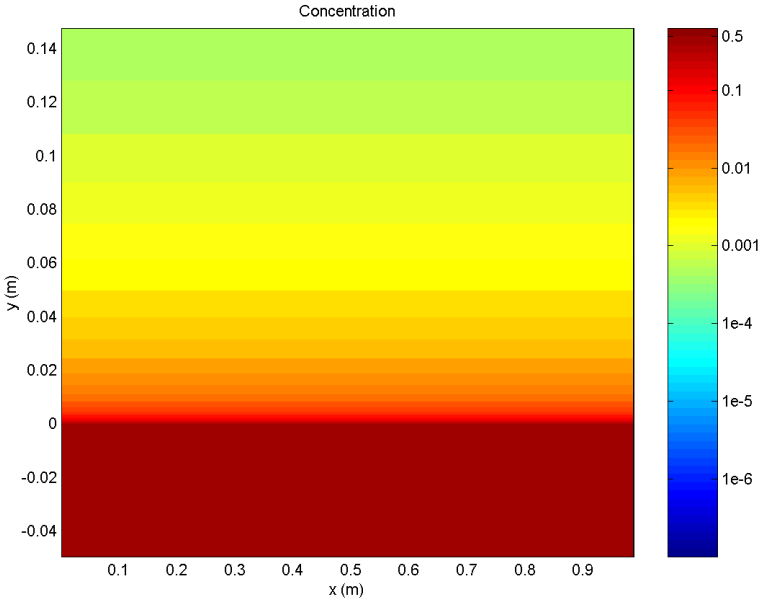

(b)

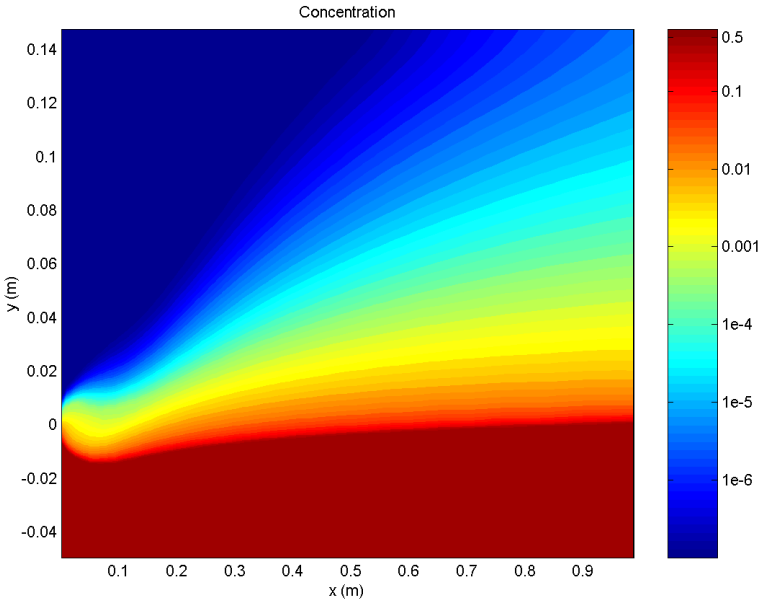

Figure 8.5: Snapshots of the concentration field at (a) $t = 0s$, (b) $t = 10s$, (c) $t = 20s$ and (d) $t = 35s$ for $u_{\star 0} = 3.69cm/s$, $D_{50} = 0.25mm$, $K_{s0} = 2.5D_{50}$ and $X_{rbc} = 1.0m$.

Figure 8.5 (continued).
(c)

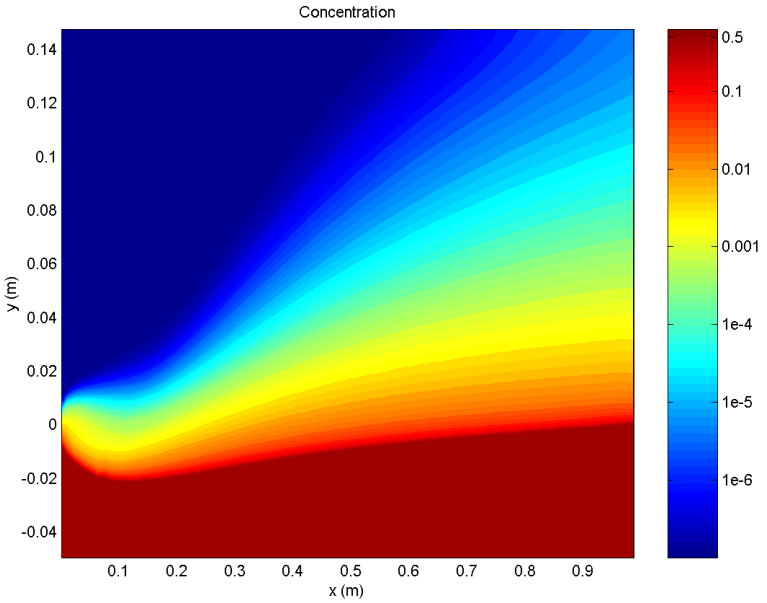

(d)

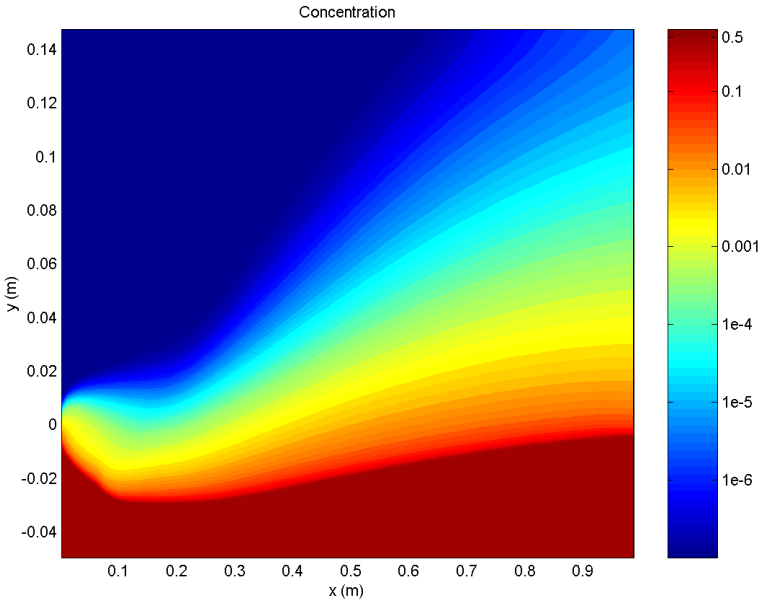

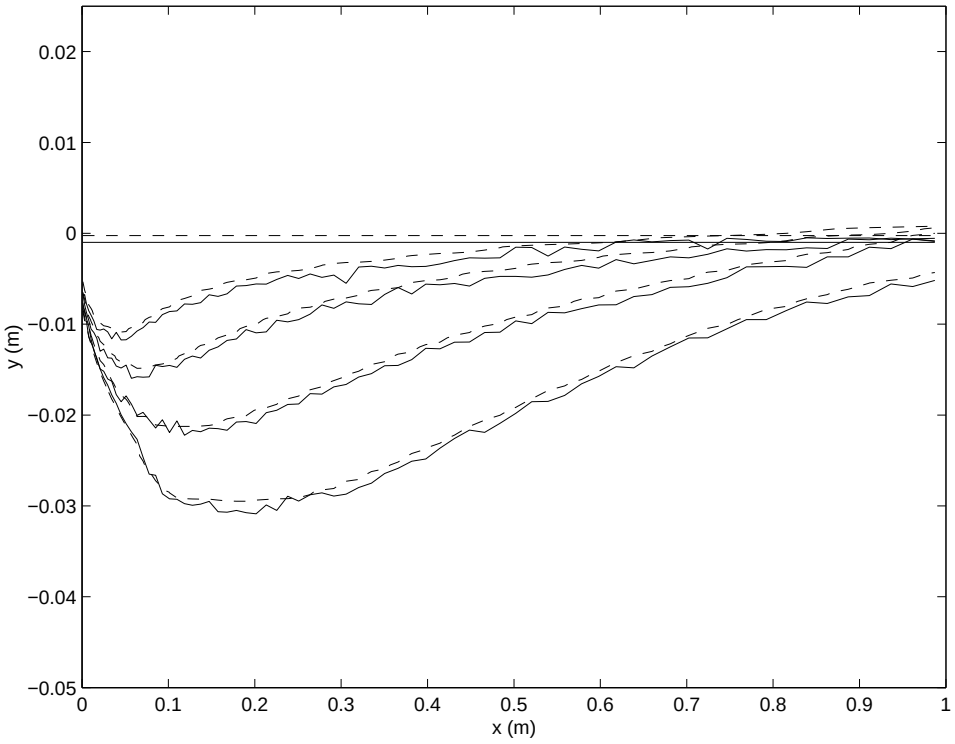

Figure 8.6: Bed location as approximated by the contour of $\bar{c} = 0.5$ (dashed line) and failure bed (solid line) at $t = 0s$, $t = 5s$, $t = 10s$, $t = 20s$ and $t = 35s$ for $u_{\star 0} = 3.69$ cm/s, $D_{50} = 0.25$ mm, $K_{s0} = 2.5D_{50}$ and $X_{rbc} = 1.0$ m and an OBC.

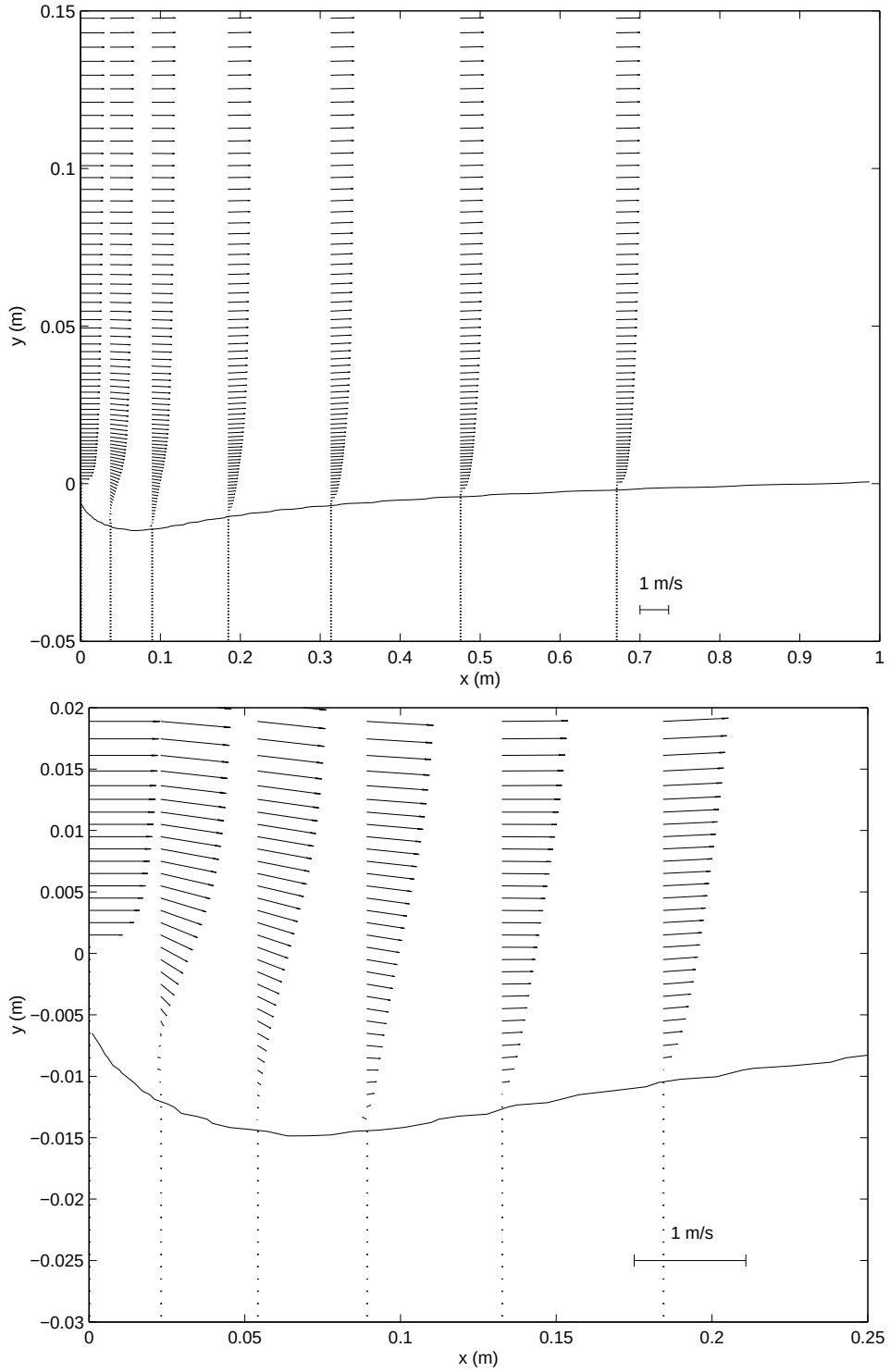

Figure 8.7: Velocity profiles at different locations downstream of the apron at $t = 10$ s for $u_{\star 0} = 3.69$ cm/s, $D_{50} = 0.25$ mm, $K_{s0} = 2.5D_{50}$ and $X_{rbc} = 1.0$ m and an OBC.

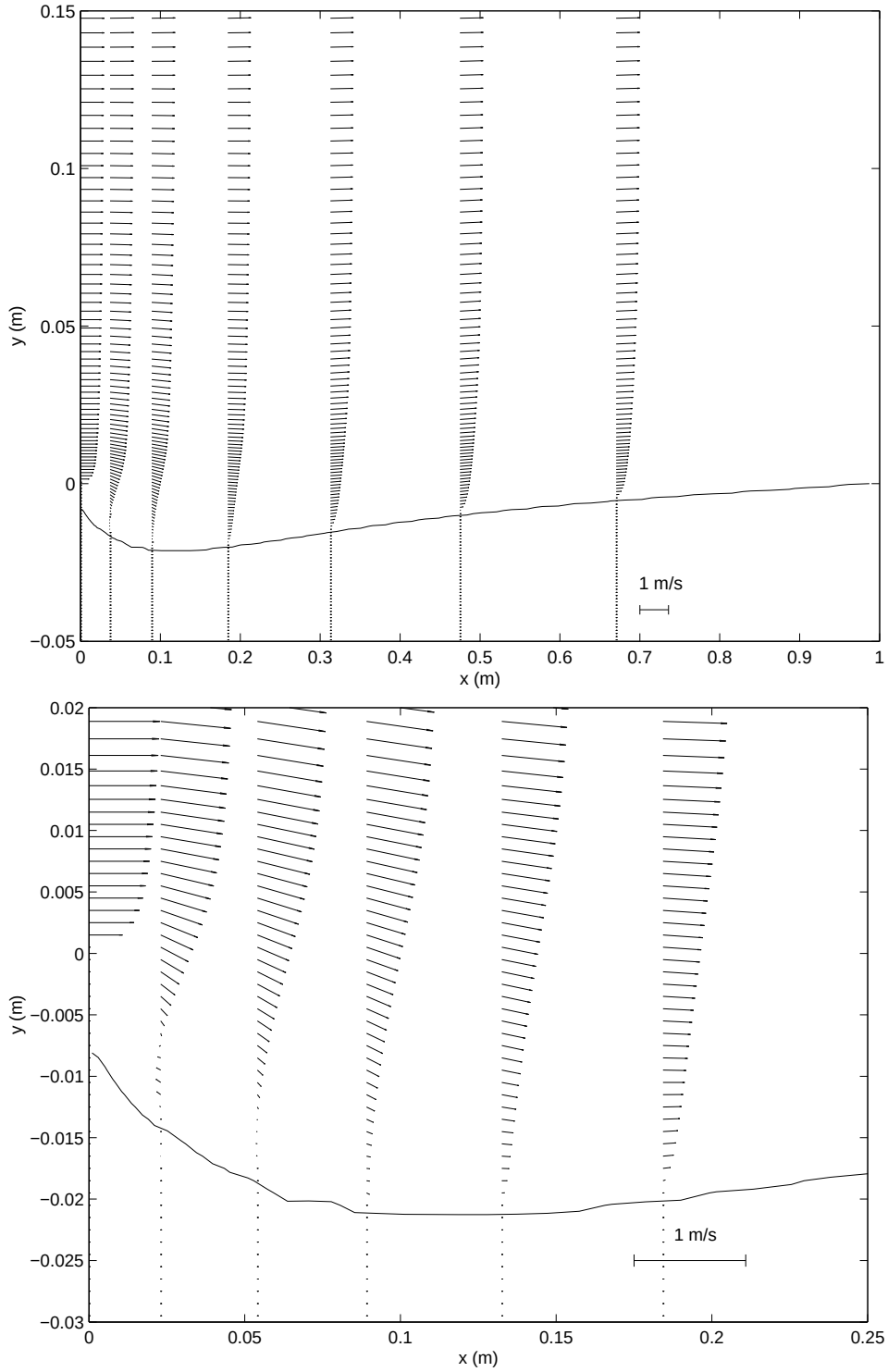

Figure 8.8: Velocity profiles at different locations downstream of the apron at $t = 20$ s for $u_{\star 0} = 3.69$ cm/s, $D_{50} = 0.25$ mm, $K_{s0} = 2.5D_{50}$ and $X_{rbc} = 1.0$ m and an OBC.

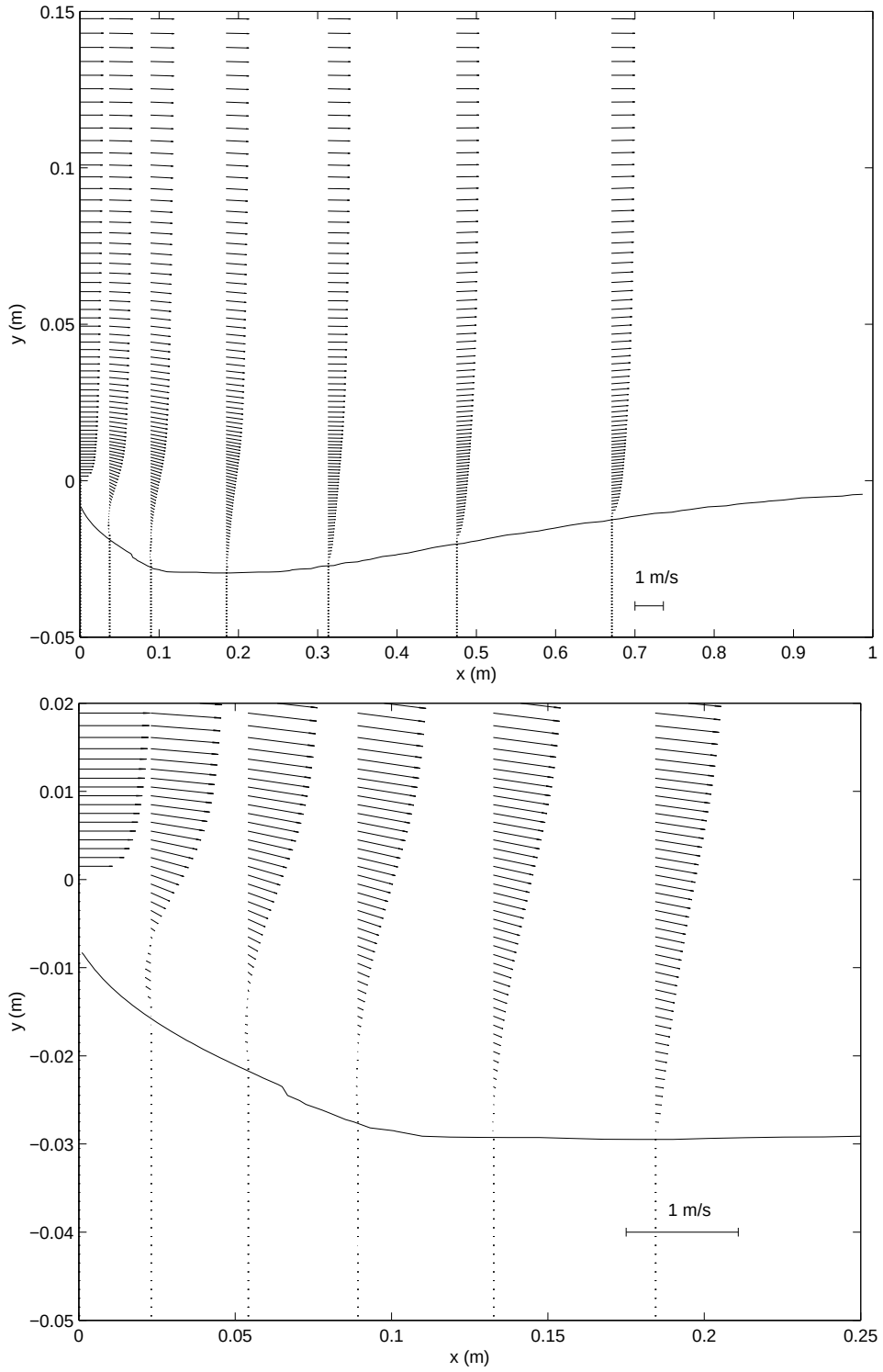

Figure 8.9: Velocity profiles at different locations downstream of the apron at $t = 35$ s for $u_{\star 0} = 3.69$ cm/s, $D_{50} = 0.25$ mm, $K_{s0} = 2.5D_{50}$ and $X_{rbc} = 1.0$ m.

the elevation above the bed. The linear profile in this case is not connected to the enduring contact region (see chapter 6), as the moderate concentration values (see figure 8.5) prove. Instead it is due to the ambient flow modification by the scour hole. Further downstream from the maximum scour depth, the velocity gradually recovers profiles resembling that of the law of the wall and the one-dimensional velocity profile above mobile sediment beds (see section 6.1.1). The fact that the flow reversal is only observed on the windward slope hints that the reattachment point is located upstream of the maximum scour depth. The local Shields parameter value also reflects the existence of the flow reversal: it is negative upstream of the maximum scour depth and positive downstream. Furthermore it changes sign (negative to positive) just upstream of the maximum scour depth, thus giving an indication on the location of the reattachment point. Velocity profiles have also been measured experimentally (*Breusers*, 1966) in a scour hole and the main qualitative findings are consistent between the experiments and the numerical simulations: both the small flow reversal and the linear velocity profiles were observed by *Breusers* (1966).

Sediment transport rate

Figure 8.10 presents the sediment transport rate in non-dimensionalized form as a function of the distance downstream from the apron for several different times. Just downstream of the apron the sediment transport rate is almost zero, and its derivative respect to x is also very small. Such a behavior is related to the equilibrium of the upstream scour slope.

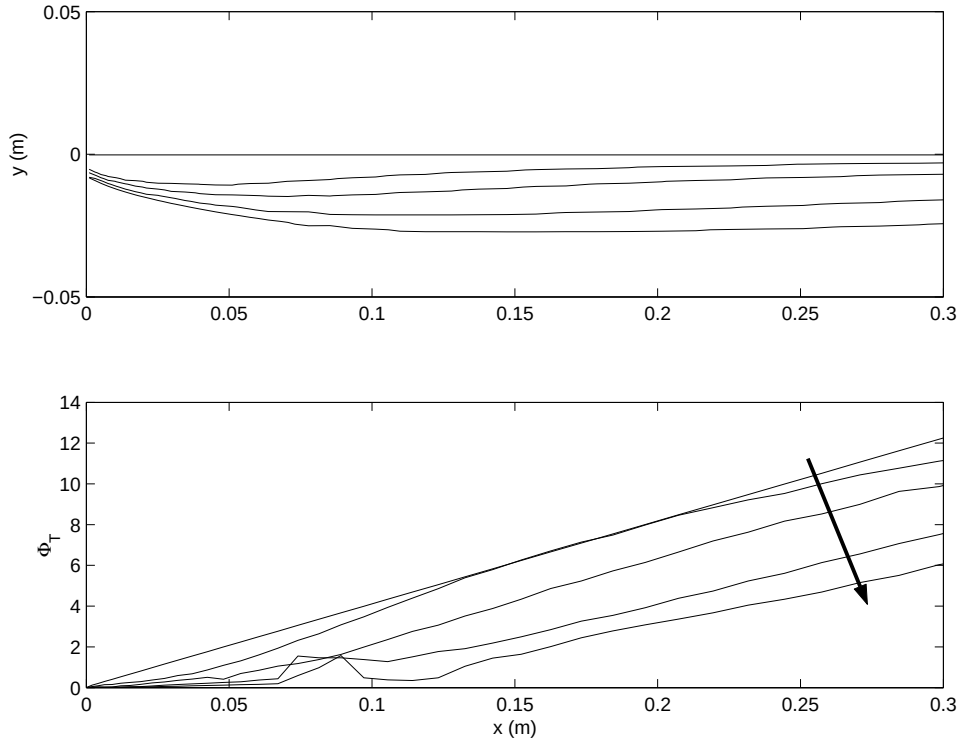

Figure 8.10: Sediment transport rate at different times $t = 0s$, $t = 5s$, $t = 10s$, $t = 20s$ and $t = 30s$. The arrow indicates increasing time and the corresponding bed profiles are presented in the upper panel.

8.3.2 Geometric characteristics of the scour hole

So far, the numerical results have only been shown to be qualitatively correct. More quantitative conclusions on the quality of the numerical simulations need to be made. To that end, we will focus on the scour hole geometric characteristics, which are well documented experimentally (e.g., *Breusers*, 1966, 1967; *Dietz*, 1969; *Buchko et al.*, 1987). In particular, we will look at the upstream slope of the scour hole, which is the bed slope just downstream of the apron, and which is of importance because of the implications for the stability of the structure or apron. We will also look at the evolution of the maximum scour depth.

Upstream scour slope

The numerical results for the upstream scour slope have been shown to be independent of both the downstream boundary condition and the initial condition. The numerical simulations should then provide an accurate representation of the upstream scour slope. The evolution of the upstream slope of the scour hole with time is presented in figure 8.11. The upstream scour slope first increases before reaching an equilibrium after ten to fifteen seconds. Although high frequency fluctuations that could be due to the discretization employed have been smoothed by a moving average technique, some fluctuations around the "mean" expected behavior in the dashed curve still remain. The constant slope with time is due to a balance between driving forces of the fluid on the sediment and of the stabilizing forces (gravity). For a plane bed, the stabilizing force is taken to be $F_s = W \tan\psi$, where W is the weight of particles and ψ the static friction angle (e.g., *Fredsoe and Deigaard*, 1992). For an inclined bed (with an angle α_{s0} with the horizontal, the stabilizing force due to gravity will then be $F_s = W\left(\tan\psi\cos\alpha_{s0} + \sin\alpha_{s0}\right)$ Around the equilibrium value, an increase of the absolute value of the upstream

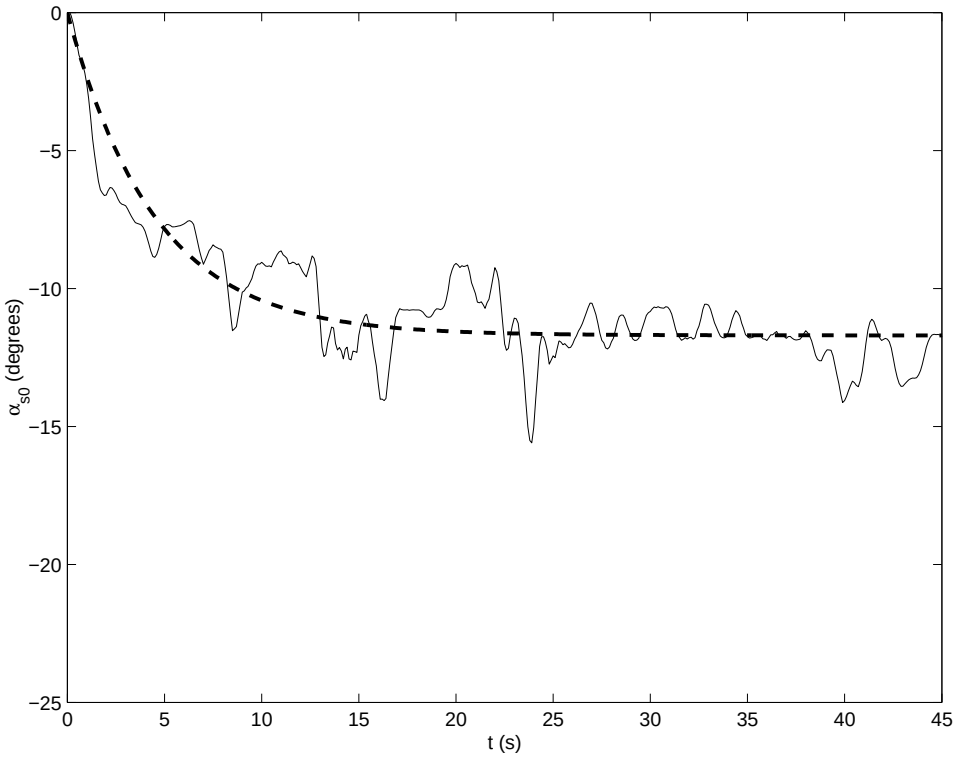

Figure 8.11: Scour hole initial slope as function of time for $u_{\star 0} = 3.69$ cm/s, $D_{50} = 0.25$ mm and $K_{s0} = 2.5D_{50}$. Numerical results (thin solid line) and fit to equation 8.7 with $T_{\alpha s} = 4$ s and $\alpha_{s0}(\infty) = -11.4$ degrees (thick dashed line).

slope will then lead to an increase of the stabilizing force and thus a return to equilibrium of the slope. Inversely, a decrease of the slope absolute value will lead to a decrease of the stabilizing force and again a return to the slope equilibrium.

Since the upstream scour slope seems to reach equilibrium relatively fast (ten to fifteen seconds), we can get a reasonable estimate of its equilibrium value from the numerical results. Although we could just average the results for $t > 20$ s, the following equation will better describe the upstream scour slope by considering the time dependent portion and the equilibrium:

$$\alpha_{s0}(t) = \alpha_{s0}(\infty)\left[1 - \exp\left(-\frac{t}{T_{\alpha s}}\right)\right] \tag{8.7}$$

where $\alpha_{s0}(\infty)$ is the equilibrium value and $T_{\alpha s}$ is a measure of the initial time derivative and is related to the time required to reach equilibrium. $\alpha_{s0}(\infty)$ and

$T_{\alpha s}$ can then be determined by fitting equation 8.7 to the numerical results and minimizing the root mean square error. For the case presented in this section ($u_{\star 0}$ = 3.69 cm/s, D_{50} = 0.25 mm and $K_{s0} = 2.5D_{50}$), we find $T_{\alpha s}$ = 4 s and $\alpha_{s0}(\infty) = -11.4$ degrees which is consistent with the experimental values of the initial slope reported in *Breusers and Raudkivi* (1991) (equation 8.4).

Maximum scour hole depth

The time evolution of the maximum scour depth is presented in figure 8.12 using linear coordinates, and in figure 8.13 using logarithmic coordinates. In both figures, the numerical results are shown in the solid line while a fit to equation 8.2 is the dashed line. The values for n_s and T_s are determined by minimizing the root mean square error, but are fairly sensitive to the range in time over which the fit is done. Figure 8.13 indicates that such a fit should be performed for times later than about 10 seconds, and we choose here to do it for $t > 3T_{\alpha s}$ so that the upstream scour slope has almost reached it equilibrium value. The maximum scour depth does indeed evolve following equation 8.2, and while the dashed curve under-predicts the numerical results at small times ($t < 10s$), another law of the type of equation 8.2 could be fitted there with a lower power.

For the present case ($u_{\star 0}$ = 3.69 cm/s, D_{50} = 0.25 mm and $K_{s0} = 2.5D_{50}$), we find that n_s = 0.56 and T_s = 600. Both n_s values are in the same range as the experimental value of 0.38, in that they are less than 1 and thus imply that the scouring process slows down with time. Furthermore, even though both values are significantly higher than 0.38, they are not unrealistic since *Buchko et al.* (1987) did observe value of n_s higher than 0.38 for times under 10 minutes.

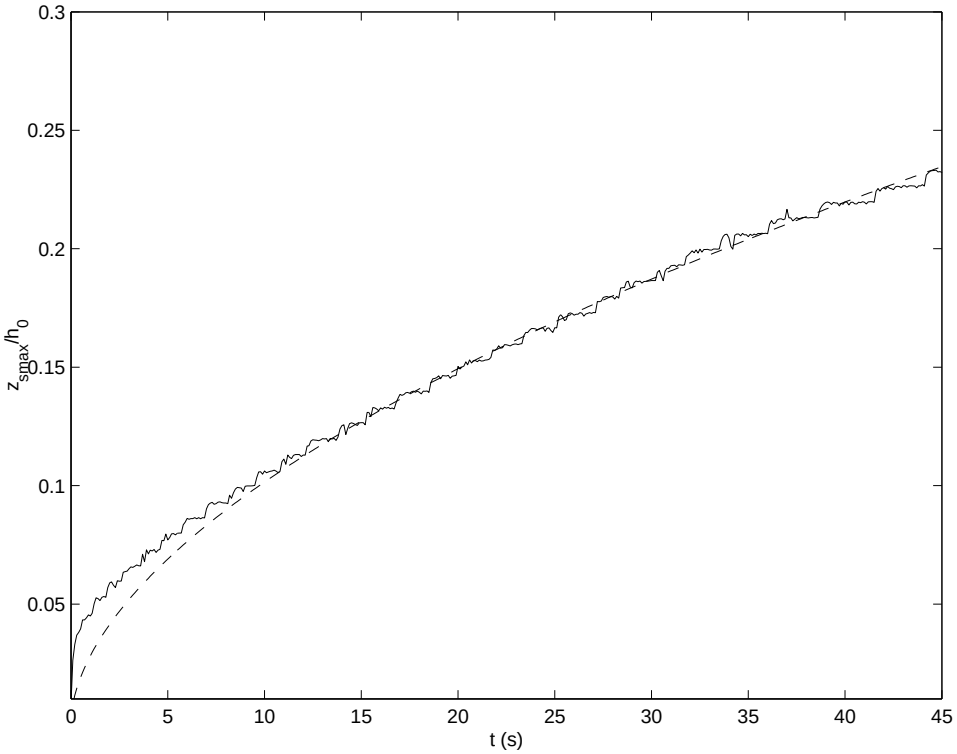

Figure 8.12: Scour hole maximum scour hole depth as function of time for $u_{\star 0} = 3.69$ cm/s, $D_{50} = 0.25$ mm and $K_{s0} = 2.5D_{50}$ in linear coordinates. Solid line: Numerical results. Dashed line: equation 8.2 with $T_s = 600$ s and $n_s = 0.56$.

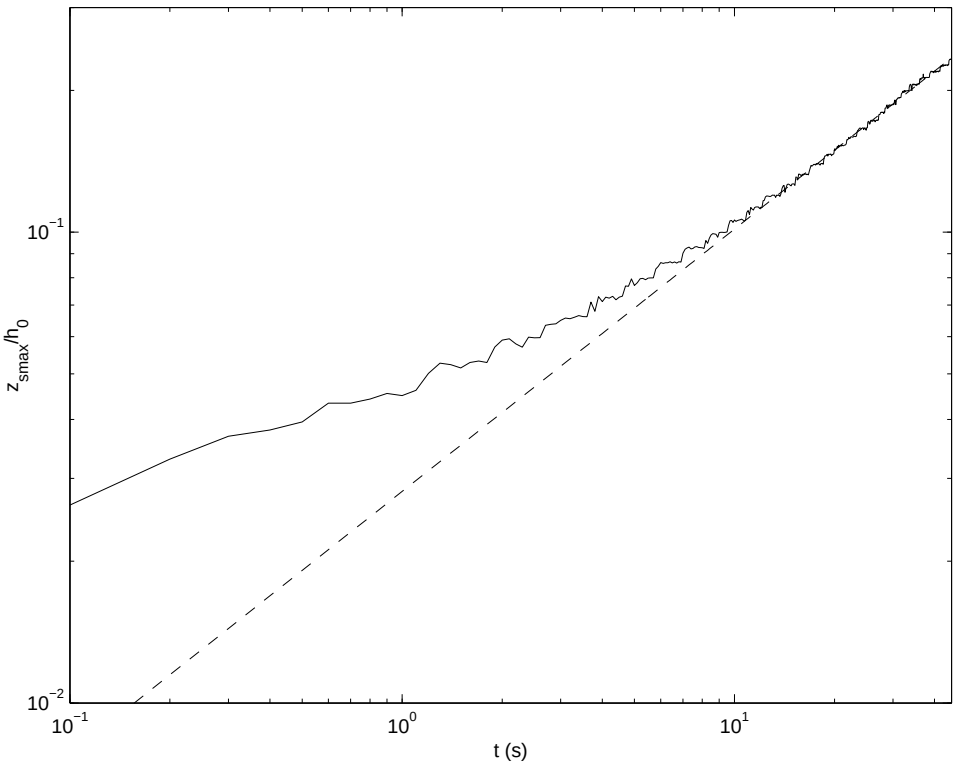

Figure 8.13: Scour hole maximum scour hole depth as function of time for $u_{\star 0} = 3.69$ cm/s, $D_{50} = 0.25$ mm and $K_{s0} = 2.5D_{50}$ in logarithmic coordinates. Solid line: Numerical results. Dashed line: equation 8.2 with $T_s = 600$ s and $n_s = 0.56$.

Table 8.1: Scour hole characteristics for different upstream friction velocities, $D_{50} = 0.25mm$ and $K_{s0} = 2.5D_{50}$.

$u_{\star 0}$ (cm/s)	θ_0	n_s	T_s (s)	α_{s0} (degrees)	$T_{\alpha s}$ (s)
2.77	0.19	0.57	877	-8.5	4
3.69	0.34	0.56	600	-11.4	4
4.62	0.53	0.56	390	-12.7	4

8.4 Influence of the upstream flow conditions

Breusers (1966, 1967) found that both n_s and α_{s0} were independent of the upstream flow velocity, while *Dietz* (1969) disagreed for the upstream scour slope and found it to depend on the flow velocity at small and moderate values. They both also found that is inversely proportional to the fourth power of the flow velocity. Finally, *Buchko et al.* (1987) confirmed both by doing experiments in a water tunnel at high velocities and finding that both n_s and α_{s0} were more or less constant. We also investigate the behavior of the scour hole characteristics with the upstream flow velocity and seek further validation of the numerical results.

Table 8.1 presents the numerical results for different parameters describing the scour hole in the case of three different upstream flow intensities. A fourth case of higher upstream velocity but same sediment median diameter and upstream roughness only yielded meaningful results for the initial slope ($\alpha_{s0} = -14.8$ degrees for $u_{\star 0} = 5.77$ cm/s or $\theta_0 = 0.82$) and is not included in table 8.1.

In spite of the debatable values for n_s, we do confirm that it is constant with the flow velocity. We also confirm that T_s decreases with increasing velocity. However, the empirical relationship found by *Breusers* (1967) and *Dietz* (1969) is not reproduced by the numerical results. In particular, the values are much smaller that those found experimentally (e.g., *Buchko et al.*, 1987). Since T_s represents the time required for the maximum scour depth to reach h_0, an explanation is the difference

of initial condition between experimental and numerical results. Experimentally, both the fluid flow and the sediment motions start from rest. Numerically, we can not resolve the sediment motion initiation and we thus have to implement an artificial condition for which both the fluid flow and the sediment motion do not start from rest.

We observe that the initial evolution of the upstream scour slope is the same for all velocities since $T_{\alpha s}$ is a constant. The equilibrium values (α_{s0}) do agree with the indicative values presented in *Breusers and Raudkivi* (1991) (equation 8.4) and we find a slight increase of the slope with increasing upstream friction velocity. Such a behavior was also observed experimentally (*Dietz*, 1969) and is due to the moderate range of upstream flow intensities simulated. Both *Dietz* (1969) and *Buchko et al.* (1987) presented their upstream scour slope results by reporting the value of the cotangent of the slope as a function of the depth averaged upstream velocity. For consistency, we present the results of table 8.1 in the same manner in figure 8.14 along with the experimental data. The horizontal axis in figure 8.14 is then the difference between the depth averaged upstream flow velocity and the depth averaged critical velocity for incipient motion, made dimensionless in the same manner as for the Shields parameter. A relation between the depth averaged velocity and the friction velocity can be obtained if the velocity profile is known, but will usually also require knowledge of the wall roughnesses (lacking for the apron in *Dietz* (1969) and for the ceiling in *Buchko et al.* (1987)). The good agreement between the numerical results and the experimental data in figure 8.14 constitutes another validation of the two-dimensional model used to model scour downstream of aprons.

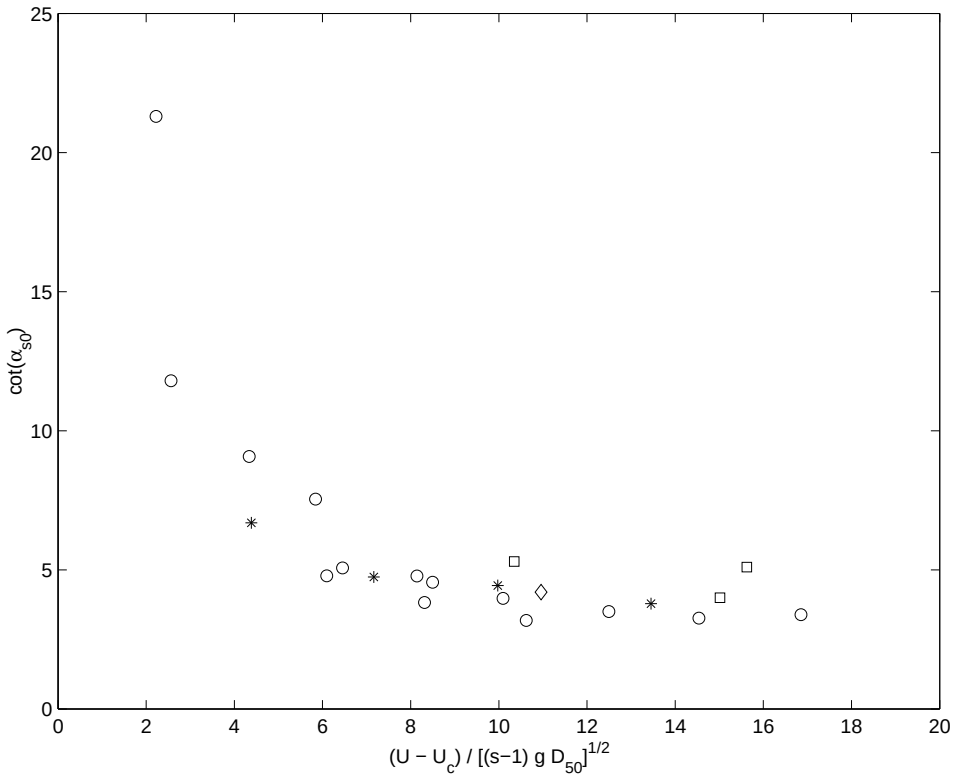

Figure 8.14: Initial slope of scour hole for different upstream flow intensities. $\star$: present numerical study. $\circ$: Experimental data for fine sand (*Dietz*, 1969). $\square$: Tunnel experimental data from *Buchko et al.* (1987). $\Diamond$: Open channel flow experimental data from *Buchko et al.* (1987).

8.5 Summary

In this chapter, we investigated scour downstream of aprons with the two-phase two-dimensional sediment transport model introduced in chapters 3 and 7. Most two-dimensional traditionally use a mass conservation concept to calculate the bed location: the erosion equation relates the time rate of change of the bed location to the horizontal rate of change of the horizontal sediment transport rate. However, sediment mass conservation for the entire water column can be expressed as:

$$\int_0^\infty \left[\frac{\partial c(x,z,t)}{\partial t} + \frac{\partial}{\partial x} c(x,z,t) u_s(x,z,t) \right] dz = 0 \tag{8.8}$$

and further assumptions are thus need to derive the so-called erosion equation (in particular on how to relate the integral of the concentration to the bed location). The present model thus presents an important theoretical advantage respect to traditional models in that no assumptions are required to derive an erosion equation.

We discussed the dependence of the numerical results on the downstream boundary condition and on the initial condition. We found that an open radiative boundary condition is more appropriate for the problem studied here, both theoretically and computationally. Although boundary effects remain, the computational domain can be chosen in order to minimize such effects (simulate larger domains). We also found that the artificial initial condition was completely advected out of the numerical domain in a short time and that the numerical results are then independent of this condition. Still the lack of representation of the initiation of the fluid flow and of the sediment motions might lead to erroneous results on the time scales of the scour process.

Both flow characteristics and scour geometry characteristics have been discussed in one particular case. The existence of a flow reversal just downstream of the apron is verified. The upstream scour slope does reach an equilibrium quickly

and the total sediment transport rate derivative is indeed zero at the origin of the horizontal axis. The upstream scour slope numerical value also compares well with previous experimental data. Finally, the dependence of the scour on the upstream flow velocity found by the numerical simulations agrees with the existing experimental data.

CHAPTER 9

CONCLUDING REMARKS AND FUTURE WORK

We presented in this dissertation a sediment transport model that is based on a two-phase flow approach and which is able to resolve sediment and fluid motions for the entire water column including within the stationary bed and the bed location. Averaged equations of motion for both a sediment phase and a fluid phase are solved. The velocity-concentration covariance is modeled using a gradient diffusion hypothesis. The turbulent fluid stresses are modeled using the turbulent viscosity hypothesis and a $k - \varepsilon$ turbulence model, modified to account for the two-way interaction between sediment particles and fluid turbulence. Finally, the sediment stresses are modeled using a collisional granular flow theory.

Three problems were investigated using this two-phase sediment transport model. First, the specification of near-bed boundary conditions and of the velocity-concentration covariance were investigated for dilute flows. A concentration dependent sediment diffusivity was introduced, and two near-bed boundary conditions were compared.

A more advanced turbulence modeling closure was introduced for the complete model (sediment stresses not neglected). Sediment transport characteristics in the sheet flow regime were investigated for steady flows, oscillatory boundary layers and a pulsating flow. Several well known results where confirmed and new insight on sheet flows was provided by the numerical results.

Finally, a two-dimensional benchmark case was tested with the present two-phase sediment transport model. Scouring downstream of an apron (backward-facing step) was simulated. The relatively good accordance with existing experimental data proves that this model is able to represent multi-dimensional situations (two dimensions so far).

Even though the present study does improve the current understanding of sediment transport processes both for one-dimensional flows (sheet flow regime) and two-dimensional flows, more work has to be done. A few examples are discussed next.

9.1 Further use of the present model

The current two-phase sediment transport model has only been used to study a limited number of situations. As long as the fundamental assumptions of the model remain valid (see discussions at the start of chapters 6 and 8), any other problem could also be investigated. Sediment transport formulae could be confirmed, invalidated, or even derived. Already, from the results discussed in chapter 6, more appropriate near-bed boundary conditions for the vertical sediment flux in the dilute model can be pursued. More complex flow conditions than those considered in chapters 4, 5 and 6 can also be investigated (e.g., *Hsu and Hanes*, 2004).

In most previous multidimensional studies, the bed location is related to the sediment (bed load usually) transport rate which, in turn, has to be calculated based on the flow conditions. This is usually done by relating it to the local Shields parameter through expressions of the type of equation 2.23 for example. In such expressions, a possible slope in the flow direction has to be considered and this has traditionally been done by modifying the Shields parameter (e.g., *Fredsoe and Deigaard*, 1992):

$$\theta_\alpha = \theta \cos\alpha_s \left(1 - \frac{\tan\alpha_s}{\tan\psi}\right) \tag{9.1}$$

where α_s is the slope of the bed, and ψ the static friction angle. The present model would provide an interesting alternative method to investigate the sediment transport rates in the case of plane sloping beds.

This two-phase sediment transport model can also be used to study other two-

dimensional problems. As mentioned in the opening discussion of chapter 8, the presence of solid obstacles has been numerically implemented and thus allows simulations of scour around structures in general. In addition, different boundary conditions (lateral and top boundary conditions) can be implemented to simulate different problems. In particular, flow variables can be specified at the top boundary with periodic lateral boundary to simulate sediment transport under standing waves for example. Experimental studies for such cases (e.g., *O'Hare and Davies*, 1993; *Landry et al.*, 2007) have shown that coarse sand accumulates under the nodes, while the fine sediment accumulates at the antinodes and the qualitative explanation lies in the mass transport due to the turbulent stresses near the bed.

Another important issue in sediment transport concerns the inception of sheet flow. Although several empirical relationships have been introduced to describe the sheet flow inception, little is known on the mechanisms of the transition between the plane bed regime and ripples regime. Again, numerical simulations on this transition could provide new insight on both the processes and the parameterization.

9.2 Modeling improvements

The two-phase model introduced in chapter 3 uses several simplifying assumptions. For example, lift and added-mass forces are neglected. So are the small-scale turbulence and some terms in the averaged equations of motion (e.g., the pressure gradient concentration covariance). The inter-particle interactions are modeled using only a collisional theory. Both justifications and discussions on the validity of these assumptions have been included (mostly in chapter 3). Still, even though the model-data comparisons performed have been satisfactory (see chapters 4, 5 and 8), we believe that further improvements can be made. In particular, we believe that

the "kinks" observed in the vertical profiles of some quantities (e.g., sediment flux in figure 6.10) may be due to an insufficient description of the processes involved.

We only account for collisional inter-particle interactions in the model whereas different types of interactions have been observed experimentally (*Bagnold*, 1954; *Savage and McKeown*, 1983). Traditionally and following the results of *Bagnold* (1954), the type of interaction depends on the value of the so-called Bagnold number (see chapter 2): the grain inertia (collisional) regime occurs for large Bagnold numbers while a macro-viscous regime occurs for small Bagnold numbers. For simplicity we chose in this dissertation to relate these regimes to values of the friction Reynolds number $Re_\star$ and we represented them graphically in figures 2.4 and 5.1 along with experimental conditions. Most experimental conditions for sand are actually in the transition region, and the finer sand condition ($D_{50} = 0.13$ mm) lies at the limit of the macro-viscous regime. This points out that only using a collisional theory might not be sufficient to describe appropriately the inter-particle interactions in such cases. Even though adding a theory for the macro-viscous regime (e.g., *Carpen and Brady*, 2002) was experimented unsuccessfully for $D_{50} = 0.32$ mm, smaller sediments could benefit from considering a more complete description of the inter-particle interactions. In addition, in most sediment transport application the view will be more complicated than that of *Bagnold* (1954) because the Bagnold number can depend both on location and time ($B = B(x, z, t)$). Providing a better picture of the interparticle interactions as function of the local Bagnold number could then result in improvements of both the time and spatial dependence of the sediment transport predictions.

Another of the least satisfactory assumptions concerns the small-scale turbulence. In chapter 3, it was neglected partly based on scaling argumentation but also for simplicity. It is now possible to re-estimate this assumption using the

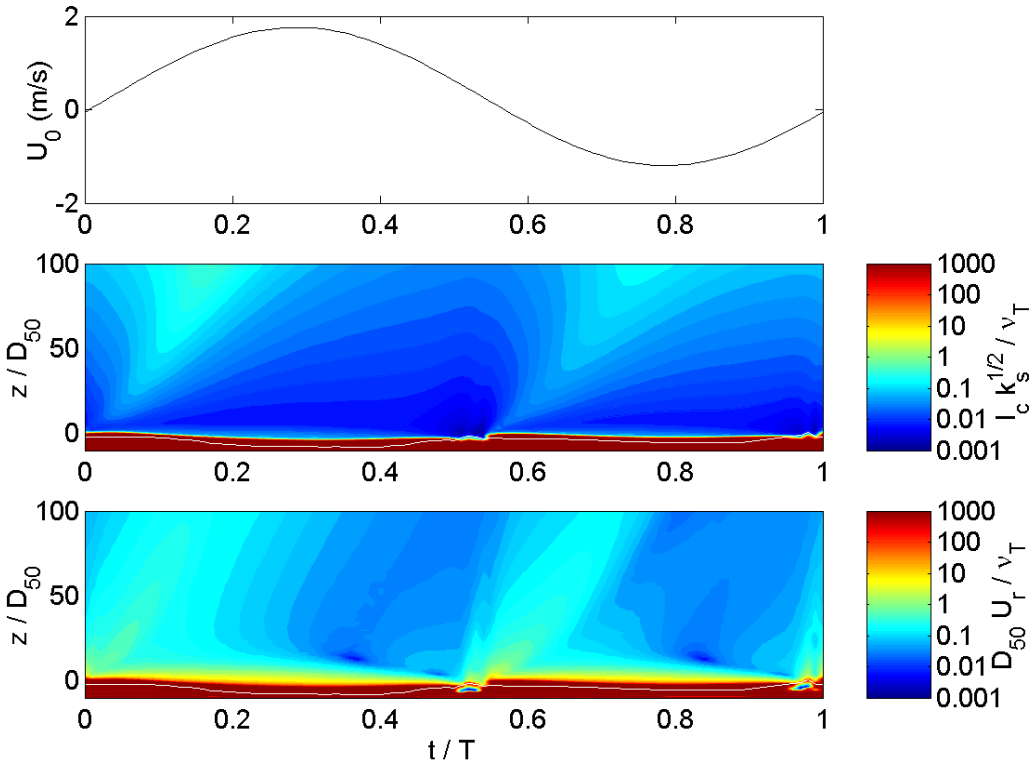

Figure 9.1: Comparison of the relative importance of the small-scale eddy viscosity and the large-scale turbulent viscosity for a particular case (case 1 of table 5.1).

numerical results. In chapter 3, the small-scale turbulence was divided into two parts: one generated by the flow of the interstitial fluid around sediment particles for which the small-scale eddy viscosity ν_t was scaled as $\nu_t \sim D_{50}U_r$, and the other induced by the small-scale particle velocity fluctuations for which the small-scale eddy viscosity was scaled as $\nu_t \sim l_c\sqrt{k_s}$, with l_c being the mean free path of the particles. Figure 9.1 presents the ratio ν_t/ν_T for both small scale turbulence mechanisms in the near bed region for case 1 of table 5.1. The white solid lines in the colored maps represent the location of the failure bed as a function of time (below the line, sediment is stationary). Figure 9.1 clearly indicates that the small scale turbulence is not always negligible. Very close to the failure bed, the small scale viscosity is dominant in the enduring contact region where the large-scale turbulence is very small. Still, in this region the fluid turbulence has a small impact on the overall model (the flow is actually controlled by the particle motions) and neglecting the small scale viscosity should be valid. Very quickly going away from the bed, the large scale scale viscosity ν_T dominates $l_c\sqrt{k_s}$ but not always $D_{50}U_r$. This brief re-evaluation of the importance of the small scale turbulence indicates that the small scale turbulence due to the small-scale particle velocity fluctuations is indeed small, but the small scale turbulence generated by the flow of the interstitial fluid around the particles might not and should thus be accounted for in a more detailed model.

It also has to be noted that the large scale turbulence modeling is subject to possible improvements. We presented in chapter 5 how the $k-\varepsilon$ model is improved by better taking into account the two way interaction between particles and fluid turbulence. First, one has to recognize the advantages and the drawbacks of the $k-\varepsilon$ model. Although it is generally viewed as computationally inexpensive and easy to use, several empirical parameters have to be specified and the $k-\varepsilon$ model

is known to perform poorly in presence of strong pressure gradients (e.g., *Pope*, 2000). For oscillatory boundary layers, the $k-\omega$ model was found to perform better (*Guizien et al.*, 2003). Second, we used in chapter 5 existing numerical data for homogeneous isotropic turbulence. However, in presence of shear, particles change the turbulence energy production rate (e.g., *Pan and Banerjee* (1996) for wall turbulence, *Ahmed and Elghobashi* (2000) for homogeneous shear turbulence). Such influence of the particles on the fluid turbulence is absent in homogeneous isotropic turbulence and was thus not included in the present sediment transport model. Last, even though more complicated and more advanced turbulence models (even further modification of the $k-\varepsilon$ model) could better capture the physical processes involved, the benefits gained in doing so might not prevail versus the drawbacks and costs.

9.3 Numerical improvements

The numerical model (the discretization and the algorithms used) is also an important part of the current study and has been discussed in more details in chapter 7 and appendix B. One of the main issues for the present model is the computational cost, which is impacted by both the spatial discretization and the time step size (see previous chapter). Still, the time step size is dynamically adjusted based on several stability conditions and it turns out to be a major issue as it is reduced by two orders of magnitude when the sediment equations are solved as compared with clear fluid simulations. Further investigations on reducing the computational cost of this sediment transport model are thus necessary and will require to combine physical and numerical issues.

An important step to that end is to evaluate the relative importance of the different terms in the modeled equations. Figure 9.2 presents such an evaluation

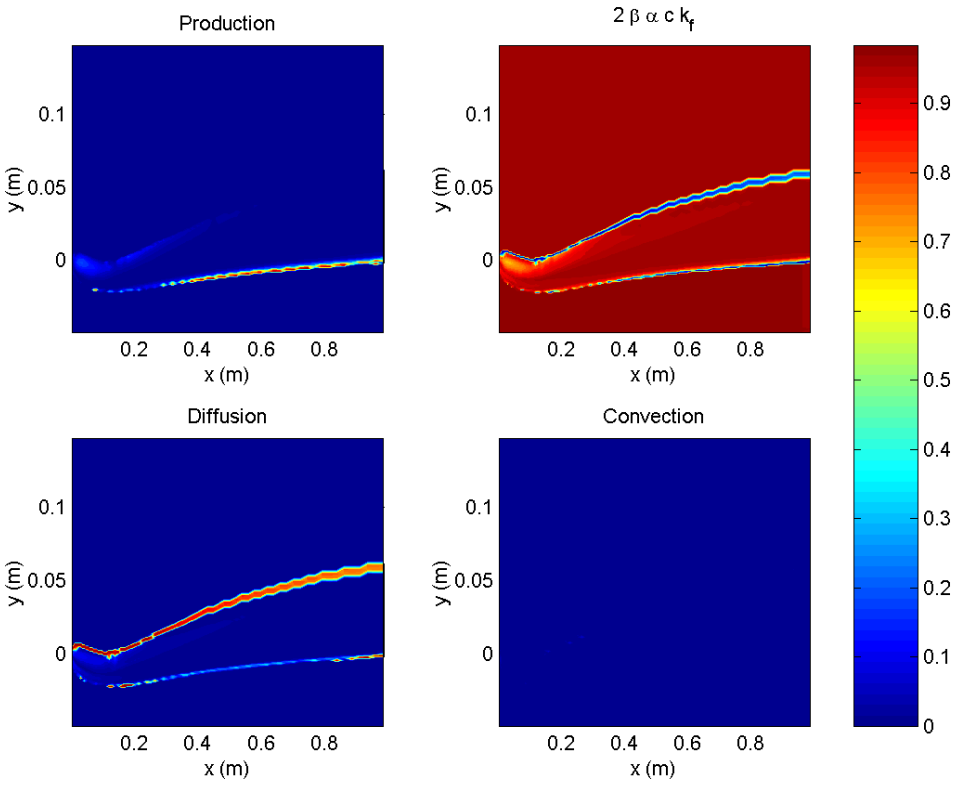

Figure 9.2: Relative importance of the production, phase interaction, diffusion and convection terms in the sediment energy equation right hand side.

for some of the terms in the sediment fluctuation energy equation. Only the terms that are calculated at time step n in obtaining the sediment energy at time step $n+1$ are shown here: i.e. the production, the diffusion, the phase interaction term ($2\beta\bar{c}\alpha k_f$) and the convective term. Both the dissipation and the "drag term" ($2\beta k_s$) are expressed at time step $n+1$. Only an example for a given time is shown in figure 9.2. The results for both the diffusion and the convection are the most interesting because these two terms are the terms that are or can be negative, can then lead to negative values of k_s at time step $n+1$ and in turn to smaller time steps. In particular, the diffusion term is dominant at the top of the collisional layer (layer for which the sediment stresses are calculated). At this location (that depends on x), a "discontinuity" is introduced in the numerical model (sediment stresses are calculated below and neglected above) and results in artificial numerical diffusion for k_s. Removing such diffusion could then reduce the constraint imposed on the time step size, and consequently the overall cost of simulations.

APPENDIX A

COMPLETE FLUID TURBULENCE GOVERNING EQUATIONS

A.1 Derivation of the turbulent kinetic energy balance equation

Defining the mean kinetic energy of the fluid based on the instantaneous fluid velocity as

$$K_f \equiv \frac{1}{2}\overline{(1-c)u_i^f u_i^f}, \tag{A.1}$$

the kinetic energy of the concentration-weighted velocity as

$$\tilde{K}_f \equiv \frac{1}{2}(1-\bar{c})\tilde{u}_i^f \tilde{u}_i^f, \tag{A.2}$$

and the turbulence kinetic energy as

$$k_f \equiv \frac{1}{2(1-\bar{c})}\overline{(1-c)\Delta u_i^f \Delta u_i^f}, \tag{A.3}$$

we obtain that

$$K_f = \tilde{K}_f + (1-\bar{c})k_f \tag{A.4}$$

The governing equation for K is found by multiplying the fluid momentum equation by u_i^f and then taking the Favre average. The fluid momentum equation is given by:

$$\begin{aligned}\frac{\partial \rho^f (1-c)u_i^f}{\partial t} + \frac{\partial \rho^f (1-c)u_i^f u_j^f}{\partial x_j} &= \rho^f (1-c)g_i - (1-c)\frac{\partial P^f}{\partial x_i} - \beta c\left(u_i^f - u_i^s\right) \\ &\quad + \frac{\partial (1-c)T_{ij}^f}{\partial x_j}\end{aligned} \tag{A.5}$$

which leads to:

$$\begin{aligned}\frac{\partial \rho^f \frac{1}{2}(1-c)u_i^f u_i^f}{\partial t} &= -\frac{\partial \rho^f \frac{1}{2}(1-c)u_i^f u_i^f u_j^f}{\partial x_j} + \rho^f (1-c)u_i^f g_i - (1-c)u_i^f \frac{\partial P^f}{\partial x_i} \\ &\quad -\beta c u_i^f \left(u_i^f - u_i^s\right) + u_i^f \frac{\partial (1-c)T_{ij}^f}{\partial x_j}\end{aligned} \tag{A.6}$$

Applying the Favre average to the previous equation we have:

$$\frac{1}{2}\overline{(1-c)u_i^f u_i^f u_j^f} = \tilde{u}_j^f K_f + \frac{1}{2}\overline{(1-c)u_i^f u_i^f \Delta u_j^f} \tag{A.7}$$

and so we obtain

$$\begin{aligned}\frac{\partial \rho^f K_f}{\partial t} &= -\frac{\partial \rho^f K_f \tilde{u}_j^f}{\partial x_j} + \rho^f(1-\bar{c})\tilde{u}_i^f g_i - \overline{(1-c)u_i^f \frac{\partial P^f}{\partial x_i}} - \beta\overline{cu_i^f\left(u_i^f - u_i^s\right)} \\ &\quad -\frac{1}{2}\frac{\partial \rho^f \overline{(1-c)u_i^f u_i^f \Delta u_j^f}}{\partial x_j} + \overline{u_i^f \frac{\partial (1-c)T_{ij}^f}{\partial x_j}} + \overline{u_i^f \frac{\partial (1-c)T_{ij}^f}{\partial x_j}}\end{aligned} \tag{A.8}$$

The governing equation for $\tilde{K}$ is found by multiplying the Favre-averaged fluid momentum equation by $\tilde{u}_i^f$. The Favre-averaged momentum equation being:

$$\begin{aligned}\frac{\partial \rho^f(1-\bar{c})\tilde{u}_i^f}{\partial t} + \frac{\partial \rho^f(1-\bar{c})\tilde{u}_i^f \tilde{u}_j^f}{\partial x_j} &= \rho^f(1-\bar{c})g_i - (1-\bar{c})\frac{\partial \bar{P}^f}{\partial x_i} + \overline{c'\frac{\partial P^{f\prime}}{\partial x_i}} \\ &\quad -\beta\bar{c}\left(\tilde{u}_i^f - \tilde{u}_i^s\right) - \beta\overline{c\Delta u_i^f} \\ &\quad +\frac{\partial}{\partial x_j}\left(R_{ij}^f + \overline{(1-c)T_{ij}^f}\right)\end{aligned} \tag{A.9}$$

we obtain:

$$\begin{aligned}\frac{\partial \rho^f \tilde{K}_f}{\partial t} + \frac{\partial \rho^f \tilde{K}_f \tilde{u}_j^f}{\partial x_j} &= \rho^f(1-\bar{c})\tilde{u}_i^f g_i \\ &\quad -\left[(1-\bar{c})\tilde{u}_i^f \frac{\partial \bar{P}^f}{\partial x_i} - \tilde{u}_i^f \overline{c'\frac{\partial P'^f}{\partial x_i}}\right] \\ &\quad +\tilde{u}_i^f \frac{\partial}{\partial x_j}\left[\overline{(1-c)T_{ij}^f} + R_{ij}^f\right] \\ &\quad -\beta\left[\bar{c}\tilde{u}_i^f\left(\tilde{u}_i^f - \tilde{u}_i^s\right) + \tilde{u}_i^f \overline{c\Delta u_i^f}\right]\end{aligned} \tag{A.10}$$

Substracting equation A.10 from equation A.9 we obtain an equation governing the turbulence kinetic energy,

$$\frac{\partial \rho^f(K_f - \tilde{K}_f)}{\partial t} + \frac{\partial \rho^f(K_f - \tilde{K}_f)\tilde{u}_j^f}{\partial x_j} = -\mathcal{R}_1 + \mathcal{R}_2 - \mathcal{R}_3 - \frac{1}{2}\frac{\partial \rho^f \overline{(1-c)u_i^f u_i^f \Delta u_j^f}}{\partial x_j} \tag{A.11}$$

where

$$\mathcal{R}_1 = \overline{(1-c)u_i^f \frac{\partial P^f}{\partial x_i}} - (1-\bar{c})\tilde{u}_i^f \frac{\partial \bar{P}^f}{\partial x_i} + \tilde{u}_i^f \overline{c'\frac{\partial P'^f}{\partial x_i}} \tag{A.12}$$

is the pressure term,

$$\mathcal{R}_2 = \overline{u_i^f \frac{\partial (1-c) T_{ij}^f}{\partial x_j}} - \tilde{u}_i^f \frac{\partial}{\partial x_j} \left[\overline{(1-c) T_{ij}^f} + R_{ij}^f \right] \tag{A.13}$$

is the stress term and

$$\mathcal{R}_3 = \beta \left[\overline{c u_i^f \left(u_i^f - u_i^s \right)} - \bar{c} \tilde{u}_i^f \left(\tilde{u}_i^f - \tilde{u}_i^s \right) - \tilde{u}_i^f \overline{c \Delta u_i^f} \right] \tag{A.14}$$

is the drag term. Because of the definitions of the concentration weighted average, gravity does not contribute to the balance of the turbulent kinetic energy. All three terms (pressure, stress and drag) can be simplified and written as follows:

$$\mathcal{R}_1 = \overline{(1-c) \Delta u_i^f \frac{\partial P'^f}{\partial x_i}} \tag{A.15}$$

$$\mathcal{R}_2 = \overline{\Delta u_i^f \frac{\partial (1-c) T_{ij}^f}{\partial x_j}} - \tilde{u}_i^f \frac{\partial R_{ij}^f}{\partial x_j} \tag{A.16}$$

$$\mathcal{R}_3 = \beta \left[\left(\tilde{u}_i^f - \tilde{u}_i^s \right) \overline{c \Delta u_i^f} + \overline{c \Delta u_i^f \left(\Delta u_i^f - \Delta u_i^s \right)} \right] \tag{A.17}$$

The balance equation for the turbulence kinetic energy is then given by

$$\begin{aligned} \frac{\partial \rho^f (1-\bar{c}) k_f}{\partial t} = & -\frac{\partial \rho^f (1-\bar{c}) k_f \tilde{u}_j^f}{\partial x_j} + R_{ij}^f \frac{\partial \tilde{u}_i^f}{\partial x_j} - \rho^f (1-\bar{c}) \varepsilon_f + \frac{\partial Q_j^f}{\partial x_j} + \overline{P'^f \frac{\partial \Delta u_j^f}{\partial x_j}} \\ & -\beta \overline{c \Delta u_j^f} \left(\tilde{u}_j^f - \tilde{u}_j^s \right) - \beta \overline{c \Delta u_j^f \left(\Delta u_j^f - \Delta u_j^s \right)} \end{aligned} \tag{A.18}$$

where ε_f is the fluid turbulent dissipation rate

$$\varepsilon_f = \frac{1}{\rho^f (1-\bar{c})} \overline{(1-\bar{c}) T_{ij}^f \frac{\partial \Delta u_i^f}{\partial x_j}} \tag{A.19}$$

and Q_j^f is the energy flux

$$Q_j^f = \overline{T_{ij}^f (1-\bar{c}) \Delta u_i^f} - \frac{\rho^f}{2} \overline{(1-c) \Delta u_i^f \Delta u_i^f \Delta u_j^f} - \overline{(1-c) \Delta u_j^f P^{f'}} \tag{A.20}$$

A.2 $k - \varepsilon$ modeled equations

The equation just derived does reduce to the balance equation for turbulence kinetic energy of a clear fluid when the concentration reaches zero. Due to lack of

information, the correlation between the pressure fluctuation and the divergence of the velocity fluctuations will be neglected. We will follow modelling efforts made for clear fluids to express both the energy flux and the turbulent dissipation rate. The energy flux is modelled with a gradient diffusion hypothesis as

$$Q_j^f = \left(\nu + \frac{\nu_T}{\sigma_k}\right) \frac{\partial \rho^f (1-\bar{c}) k_f}{\partial x_j} \tag{A.21}$$

while the turbulent dissipation rate is determined by a balance equation taken to be similar to that of clear fluid turbulence:

$$\begin{aligned} \frac{\partial \rho^f (1-\bar{c}) \varepsilon_f}{\partial t} &= -\frac{\partial \rho^f (1-\bar{c}) \varepsilon_f \tilde{u}_i^f}{\partial x_i} + C_{\varepsilon 1} \frac{\varepsilon_f}{k_f} R_{ij}^f \frac{\partial \tilde{u}_i^f}{\partial x_j} - C_{\varepsilon 2} \frac{\varepsilon_f}{k_f} \rho^f (1-\bar{c}) \varepsilon_f \\ &\quad - C_{\varepsilon 3} \frac{\varepsilon_f}{k_f} \beta \left[\overline{c \Delta u_j^f} \left(\tilde{u}_j^f - \tilde{u}_j^s \right) + \overline{c \Delta u_j^f \left(\Delta u_j^f - \Delta u_j^s \right)} \right] \\ &\quad + \frac{\partial}{\partial x_i} \left[\left(\nu + \frac{\nu_T}{\sigma_\varepsilon} \right) \frac{\partial \rho^f (1-\bar{c}) \varepsilon_f}{\partial x_i} \right] \end{aligned} \tag{A.22}$$

The interphase momentum transfer contributes in both the turbulent kinetic energy and the turbulent dissipation rate equations. One term involves the turbulent suspension per se and the averaged velocities. The second term correlates the fluid velocity fluctuations and the sediment velocity fluctuations, and is an important additional dissipative term. This term will be modelled similarly to *Hsu et al.* (2004). The balance equations for the turbulent kinetic energy and the turbulent dissipation rate can then be written as

$$\begin{aligned} \frac{\partial \rho^f (1-\bar{c}) k_f}{\partial t} &= -\frac{\partial \rho^f (1-\bar{c}) k_f \tilde{u}_j^f}{\partial x_j} + R_{ij}^f \frac{\partial \tilde{u}_i^f}{\partial x_j} - \rho^f (1-\bar{c}) \varepsilon_f \\ &\quad + \frac{\partial}{\partial x_j} \left[\left(\nu + \frac{\nu_T}{\sigma_k} \right) \frac{\partial \rho^f (1-\bar{c}) k_f}{\partial x_j} \right] \\ &\quad + \beta \left[\frac{\nu_T}{\sigma_c} \frac{\partial \bar{c}}{\partial x_j} \left(\tilde{u}_j^f - \tilde{u}_j^s \right) - 2(1-\alpha) \bar{c} k_f \right] \end{aligned} \tag{A.23}$$

and

$$\begin{aligned}\frac{\partial \rho^f (1-\bar{c})\varepsilon_f}{\partial t} &= -\frac{\partial \rho^f (1-\bar{c})\varepsilon_f \tilde{u}_i^f}{\partial x_i} + C_{\varepsilon 1}\frac{\varepsilon_f}{k_f} R_{ij}^f \frac{\partial \tilde{u}_i^f}{\partial x_j} - C_{\varepsilon 2}\frac{\varepsilon_f}{k_f}\rho^f (1-\bar{c})\varepsilon_f \\ &+\frac{\partial}{\partial x_i}\left[\left(\nu + \frac{\nu_T}{\sigma_\varepsilon}\right)\frac{\partial \rho^f (1-\bar{c})\varepsilon_f}{\partial x_i}\right] \\ &+C_{\varepsilon 3}\frac{\varepsilon_f}{k_f}\beta\left[\frac{\nu_T}{\sigma_c}\frac{\partial \bar{c}}{\partial x_j}\left(\tilde{u}_j^f - \tilde{u}_j^s\right) - 2(1-\alpha)\bar{c}k_f\right] \end{aligned} \tag{A.24}$$

where α is a parameter that measures the degree of correlation between the fluid velocity fluctuations and the sediment velocity fluctuations and is a function of various time scales in the two-phase system. For the dilute flow model, only the particle response time $T_P = \rho^s/\beta$, which is a measure of the time needed to accelerate a single particle from rest to the surrounding fluid velocity, and the fluid turbulence time scale $T_F = 0.165 k_f/\varepsilon_f$ are involved:

$$\alpha = \frac{1}{1 + T_p/T_F}. \tag{A.25}$$

For the sheet flow model, the time between collisions also has to be considered:

$$\alpha = \frac{1}{1 + T_p/\min(T_F, T_c)}. \tag{A.26}$$

the time between collisions is given bys

$$t_c = \frac{l_c}{\sqrt{k_s}} \tag{A.27}$$

with l_c the mean free path

$$l_c = \frac{\sqrt{\pi} d}{24 G_0} \tag{A.28}$$

APPENDIX B

ONE DIMENSIONAL NUMERICAL MODEL

B.1 Computational mesh

The two-phase governing equations presented in chapters 4 and 5 have been incorporated into a wave-hydrodynamic model called COBRAS (*Lin and Liu*, 1998a,b) and are solved by a finite difference scheme on a staggered grid system (*Hsu and Liu*, 2004). In such a system, the fluid horizontal velocity $\tilde{u}^f$, the sediment horizontal velocity $\tilde{u}^s$ and the scalar quantities (concentration $\bar{c}$, fluid pressure $\bar{P}^f$, fluid turbulent kinetic energy k_f, fluid turbulence dissipation rate ε_f and the sediment fluctuation energy k_s) are all defined at the grid center. The vertical fluid and sediment velocities $\tilde{w}^f$ and $\tilde{w}^s$ are defined at the top-face of the cell.

For the one-dimensional model, only the variations of the flow quantities in the vertical direction are solved for. Consequently, the computational domain consists of a single column of cells (figure B.1). For boundary conditions purposes, ghost cells are added at the top and bottom of the domain. Two ghost columns are also added in order to implement the horizontal boundary conditions and the horizontal pressure gradient that drives the flow.

B.2 Computational cycle

The sediment phase equations are solved at the beginning of the computational cycle using a predictor-corrector scheme. After the sediment concentration, sediment velocities and fluctuation energy are found, the two-step projection method (modified for two-phase equations) is used to solve for the fluid pressure and fluid phase velocities. Finally, the $k-\varepsilon$ equations for fluid turbulence are updated at the end of the computational cycle.

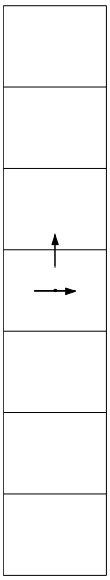

Figure B.1: Grid for the one-dimensional problem.

B.2.1 Predictor-corrector scheme for the sediment equations

Because of the singularity of the sediment equations when the concentration approaches zero, the one-dimensional sediment phase equations (equations 4.2, 4.5 and 4.6 or equations 5.2, 5.5, 5.6 and 3.56) are solved for the horizontal sediment flux $U^s = \rho^s \bar{c} \tilde{u}^s$, the sediment vertical flux $W^s = \rho^s \bar{c} \tilde{w}^s$ and $K^s = \rho^s \bar{c} k_s$. The sediment velocities and fluctuation energy are then updated from the values of $\bar{c}$, U^s, W^s and K^s.

At each time step, tentative values for $\bar{c}$, U^s, W^s and K^s are calculated from the information at the previous time step during the predictor step. Then in the corrector step, "final" values are calculated from the values at the previous time step and the values found in the predictor step. This corrector step is repeated until a predetermined convergence criterion is satisfied. More details on both the predictor step and corrector step calculations are available in *Hsu* (2002).

B.2.2 Two-step projection method

The two fluid momentum equations (equations 4.3 and 4.4 or equations 5.3 and 5.4) are solved by a two-step projection method. For the one dimensional model, the flow is driven by a given horizontal pressure gradient that can be a function of time. As such, the pressure term in the horizontal fluid momentum equation is known and the equation can be solved. For the vertical fluid momentum equation, the pressure term is unknown and solved along with the momentum equation using the two-step projection method (*Hsu*, 2002). In this method, a tentative vertical fluid velocity is calculated without the pressure term. The pressure at the new time step is then found by solving the Pressure Poisson Equation, which for the one-dimensional model reduces to solving a tridiagonal matrix equation and it done using the Thomas algorithm. Finally, the vertical velocity at the new time step is found by updating the tentative vertical velocity with the pressure term of the momentum equation.

More details on the numerical discretization used in the one-dimensional model are presented in *Hsu* (2002).

B.3 Initial condition

It has to be noted that the current model can not accurately describe the initiation of sediment motion. An artificial initial condition is thus specified. A linear profile of sediment concentration that decreases from $c^\star$ at the bed is prescribed as the initial concentration profile. The sediment and fluid velocities are initially set to zero. The flow is then first calculated with the vertical sediment velocity remaining zero (*Hsu*, 2002). After this initial process, the numerical model is driven by a horizontal pressure gradient determined so that the numerical and experimental

free stream velocities match.

B.4 Dilute model and sheet flow model

Although both the one dimensional dilute flow model and the sheet flow model are numerically implemented in similar fashion, there remains one important difference in the bottom boundary condition. Since the concentrated region is not resolved in the dilute model, the bottom of the computational domain will be taken some distance above the undisturbed bed (see figure 4.1). The boundary condition there is an integral part of the dilute model and is discussed in chapter 4, as well as its numerical implementation (discussed in section 4.3). In the sheet flow model (chapter 5), the concentrated region is resolved and the bottom boundary is located some distance within the undisturbed bed. The location is chosen so that a layer of motionless sediment remains at all times. The location of the bed is part of solution and is calculated using a Coulomb failure criterion. A direct consequence is that no bottom boundary condition is really necessary for the sediment phase quantities (they are all known and constant). Although different boundary conditions for the fluid phase could be implemented, the fluid quantities will naturally be very small in the sediment bed and the bottom boundary condition has no effect on the results above the bed. More specifically, this means that the constants specified for the logarithmic law in the dilute model (K_s and κ) do not influence the results.

BIBLIOGRAPHY

Ahmed, A. M., and S. Elghobashi (2000), On the mechanisms of modifying the structure of turbulent homogeneous shear flows by dispersed particles, *Phys. Fluids*, *12*(11), 2906–2930.

Asano, T. (1990), Two-phase flow model on oscillatory sheet flow, in *Proc. 22nd Int. Conf. of Coastal Engrg.*, pp. 2372–2384, ASCE.

Asano, T. (1995), Sediment transport under sheet-flow conditions, *J. Waterw. Port Coastal Ocean Eng.*, *121*(5), 239–246.

Bagnold, R. A. (1954), Experiments on a gravity-free dispersion of large solid spheres in a newtonian fluid under shear, *Proc. Roy. Soc. London, Ser. A*, *225*, 49–63.

Bagnold, R. A. (1966), An approach to the sediment transport problem from general physics, *Geological Survey Professional Paper*, *422-I*.

Bailard, J. A. (1981), An energetics total load sediment trasnport model for a plane sloping beach, *J. Geophys. Res.*, *86*(C11), 10,938–10,954.

Bennett, S. J., J. S. Bridge, and J. L. Best (1998), Fluid and sediment dynamics of upper stage plane beds, *J. Geophys. Res.*, *103*(C1), 1239–1274.

Bocquet, L., W. Losert, D. Schalk, T. C. Lubensky, and J. P. Gollub (2001), Granular shear flow dynamics and forces: experiment and continuum theory, *Phys. Rev. E*, *65*, doi:10.1103/PhysRevE.65.011307.

Breusers, H. N. C. (1966), Conformity and time scale in two-dimensional local scour, in *Proc. Symp. on model and prototype conformity, Hydr. Res. Lab.., Poona, India*, pp. 1–8.

Breusers, H. N. C. (1967), Time scale of two-dimensional local scour, in *Proc. 12th IAHR Congress, Ft. Collins*, 3, pp. 275–282.

Breusers, H. N. C., and A. J. Raudkivi (1991), *Scouring*, A. A. Balkema, Rotterdam.

Brørs, B. (1999), Numerical modeling of flow and scour at pipelines, *J. Hydraul. Eng.*, *125*(5), 511–523.

Buchko, M., P. Kolkman, and K. Pilarczyk (1987), Investigation of ocal scour in cohesionless sediments using a tunnel-model, in *Proc. 22nd Congress IAHR, Lausanne, Switzerland*, pp. 233–239.

Calantoni, J., K. T. Holland, and T. G. Drake (2004), Modelling sheet-flow sediment transport in wave-bottom boundary layers using discrete-element modelling, *Philos. Trans. Roy. Soc. London, A: Mathematical, Physical and Engineering Sciences*, *362*(1822), 1987–2001.

Carpen, I. C., and J. F. Brady (2002), Gravitational instability in suspension flow, *J. Fluid Mech.*, *472*, 201–210.

Chang, Y. S., and A. Scotti (2006), Turbulent convection of suspended sediments due to flow reversal, *J. Geophys. Res.*, *111*(C7), doi:10.1029/2005JC003240.

Chapman, S., and T. G. Cowling (1970), *The mathematical theory of non-uniform gases*, 3rd ed. ed., Cambridge University Press.

Chorin, A. J. (1968), Numerical solution of the navier-stokes equations, *Mathematics of Computation*, *22*(104), 745–762.

Crossett, K. M., T. J. Culliton, P. C. Wiley, and T. R. Goodspeed (2004), Popu-

lation trends along the coastal united states: 1980–2008, *Coastal trends report series*, NOAA.

Crowe, C. T., T. R. Troutt, and J. N. Chung (1996), Numerical models for two-phase turbulent flows, *Annu. Rev. Fluid Mech.*, *28*, 11–43.

Davies, A. G., R. L. Soulsby, and H. L. King (1988), A numerical model of the combined wave and current bottom boundary layer, *J. Geophys. Res.*, *93*(C1), 491–508.

Dibajnia, M., and A. Wanatabe (1992), Sheet flow under nonlinear waves and currents, in *Proc. 23rd Int. Conf. Coastal Eng.*, pp. 2015–2028.

Dietz, J. W. (1969), Kolkbildung in feinen oder elichten sohlmaterialien bei strömen dem abfluss, in *Mitteilungen des Theodor Rehbok Flussbaulaboratorium*, pp. 1–122.

Dohmen-Janssen, C. M., and D. M. Hanes (2002), Sheet flow dynamics under monochromatic nonbreaking waves, *J. Geophys. Res.*, *107*(C10), doi: 10.1029/2001JC001045.

Dohmen-Janssen, C. M., W. N. Hassan, and J. S. Ribberink (2001), Mobile-bed effects in oscillatory sheet flow, *J. Geophys. Res.*, *106*(C11), 27,103–27,115.

Dohmen-Janssen, C. M., D. F. Kroekenstoel, W. N. Hassan, and J. S. Ribberink (2002), Phase lags in oscillatory sheet flow: experiments and bed load modeling, *Coastal Eng.*, *46*, 61–87.

Dong, P., and K. Zhang (1999), Two-phase flow modeling of sediment motions in oscillatory sheet flow, *Coastal Eng.*, *36*, 87–109.

Dong, P., and K. Zhang (2002), Intense near-bed sediment motions in waves and currents, *Coastal Eng.*, *45*, 75–87.

Drake, T. G., and J. Calantoni (2001), Discrete particle model for sheet flow sediment transport in the nearshore, *J. Geophys. Res.*, *106*(C9), 19,859–.

Drew, D. A. (1983), Mathematical modeling of two-phase flow, *Ann. Rev. Fluid Mech.*, *15*, 261–291.

Drew, D. A., and R. T. Lahey (1979), Application of general constitutive principles to the derivation of multidimensional two-phase flow equations, *Int. J. Multiphase Flow*, *5*, 243–264.

Drew, D. A., L. Cheng, and R. T. Lahey (1979), The analysis of virtual mass effects in two-phase flow, *Int. J. Multiphase Flow*, *5*, 233–242.

Dudley, R. D. (2007), A boroscopic quantitative technique for sheet flow measurements, Master's thesis, Cornell University.

Einstein, H. A. (1950), The bed-load function for sediment transportation in open channel flows, *Technical Bulletin 1026*, USDA.

Elghobashi, S. (1994), On predicting particle-laden turbulent flows, *Applied Scientific Research*, *52*, 309–329.

Elghobashi, S. E., and T. W. Abou-Arab (1983), A two-equation turbulence model for two-phase flows, *Phys. Fluids*, *26*(4), 931–938.

Engelund, F., and J. Fredsøe (1976), A sediment transport model for straight alluvial channels, *Nordic Hydrology*, *7*, 293–306.

Favre, A. (1965), Equations des gaz turbulents compressibles, *J. de Mécanique*, *4*(3), 361–390.

Fredsøe, J. (1984), Turbulent boundary layer in wave-current motion, *J. Hydraul. Eng.*, *110*(8), 1103–1120.

Fredsoe, J., and R. Deigaard (1992), *Mechanics of Coastal Sediment Transport*, World Scientific, Singapore.

Garcia, M., and G. Parker (1991), Entrainment of bed sediment into suspension, *J. Hydraul. Eng.*, *117*(4), 414–435.

Gore, R. A., and C. T. Crowe (1989), Effect of particle size on modulating turbulent intensity, *Int. J. Multiphase Flow*, *15*(2), 279–285.

Grant, W. D., and O. S. Madsen (1979), Combined wave and current interaction with a rough bottom, *J. Geophys. Res.*, *84*(C4), 1797–1808.

Greimann, B. P., and F. M. Holly (2001), Two-phase flow analysis of concentration profiles, *J. Hydraul. Eng.*, *127*(9), 753–762.

Greimann, B. P., M. Muste, and F. M. Holly (1999), Two-phase formulation of suspended sediment transport, *J. Hydrau. Res.*, *37*(4), 479–500.

Guizien, K., C. M. Dohmen-Janssen, and G. Vittori (2003), 1DV bottom boundary layer modeling under combined wave and current: Turbulent separation and phase lag effects, *J. Geophys. Res.*, *108*(C1), doi:10.1029/2001JC001292.

Hagatun, K., and K. J. Eidsvik (1986), Oscillating turbulent boundary layer with suspended sediments, *J. Geophys. Res.*, *91*(C11), 13,045–13,055.

Hanes, D. M., and D. L. Inman (1985a), Observations of rapidly flowing granular-fluid materials, *J. Fluid Mech.*, *150*, 357–380.

Hanes, D. M., and D. L. Inman (1985b), Experimental evaluation of a dynamic yield criterion for granular fluid flows, *J. Geophys. Res.*, *90*(B5), 3670–3674.

Harris, C. K., and P. L. Wiberg (2001), A two-dimensional, time-dependent model of suspended sediment transport and bed reworking for continental shelves, *Computers and Geosciences*, *27*, 675–690.

Hassan, W. N., and J. S. Ribberink (2005), Transport processes of uniform and mixed sands in oscillatory sheet flow, *Coastal Eng.*, *52*, 745–770.

Hatton, K. A., D. L. Foster, P. Traykovski, and H. D. Smith (2007), Numerical simulations of the flow and sediment transport regimes surrounding a short cylinder, *IEEE J. of Oceanic Eng.*, *32*(1), 249–259.

Hetsroni, G. (1989), Particle-turbulence interaction, *Int. J. Multiphase Flow*, *15*(5), 735–746.

Hoffmans, G. C., and R. Booij (1993), The influence of upstream turbulence on local-scour holes, in *Proc. 25th IAHR Congr.*, pp. 471–478.

Hoffmans, G. J. C. M., and K. W. Pilarczyk (1995), Local scour downstream of hydraulic structures, *J. Hydraul. Eng.*, *121*(4), 326–340.

Horikawa, K., A. Wanatabe, and S. Katori (1982), Sediment transport under sheet flow condition, in *Proc. 18th Int. Conf. of Coastal Engrg.*, pp. 1335–1352, ASCE.

Hsu, T.-J. (2002), A two-phase flow approach for sediment transport, Ph.D. thesis, Cornell University.

Hsu, T.-J., and D. M. Hanes (2004), Effects of wave shape on heet flow sediment transport, *J. Geophys. Res.*, *109*(C05025), doi:10.1029/2003JC002075.

Hsu, T.-J., and P. L.-F. Liu (2004), Toward modeling turbulent suspension of sand in the nearshore, *J. Geophys. Res.*, *109*, C06018, doi:10.1029/2003JC002240.

Hsu, T.-J., J. T. Jenkins, and P. L.-F. Liu (2003a), On two-phase sediment transport: Dilute flow, *J. Geophys. Res.*, *108(C3)*, doi:10.1029/2001JC001276.

Hsu, T.-J., J. T. Jenkins, and P. L.-F. Liu (2004), On two-phase sediment transport: sheet flow of massive particles, *Proc. Roy. Soc. London, Ser. A*, *460*, doi:10.1098/rspa.2003.1273.

Hsu, T.-J., S. Elgar, and R. T. Guza (2006), Wave-induced sediment transport and onshore sandbar migration, *Coastal Eng.*, *53*, 817–824.

Hsu, T.-W., H.-K. Chang, and C.-M. Hsieh (2003b), A two-phase flow model of wave-induced sheet flow, *J. Hydrau. Res.*, *41*(3), 299–310.

Janssen, C. M. (1999), Grain size influence on sediment transport in oscillatory sheet flow, phase lags and mobile-bed effects, Ph.D. thesis, Delft Univiversity of Technology.

Jenkins, J. T. (1998), Kinetic theory for nearly elastic spheres, in *Physics of dry granular media*, edited by H. J. H. et al., pp. 353–369, Kluwer Academic Publishers.

Jenkins, J. T., and D. M. Hanes (1998), Collisional sheet flows of sediment driven by a turbulent fluid, *J. Fluid Mech.*, *370*, 29–52.

Jenkins, J. T., and S. B. Savage (1983), A theory for the rapid flow of identical, smooth, nearly elastic, spherical particles, *J. Fluid Mech.*, *130*, 187–202.

Jensen, B. L., B. M. Sumer, and J. Fredsøe (1989), Turbulent oscillatory boundary layers at high reynolds numbers, *J. Fluid Mech.*, *206*, 265–297.

Jensen, B. L., B. M. Sumer, H. R. Jensen, and J. Fredsøe (1990), Flow around and

forces on a pipeline near a scoured bed in steady current, *J. Offshore Mech. and Arctic Eng.*, *112*, 206–213.

Jiang, J., A. W.-K. Law, and N.-S. Cheng (2004), Two-phase modeling of suspended sediment distribution in open channel flows, *J. Hydrau. Res.*, *42*(3), 273–281.

Jonsson, I. G. (1966), Wave boundary layers and friction factors, in *Proc. 10th Int. Conf. on Coastal Eng.*

Katopodi, I., J. Ribberink, P. Ruol, R. Koelewijn, C. Lodahl, S. Longo, A. Crosato, and H. Wallace (1994a), Intra-wave sediment transport in an oscillatory flow superimposed on a mean current, *Report H1684.33*, Delft Hydraulics, part III.

Katopodi, I., J. S. Ribberink, P. Ruol, and C. Lodahl (1994b), Sediment transport measurements in combined wave-current flows, in *Coastal dynamics*, pp. 837–851.

Kobayashi, N., and B. D. Johnson (2001), Sand suspension, storage, advection, and settling in surf and swash zones, *J. Geophys. Res.*, *106*(C5), 9363–9376.

Kobayashi, N., and S. N. Seo (1985), Fluid and sediment interaction over a plane bed, *J. Hydraul. Eng.*, *111*(6), 903–921.

Landry, B. J., M. J. Hancock, and C. C. Mei (2007), Note on sediment sorting in a sandy bed under standing water waves, *Coastal Eng.*, *54*, 694–699.

Leatherman, S. P., B. C. Douglas, and J. L. LaBrecque (2003), Sea level and coastal erosion require large-scale monitoring, *EOS*, *84*(2).

Lees, B. J. (1981), Relationship between eddy viscosity of seawater and eddy diffusivuty of suspended particles, *Geo-Marine Lett.*, *1*, 249–254.

Lin, P., and P. L.-F. Liu (1998a), A numerical study of breaking waves in the surf zone, *J. Fluid Mech.*, *359*, 239–264.

Lin, P., and P. L.-F. Liu (1998b), Turbulence transport, vorticity dynamics, and solute mixing under plunging breaking waves in surf zone, *J. Geophys. Res.*, *103*(15), 677–694.

Liu, H., and S. Sato (2005), Modeling sediment movement under sheetflow conditions using a two-phase flow approach, *Coastal Engineering Journal*, *47*(4), 255–284.

Liu, H., and S. Sato (2006), A two-phase flow model for asymmetric sheetflow conditions, *Coastal Eng.*, *53*, 825–843.

Longo, S. (2005), Two-phase flow modeling of sediment motion in sheet-flows above plane beds, *J. Hydraul. Eng.*, *131*(5), 366–379.

Madsen, O. S., and W. D. Grant (1976), Quantitative description of sediment transport by waves, in *Proc. 15th Int. Conf. Coastal Eng.*, pp. 1093–1112.

McEwan, I. K., B. J. Jefcoate, and B. B. Willetts (1999), The grain-fluid interaction as a self-stabilizing mechanism in fluvial bed load transport, *Sedimentology*, *46*, 407–416.

McLean, S. R., J. S. Ribberink, C. M. Dohmen-Janssen, and W. N. Hassan (2001), Sand transport in oscillatory sheet flow with mean current, *J. Waterw. Port Coastal Ocean Eng.*, *127*(3), 141–151.

McTigue, D. F. (1981), Mixture theory for suspended sediment transport, *Jounal of the Hydraulics Division, Proc. ASCE*, *107*(HY6), 659–673.

Meyer-Peter, E., and R. Müller (1948), Formulas for bed-load transport, in *Proc. 2nd IAHR Congress, Stockholm.*

Minh Duc, B., T. Wenka, and W. Rodi (2004), Numerical modeling of bed deformation in laboratory channels, *J. Hydraul. Eng.*, *130*(9), 894–904.

Nielsen, P. (1992), *Coastal bottom boundary layers and sediment transport*, World Scientific, Singapore.

O'Donoghue, T., and S. Wright (2004), Concentrations in oscillatory sheet flow for well sorted and graded sands, *Coastal Eng.*, *50*, 117–138.

O'Hare, T. J., and A. G. Davies (1990), A laboratory study of sand bar evolution, *J. Coastal Res.*, *6*(3), 531–544.

O'Hare, T. J., and A. G. Davies (1993), Sand bar evolution beneath partially-standing waves: laboratory experiments and model simulations, *Cont. Shelf Res.*, *13*(11), 1149–1181.

Pan, Y., and S. Banerjee (1996), Numerical simulation of particle interactions with wall turbulence, *Phys. Fluids*, *8*(10), 2733–2755.

Pope, S. B. (2000), *Turbulent Flows*, first ed., Cambridge University Press, New York.

Rashidi, M., G. Hetsroni, and S. Banerjee (1990), Particle-turbulence interaction in a boundary layer, *Int. J. Multiphase Flow*, *16*(6), 935–949.

Ribberink, J. S. (1998), Bed-load trasnport for steady flows and unsteady oscillatory flows, *Coastal Eng.*, *34*, 59–82.

Ribberink, J. S., and A. A. Al-Salem (1994), Sediment transport in oscillatory boundary layers in cases of rippled beds and sheet flow, *J. Geophys. Res.*, *99*(C6), 12,707–12,727.

Ribberink, J. S., and A. A. Al-Salem (1995), Sheet flow and suspension of sand in oscillatory boundary layers, *Coastal Eng.*, *25*, 205–225.

Richardson, J. F., and W. N. Zaki (1954), Sedimentation and fluidization, *Trans. Instn. Chem. Egnrs.*, *32*, 35–53.

Rogers, C. B., and J. K. Eaton (1991), The effect of small particles on fluid turbulence in a flat-plate, turbulent boundary layer in air, *Phys. Fluids*, *A3*(5), 928–937.

Rose, C. P., and P. D. Thorne (2001), Measurements of suspended sediment transport parameters in a tidal estuary, *Cont. Shelf Res.*, *21*, 1551–1575.

Rouse, H. (1937), Modern conceptions of the mechanics of fluid turbulence, *Transactions, ASCE*, *102*(Paper No. 1965), 463–543.

Savage, S. B., and S. McKeown (1983), Shear stresses developed during rapid shear of concentrated suspensions of large spherical particles between concentric cylinders, *J. Fluid Mech.*, *127*, 453–472.

Savioli, J., and P. Justesen (1996), Sediment in oscillatory flows over a plane bed, *J. Hydrogr. Res.*, *35*(2), 177–190.

Sekine, M., and H. Kikkawa (1990), Mechanics of saltating grains II, *J. Hydraul. Eng.*, *118*(4), 536–558.

Shibayama, T., and K. Horikawa (1982), Sediment transport and beach transformation, in *Proc. 18th Int. Conf. Coastal Eng.*, pp. 1439–1458.

Shields, I. A. (1936), Anwendung der Aehnlichkeitsmechanik and der Turbulenzforschung auf die Geschiebebewegung, *Mitt. Preuss. Versuchanstalt.*

Sleath, J. F. A. (1978), Measurements of bed load in oscillatory flow, *J. Waterw. Port Coastal Ocean Eng.*, *104*(WW4), 291–307.

Sleath, J. F. A. (1994), Sediment transport in oscillatory flow, in *Sediment transport mechanisms in coastal environments and rivers*, edited by M. Belorgey, R. D. Rajaona, and J. F. A. Sleath, World Scientific.

Small, C., and J. E. Cohen (2004), Continental physiography, climate, and the global distribution of human population, *Current Anthropology*, *45*(2), 269–277.

Squires, K. D., and J. K. Eaton (1994), Effect of selective modification of turbulence on two-equation models for particle-laden turbulent flows, *Journal of Fluids Engineering*, *116*, 778–784.

Sumer, B. M., and J. Fredsøe (1990), Scour below pipelines in waves, *J. Waterw. Port Coastal Ocean Eng.*, *116*(3), 307–323.

Sumer, B. M., and J. Fredsøe (2002), *The mechanics of scour in the marine environment*, World Scientific.

Sumer, B. M., A. Kozakiewicz, J. Fredsoe, and R. Deigaard (1996), Velocity and concentration profiles in sheet-flow layer of movable bed, *J. Hydraul. Eng.*, *122*(10), 549–558.

Swart, D. H. (1974), Offshore sediment transport and equilibrium beach profile, *Delft.Hydr. Lab. Publ. 131*, Delft Hydraulics.

Torquato, S. (1995), Nearest-neighbor statistics for packing of hard spheres and disks, *Phys. Rev. E*, *51*(4), 3170–3182.

Trowbridge, J., and D. Young (1989), Sand transport by unbroken water waves under sheet flow conditions, *J. Geophys. Res.*, *94*(C8), 10,971–1091.

van Rijn, L. C. (1984a), Sediment transport, part I: Bed load transport, *J. Hydraul. Eng.*, *110*(10), 1431–1456.

van Rijn, L. C. (1984b), Sediment pickup functions, *J. Hydraul. Eng.*, *110*(10), 1494–1502.

van Rijn, L. C. (1984c), Sediment transport, part II: Suspended load transport, *J. Hydraul. Eng.*, *110*(11), 1613–1641.

Vanoni, V. A. (1975), *Sedimentation Engineering*, ASCE, New York.

Watanabe, A., Y. Riho, and K. Horikawa (1980), Beach profiles and on-offshore sediment transport, in *Proc. 17th Int. Conf. Coastal Eng.*, pp. 1106–1121.

Whitehouse, R. (1995), Observations of the boudary layer characteristics and the suspension of sand at a tidal site, *Cont. Shelf Res.*, *15*, 1549–1567.

Wiberg, P. L., and D. M. Rubin (1989), Bed roughness produced by saltating sediment, *J. Geophys. Res.*, *94*(C4), 5011–5016.

Wilson, K. C. (1966), Bed-load transport at high shear stress, *Journal of the hydraulics division*, *92*(HY6), 49–59.

Wilson, K. C. (1987), Analysis of bed load motion at high shear stresses, *J. Hydraul. Eng.*, *113*(1), 97–103.

Wilson, K. C. (1989), Friction of wave-induced sheet flow, *Coastal Eng.*, *12*, 371–379.

Winterwerp, J. C., and W. G. M. van Kesteren (2004), *Introduction to the physics of cohesive sediment in the marine environment*, Developments in Sedimentology 56, Elsevier.

Wu, W. (2004), Depth-averaged two-dimensional numerical modeling of unsteady flow and nonuniform sediment transport in open channels, *J. Hydraul. Eng.*, *130*(10), 1013–1024.

Yalin, M. S. (1977), *Mechanics of sediment transport*, 2nd ed., Pergamon Press.

You, Z.-J. (1999), The inception of sheet-flow in oscillatory flow, *Ocean Eng.*, *26*, 277–285.

Zala Flores, N., and J. F. A. Sleath (1998), Mobile layer in oscillatory sheet flow, *J. Geophys. Res.*, *103*(C6), 12,783–12,793.

Zedler, E. A., and R. L. Street (2006), Sediment transport over ripples in oscillatory flow, *J. Hydraul. Eng.*, *132*(2), 180–193.

Zhang, Y., and C. S. Campbell (1992), The interface between fluid-like and solid-like behaviour in two-dimensional granular flows, *J. Fluid Mech.*, *237*, 541–568.

Zhang, Y., and J. M. Reese (2003), Gas turbulence modulation in a two-fluid model for gas-solid flows, *AIChE Journal*, *49*(12), 3048–3065.

Zhang, Y., D. J. P. Swift, S. Fan, A. W. Niedoroda, and C. W. Reed (1999), Two-dimensional numerical modeling of storm deposition on the northern california shelf, *Marine Geology*, *154*, 155–167.

Zhao, Z., and H. J. S. Fernando (2007), Numerical simulation of scour around pipelines using an euler-euler coupled two-pahse model, *Environmental Fluid Mech.*, *7*, 121–142.